May 2020

Characterization of Water Pathways and Hydrolytic Weakening Within Naturally Deformed Quartz Grains Along the Willard Thrust Fault, Utah

Charles Alexander Martin
University of Wisconsin-Milwaukee

CHARACTERIZATION OF WATER PATHWAYS AND HYDROLYTIC WEAKENING WITHIN NATURALLY DEFORMED QUARTZ GRAINS ALONG THE WILLARD THRUST FAULT, UTAH

by

Charles A. Martin

A Thesis Submitted in

Partial Fulfillment of the

Requirements for the Degree of

Master of Science

in Geosciences

at

The University of Wisconsin-Milwaukee

May 2020

ABSTRACT

CHARACTERIZATION OF WATER PATHWAYS AND HYDROLYTIC WEAKENING WITHIN NATURALLY DEFORMED QUARTZ GRAINS ALONG THE WILLARD THRUST FAULT, UTAH

by

Charles A. Martin

The University of Wisconsin-Milwaukee, 2020
Under the Supervision of Professor Dyanna M. Czeck

Evidence of water infiltration was examined in naturally deformed quartzite clasts from diamictite of the Mineral Fork Formation sampled from Antelope Island in the Great Salt Lake, Utah. The diamictite deformed via subsimple shear in the footwall of the Willard thrust fault and displays spatial variations in strain intensity. Evidence of water infiltration was investigated utilizing three complimentary techniques: standard petrographic microscopy to identify microstructures and interpret deformation mechanisms; scanning electron microscopy cathodoluminescence (SEM-CL) to create maps of healed microfractures and subgrain boundaries related to pathways of fluid infiltration; and synchrotron-source Fourier-transform infrared spectroscopy (FTIR) to create micron-scale water absorbance maps in quartz grains. Integrated data from these techniques allowed for a comprehensive analysis of water pathways within quartz grains. At low strain, quartz grains exhibited healed microfractures, linear fluid inclusion traces, and microfractures, evidencing mostly brittle deformation. At moderate strain, quartz grains had more extensive healed microfracture networks, as well as undulose extinction and subgrains showing increased water infiltration and crystal plastic deformation. At high

strain, quartz grains exhibited extensive recrystallization, documenting intensified plastic deformation and resetting of microstructure with fewer microfractures present. FTIR data indicated two wavelength peaks related to infiltration of water within grains: liquid water at ~3400 cm^{-1} and OH groups contained within hydrous minerals such as mica at ~3600 cm^{-1}. Water identified at the ~3400 cm^{-1} peak is preferentially located along healed microfractures, whereas OH associated with the ~3600 cm^{-1} peak is primarily found along grain boundaries. These data indicate that water infiltrated grains through microfractures during progressive deformation. Water then entered the main crystal lattice, presumably through diffusion or movement along dislocations that intersected the microfractures, leading to increased crystal plasticity through hydrolytic weakening and strain softening. Through these progressive deformation processes, the deformation style evolved from primarily brittle to primarily ductile within the footwall of the thrust fault. This finding has important implications in relation to the understanding of crustal rheology. This study was one of the first of its kind to document the distribution of water in naturally deformed quartz grains. The innovative sample preparation technique and analysis should prove helpful to future investigators.

TABLE OF CONTENTS

LIST OF FIGURES

LIST OF TABLES

ACKNOWLEDGMENTS

I would like to thank the following:

Dr. Dyanna Czeck, my advising professor, for her guidance, patience, flexibility, and input. Her encouragement and assistance was instrumental to the completion of this thesis. I am extremely grateful for all her help.

Dr. Adolph Yonkee at Weber State University for his guidance during the fieldwork on Antelope Island. His knowledge of the area is unparalleled.

Dr. Barry Cameron and Dr. Lindsay McHenry for sitting on my thesis committee, lending their expertise for the improvement of my thesis.

My father, Dr. Thomas P. Martin, for his aid in providing edits and the motivation to keep moving forward. His help was indispensable to the completion of this thesis and I will be forever thankful.

My wife, Liz Martin, her support, sacrifice, and love are what made this all possible.

This research was funded by a UWM RGI Grant to Dyanna Czeck and used resources of the Advanced Light Source, a U.S. DOE Office of Science User Facility under contract no. DE-AC02-05CH11231.

Chapter 1: Introduction

The purpose of this study was to gain a better understanding of how water infiltration and hydrolytic weakening within the Willard thrust fault may be related to strain softening. This was done by analyzing quartz grains utilizing three complimentary techniques: standard petrographic microscopy to identify microstructures and interpret deformation mechanisms; scanning electron microscopy using a cathodoluminescence detector (SEM-CL) to create maps of healed microfractures and subgrain boundaries that may be related to pathways of fluid infiltration; and synchrotron-source Fourier-transform infrared spectroscopy (FTIR) to create micron-scale water absorbance maps of quartz grains. These findings were then used to examine how fluid infiltration could affect the interplay between brittle and ductile deformation, and therefore, the position of the brittle-ductile transition zone.

1.1 Fluids in Faults and Ductile Shear Zones

Continental fault zones are comprised of an upper seismogenic region dominated by frictional sliding and cataclastic deformation, and a lower, continuously creeping region dominated by quasiplastic deformation (Sibson, 1983). Byerlee (1968) termed the boundary between the two regions the brittle-ductile transition. Other names for this transition include the frictional quasiplastic transition (Sibson, 1983) and the brittle-plastic transition (Rutter, 1986). The brittle-ductile transition corresponds with the onset of dislocation creep in quartz at temperatures greater than 300 °C, which also corresponds with the lower limit of microseismic activity in continental regions (Sibson, 1984). The depth of the brittle-ductile transition

boundary is different for every fault system and is dependent on many factors including: geothermal gradient, lithology, water content, strain rate, effective pressure, and mode of faulting (Sibson, 1984). For this study, we are most interested in constraining the role water plays in the behavior of the fault system, especially at the brittle-ductile transition.

Faults can act as conduits or barriers to fluid flow depending on their accommodation features and whether they enhance or reduce permeability. Many brittle fault processes enhance the permeability of rocks within the frictional zone including particulate flow via deformation bands, fracturing, and brecciation; while other processes reduce permeability such as particulate flow via sediment mixing, phyllosilicate smearing, and cataclasis (Bense et al., 2013). Faults that have increased permeability can act as excellent conduits for fluids which in turn can affect the movement of the fault. Even trace quantities of water on the surfaces of faults markedly lowers the friction coefficient (Dieterich & Conrad, 1984). This is due to fracture surfaces adsorbing chemical species from aqueous solutions which reduces surface energies and therefore the critical stress for sliding (Dunning et al., 1984).

It is not difficult to understand how fluids are able to move through permeable brittle faults systems, however, less intuitively, fluids are also able to move through shear zones within the quasiplastic region. Many studies show that shear zones below the brittle-ductile transition can be important conduits for fluid movement in crustal rocks as deep as 25 km (Beach & Fyfe, 1972; Lobato et al, 1983; Kerrich, 1986; McCaig, 1988; Carter et al., 1990). Fyfe et al. (1978) showed that oxygen isotopes had been mobile from hundreds to thousands of meters within shear zones and concluded that mass transport on that scale could only have occurred by fluid infiltration.

Due to the evidence for fluids within shear zones and their impacts on deformation, it is important to understand from where these fluids are sourced and the processes by which they enter shear zones. The two primary sources for fluids in shear zones are deep-seated metamorphic or magmatic waters, which are released from rocks below the shear zone and migrate upward (Kerrich, 1986), and surface-derived meteoric waters. Two possible pathways for meteoric water to enter a shear zone are through tectonic emplacement and seismic pumping. Tectonic emplacement occurs in contractional regimes when fluid reservoirs are emplaced beneath shear zones (Beach & Fyfe, 1972) and requires a significant amount of displacement along the overthrusting fault to place a shear zone over wet sediments (McCaig, 1988). Seismic pumping occurs due to opening and closing of microcrack networks before and after earthquakes. In the period before an earthquake, stresses rise leading to increased dilatancy and drawing-in of fluids into stressed rock. Stresses drop rapidly when rupture occurs, forcing fluids out as the networks of microcracks close (Sibson, 1981). Seismic pumping mostly occurs in the seismogenic zone, but it is also possible for fluids to move downward across the brittle-ductile transition boundary and into shear zones via this process.

1.2 Fluids in Deformation

Faults and ductile shear zones are important to study because localized deformation along them is responsible for large fractions of displacements at the lithospheric scale (Carter, 1990). The infiltration of fluids into these systems along grain edges and in pore spaces can have a huge effect on the deformational processes that take place (Wawrzyniec et al., 1989).

Fluids can enhance ductility through grain-boundary migration and hydrolytic weakening which enhances ductile crystal-plastic flow through strain softening (Griggs, 1967). Conversely, fluids can also induce brittle failure and hydraulic fracturing if fluid pressure instantaneously exceeds rock strength (Fischer & Patterson, 1989; Axen et al, 2001). Whether ductility is increased or decreased when fluids infiltrate a rock is dependent on many factors including composition of both the rock and fluids, pressure, fluid pathways, and the interconnectivity of pore space (Watson & Brenan, 1987; Wawrzyniec et al., 1999). Therefore, dependent on these factors, the addition of fluids can either raise or lower the depth of the brittle-ductile transition.

Fluids can display wetting or nonwetting behavior in metamorphic rocks which can affect deformation in inverse ways. Wetting behavior occurs when aqueous fluids ($H_2O \pm NaCl$) form a discrete phase which is capable of flow along interconnected grain edges in low-permeability rocks (Watson & Brenan, 1987). The fluid pressure of wetting fluids will be near lithostatic pressure (Etheridge et al., 1984). Nonwetting behavior occurs when fluids do not flow under similar temperature and pressure conditions under which wetting fluids would flow. This can happen when fluids are trapped in isolated pore spaces or when the fluids are carbonic (CO_2-$H_2O \pm NaCl$), which are unable to flow (Watson & Brenan, 1987; Chernak et al., 2009). Due to their inability to flow, nonwetting fluids can instantaneously exceed lithostatic pressure leading to a reduction in effective stress which can induce microcracking or faulting (brittle deformation) even under conditions of nominally plastic deformation (Fischer & Paterson, 1989). Wetting and nonwetting fluids can be produced episodically or continuously during prograde metamorphism (Wawrzyniec et al., 1999) and the deformation itself may cause temporary changes from nonwetting to wetting behavior (Tullis et al., 1996).

Wawrzyniec et al. (1999) performed a study examining the effects of aqueous and carbonic fluids on the footwall of the Simplon low-angle normal fault in Switzerland. The northern fault zone contained ductile postmylonitic structures such as extension veins and kinkbands while the southern fault zone contained brittle postmylonitic structures such as semibrittle shears and brittle faults. The temperature (>500 °C) and pressure (>5 kbar) conditions were estimated to be the same in both areas, which were within the range of plastic deformation for quartzofeldspathic rocks. Analysis of fluid inclusions showed a difference in fluid composition within the footwall, which caused the difference in deformation style. Fluid inclusions in the north were aqueous, which led to hydrolytic weakening and diffusion-controlled deformation, while fluid inclusions in the south were carbonic, which led to nonwetting conditions and brittle deformation even at temperatures and pressures where ductile deformation would normally occur. This difference in fluid chemistry was due to a relatively greater abundance of carbonate and graphite in the south which led to the fluids being carbonic rather than aqueous as they were in the north. This study shows how fluids can play an important role in deformation along faults and shear zones.

Fluids can also influence deformation by accelerating softening processes and retrograde metamorphic reactions. Comminution, dynamic recrystallization, metamorphic reactions, and phase changes can cause large grain size reductions within shear zones. A large reduction in grain size allows extensive fluid infiltration which enhances diffusion mechanisms such as dislocation creep. This increases strain rates which in turn accelerates softening processes, driving the system toward ductile deformation (Carter, 1990). This reaction

softening caused by fluid infiltration may be essential to strain localization within shear zones (Segall & Simpson, 1986).

1.3 Fluids in Quartz

Hydrolytic weakening occurs when water infiltrates an otherwise anhydrous mineral such as quartz and allows it to deform plastically under lower temperatures and pressure than would normally be required. This process is catalyzed by the hydrolysis of the Si-O-Si bridges in the silicate structure which causes the crystals to weaken and deform plastically by dislocation propagated slip (Griggs, 1967).

$$\text{Si-O-Si} + H_2O \rightarrow \text{Si-OH . HO-Si}$$

The bond between the two SiOH groups is a hydrogen bond which is weaker than the Si-O or Si-OH bonds by an order of magnitude (Griggs, 1967). Hydrolytic weakening occurs when a hydrolyzed dislocation can exchange hydrogen bonds with a neighboring hydrolyzed silicon-oxygen bridge allowing the dislocation to move via kink migration (Griggs, 1967). This process produces a tenfold reduction in the strength of silicates in the ductile regime (Griggs, 1967).

Dislocation creep of quartz is well known to be affected by water through nucleation, glide, climb and recovery of dislocations, and recrystallization (Kronenberg et al., 2017). It has been shown in many experiments, that at high confining pressure, the addition of water to quartz samples quickly and significantly decreases their flow strength compared to dry samples (Griggs, 1967; Tullis & Yund, 1989). This is because hydrolytic weakening affects volume

diffusion rates, enhancing dislocation climb and leading to less work hardening and an increased recovery rate which allows steady state flow to occur at a lower differential stress at a given temperature (Tullis & Yund, 1989).

There are three types of O-H species found in quartz: fluid inclusions of molecular water, OH's or H's related to impurities, and OH point defects, with fluid inclusions being the most common (Cordier & Doukhan, 1989; Kronenberg & Wolf, 1990). One way that water infiltrates quartz grains, is through fluids entering cracks in the grains which are subsequently healed. These cracks in the quartz can heal rapidly above 200 °C (Smith & Evans, 1984) and leave behind fluid inclusions (Carter et al., 1990). Fluid infiltration during dilatant fracturing often precedes the onset of ductile deformation (Segal & Simpson, 1986). Kronenberg et al. (1990) studied this in a ductile shear zone in granitic rocks near Roses, northeast Spain. They hypothesized that fluids originally penetrated the rocks along dilatant microcracks which promoted more crack growth as well as aiding in crack healing. After the cracks healed, additional transportation of water occurred along dislocations that intersected fluid inclusions along the healed microcracks. Kronenberg et al. (1990) therefore proposed that the mean spacing of fluid inclusions within the grains may be more important than the bulk water content within the grain.

1.4 Research Goals

The purpose of my research is to investigate how fluids influence deformation in naturally deformed rock by identifying how fluids infiltrated quartz grains along the Willard

thrust fault and showing how fluid infiltration relates to deformation style and intensity. Quartz was chosen as the focal point of this study because its flow laws are often used as a proxy for that of continental crust (Brace and Kohlstedt, 1980). Feldspars are more abundant than quartz in the crust, but are more rigid and do not deform as readily. Due to this, quartz potentially plays a role larger than that of feldspars on the strength of continental crust. Another reason quartz was chosen, is because it is one of the most widely studied minerals in experimental deformation (Cordier & Doukhan, 1989; Chernak et al., 2009), however, much less has been done on naturally deformed quartz due to the difficulty of identifying and tracking possible fluid pathways by which water could infiltrate the grains (Kronenberg et al., 1990; Gleason & DeSisto, 2008).

This study investigates evidence of water infiltration into naturally deformed quartz grains by using three complimentary techniques: standard petrographic microscopy to identify microstructures and interpret deformation mechanisms; scanning electron microscopy using a cathodoluminescence detector (SEM-CL) to create maps of healed microfractures and subgrain boundaries that may be related to pathways of fluid infiltration; and synchrotron-source Fourier-transform infrared spectroscopy (FTIR) to create micron-scale water absorbance maps of quartz grains. The data from these techniques were spatially referenced and visually overlain allowing for a comprehensive interpretation of the pathways used by water to infiltrate the quartz grains. The evidence for water infiltration was then related to strain magnitude measurements from Yonkee et al. (2013) to show how it affected strain softening.

This study is important because most research into fluid interactions with quartz have been done experimentally, which necessitates small samples and fast strain rates (Paterson,

2001). My research adds to the analyses conducted on naturally deformed rocks, which have strain rates much slower than could ever be achieved in a laboratory setting. Gaining further knowledge on hydrolytic weakening in quartz is important for understanding how it affects the brittle-ductile transition boundary and therefore deformation within the crust as a whole.

Chapter 2: Geologic Background

2.1 Regional Geology

2.1.1 The Sevier Orogeny

The Sevier orogeny took place from the Middle Jurassic to the Early Tertiary as the North American plate was moving westward and the Farallon plate was being subducted beneath it in the vicinity of modern day central California (Armstrong, 1968; Willis, 1999). This collision formed the Cordilleran thrust system which extends from Mexico to Alaska. The portion of the Cordilleran thrust system stretching from southern Nevada through Utah to Wyoming is called the Sevier thrust system (Fig. 1; Willis, 1999). The Sevier thrust system is comprised of a thrust belt, a foredeep basin, a forebulge, and a back-bulge basin that migrated from west to east. The thrust belt is characterized by thrust faults with an overall trend of NNW above a regional decollement (Armstrong, 1968; Yonkee & Weil 2015). Localized thrusting began as early as the Middle Jurassic, but the majority took place between the Early Cretaceous and Paleogene and in total accommodated ~150-300 km of shortening (Yonkee & Weil 2015). Thrusts show a "stair-step" pattern due to sheets becoming too thick resulting in thrusting "stepping" forward to new faults (Willis, 1999; Yonkee & Weil 2015). Through this process sheets stacked on top of each other, up to five deep in certain locations, creating a mountain chain that may have been equivalent to the modern day Andes (Willis, 1999).

The Wyoming salient of the Sevier belt (Fig. 1) extends from northern Utah through Wyoming with a NW trend in the north and a NE trend in the south and is divided into two

major thrust systems: a western and an eastern. The western system is composed of the Willard, Paris, and Meade thrusts which transported thick Neoproterozoic to Paleozoic strata; and the eastern system is composed of the Crawford, Absaroka, and Hogsback-Darby-Prospect thrusts which transported thinner Paleozoic strata (Yonkee & Weil 2015). The western system is older than the eastern, with slip occurring on the Willard, Paris, and Meade thrusts from ~125-90 Ma, while slip occurred on the Crawford and Absaroka thrusts from ~90-80 Ma, and on the Hogsback-Darby-Prospect thrusts from ~70-50 Ma (Yonkee & Weil, 2015), reflecting the general pattern of active thrusting stepping from west to east through the orogeny.

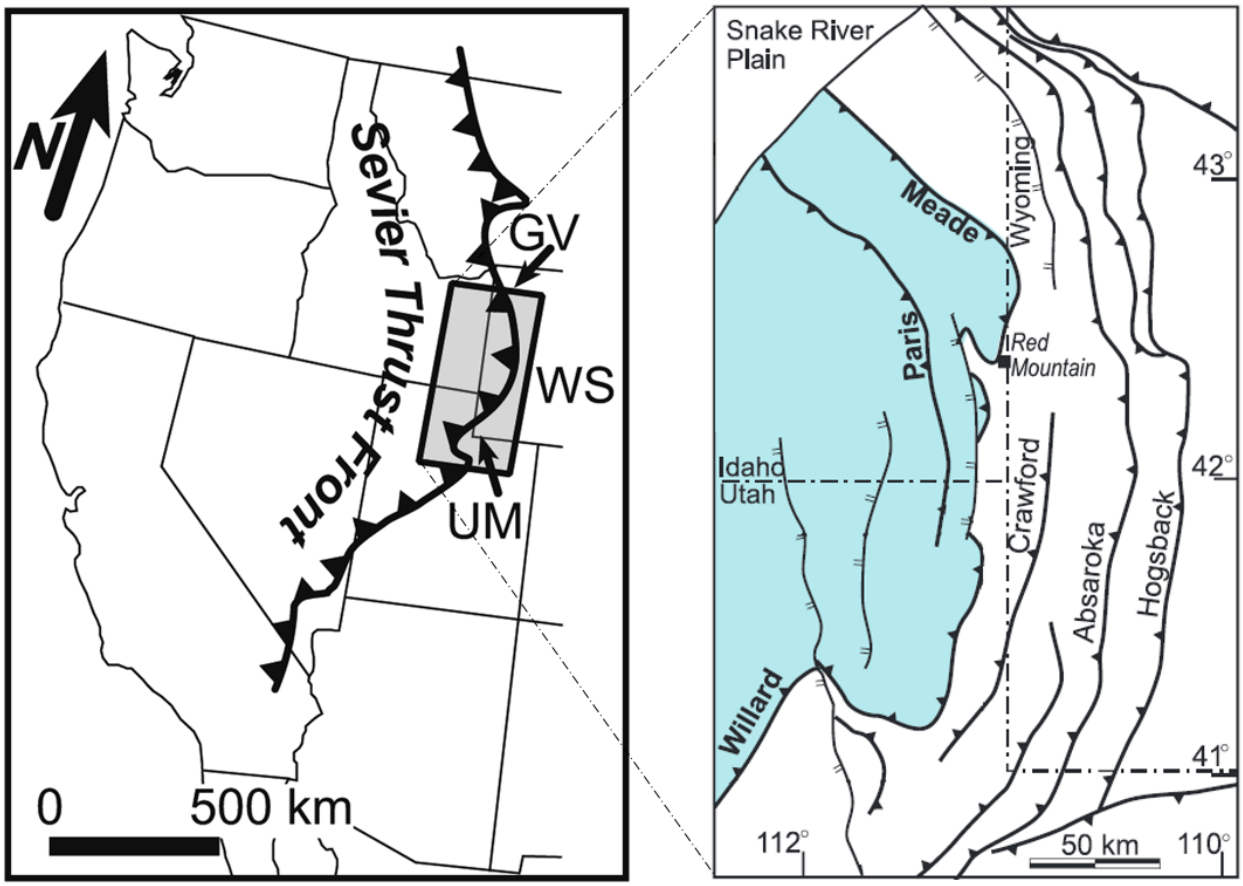

Figure 1: The left map shows the general location of Sevier thrust front with a gray box highlighting the Wyoming salient. Modified from Weil & Yonkee (2010). The inset on the right zooms in on the Wyoming salient, showing major thrusts in the region. The Willard-Paris-Meade sheet is highlighted in blue. Modified from Yonkee et al. (2019).

2.1.2 The Willard Thrust

The Willard thrust fault formed during the Sevier orogeny and was active from about 140 to 90 million years ago (Fig. 2A&B; DeCelles et al. 1993; Yonkee, 1997). The thrust has a "stair-step" geometry with the western base cutting through micaceous Neoproterozoic to lower Cambrian strata, a central flat cutting through Cambrian shale and limestone, an eastern ramp through Cambrian to lower Jurassic strata, and an eastern flat in Jurassic evaporate-bearing strata (Fig. 2B; Yonkee, 2005). The Willard thrust separated the 10- to 15-km-thick Willard thrust sheet and transported it 50 km ESE (Yonkee, 1997; Yonkee, 2005). Additional shortening was accommodated within the sheet by imbricate thrusts and large-scale folds (Yonkee & Weil, 2015). The Willard thrust sheet is composed of a lower section of micaceous Neoproterozoic strata, a middle section of quartz-rich upper Neoproterozoic to lower Cambrian strata, and an upper section of carbonate rich Paleozoic strata (Fig. 2B; Crittenden, 1972; Yonkee, 2005). The upper levels of the thrust sheet went through relatively little deformation, but internal deformation increased downward and westward as evidenced by the development of cleavage, minor folds, and vein arrays nearer the fault (Crittenden, 1972; Yonkee, 2005).

The lower level of the Willard thrust sheet was metamorphosed to greenschist facies (biotite zone) and experienced a peak temperature of ~350-400 °C with a burial depth of 12-15 km (Condie, 1967; Yonkee et al, 2003; Yonkee, 2005). The footwall was also internally deformed as indicated by the development of cleavage (Evans & Neves, 1992; Yonkee et al., 2000); but was only metamorphosed to greenschist facies (chlorite zone) due to a slightly lower peak temperature of ~300 to 350 °C (Yonkee et al., 2003; Yonkee et al., 2013). The deformation near the fault, both in the hanging wall and footwall, was aided by fluids flowing along the fault.

Based on unique alteration patterns in the hanging and foot walls, Yonkee et al. (2013) concluded that the fluids from the footwall and hanging wall were of different compositions, and thus the Willard thrust fault acted as a conduit for fault-parallel flow but a barrier for cross-fault flow. The fluids in the hanging wall flowed downward (up temperature) and were thus undersaturated in quartz; while the fluids in the footwall flowed upward (down temperature) and were thus at or near quartz saturation (Fig. 2C; Yonkee et al., 2013). Since the fluids flowing through the footwall were at or near quartz saturation, there was limited volume change within the rocks, with quartz dissolution and precipitation being approximately balanced (Yonkee et al., 2013). Yonkee et al. (2013) proposed that the fluids flowing along the Willard thrust fault caused hydrolytic weakening within the quartz grains, and altered feldspars to muscovite causing softening, which led to increased deformation.

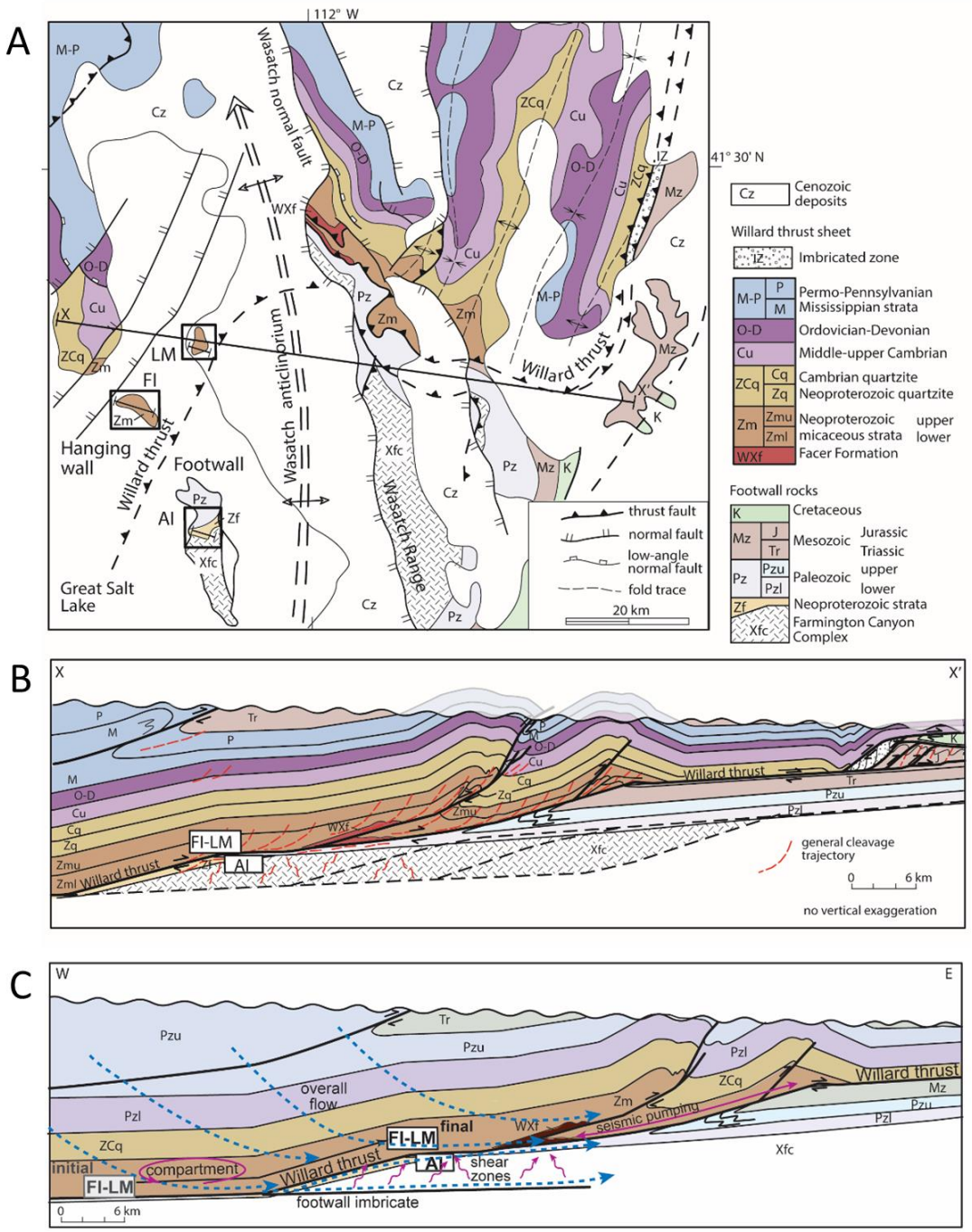

Figure 2: (A) Generalized geologic map of the area around the Willard thrust in north-central Utah. Antelope Island (AI) is in the SW corner of the map in the footwall of the Willard thrust. Fremont Island (FI) and Little Mountain (LM) are field sites located in the hanging wall which were used for previous research. The Mineral Fork diamictites are represented by Zf in the footwall and Zm in the hanging wall. (B) Early Cretaceous cross-sectional view X-X' of the Willard thrust with subsequent thrusting and late normal faulting restored, showing the location of Antelope Island (AI) in the footwall. (C) Schematic cross-section indicating directions of fluid flow. Modified from Yonkee et al. (2013).

2.2 Study Area

2.2.1 Antelope Island

The Willard thrust sheet and its footwall are well exposed in northern Utah due to uplift caused by the Wasatch anticlinorium and subsequent erosion (Fig. 2A; Yonkee, 2005). This study focuses on deformation in the footwall which is well exposed on Antelope Island (Fig. 2A). Antelope Island is located within the Great Salt Lake in northern Utah (Fig. 3). It is the largest island in the lake at ~24 km in length, ~8 km across, and reaching a height of ~732 m above lake level (Willis et al., 2000). The island, lying entirely within the Willard footwall, is composed of Archean to early Proterozoic basement rocks unconformably overlain by late Proterozoic to Cambrian deformed sedimentary strata, which are then unconformably overlain by post-thrusting Tertiary sedimentary strata (Fig. 4; Willis, et al., 2000).

The basement rocks exposed on Antelope Island are igneous and metamorphic rocks of the Farmington Canyon Complex. They are indeed "complex," consisting of eleven identified rock types (Willis et al., 2000; Yonkee et al., 2000). The complex began with Archean igneous protoliths, which went through high-grade metamorphism about 2.6 billion years ago. During and after this metamorphism, mafic and igneous rocks intruded into the complex. All of the rocks were then intensely deformed 1.7 billion years ago during high temperature (650-800 °C), deep (12-20 km) metamorphism with some partial melting (Barnett et al., 1993).

The Farmington Canyon Complex is overlain by a series of Neoproterozoic to Cambrian units. The Mineral Fork Formation is 770-720 Ma in age and is composed of diamictites, largely sourced from the Farmington Canyon Complex along with some input from the Wyoming

Province (Yonkee et al., 2000; Yonkee et al., 2013). It is separated from the Farmington Canyon Complex by an unconformity, which represents almost one billion years of missing time. The Mineral Fork formation is overlain by the Kelley Canyon Formation, which is 720-600 Ma in age and is composed of a lower dolomite member and an upper slate member (Yonkee et al., 2000). The Kelley Canyon Formation is overlain by the Cambrian Tintic Quartzite and is composed of about 60% fine to medium grained quartzite, 20% coarse-grained quartzite, and 20% conglomerate (Yonkee et al., 2000). The Mineral Fork Formation, Kelley Canyon Formation, and Tintic Quartzite were all metamorphosed during the Sevier orogeny (Yonkee et al., 2000). There is no preservation of middle Cambrian to Mesozoic strata on Antelope Island due to erosion. The Quartzite is overlain by much younger post-thrusting Tertiary strata (Yonkee et al., 2000), which are not relevant to this study.

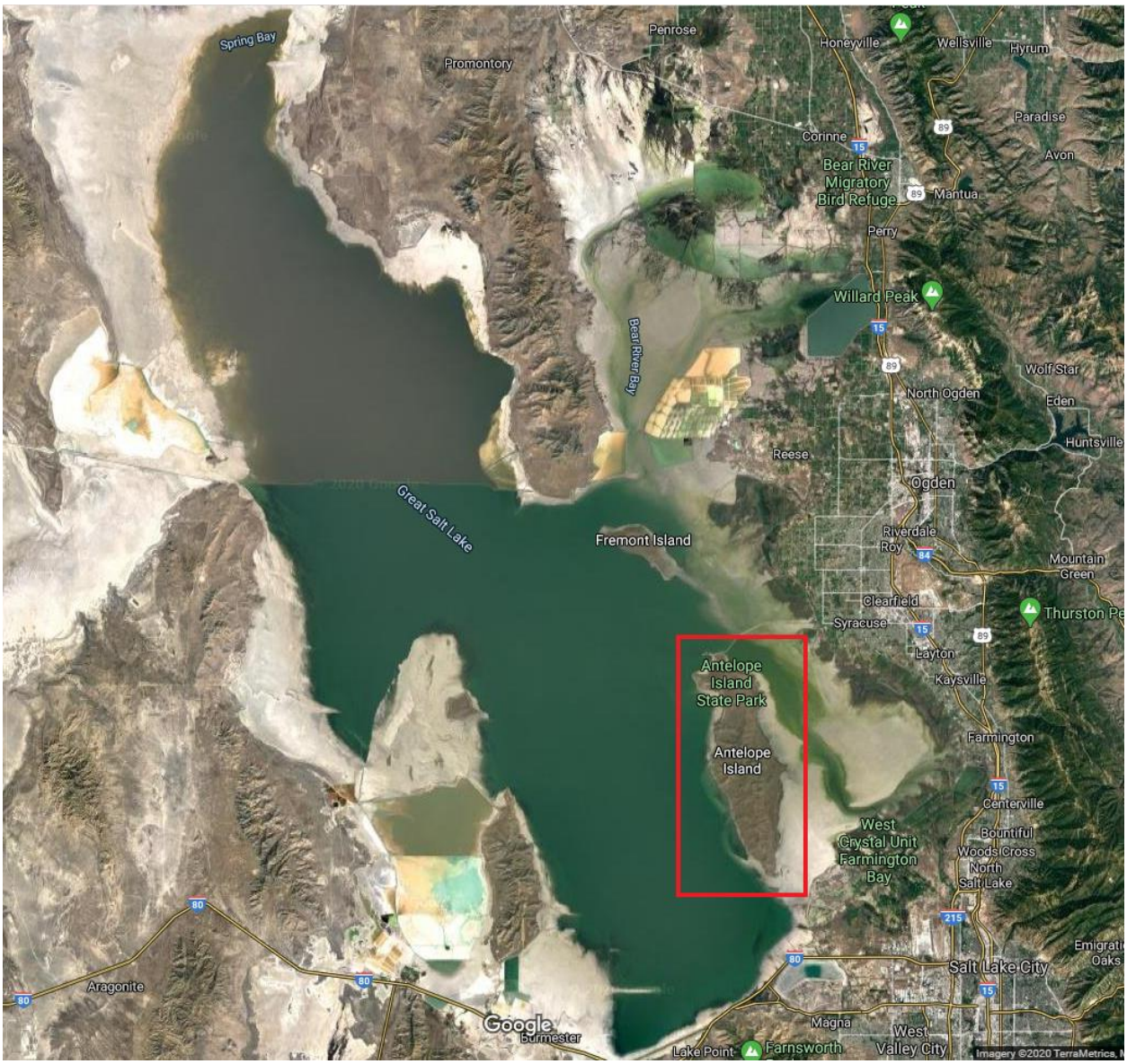

Figure 3: Map showing Antelope Island located in the SE corner of the Great Salt Lake, UT. Modified from https://www.google.com/maps

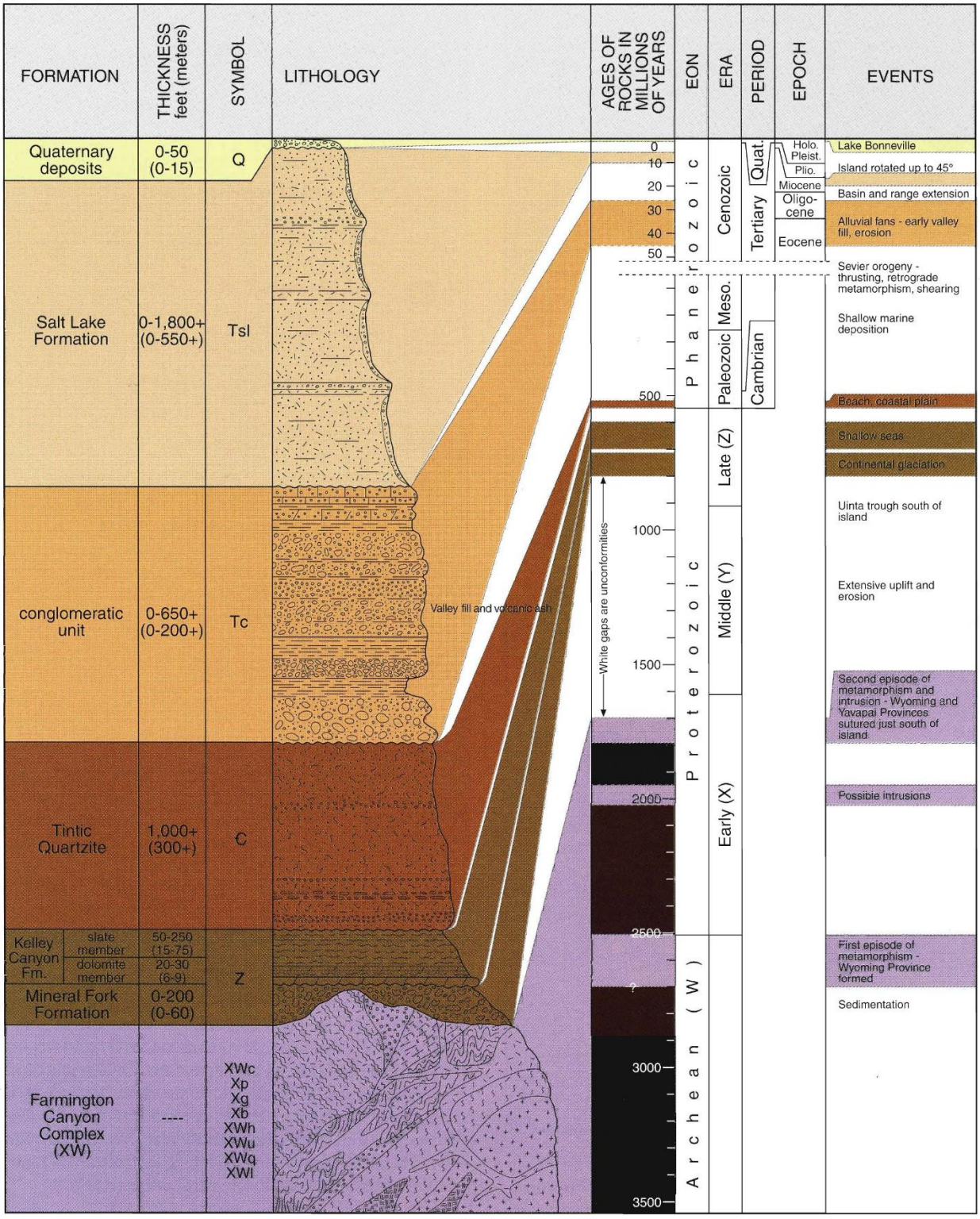

Figure 4: Lithologic column showing rock units found on Antelope Island. The Neoproterozoic Mineral Fork and Kelley Canyon Formations (Z) are represented in brown. From Willis et al. (2000).

2.2.2 Mineral Fork Diamictite

The Mineral Fork diamictite is the focus of this study. It is exposed along an east-west strip near the center of Antelope Island (Fig. 2A; Fig. 5). It is poorly sorted and composed of 10-30% boulder to pebble size clasts and 10-30% pebble to coarse sand size clasts, which are suspended in a sandy micaceous matrix that makes up the remaining 50-80% of the unit (Yonkee et al., 2013). The diamictite is interpreted as glaciogenic in origin (Crittenden et al., 1983) and largely sourced from the underlying Farmington Canyon Complex as determined by detrital zircon analysis (Yonkee et al., 2013). Granite, paragneiss, and quartzite are the three primary clast types found within the unit with granite and paragneiss making up 70-95% of all clasts greater than 0.5 inches and quartzite cobbles to boulders making up the other 5-30% (Yonkee et al., 2000).

The diamictite was deformed during movement along the Willard Thrust, forming a well-developed cleavage defined by subparallel partings in the matrix and flattened clasts (Yonkee, 1992). The unit as a whole shows a distinct strain gradient on Antelope Island with lower strains and less developed cleavage in the east transitioning to higher strains and strongly developed cleavage towards the west (Fig. 6; Fig. 7; Yonkee et al., 2013). Diamictites are excellent for studying heterogeneous strain due to the contrasting material properties of the matrix and the clasts (Treagus and Treagus, 2002; Czeck et al., 2009). In addition, the Mineral Fork diamictite is an especially useful example because of the larger relative spacing between clasts leading to reduced clast interactions (Yonkee et al, 2013).

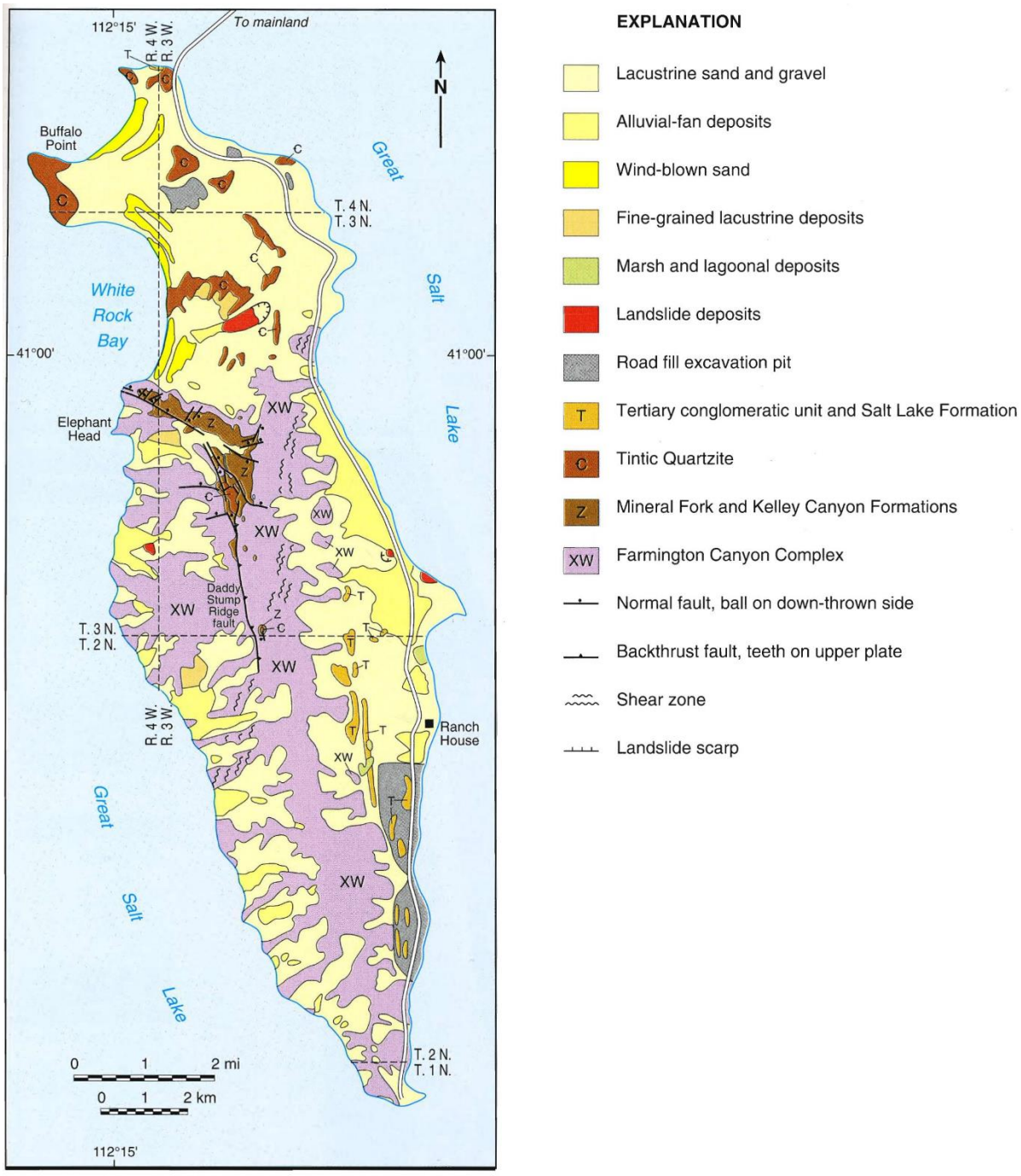

Figure 5: Geologic map of Antelope Island. The Mineral Fork and Kelley Canyon Formations (Z) are collectively the brown unit in the center of the island. From Willis et al. (2000).

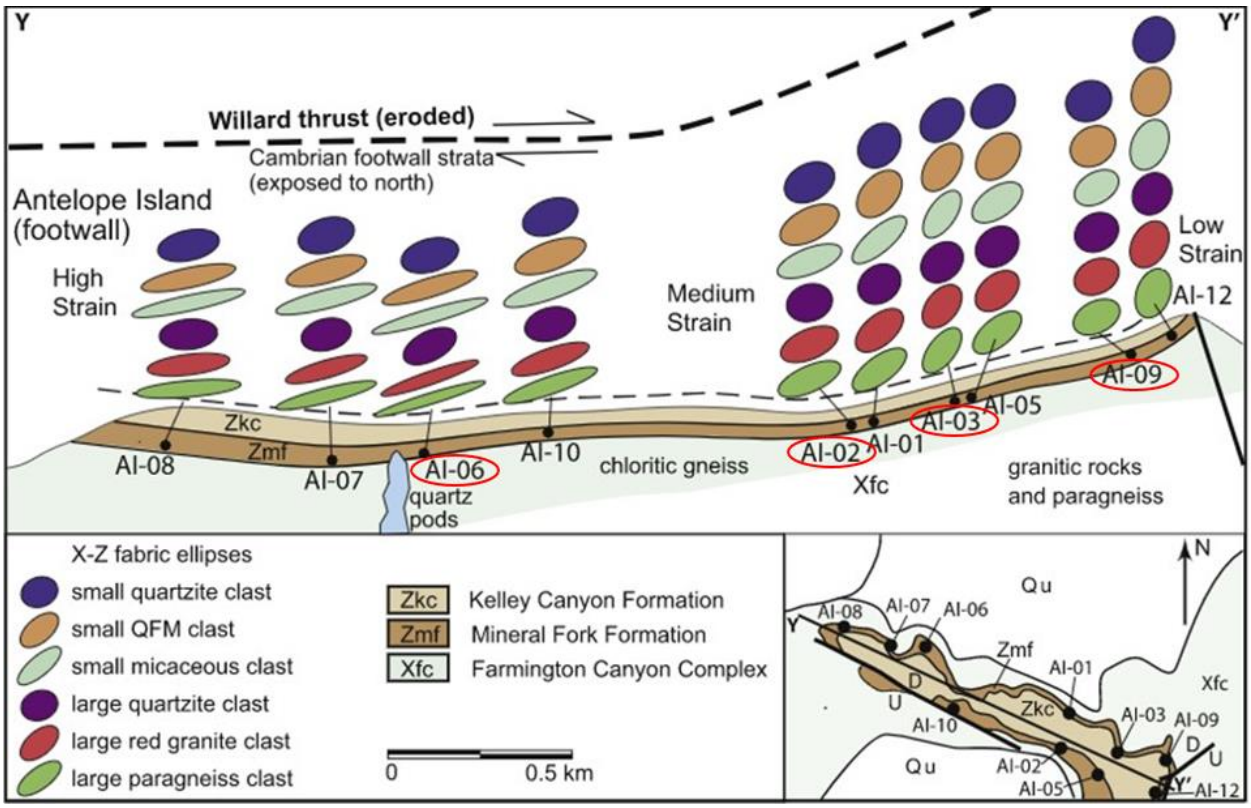

Figure 6: Cross-section across the Mineral Fork Formation exposed near the center of Antelope Island (location shown on lower right inset map). 2D strain ellipses of various diamictite components (key in lower left) show a distinct strain gradient with lower strains in to the east and higher strains to the west. Sample locations for this study are circled in red. Modified from Yonkee et al. (2013).

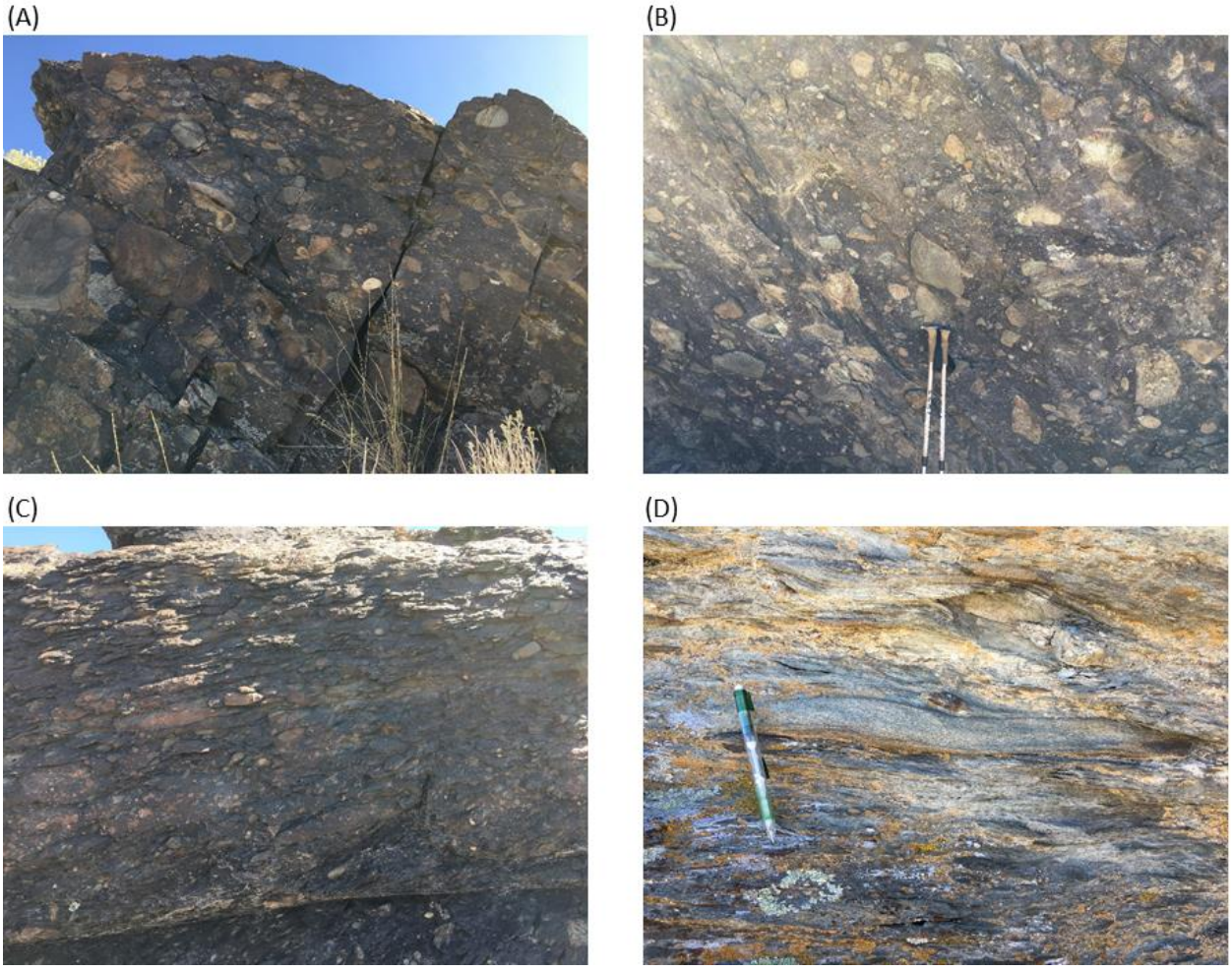

Figure 7: Photographs of Mineral Fork diamictite outcrops showing differences in strain. All photographs were taken in a subvertical orientation and approximately perpendicular to strike. (A) Low-strain from AI-09 on the eastern side of Antelope Island (approximately 3 m across). (B) Medium-strain from AI-03 near the center of the island (walking sticks for scale). (C) Medium-strain from AI-02 near the center of the island (approximately 3 m across). (D) High-strain from AI-06 on the western side of the island (pencil for scale).

2.2.3 Previous Work

Much work has previously been conducted on the Mineral Fork diamictite exposed on Antelope Island due to it being an ideal location to study heterogeneous strain. Yonkee et al. (2013) performed a large study which included strain analysis, geochemical analysis, and microstructural analysis that documented the paired strain accumulation and fluid-rock interaction related to deformation along the Willard Thrust Fault. In the low-strain zone, feldspar grains are cut by microfractures and variably altered to muscovite that has weak shape preferred orientations. In the high-strain zone, feldspars are almost completely altered to muscovite and have strong preferred shape orientations. Alteration was confirmed by results from major element geochemical analysis conducted by X-ray fluorescence (XRF), which showed that granitic clasts within the diamictite were ~90% depleted in Na, ~60% depleted in Ca, and ~190% enriched in Mg compared to the Farmington Canyon Complex source rocks. Yonkee et al. (2013) proposed that the alteration of K-feldspar and plagioclase to phengitic muscovite during fluid-rock interactions led to softening, which was one of the causes for increased deformation.

Quartz grains in the low-strain zone experienced limited crystal plastic deformation. They are slightly flattened and feature fluid inclusion trails, undulose extinction, subgrains, deformation bands, and healed microfractures. Quartz grains in the high-strain zone are flattened and have been extensively recrystallized, mostly by subgrain-rotation and local bulge migration, recording increased plastic deformation (Barszewski, 2012; Yonkee et al., 2013). There was no significant volume change in quartz between the strained areas and the source

rocks, but quartz did undergo local dissolution and reprecipitation as evidenced by microveins and strain shadows (Yonkee et al., 2013). This again shows evidence of fluids in the system.

The R_{xz} value is the ratio between the amount of greatest stretching (X) and the amount of greatest shortening (Z). Yonkee et al. (2013) calculated R_{xz} values across the shear zone for a variety of components of the diamictite, generally finding lower values to the east (below the thrust ramp) and higher values to the west (below the thrust flat). The average R_{xz} values for the matrix and the major three clast types were as follows: in the low-strain zone (east), matrix ≈ 1.5, paragneiss ≈ 1.5, granite ≈ 2.0, and quartzite ≈ 1.0; in the medium-strain zone, matrix ≈ 2.2, paragneiss ≈ 3.0, granite ≈ 2.3, and quartzite ≈ 1.3; in the high-strain zone (west), matrix ≈ 9.0, paragneiss ≈ 10.7, granite ≈ 7.3, and quartzite ≈ 1.6 (Table 1, Yonkee et al., 2013). This shows that the rocks closer to the fault were significantly more deformed than the rocks further away.

Yonkee et al. (2013) concluded that fluids interacted with rocks during deformation, enhancing and affecting the style of deformation. The fluid influx caused softening by altering feldspars to phengitic muscovite, hydrolytic weakening by infiltrating the quartz grains and making them easier to deform, and diffusive mass transfer by dissolving and reprecipitating minerals (Yonkee et al., 2013). All of these processes led to a positive feedback between more deformation and more fluid interactions. This means that more deformation would be expected to occur near the fault, at least in part due to the fluids flowing along it. The Willard is not unique in this aspect, as many faults have been shown to have a conduit-barrier pattern of fluid flow, where fluid is channeled along the fault itself (Caine et al., 1996; Barnes et al., 2004; Bense and Person, 2006).

Clast Type	Low-strain avg. R_{xz}	Medium-strain avg. R_{xz}	High-strain avg. R_{xz}
Matrix	1.5	2.2	9.0
Paragneiss	1.5	3.0	10.7
Granite	2.0	2.3	7.3
Quartzite	1.0	1.3	1.6

Table 1: R_{xz} values by clast type and amount of strain. (Yonkee et al., 2013)

Chapter 3: Methods

3.1 Field Methods

Samples for this study were collected from Antelope Island, Utah in the summer of 2018. Samples were collected from four separate outcrops of the Mineral Fork diamictite representing the strain gradient from low to medium to high along the footwall of the Willard Thrust Fault. The outcrops were selected from those for which strain measurements were available from a previous study (Yonkee et al., 2013), and the same outcrop nomenclature was used for this study. The Mineral Fork diamictite contains three primary clast types; granite, paragneiss, and quartzite. This study focuses solely on the quartzite clasts because they are composed almost entirely of quartz, which in addition to being the mineral of interest, provides the samples with the integrity needed to survive the sample preparation process. A total of twenty quartzite samples were collected ranging in size from 7-18 cm. Five samples were collected from each of the following four outcrops: AI-09 (low strain), AI-03 (medium strain), AI-02 (medium strain), and AI-06 (high strain) (Figs. 6 & 7). Prior to sampling, each quartzite was marked with a north arrow and horizontal lines on two separate faces so orientation could be preserved.

3.2 Sample Preparation

In the lab, samples were reoriented in a sandbox by making sure the north arrow and horizontal lines that were marked in the field were properly aligned. The XZ plane was then marked on every sample and a rock saw was used to cut billets along this plane. The XZ plane of strain was chosen because it is parallel to lineation and perpendicular to foliation, showing the greatest difference in strain. The orientation of the XZ plane at each outcrop was determined in the field by Dr. Adolph Yonkee using visible metamorphic fabrics (Table 2).

Once the billets were cut, one side was ground smooth using a Logitech CL50 lapping machine and 15 micron silicon carbide powder. The samples were then hand finished using diamond encrusted lapping film down to a 1 micron grit to produce a mirror finish. The polished side of the sample was then adhered to a glass slide using Crystalbond^{TM} 509, which is a heat removable epoxy (Kronenberg et al., 2017). Next, the excess billet was cut off using a rock saw and the rough edge of the sample was ground down using the lapping machine. Due to the unknown thickness of the dried epoxy, slides were only ground down to about 250 microns in thickness so as not to lose the sample. The samples were then finished by hand using lapping film and were ground down until the quartz grains appeared in gray scale on a petrographic microscope under crossed polars. This resulted in samples ~30 microns thick. At this point, a mirror finish was put on the final side of the sample using 1 micron lapping film. This process produced a sample which consisted of a glass slide, approximately 150-200 microns of epoxy, and a 30 micron thick rock sliver with a mirror finish on both sides. The ideal thickness of 30 microns was selected because it allows for standard petrographic observation of microstructures and also increases the likelihood that only a single grain will be analyzed with

FTIR as the beam penetrates the entire sample. Due to time constraints, thin sections were only prepared for eight of the twenty samples collected: two from AI-09, one from AI-03, two from AI-02, and three from AI-06.

Outcrop	Orientation of XZ Plane
AI-09	290, 90
AI-03	290, 90
AI-02	300, 80N
AI-06	295, 85S

Table 2: Strike and dips of the orientation of the XZ plane for each outcrop location as determined by Dr. Adolph Yonkee.

3.3 Petrographic Microscopy

Petrographic microscopy served two purposes for this study. The first was to search for deformation microstructures to see if they were in agreement with the findings of Barszewski (2012). The second was to create thin section maps of each sample, which were used to locate individual grains for analysis on multiple instruments. A Leica M420 petrographic microscope was used to inspect thin sections using both plane and crossed polarized light. This facilitated the search for microstructures that are associated with 1) crystal plastic deformation such as undulose extinction, subgrains, and bulged grain boundaries, and 2) brittle processes including microfractures and fluid inclusion planes. After microstructures were identified, the entire thin section was photographed at 20x magnification in overlapping intervals. This was done in both plane and crossed polarized light and resulted in 15-20 pictures per slide. The pictures were then stitched together into a mosaic of the whole thin section using Adobe Photoshop (Fig. 8). These mosaics were printed on 11x17 paper to create thin section maps, which were taken to the SEM and FTIR microscopes to help locate individual grains. The maps were a tremendous help as it can be very difficult to orient yourself on the slide in SEM and FTIR because of the high magnification of those instruments.

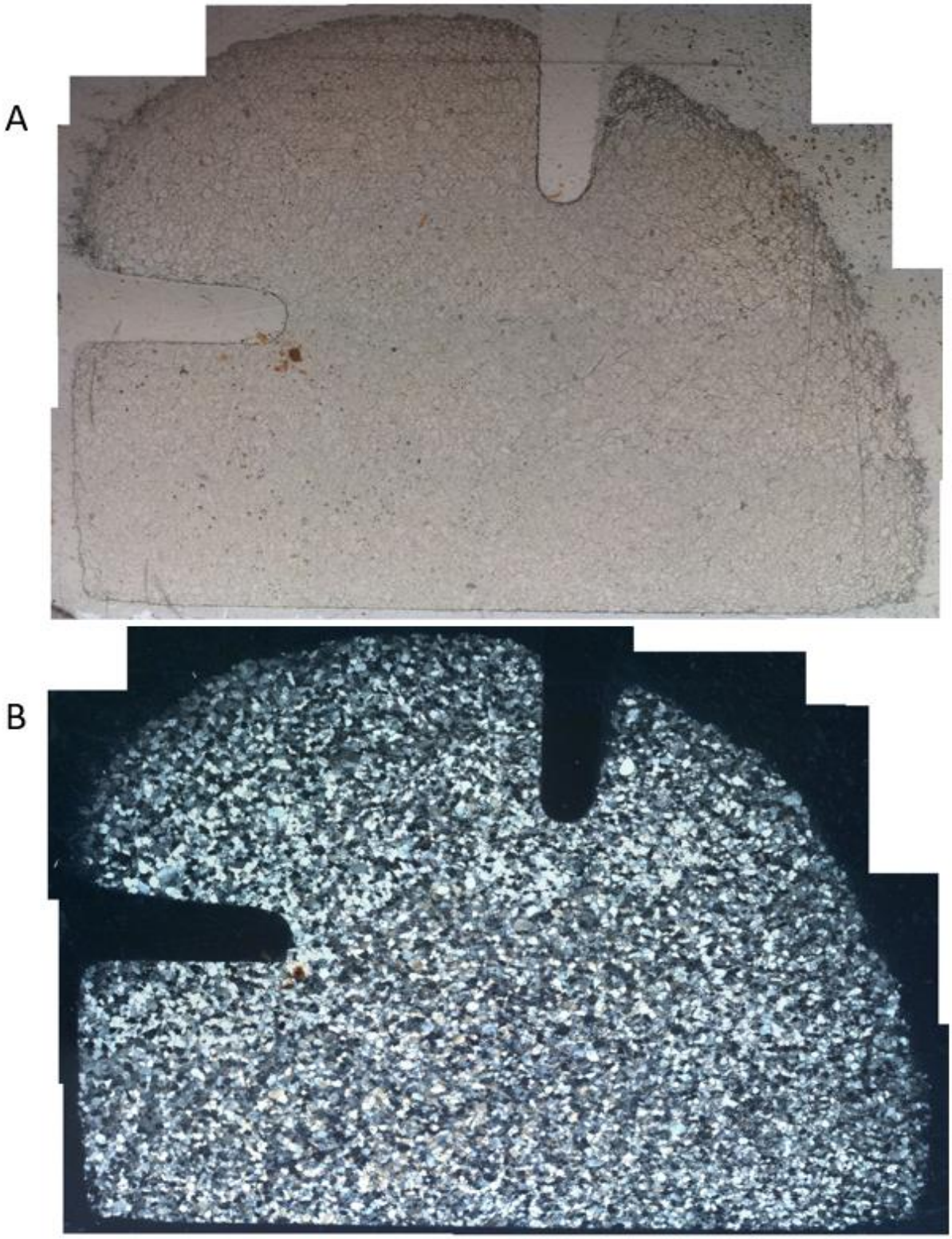

Figure 8: Photomosaic map of AI-08-06-Q12. (A) 20x magnification with plane polarized light. (B) 20x magnetization with cross polarized light.

3.4 Scanning Electron Microscopy Cathodoluminescence (SEM-CL)

Cathodoluminescence (CL) is the emission of light caused by bombarding a mineral with high energy electrons (Crookes, 1879). CL illuminates textures that are not observable by other methods, such as transmitted light, secondary electrons (SE), and backscattered electrons (BSE) (Frelinger et al., 2015). CL detectors are usually attached to scanning electron microscopes (SEM, SEM-CL) because the high resolution, magnification, and ability to detect emissions outside of the visible range, allow for improved observations of CL textures such as growth histories, dissolution, replacement, and microfracturing (Marshal, 1988; Frelinger et al., 2015). Quartz is an excellent mineral to study under CL due to its strong luminescence. This is because the high purity of quartz allows only a limited number of trace elements in its crystal structure, such as Ti and Al, which are both correlated with bright cathodoluminescence (Baline, 2007; Frelinger et al., 2015). However, metamorphic quartz typically emits a dull and homogenous CL response (Rusk, 2012). Annealing of quartz grains by recrystallization effectively increases the crystal order, reducing the number of structural defects and purifying the crystal by removing impurities such as Ti and Al, resulting in low levels of luminescence (Boggs et al., 2002). This contrast between the bright luminescing original quartz and dull metamorphic quartz in these samples, as described by Barszewski (2012), is what allowed for the identification of the healed microfractures, which were the focus of this study (Fig. 9).

Cathodoluminescence was performed at the University of Wisconsin-Madison Department of Geoscience using a Hitachi S3400 variable pressure scanning electron microscope with a Gatan PanaCL cathodoluminescence attachment. Since quartz is a nonconductive mineral, the sample slides needed to be carbon coated so as not to accumulate

a static charge while running on the SEM. While in the SEM, samples were first scanned in CL to search for grains that showed evidence of microfractures. When a good candidate was discovered, images were captured of the grain in both CL and BSE at ~100x magnification. Then the SEM was switched over to SE and zoomed out to ~20x magnification to locate the grain within the slide. Once identified, the location was marked on the printed thin section map so it could be found again when needed. In total, 82 quartz grains were identified and mapped as possible candidates for FTIR.

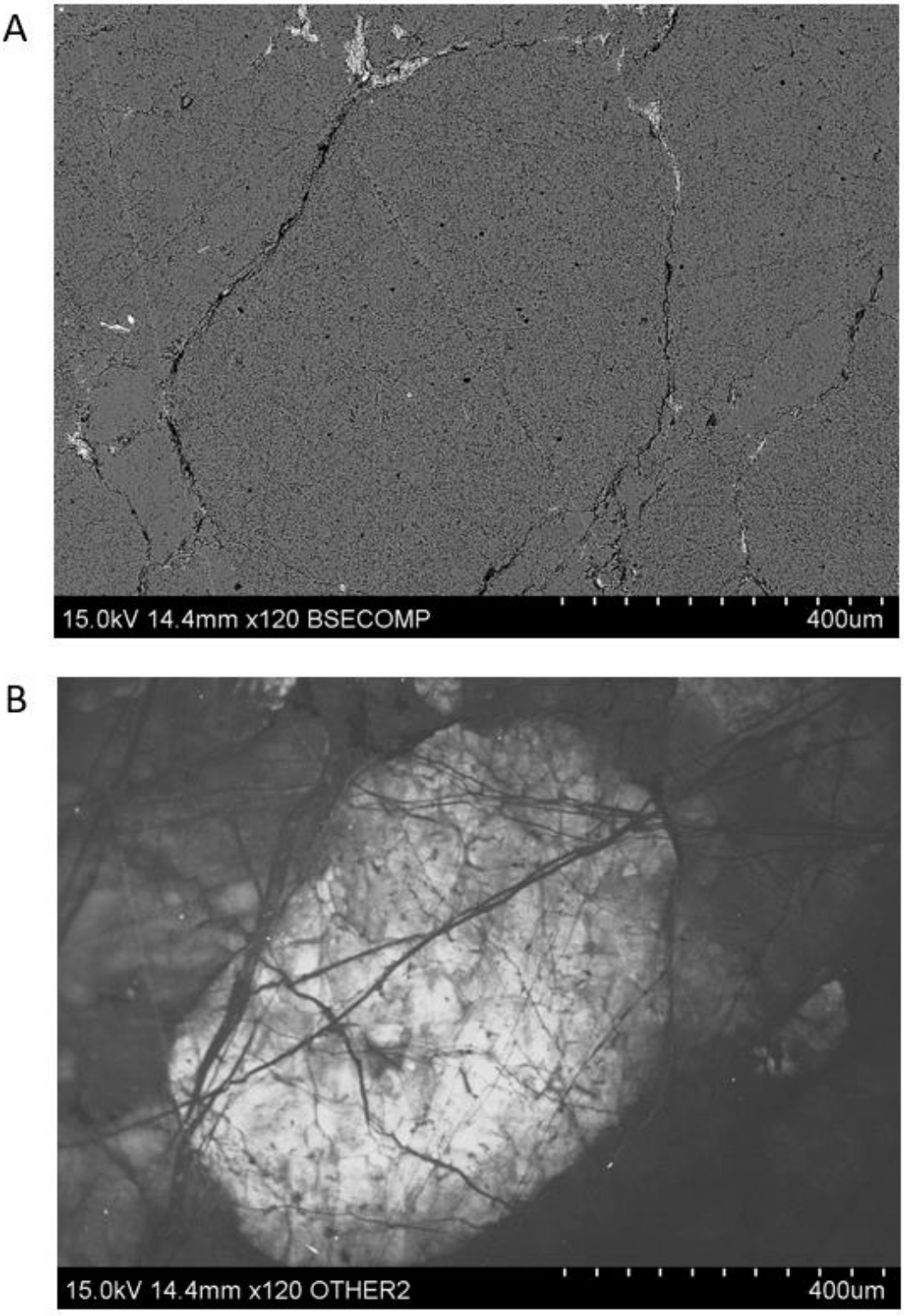

Figure 9: SEM-CL image captures from sample AI-08-02-Q14-03. (A) BSE image showing very few features of interest due to sample being composed almost entirely quartz. (B) CL image showing extensive network of healed microfractures due to the different luminescence between the original and metamorphically recrystallized quartz.

3.5 Fourier-Transform Infrared Spectroscopy (FTIR)

Fourier-transform infrared spectroscopy (FTIR) provides data on the chemical structure of a sample on the molecular scale. It does this by monitoring absorption of infrared (IR) radiation that occurs when a photon transfers to a molecule, exciting it to a higher energy state. This produces vibrations of molecular bonds, which occur at varying wavenumbers in the IR light spectrum. The wavenumber of each IR absorbance peak is unique to the corresponding molecule and determined by its intrinsic physiochemical properties, making it diagnostic (Chen et al., 2015). This makes FTIR an excellent tool for characterizing the heterogeneity of geologic samples at the microscopic scale.

The ability of FTIR to characterize and measure OH absorption bands, related to different hydrogen defects and forms of molecular water within quartz interiors, has resulted in this instrument playing a key role in experimental studies of hydrolytic weakening (Kronenberg et al., 2017). The two primary wavelength peaks of interest to this study were ~3400 cm^{-1} and ~3600 cm^{-1}. A broad band at ~3400 cm^{-1} is characteristic of OH from molecular water, while a thinner absorption band at ~3600 cm^{-1} is associated with OH locked in micas (Kronenberg et al., 2017). Both peaks can occur on their own or in combination (Fig. 10), however, it is the ~3400 cm^{-1} peak that is of primary interest for water weakening of quartz (Kekulawala et al., 1978). Kronenberg et al. (2017) have shown that variations in the ~3400 cm^{-1} band represent real variations in water content and not variations in quartz grain orientation, meaning the larger the area under a peak, the more water there is. This finding, however, is specific to FTIR analysis of a pure rock samples because epoxy or glass slides likely contain OH molecules that complicate interpretation of the IR spectra.

FTIR work was performed at the Advanced Light Source (ALS) synchrotron at Lawrence Berkeley National Laboratory in Berkeley, California. Samples were run on a Thermo Fisher Scientific Nicolet Continuμm IR Microscope connected to a synchrotron sourced Thermo Fisher Scientific Nicolet iS50 FTIR. A synchrotron sourced FTIR was important for this study because it produces a 3-5 micron thick beam that provides the resolution needed to map individual grains. All data were created and analyzed using the Thermo Fisher Scientific Omnic software with the Atlμs add-on, which allows for the creation of absorption maps.

The first step in running the samples on FTIR was to delicately remove them from their glass slide and epoxy. This was done on location at the ALS because the glass slides were needed for the samples to survive transport. The samples were placed on a hot plate to melt the Crystalbond™ 509 epoxy, and then the rock sliver was delicately removed from the slide using tweezers and placed in an acetone bath to remove any additional epoxy. After all the epoxy residue had dissolved from the sample, it was removed from the acetone, dried, and placed on the microscope stage. Even though the quartzite was competent at a thinness of ~30 μm and could be handled without being attached to a slide, it was a difficult procedure that resulted in several accidental breaks. Future studies will need to find a way to keep weaker rock types from disintegrating when removing them from the slide.

Once the sample was on the microscope stage, the grain of interest was located. This was done by scouring the sample at 10x magnification while using the thin section map as a guide. The microscope was then switched to 32x magnification and a photomosaic of the area was created using the computer software. This allowed for a larger view of the area at a higher magnification than was possible looking through the eyepiece. The photomosaic on the

computer was used to select the area where absorption data was to be collected. The sample was then ready for analysis.

FTIR can be run in either reflectance mode, which measures the IR waves reflected off the surface of a sample, or transmission mode, which measures the IR waves that pass through a sample. This study was based on absorbance data, which is how much of the IR signal is absorbed passing through a sample. Therefore, the FTIR was set to transmission mode.

A background reading was collected for each sample by moving the sample stage outside of the collection area and taking a reading through open air. Each background reading consisted of 256 scans. The data set from these scans was subtracted from readings taken during the actual sample run. This accounted for any ambient absorption effects that may have been taking place. Each sample run used a step size of 5 μm, with 64 scans at each step, and a spectral resolution of 4 cm^{-1}. A single sample run could take anywhere from 8 to 17 hours to complete. This greatly limited the number of datasets that could be collected during the six days of beam time awarded at the ALS for this study. In total ten absorption data sets were collected from eight quartz grains.

After sample runs were completed, absorption maps were created and analyzed using Atlμs. Due to the time constraints at the ALS, this work was largely done in Milwaukee by remotely logging in to computers at the ALS that had the Atlμs software installed. The peak height function, which calculates the area under a specific wavelength peak, was used to create absorption maps specifically for wavelengths of interest (Fig. 11). A separate absorption map was created from each run for both the ~3400 cm^{-1} and the ~3600 cm^{-1} peaks. An absorption

map is essentially a colored contour map that shows areas with high wavelength peaks in red and transitions through yellow and green to areas with low peaks in blue. The maps can be fine-tuned by adjusting the intensity range so that the areas of interest are more distinct. This was done for each sample run, and images were captured for further analysis.

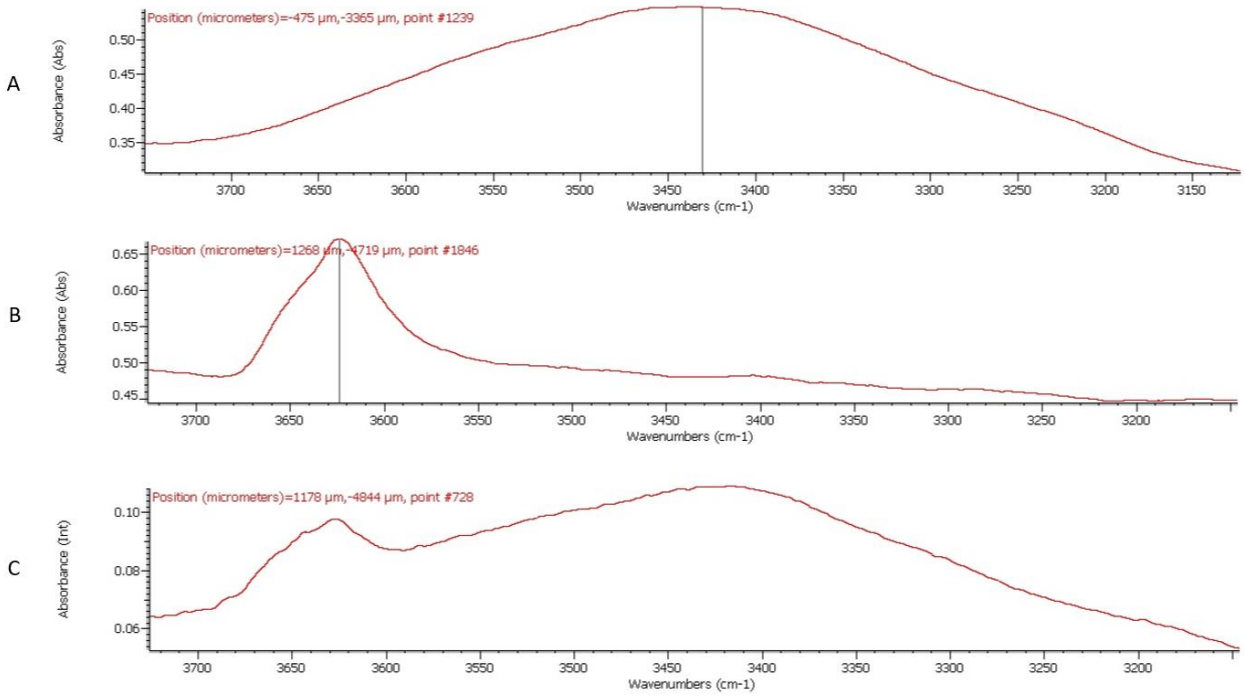

Figure 10: Examples of FTIR absorbance peaks. (A) A broad peak at ~3400 cm-1 is associated with OH from molecular water. (B) A thinner peak at ~3600 cm-1 is associated with OH locked in micas. (C) Both peaks can often be found together.

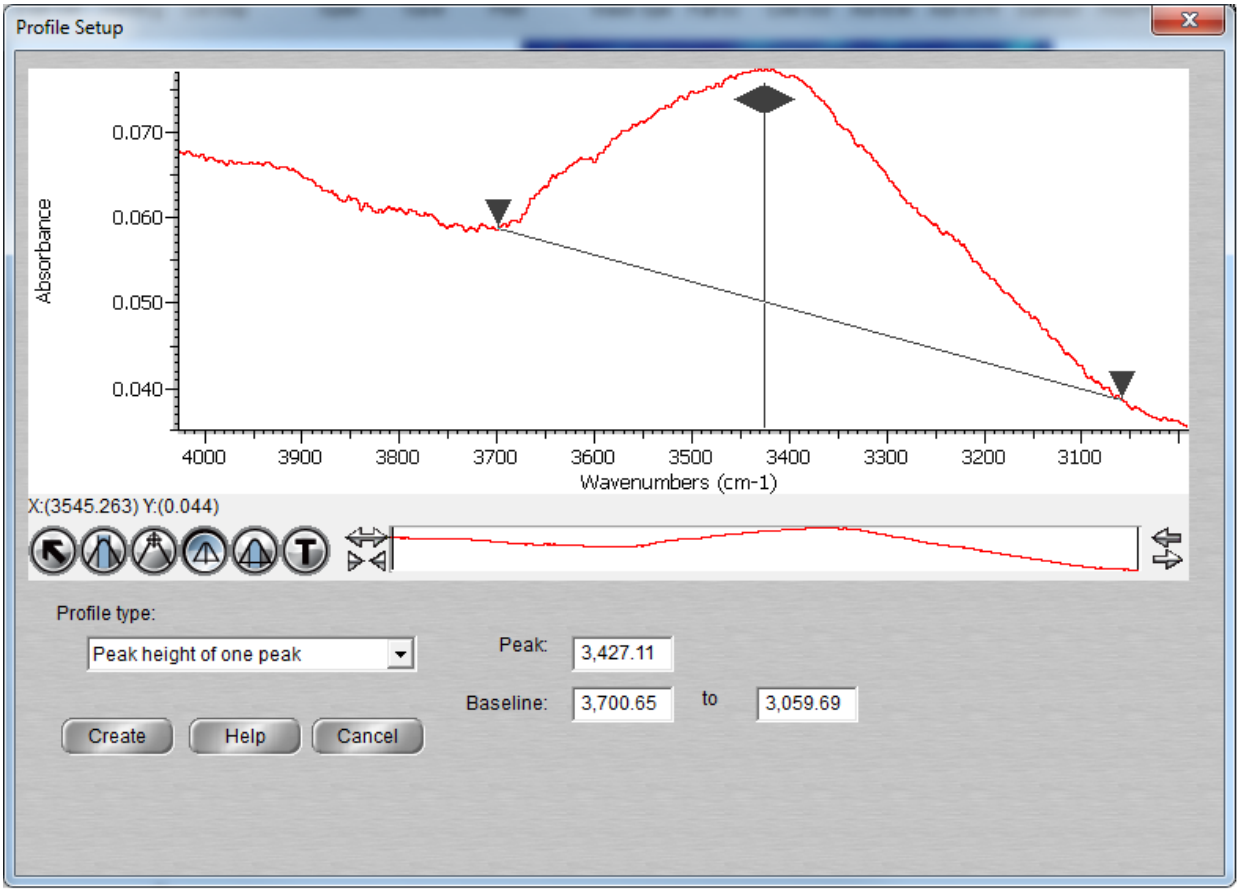

Figure 11: The peak height function was used to restrict data contouring to the wavelengths of interest. The highest point on the peak of interest was selected as well as a baseline to which it was compared.

3.6 Data Analysis

To determine if the water absorption maps created from the FTIR were related to the microfractures found in SEM-CL, the FTIR images were overlain on the SEM-CL images using Microsoft PowerPoint. Once the images were combined, they were analyzed to see if the ~3400 cm^{-1} and/or ~3600 cm^{-1} bands correlated with microfractures or any other observable features. The results from grains were compared to determine if there was a relationship between the extent of microfracturing, the location of water, and the degree of strain.

Chapter 4: Results

4.1 Petrographic Microscopy

Barszewski (2012) performed a microstructural analysis of quartz grains found in Mineral Fork diamictite clasts collected from the same region as this study, including some of the same outcrops on Antelope Island. She analyzed quartz grains from all three clast types found in the Mineral Fork diamictite: granite, paragneiss and quartzite. The current study only included quartzite clasts; however, the microstructural trends observed were similar to those found by Barszewski (2012).

Barszewski (2012) found that microstructures associated with brittle deformation mechanisms, such as microfractures and veins, were most common in low-strain samples and decreased as strain increased. She also found that microstructures associated with crystal plastic deformation and dislocation creep, such as undulose extinction, subgrains, and bulged boundaries, were limited in the low-strain samples, but increased as strain increased. The highest strain quartz samples (AI-06), however, were found to have fewer crystal plastic deformation features. These samples also showed a reduction in grain size compared to lower strain sites. Barszewski (2012) proposed that this was due to recrystallization which reset the crystal structure.

Quartzite is more competent than granite or paragneiss, which is evidenced by quartzite clasts having much lower R_{xz} values than granite or paragneiss clasts, even in the high-strain zone (Table 1; Fig. 6). This difference in strain accumulation has an effect on the

microstructures present in the sample. For instance, microfractures formed in quartz grains within a paragneiss under lower bulk strain than would be needed for them to form in quartz grains within a quartzite. Despite this, the general trends found by Barszewski (2012) were also found in this study. Low-strain samples showed signs of mostly brittle deformation including microfractures and veins (Fig. 12A). Medium-strain samples showed signs of both brittle deformation and crystal plastic deformation including microfractures, undulose extinction, subgrains, and bulged boundaries (Fig. 12B). High-strain samples showed mostly signs of crystal plastic deformation such as undulose extinction, subgrains, and bulged boundaries; however, some microfractures could still be found in larger grains (Fig. 12C). Some high-strain samples showed extensive recrystallization.

Barszewski (2012) found that high-strain samples (from AI-06) had a decrease in crystal plastic deformation features compared to medium-strain samples due to recrystallization. This, however, was not necessarily the case for samples from this study. While there was evidence of smaller grain sizes and some recrystallization, larger non-recrystallized grains often still showed features of crystal plastic deformation and even some brittle deformation. This is most likely due to quartzite being stronger than the paragneiss or granite samples, so full recrystallization did not occur and many brittle and crystal plastic microstructural features were preserved.

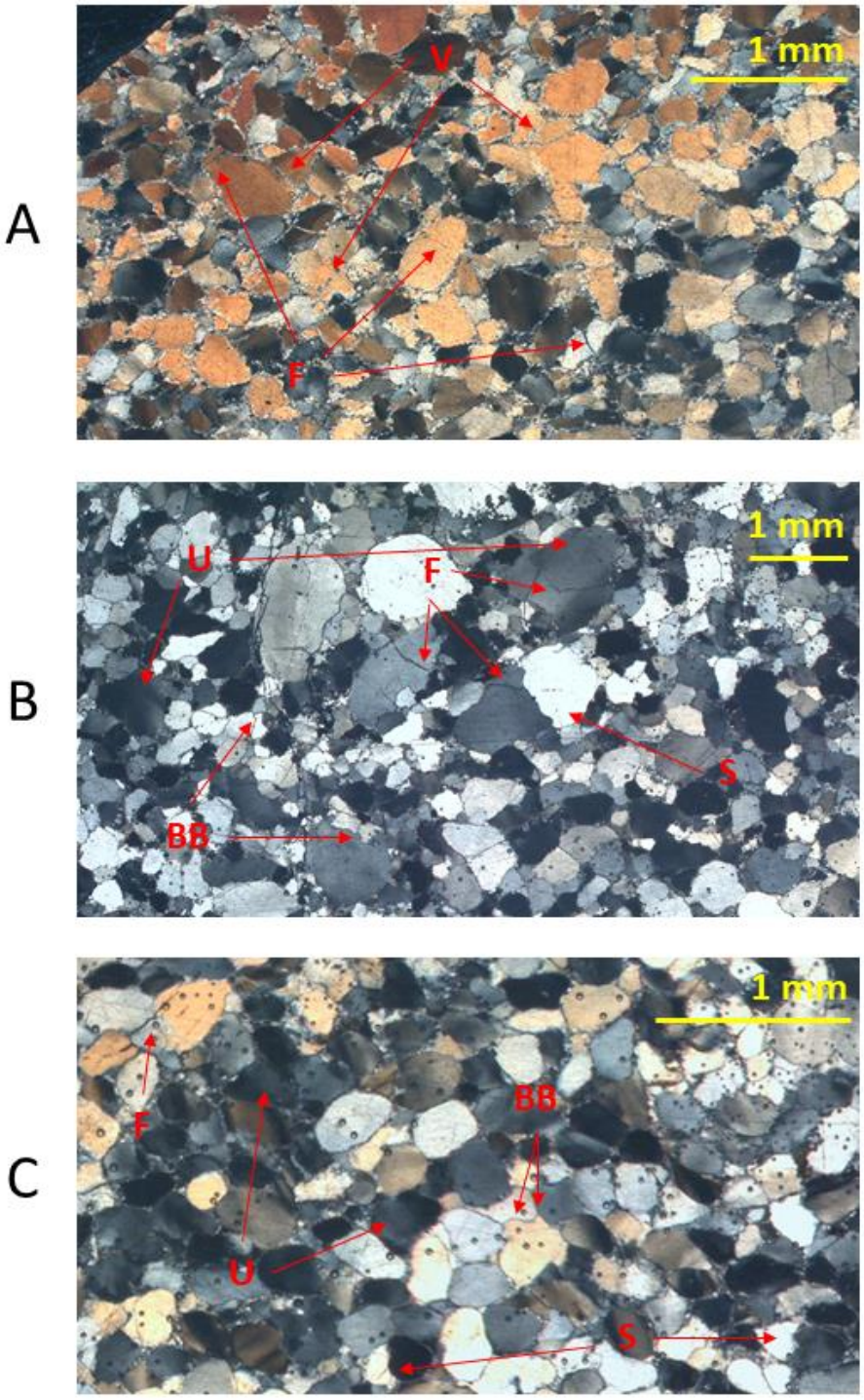

Figure 12: Photomicrographs of microstructures in quartzite clasts, all oriented on the XZ plane. Quartz grains showing microfractures (F), veins (V), undulose extinction (U), subgrains (S), and bulged boundaries (BB). (A) Low-strain from AI-08-09-Q13. (B) Medium-strain from AI-08-02-Q14. (C) High-strain from AI-08-06-Q13. Evidence for crystal-plastic deformation mechanisms generally increases with strain while evidence for brittle deformation mechanisms increases between low and medium strain, and decreases with further strain.

4.2 Scanning Electron Microscopy Cathodoluminescence (SEM-CL)

The SEM-CL results of this study consisted of digital images that showed the contrast in luminescence between older original quartz and newer quartz within individual quartz grains. The newer quartz formed along healed microfractures and generally had low luminescence compared to the original grains allowing them to be easily identified in SEM-CL. These healed microfractures were not visible under the petrographic microscope nor on the SEM under either secondary electrons (SE) or backscattered electrons. SEM-CL allowed for the identification of extensive microfracturing within these samples that would otherwise have been undetectable, a result first found by Barszewski (2012). Microfractures were identified in all strain zones, however, there were differences in the extent of fracturing between the low, medium, and high-strain zones.

Most quartz grains in the low-strain clasts did not have microfractures, but many microfractures could be found in some. The microfractures were usually quite thin and constrained within a single grain (Fig. 13). In the medium-strain clasts, microfractures were extensive and present within almost every grain. These microfractures were usually thicker than those within the low-strain samples, and there were many instances of the fractures extending through multiple grains (Fig. 14). The high-strain clasts showed a decrease in visible fractures with most of the grains showing a dull “mottled” appearance. According to Barszewski (2012), this was most likely due to recrystallization. Although microfractures were rare, they could still be found in certain, usually larger, grains (Fig. 15). These results show a general progression of quartz grains that are beginning to show evidence of fracturing in the low-strain

zone, are extensively fractured in the medium-strain zone, and are extensively recrystallized in the high-strain zone. SEM-CL images for all imaged grains can be found in Appendix A.

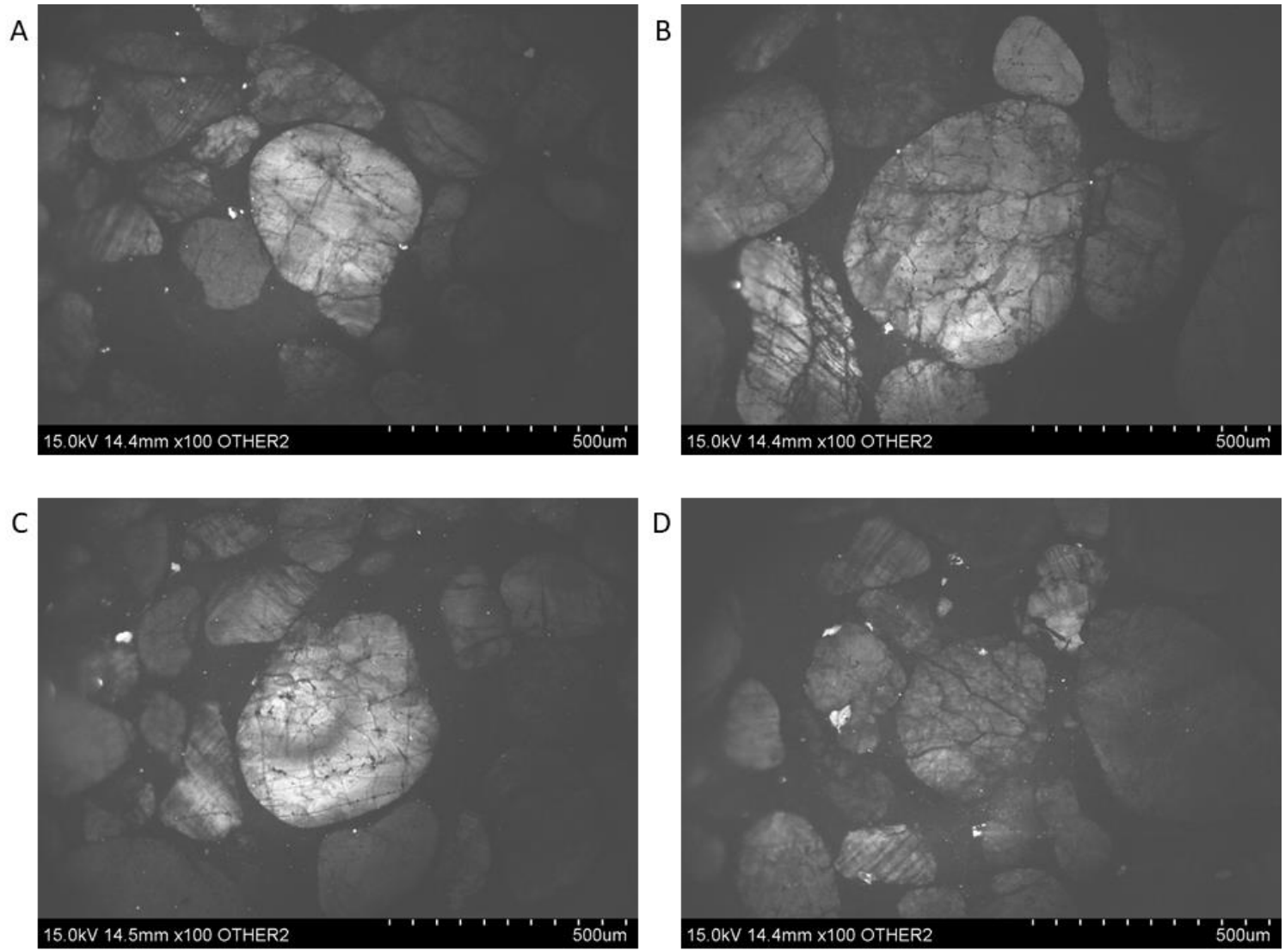

Figure 13: SEM-CL images of quartz grains from the low-strain zone. Grains show thin "hairline" microfractures that are contained within a single grain. (A) AI-08-09-Q14-1 (B) AI-08-09-Q14-2 (C) AI-08-09-Q14-5 (D) AI08-09-Q14-6

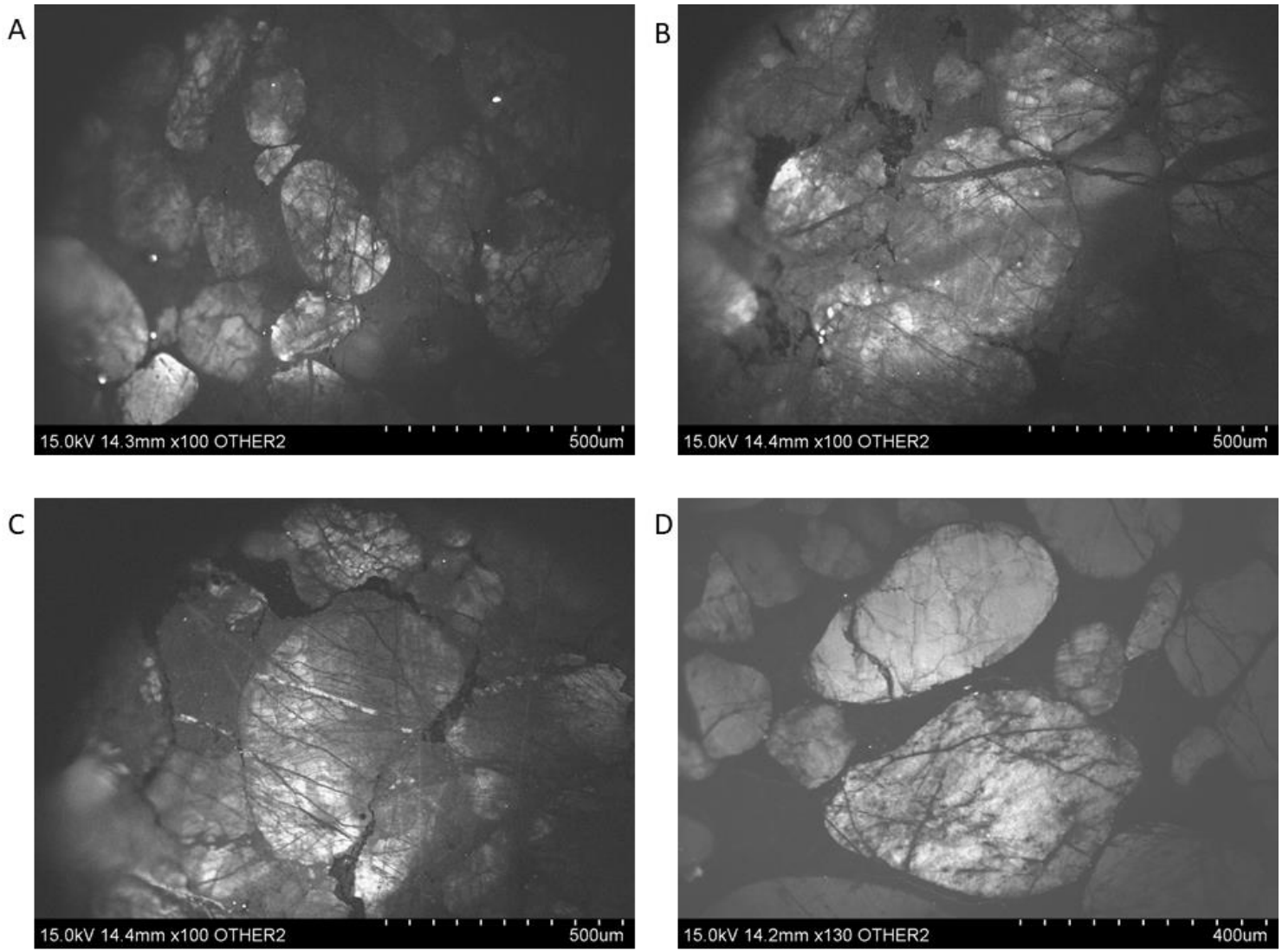

Figure 14: SEM-CL images of quartz grains from the medium-strain zone. Images show extensive microfractures. Most are thicker than the fractures present in low-strain samples and many extend through several grains. (A) AI-08-02-Q12-7 (B) AI-08-02-Q14-9 (C) AI-08-02-Q14-2 (D) AI-08-03-Q12-3

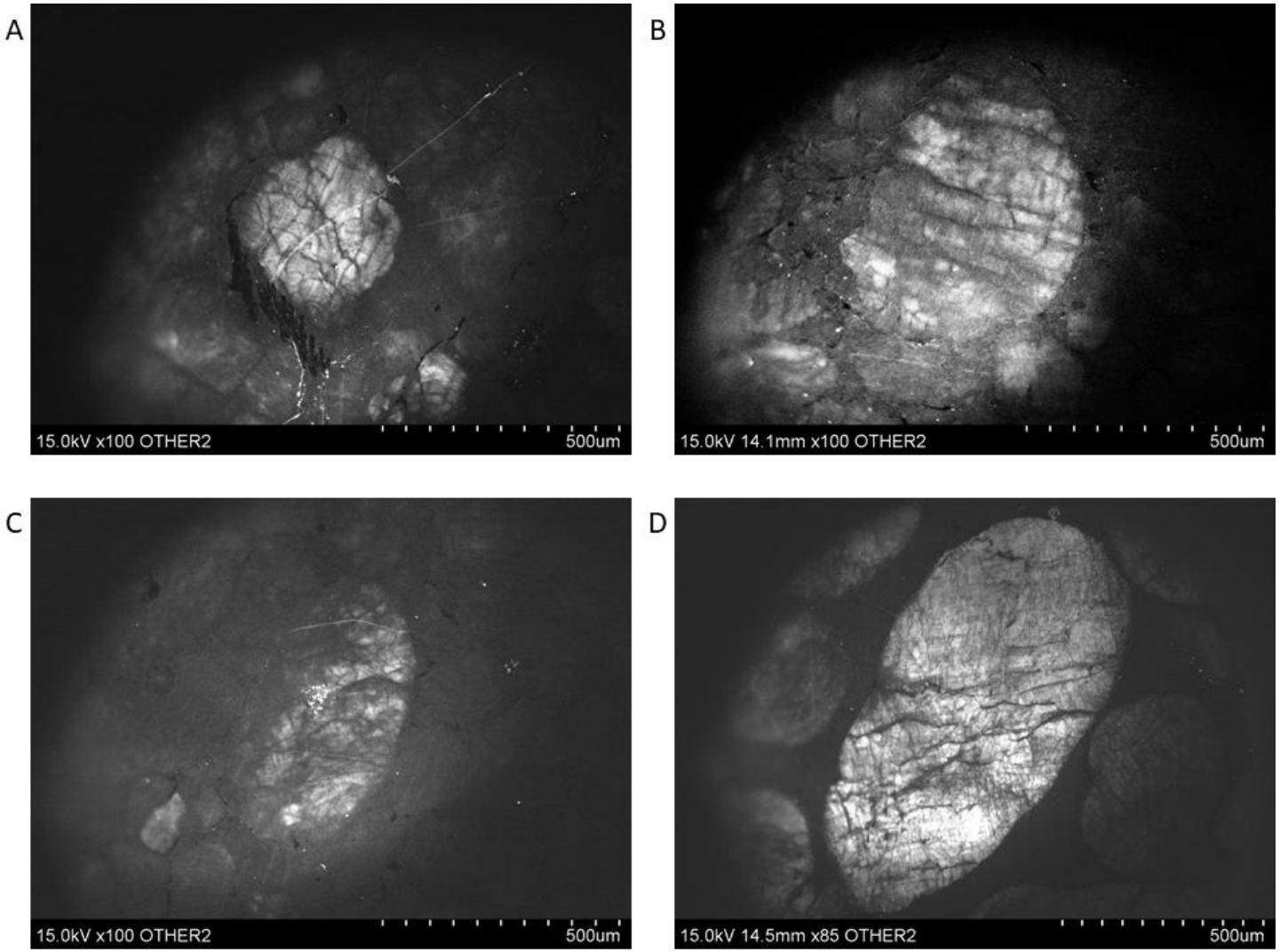

Figure 15: SEM-CL images of quartz grains from the high-strain zone. Most grains show a "mottled" appearance due to recrystallization, however, some microfractures are still visible. (A) AI-08-06-Q11-17 (B) AI-08-06-Q12-1 (C) AI-08-06-Q12-6 (D) AI-08-06-Q13-11

4.3 Fourier-Transform Infrared Spectroscopy (FTIR)

FTIR results showed that it is possible to determine if water is present, and to spatially constrain where it is located within individual quartz grains with micron level precision. However, it was beyond the scope of this study to accurately quantify the amount of water contained in any given location. This is because the thickness of the sample needs to be known to micron level precision to properly calculate the amount of water from the height of the OH wavelength peak. Since the samples used in this study were finished by hand using lapping film, their precise thickness was not readily obtainable. However, using an estimated sample thickness of ~30 ± 5 µm, it was still possible to make rough calculations of water concentration using the maximum peak height found within a map and the Beer-Lambert Equation:

$$c_w = \frac{M_w \cdot A}{\rho \cdot t \cdot \varepsilon}$$

where c_w is the concentration of water (in wt. %), M_w is the molecular weight of water (18.02 g/mol), A is the absorbance height of the peak of interest (3400 cm^{-1} in this case), ρ is the density of quartz (2320 g/l), t is the thickness of the area analyzed (cm), and ε is the molar absorptivity of quartz (78 l/mol·cm) (Hetherington & Jack, 1962; Paterson, 1982; Nichols & Wysoczanski, 2007). The values calculated are within range of other studies (Kronenberg & Wolf 1990; Kronenberg et al., 2017) and show the highest concentration of water in a sample from AI-06 (high-strain) that is near extensive veining and the lowest concentration in a sample from AI-03 (medium-low strain) (Table 3).

Though it was not possible to precisely quantify the amount of water in a grain, it was possible to show the relative amount from one location to another using absorption maps. The

absorption maps created in this study were composed of thousands of points where individual spectra were collected (Fig. 16A). Most of the absorption maps contained ~3000 spectra. Thus, only the absorption maps are shown in this study, as it was not practical to include all the individual spectra. Absorption maps are sufficient to show where water was located within each sample.

Upon completion of an FTIR mapping run, the Atlμs program would first create a general absorption map containing averages of the entire spectrum collected at each location. Once this was completed, the user could select a certain wavenumber to highlight, such as in our case, to highlight the part of the spectrum practical for detection of OH. These maps, however, were not the most useful because they contained a lot of noise (Fig. 16C). Two refinement procedures were used to improve the efficacy of the absorption maps. The first was to limit the absorption map to the peak of interest. This was done by running the peak height function in Atlμs, which used a selected peak highpoint and compared it against a selected baseline (Fig. 16B). This created an absorption map that was peak specific (Fig. 16D). Although the new absorption map showed truer values for the peak of interest, the map was still quite noisy. To fix this, the intensity range was altered to get rid of any really high or low values that were skewing the map. This created a final absorption map that was relevant to the peak of interest and contained very little noise (Fig. 16E). This process was completed on every sample for both the ~3400 cm^{-1} OH peak (associated with liquid water, Fig. 16E) and the ~3600 cm^{-1} OH peak (associated with micas or other minerals containing OH groups, Fig. 16F).

The results of the final absorption maps showed evidence of the ~3400 cm^{-1} OH peak within individual grains of quartz (Fig. 16E), indicating that liquid water had entered the grain at

some point. The ~3400 cm^{-1} peak was usually concentrated along linear paths crossing through a grain that correspond with microfractures (Fig. 16E), a specific fluid inclusion within a grain, or along the grain boundaries. The ~3600 cm^{-1} peak was usually concentrated on grain boundaries, however, slight amounts could still be found within certain quartz grains along similar linear paths marked by the ~3400 cm^{-1} peak (Fig. 16F). Absorption maps for each sample are shown in the discussion section overlain with the SEM-CL images. Images showing the peak function and intensity ranges used for each absorption map can be found in Appendix B.

Sample ID	Strain	3400 cm^{-1} Peak Height	H_2O Concentration by Thickness (molar ppm)		
			25 µm	30 µm	35 µm
AI-08-03-Q12-5	Medium	0.08	3000	2500	2100
AI-08-02-Q12-1	Medium	0.13	5200	4300	3700
AI-08-02-Q12-2	Medium	0.28	11200	9300	8000
AI-08-02-Q14-4	Medium	0.17	6800	5600	4800
AI-08-06-Q11-15	High	0.5	19900	16600	14200
AI-08-06-Q11-1	High	0.15	6000	5000	4300
AI-08-06-Q13-6	High	0.15	6000	5000	4300
AI-08-06-Q13-8	High	0.3	11900	10000	8500

Table 3: Rough water concentration calculations using the Beer-Lambert Equation. The value from the highest 3400 cm^{-1} wavelength peak in each sample was used for the equation and the concentration was calculated for possible sample thicknesses of 25 µm, 30 µm, and 35 µm.

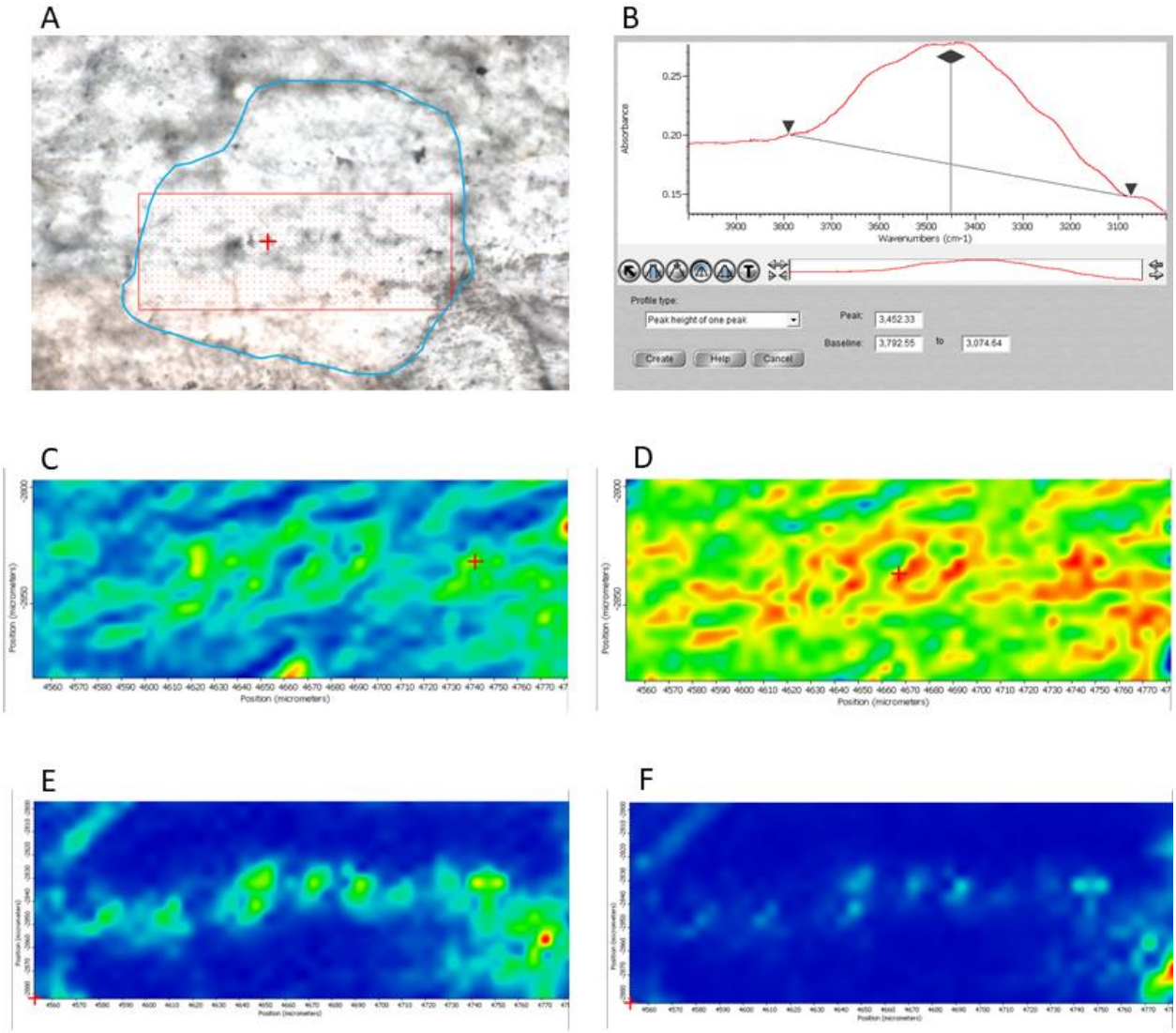

Figure 16: Images showing example of progression of FTIR data capture and refinement. (A) Image of sample AI-08-02-Q12-2. The blue line shows the outline of the quartz grain. The red box shows the outline of the FTIR mapping run with each red dot representing the location where a specific spectrum was recorded, 720 in total. (B) The ~3400 cm^{-1} peak used for the peak height function when refining the data. (C) Image showing the absorption map for the ~3400 cm^{-1} peak before refinement (step shown in B). (D) Image showing the absorption map for the ~3400 cm^{-1} peak after running the peak height function (step shown in B, which was used to refine the part of the spectrum analyzed). (E) Image showing the final absorption map for the ~3400 cm^{-1} peak after adjusting the intensity range to emphasize features. It shows a general line of liquid water across the center of the grain. (F) Image showing the final absorption map for the ~3600 cm^{-1} peak after following the same procedure used to produce E. A peak high can be seen in the lower right hand corner, which corresponds to the grain boundary.

Chapter 5: Discussion

5.1 Combined FTIR-CL Analysis

The culmination of this study was the creation of figures which were composed of FTIR absorption maps overlain on the SEM-CL images (Figs. 17-32). These final images allowed for the analysis of whether the location of water within a grain was correlated with the location of microfractures. This analysis found that there was strong evidence of the 3400 cm^{-1} wavelength peak, which is associated with OH from molecular water, being found along healed microfractures. There was also strong evidence of the 3600 cm^{-1} wavelength peak, which is associated with OH locked in micas, being largely constrained to the grain boundaries. These results were found in both the medium and high-strain zones. There were no final figures created for the low-strain zone because there were no FTIR results from this zone. This was due to a combination of time constraints at the synchrotron where time was focused on samples with obvious microfracturing, and one of the low-strain samples being destroyed when attempting to remove it from the slide. All images are oriented so the X direction (lineation) is vertical and the Z direction is horizontal.

5.1.1 Medium-Strain: Outcrop AI-03 - Sample AI-08-03-Q12-5

Figures 17 shows a ~750 µm quartz grain with many healed microfractures surrounded by many smaller grains. The absorption map covers the lower-left side of the grain and extends into the matrix. There is strong evidence of molecular water (3400 cm^{-1} peak) within the grain following along a thin microfracture that runs top-left to bottom-right in the upper-right section of the absorption map (Figs. 17A & 18A). There also seems to be some correlation between molecular water and another thin top-left to bottom-right microfracture in the center of the map, as well as a thicker fracture running left to right. The matrix surrounding the grain boundary shows a lot of molecular water as well. There is no evidence of the 3600 cm^{-1} peak within the grain (Figs. 17B & 18B). There is a thin coating along the southwest grain boundary and trace amounts within the matrix.

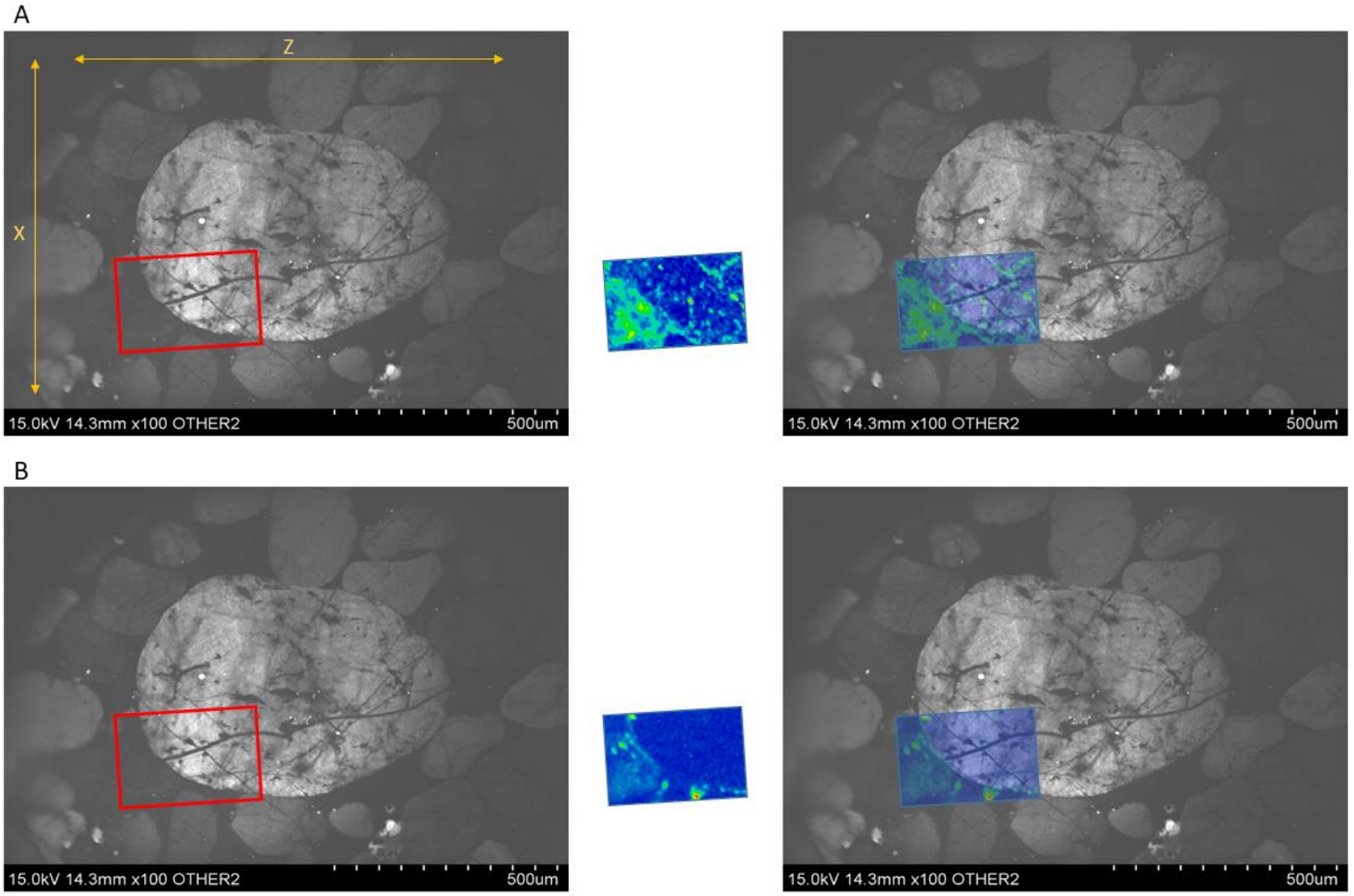

Figure 17: Combined FTIR-CL image for medium-strain sample AI-08-03-Q12-5. XZ section with lineation along the vertical direction with down-plunge toward the bottom. (A) 3400 cm^{-1} peak. (B) 3600 cm^{-1} peak.

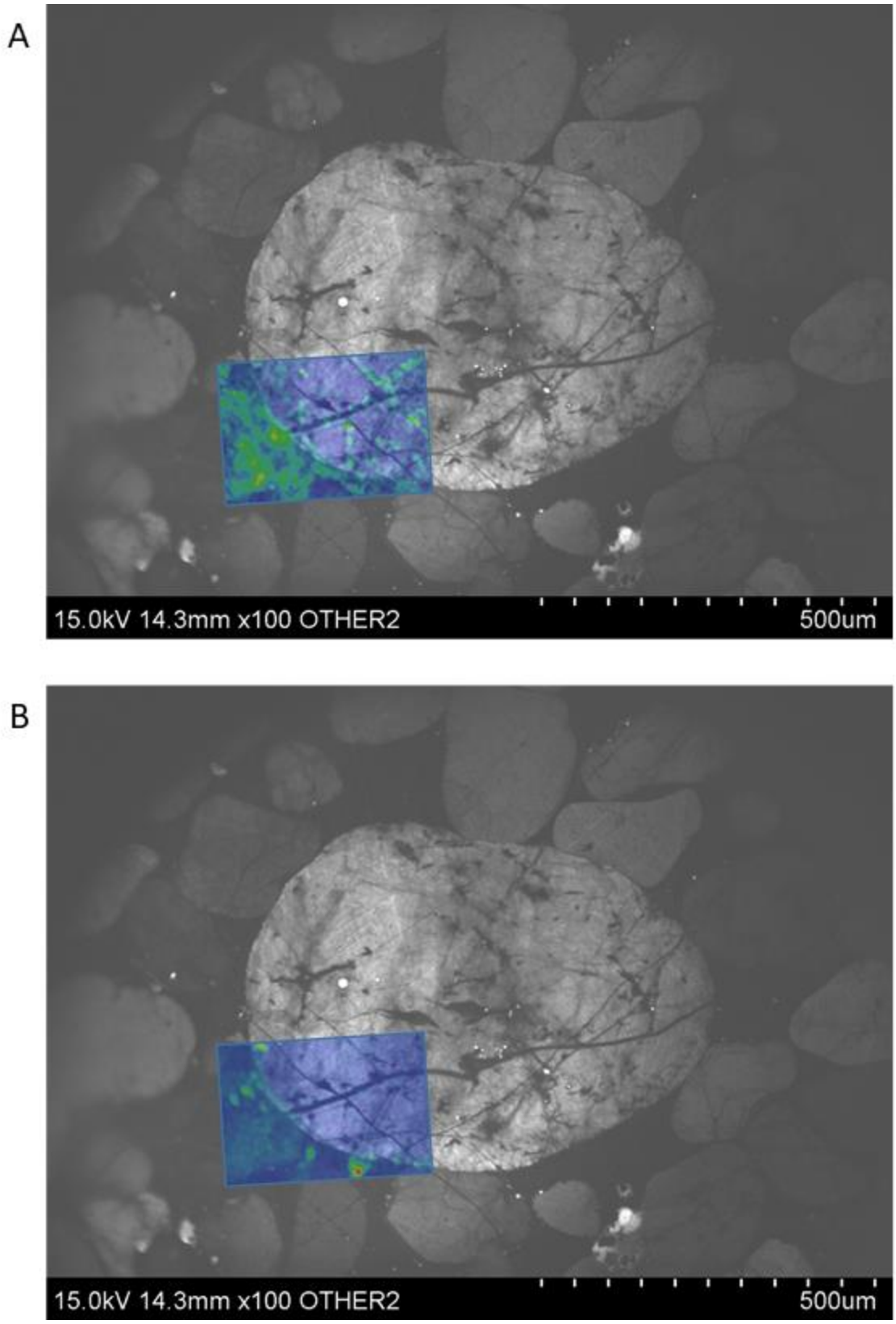

Figure 18: Larger FTIR-CL images for medium-strain sample AI-08-03-Q12-5. (A) 3400 cm^{-1} peak. (B) 3600 cm^{-1} peak.

5.1.2 Medium-Strain: Outcrop AI-02 - Sample AI-08-02-Q12-1

Figure 19 shows a ~300 µm quartz grain surrounded by smaller grains as well as some of equal size. There is a microfracture running top to bottom through the center of the grain that extends through the grain above. The absorption map covers most of the grain and grain boundary except for the top-left portion. The 3400 cm^{-1} peak correlates strongly with the top-bottom microfracture with some additional spots along the grain boundary (Figs. 19A & 20A). The 3600 cm^{-1} peak is mostly constrained to the grain boundary but there is a faint top-bottom line through the center that matches the microfracture (Figs. 19B & 20B).

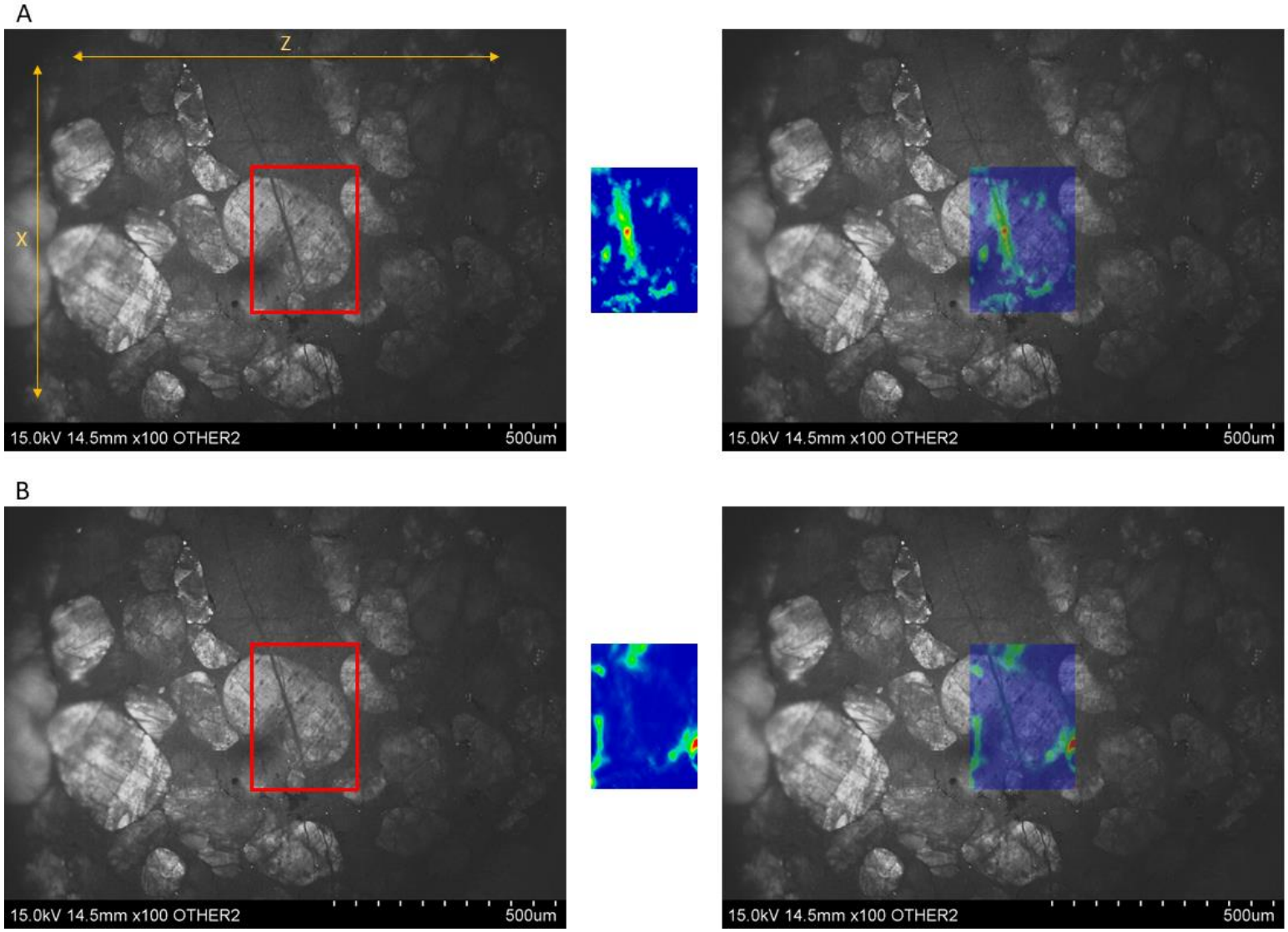

Figure 19: Combined FTIR-CL image for medium-strain sample AI-08-02-Q12-1. XZ section with lineation along the vertical direction with down-plunge toward the bottom. (A) 3400 cm^{-1} peak. (B) 3600 cm^{-1} peak.

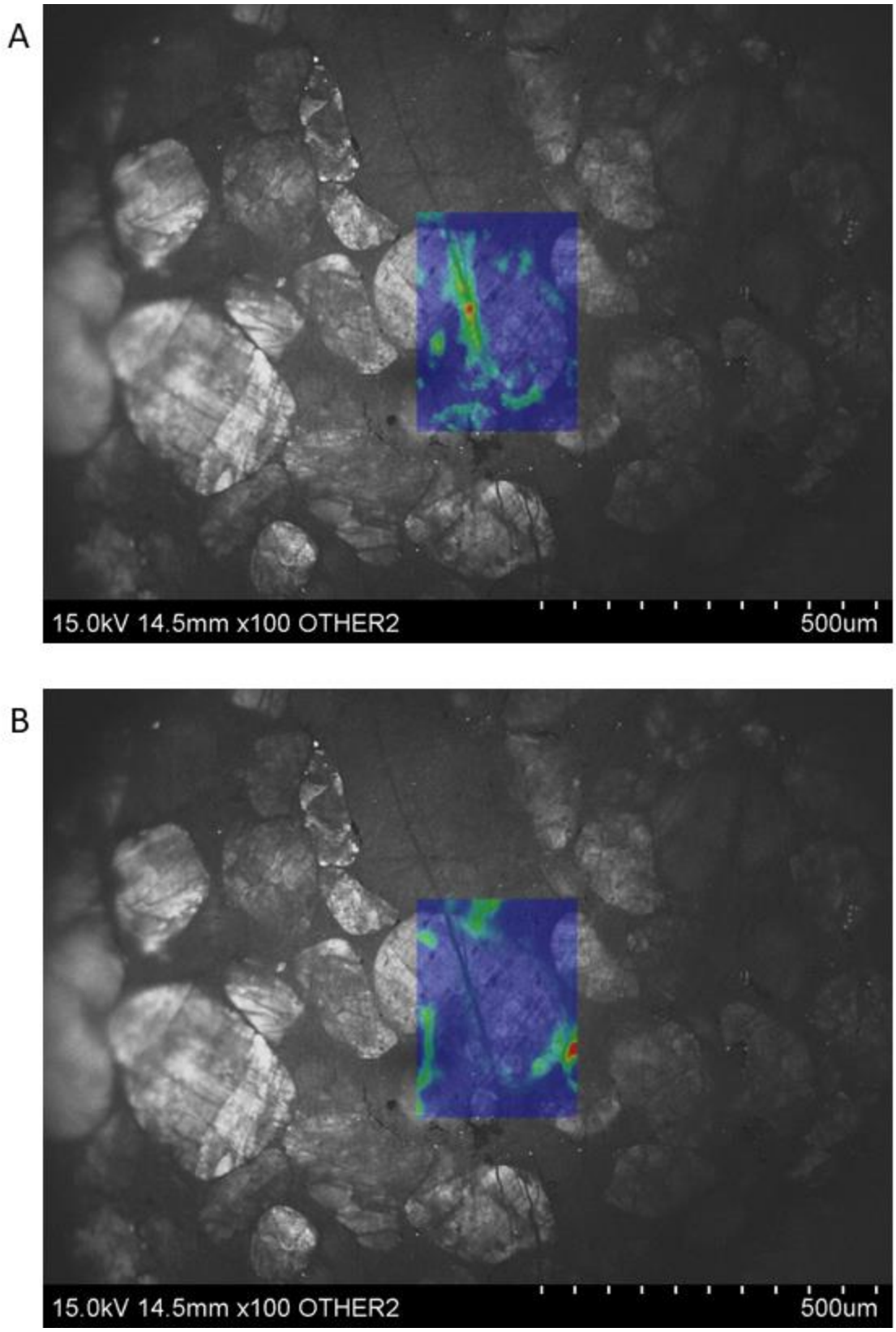

Figure 20: Larger FTIR-CL images for medium-strain sample AI-08-02-Q12-1. (A) 3400 cm^{-1} peak. (B) 3600 cm^{-1} peak.

5.1.3 Medium-Strain: Outcrop AI-02 – Sample AI-08-02-Q12-2

Figure 21 shows a ~200 µm quartz grain with two large microfractures running top to bottom through the grain, one in the center and one to the right. The FTIR data came from a single run, however, due to some faulty data points caused by a temporary beam shut down, it needed to be split into two absorption maps. Combined, they cover most of the grain as well as the grain boundary to the top and bottom. The 3400 cm^{-1} peak correlates strongly with both of the microfractures (Figs. 21A & 22A). There is additional molecular water at the lower end of the center microfracture where there are several smaller microfractures in close proximity. There is also evidence of molecular water along the upper grain boundary running top-left to bottom-right. There is some evidence of the 3600 cm^{-1} peak along the center top-bottom microfracture, although it is faint (Figs. 21B & 22B). There is no significant evidence of the 3600 cm^{-1} along the right-hand top-bottom microfracture. The 3600 cm^{-1} peak is visible along the grain boundary with one hotspot in the upper-right and one in the lower-left. There is most likely larger concentrations of mica in these locations.

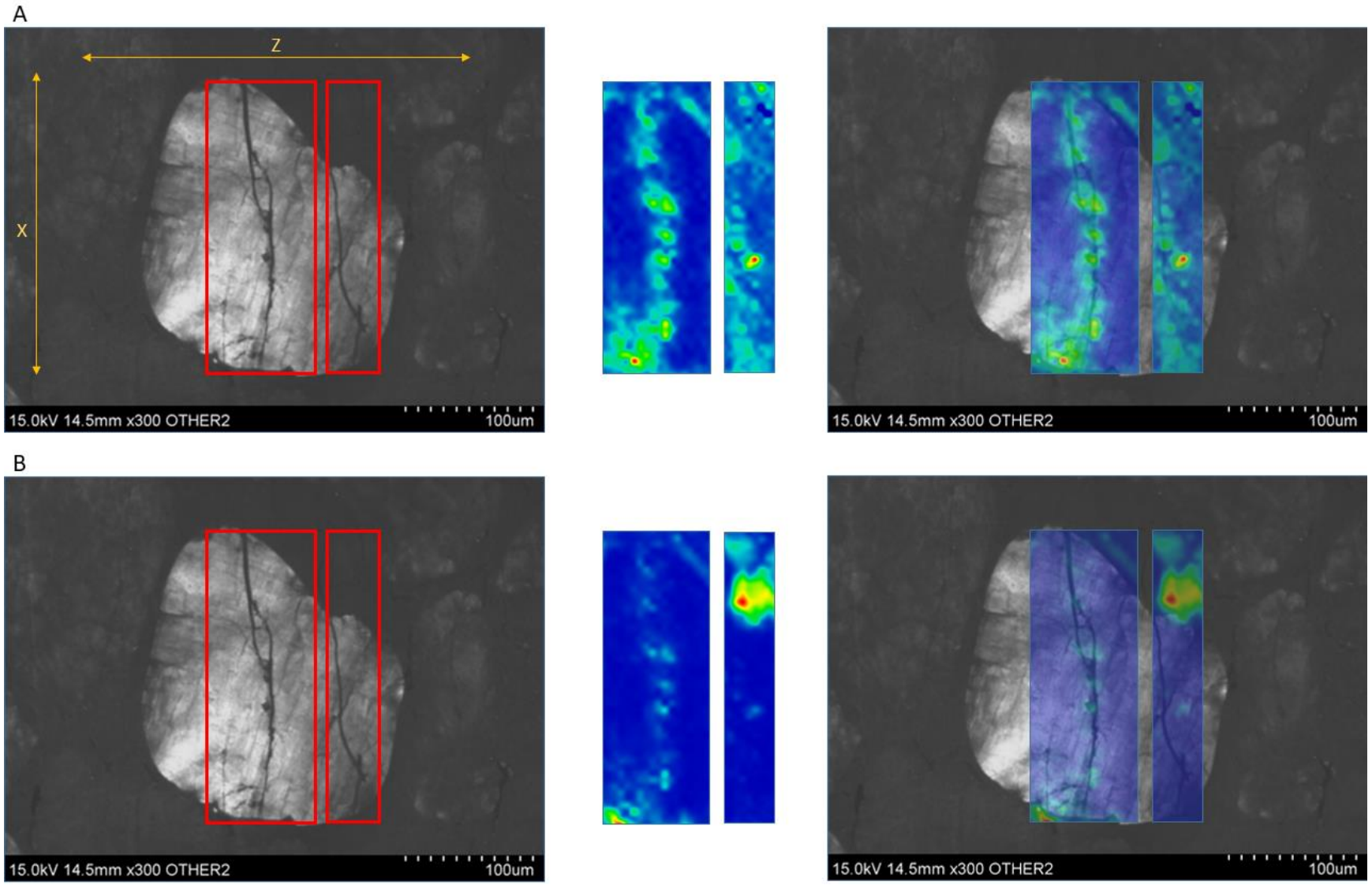

Figure 21: Combined FTIR-CL image for medium-strain sample AI-08-02-Q12-2. XZ section with lineation along the vertical direction with down-plunge toward the bottom. (A) 3400 cm^{-1} peak. (B) 3600 cm^{-1} peak

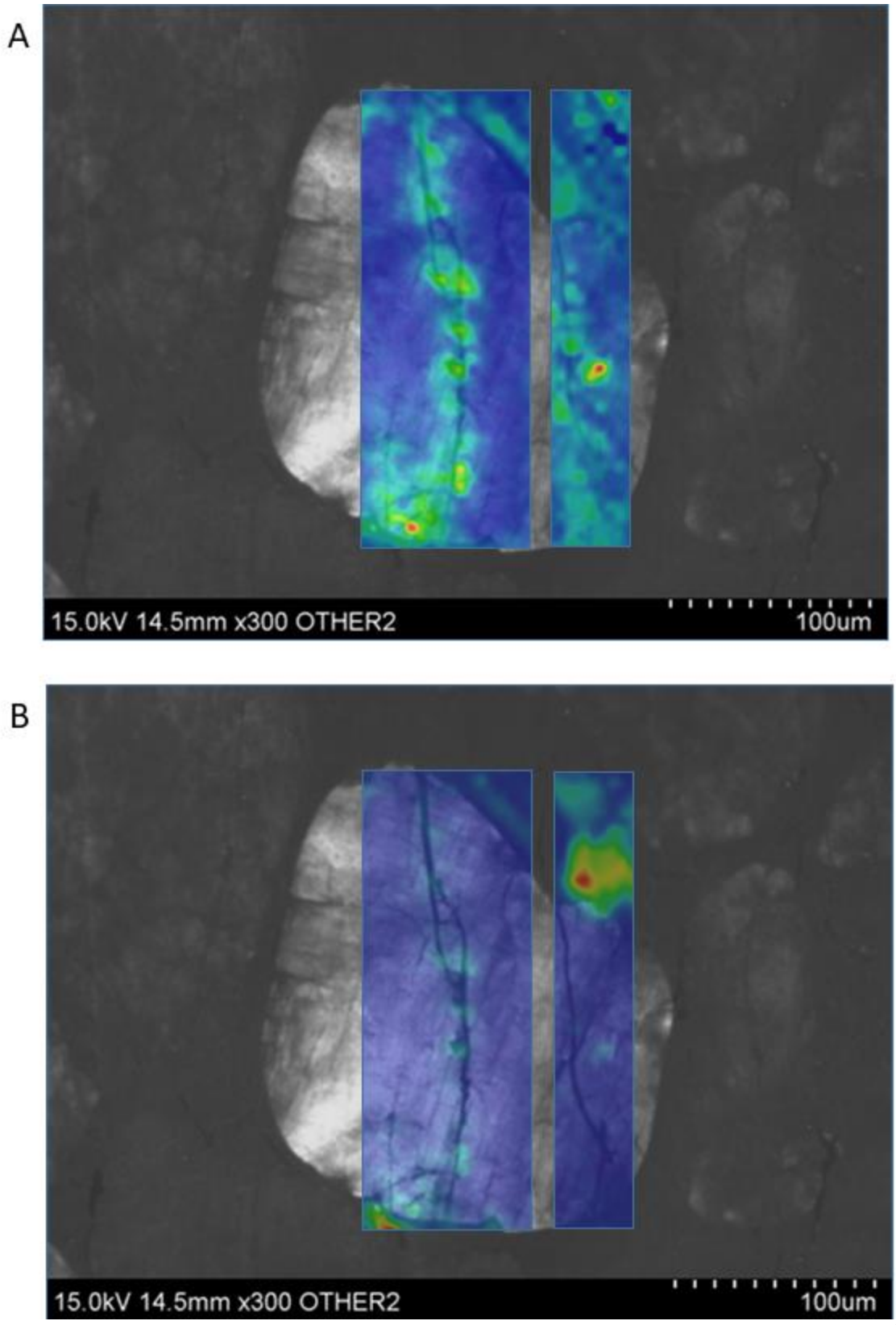

Figure 22: Larger FTIR-CL images for medium-strain sample AI-08-02-Q12-2. (A) 3400 cm^{-1} peak. (B) 3600 cm^{-1} peak.

5.1.4 Medium-Strain: Outcrop AI-02 – Sample AI-08-02-Q14-4

Figure 23 shows a ~500 µm quartz grain with many thin microfractures that have various orientations. There are also two large microfractures in the center of the grain, one running top-left to bottom-right and one running bottom-left to top-right. The surrounding grains are near equal in size and equally fractured. Microfractures can be seen extending through multiple grains. The absorption map covers the entire grain and grain boundary. There is significant evidence of molecular water within the grain and the 3400 cm^{-1} peak strongly correlates with at least nine microfractures (Figs. 23A & 24A). Molecular water can be seen following the microfractures in the upper-right of the absorption map through multiple grains. There are hotspots along the thicker top-left to bottom-right microfracture, which shows more molecular water associated with the thicker fracture. There is faint evidence of the 3600 cm^{-1} peak along this microfracture as well, showing that trace mica infiltrated the fracture before it healed (Figs. 23B & 24B). The rest of the 3600 cm^{-1} map correlates with the grain boundary, especially on the left and top sides of the grain. These hotspots match dark segments on the CL image, which are most likely micas.

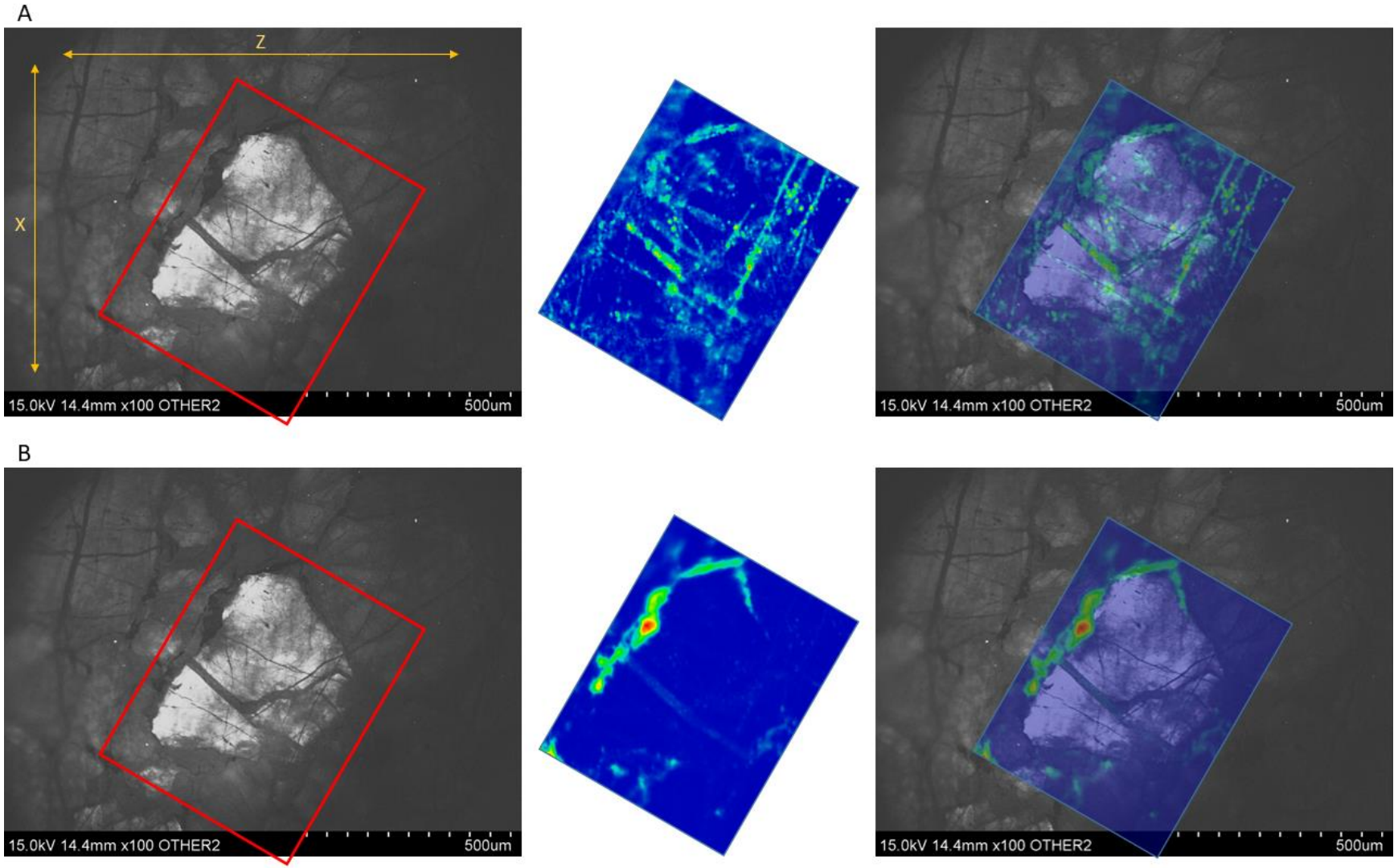

Figure 23: Combined FTIR-CL image for medium-strain sample AI-08-02-Q14-4. XZ section with lineation along the vertical direction with down-plunge toward the bottom. (A) 3400 cm^{-1} peak. (B) 3600 cm^{-1} peak.

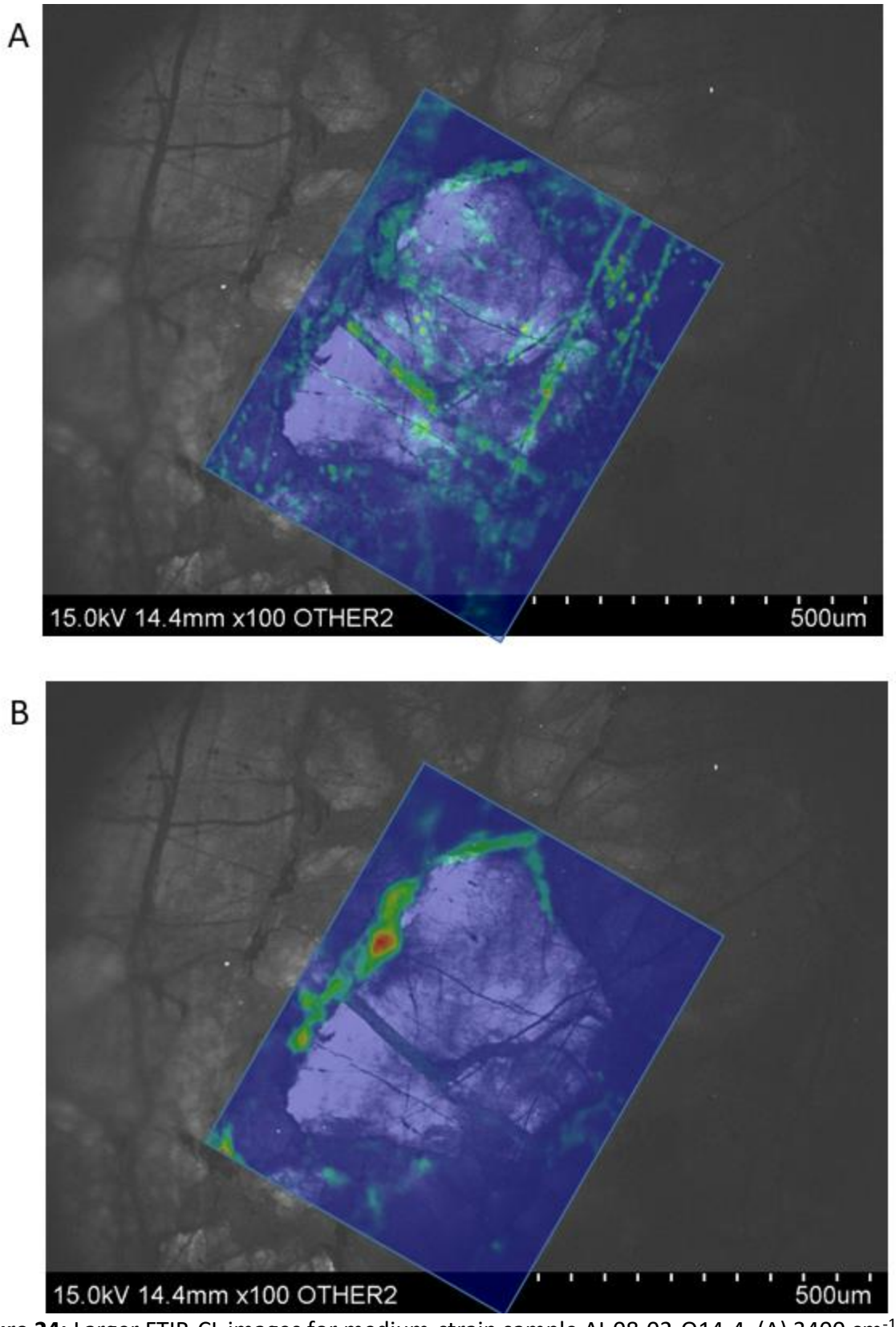

Figure 24: Larger FTIR-CL images for medium-strain sample AI-08-02-Q14-4. (A) 3400 cm^{-1} peak. (B) 3600 cm^{-1} peak.

5.1.5 High-Strain: Outcrop AI-06 – Sample AI-08-06-Q11-15

Figure 25 shows a ~600 µm quartz grain surrounded by smaller grains. The grain has a mostly mottled appearance showing some recrystallization. There are three thick microfractures that run top to bottom through the center of the grain as well as two that run left to right. The absorption map is contained completely within the grain, not showing any of the grain boundary. Both the 3400 cm^{-1} peak and the 3600 cm^{-1} peak show similar patterns in their absorption maps (Fig. 25A&B, Fig. 26A&B). They have a general top-bottom trend along the microfractures, although they don't follow them exactly. The lower left-right fracture is similar in this regard. It appears that the microfractures allowed both molecular water and trace micas to enter the grain. It appears that, as the grain recrystallizes and features reset, the wavelength peaks have less of a correlation to the features that caused them than they would in a lower strain setting.

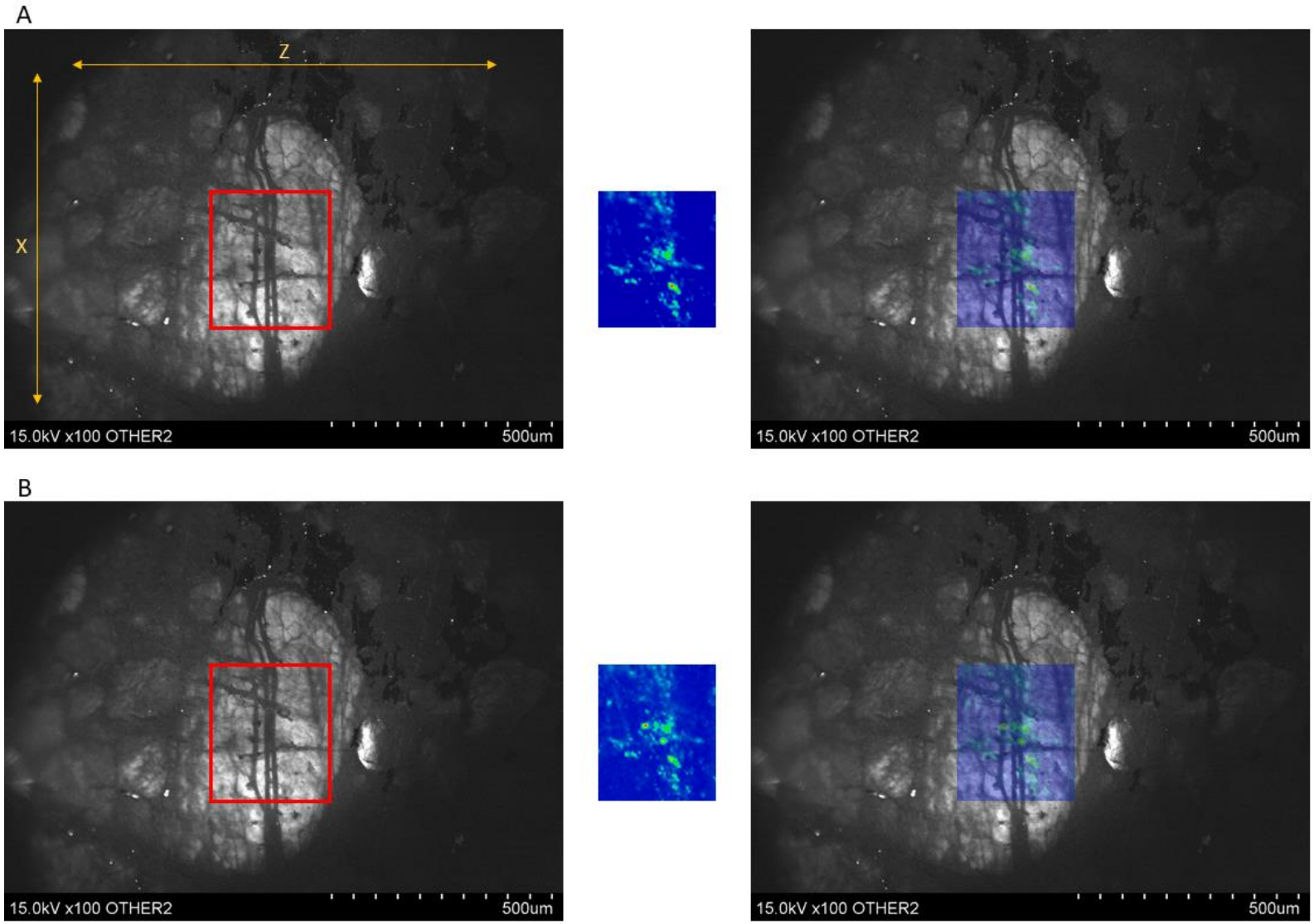

Figure 25: Combined FTIR-CL image for high-strain sample AI-08-06-Q11-15. XZ section with lineation along the vertical direction with down-plunge toward the bottom. (A) 3400 cm^{-1} peak. (B) 3600 cm^{-1} peak.

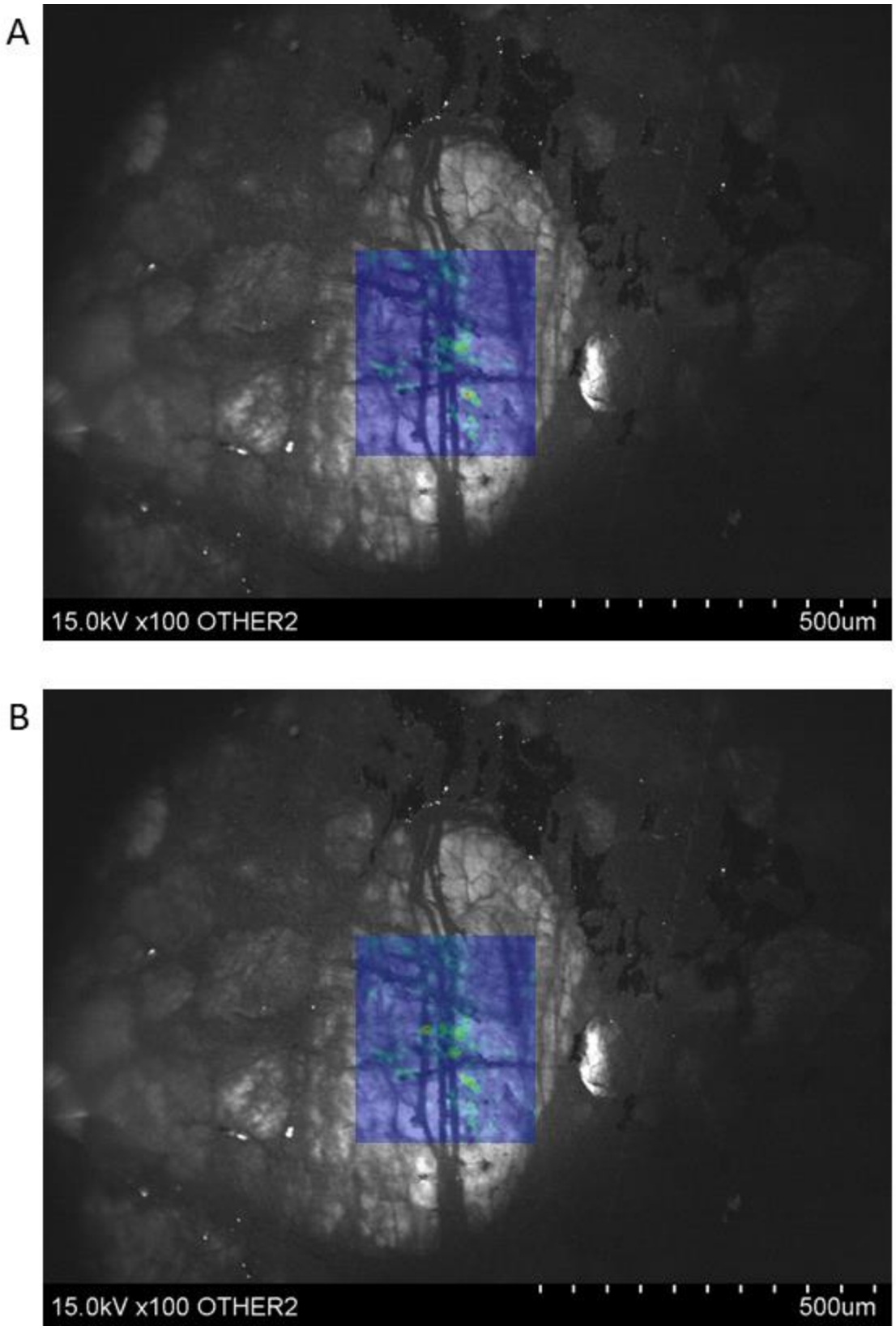

Figure 26: Larger FTIR-CL images for high-strain sample AI-08-06-Q11-15. (A) 3400 cm^{-1} peak. (B) 3600 cm^{-1} peak.

5.1.6 High-Strain: Outcrop AI-06 – Sample AI-08-06-Q11-16

Figure 27 shows a ~400 µm quartz grain with a completely mottled appearance, showing recrystallization. The surrounding grains are mostly smaller in size and have an equally mottled appearance. The absorption map is contained completely within the grain and does not include any of the grain boundary. Both the 3400 cm^{-1} peak and the 3600 cm^{-1} peaks show similar patterns in their absorption maps (Fig. 27A&B, Fig. 28 A&B). They both show two small points in the center of the map. The 3600 cm^{-1} peak map also shows a hot spot in the bottom-left corner of the map. The features on both maps do not correlate with anything on the CL image and are most likely inclusions. This figure again shows that the recrystallized grains are largely devoid of water within the grain.

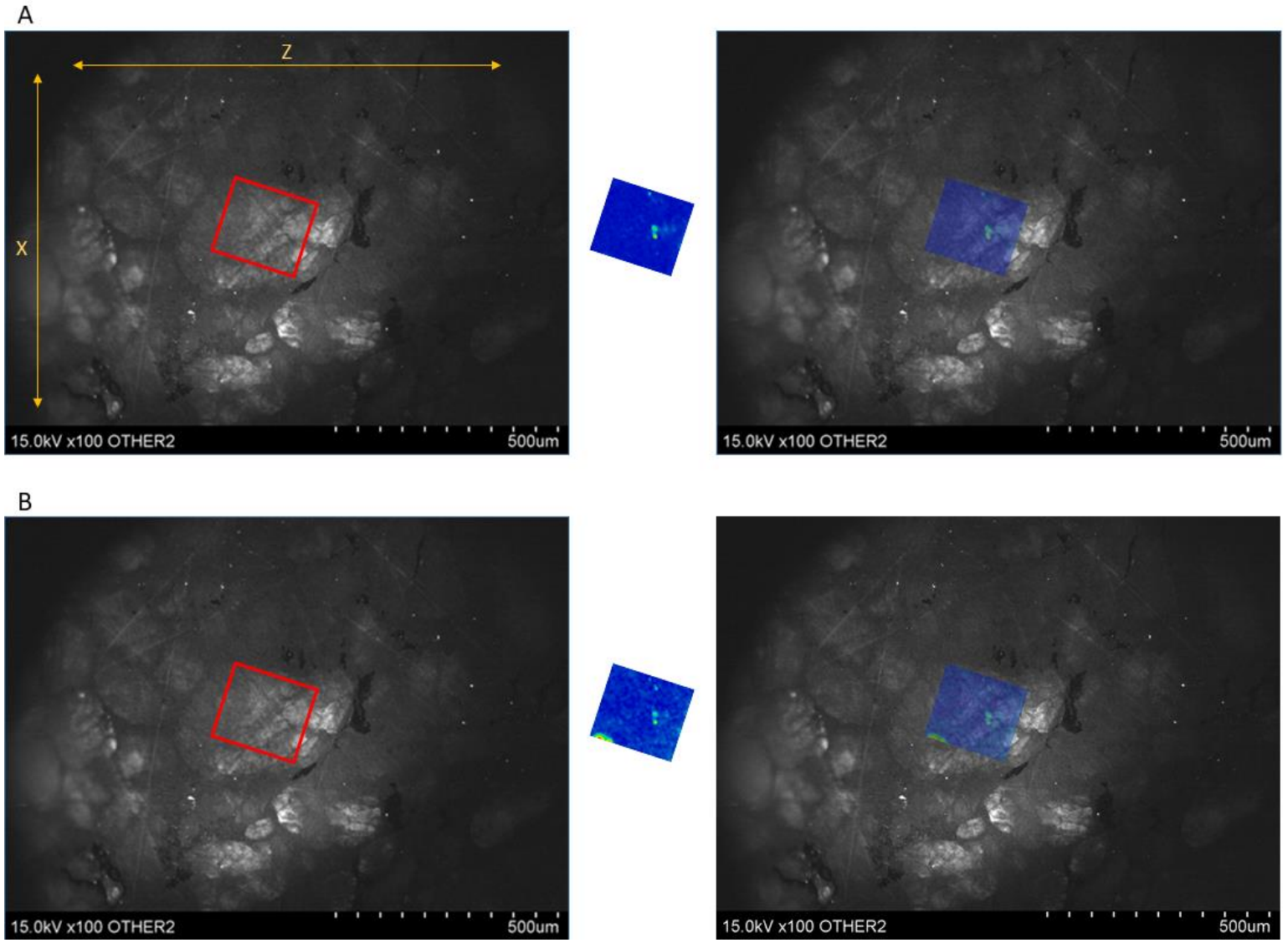

Figure 27: Combined FTIR-CL image for high-strain sample AI-08-06-Q11-16. XZ section with lineation along the vertical direction with down-plunge toward the bottom. (A) 3400 cm^{-1} peak. (B) 3600 cm^{-1} peak.

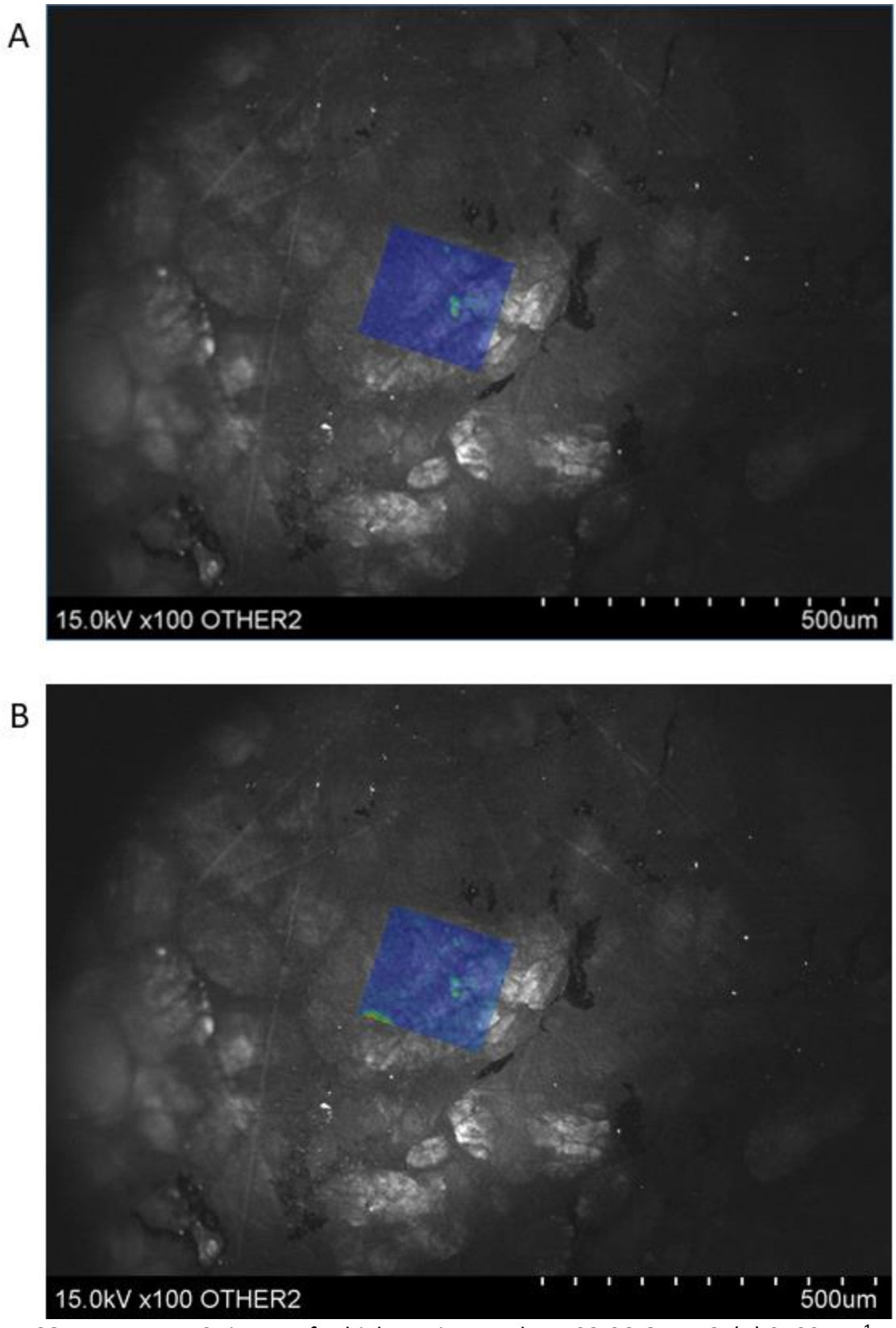

Figure 28: Larger FTIR-CL images for high-strain sample AI-08-06-Q11-16. (A) 3400 cm^{-1} peak. (B) 3600 cm^{-1} peak.

5.1.7 High-Strain: Outcrop AI-06 – Sample AI-08-06-Q13-6

Figure 29 shows a ~400 µm quartz grain with two microfractures oriented bottom-left to top-right and two that are oriented left to right. The bottom-left to top-right microfracture in the upper half of the grain appears to extend into the grain above. There is some slight offset showing probable rotation. The absorption map is located over the upper section of the grain and covers a left-right microfracture, part of a bottom-left to top-right microfracture, and some of the grain boundary. The 3400 cm^{-1} peak correlates with the bottom-left to top-right microfracture in the center of the absorption map, however, there does not seem to be any correlation with the left-right microfracture (Figs. 29A & 30A). There is also evidence of molecular water along the grain boundary. The 3600 cm^{-1} peak is completely absent from the inside of the grain and resides solely on the grain boundary (Figs. 29B & 30B). The red hotspots on both absorption maps are in the same location and are correlated with a dark black area on the CL, which is most likely a mica grain.

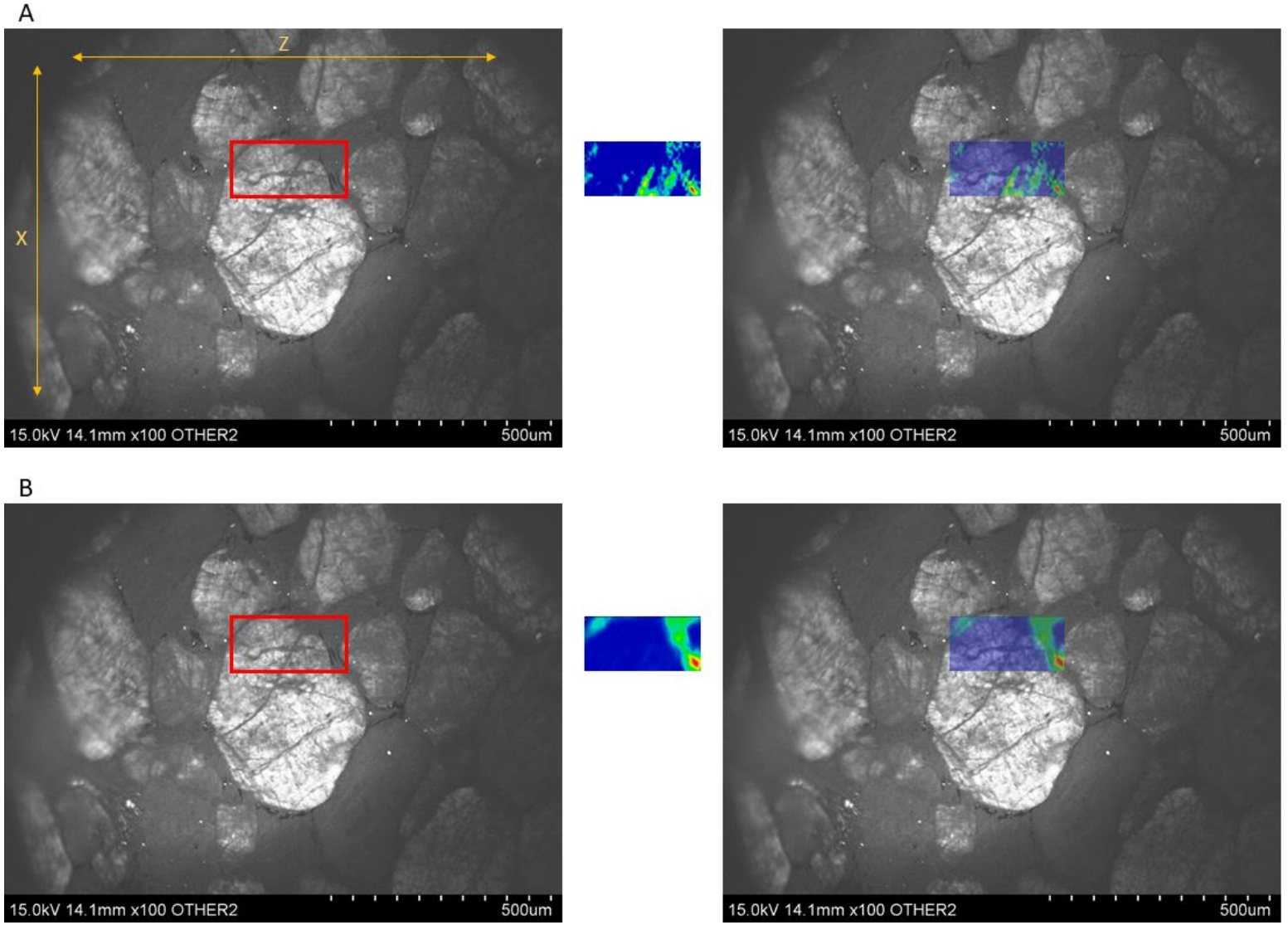

Figure 29: Combined FTIR-CL image for high-strain sample AI-08-06-Q13-6. XZ section with lineation along the vertical direction with down-plunge toward the bottom. (A) 3400 cm^{-1} peak. (B) 3600 cm^{-1} peak.

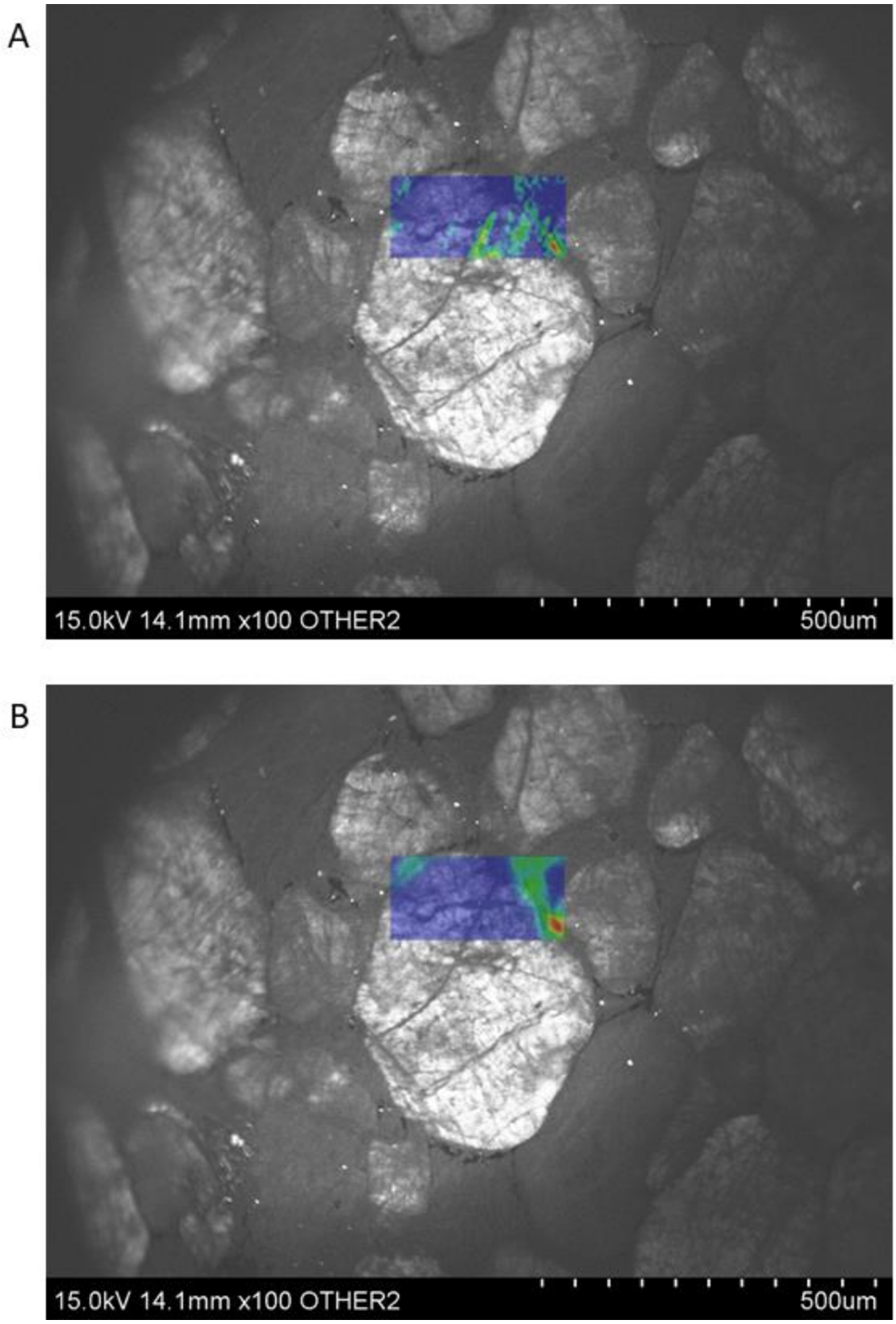

Figure 30: Larger FTIR-CL images for high-strain sample AI-08-06-Q13-6. (A) 3400 cm^{-1} peak. (B) 3600 cm^{-1} peak.

5.1.8 High-Strain: Outcrop AI-06 – Sample AI-08-06-Q13-8

Figure 31 shows three quartz grains ~350 to ~550 µm in size surrounded by other grains of similar size. The grains are heavily fractured. Most of the microfractures have a top-left to bottom-right orientation with some having a left to right orientation and one having a bottom-left to top-right orientation. The microfractures extend through multiple grains and are offset, showing rotation. Four absorption maps were collected at this location due to the high level of activity visible. Combined, they cover sections of all three grains and their grain boundaries. The 3400 cm^{-1} peak is correlated with the top-left to bottom-right microfractures in all three grains (Figs. 31A & 32A). The lower-left absorption map has additional molecular water in the center of the map where multiple microfractures intersect. The upper-right and lower-right absorption maps both show molecular water along the bottom-left to top-right microfracture as well. There is some evidence of the 3400 cm^{-1} peak along the grain boundaries but it is sparse. The 3600 cm^{-1} peak is almost completely absent from any of the grains and resides largely on the grain boundaries (Figs. 31B & 32B). There are many hotspots, most likely associated with micas.

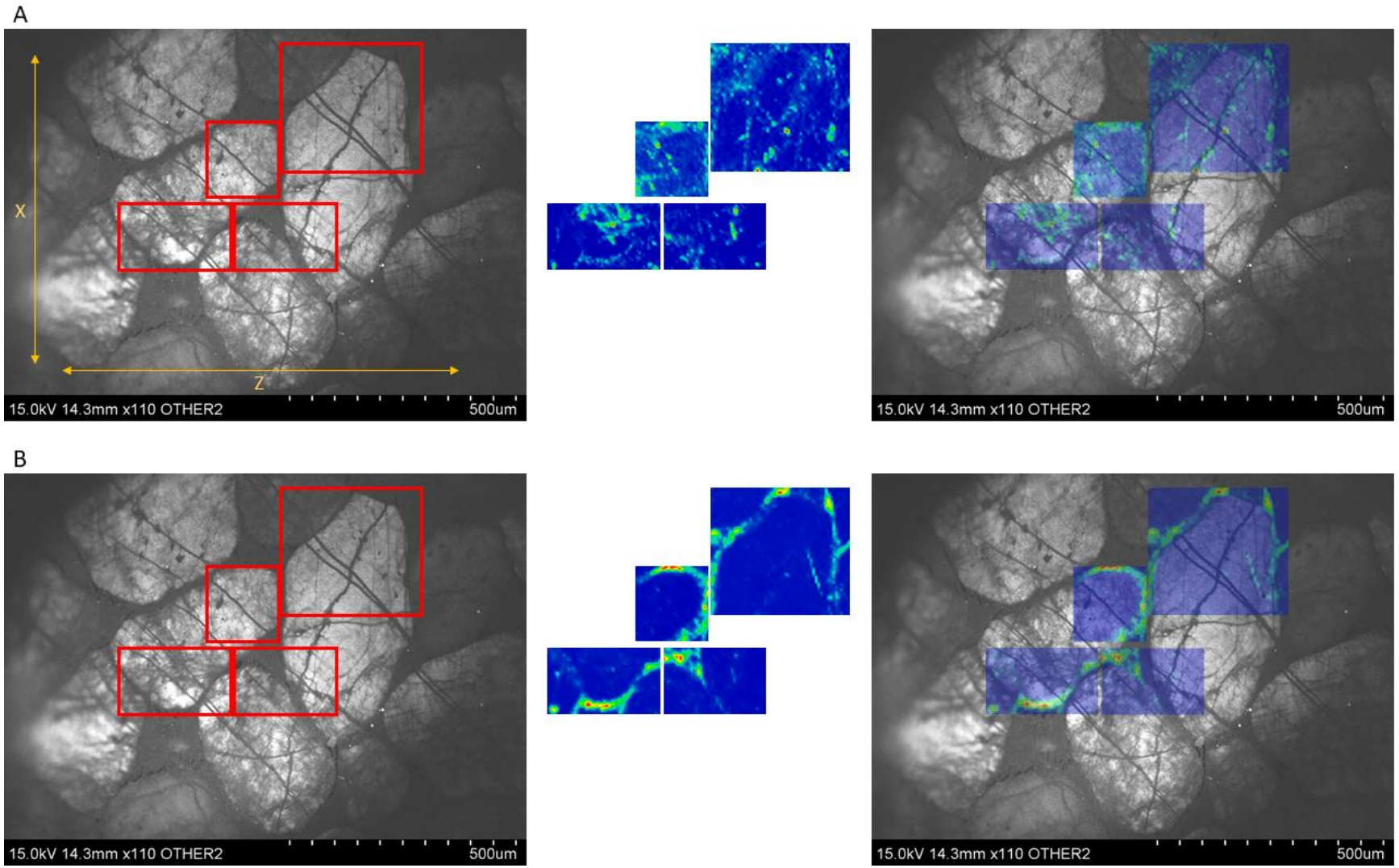

Figure 31: Combined FTIR-CL image for high-strain sample AI-08-06-Q13-8. XZ section with lineation along the vertical direction with down-plunge toward the bottom. (A) 3400 cm^{-1} peak. (B) 3600 cm^{-1} peak.

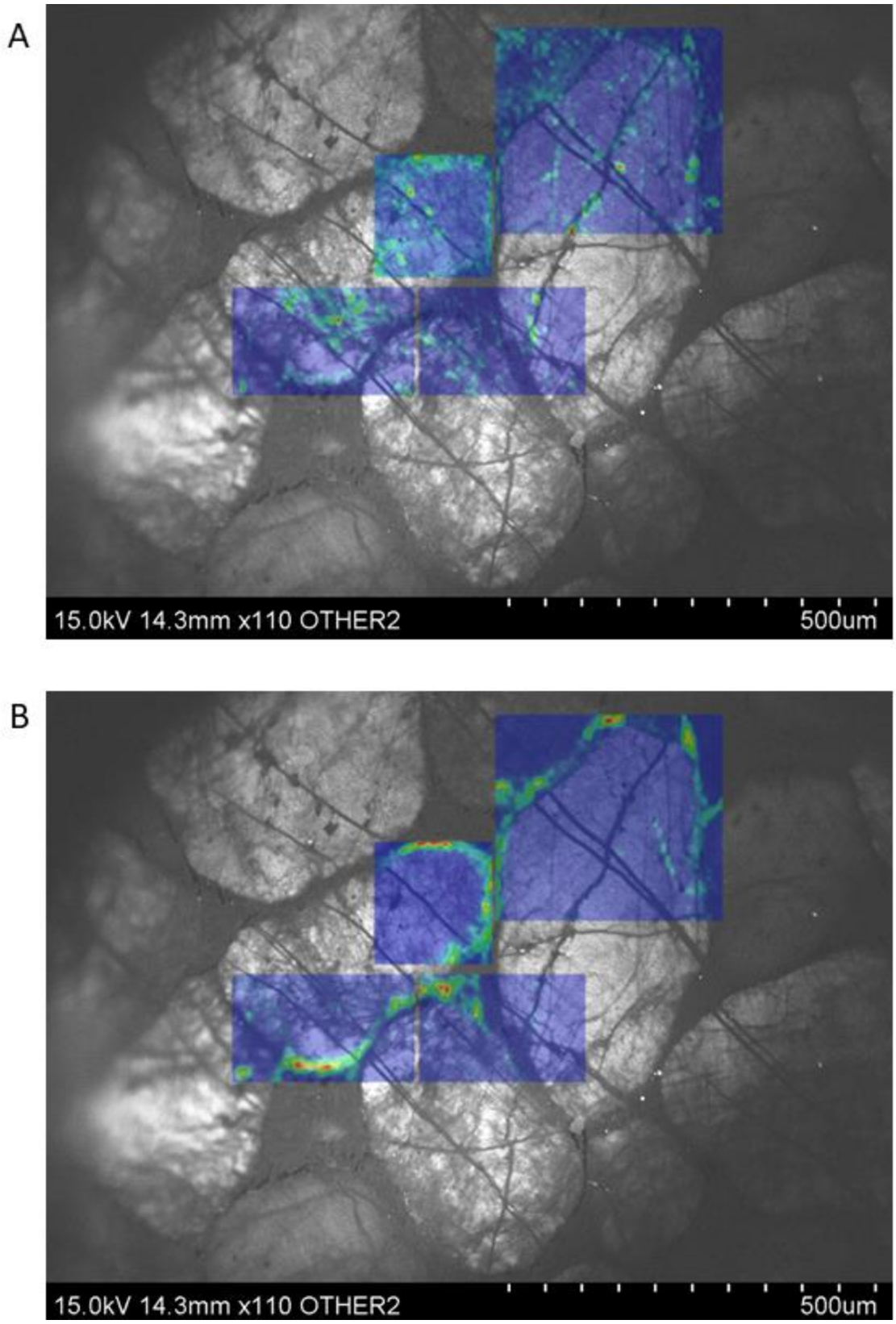

Figure 32: Larger FTIR-CL images for high-strain sample AI-08-06-Q13-8. (A) 3400 cm^{-1} peak. (B) 3600 cm^{-1} peak.

5.2 Microstructural Evolution

The results from both the petrographic and SEM-CL analyses show an overall transition from brittle deformation in the low-strain zone to crystal plastic deformation in the high-strain zone. In the low-strain zone, petrographic results show microfractures and veins. The SEM-CL results show thin healed microfractures. All of these features are associated with brittle deformation. In the medium-strain zone, petrographic results show microfractures, undulose extinction, subgrains, and bulged boundaries. The SEM-CL results show an increase in both the number and thickness of healed microfractures. This combination of features points to a transition where both brittle and crystal plastic deformation processes have taken place. In the high-strain zone, petrographic results show undulose extinction, subgrains, and bulged boundaries. The SEM-CL results show mostly mottled/recrystallized grains with healed microfractures only visible in rare grains. These features show increased crystal plastic deformation and the microstructural resetting of many grains.

5.3 Fluids in Quartz

Results from the petrographic microscope showed evidence of crystal plastic deformation and dislocation creep within quartz grains, however, the footwall of the Willard thrust fault did not reach the temperatures and differential stress conditions where this should theoretically occur. The footwall was buried 12-15 km deep which is equivalent to ~300-400 MPa of confining pressure. It reached temperatures of ~300-350 °C with differential stresses of ~30-40 MPa and strain rates of ~10^{-15} s^{-1} (Yonkee et al., 2013). Rutter (1976) developed a

deformation mechanism map for quartz that extrapolates experimental results to natural conditions and predicts dominant deformation mechanisms. Temperature and differential stress conditions estimated for the Willard footwall fall within the dominant dissolution creep field of the map. In this map, dislocation creep in quartz should dominate at natural strain rates starting at temperatures around 600° C, and differential stresses should not accumulate higher than about 10 MPa.

The results from the FTIR-CL analysis show that molecular water was able to infiltrate quartz grains through microfractures. This alone would not have been enough to increase crystal plasticity, however, if water infiltrates a normally anhydrous mineral such as quartz, and then invades the primary grain, it can lead to hydrolytic weakening. This allows the grains to deform plastically under much lower temperatures and pressures than would normally be required. There are two possible mechanisms for water to permeate the main part of the grain after its introduction through microcracking: motion along dislocations that intersect the fractures and diffusion (Kronenberg et al., 2017), one or both of which are likely to have happened in the footwall of the Willard thrust, possibly in tandem. Water can move along the dislocations and diffuse into the grain along them. This may be the primary method because diffusion along dislocations takes less activation energy and the diffusion coefficient is higher than for bulk diffusion (Bakker & Jansen, 1994).

5.4 Fluids in Deformation

The FTIR-CL results, in conjunction with the petrographic and SEM-CL results, allow for an interpretation of how water affected the type and extent of deformation within the shear zone along the Willard thrust fault. At low strain, deformation was almost exclusively brittle, causing microfractures to form in the quartz grains. The Willard thrust fault acted as a conduit for fluids, allowing water to move through the system. Water was able to infiltrate the quartz grains through microfractures and enter the crystal lattice by diffusion or motion along dislocation lines during healing or subsequent deformation. This introduction of water caused hydrolytic weakening which allowed the quartz grains to deform more easily leading to increased strain. At medium strain, an increase in fractures led to an increase in water infiltration into quartz grains which, in turn, led to increased hydrolytic weakening and plasticity within the grains. This allowed for even more strain to accumulate. At high strain, the quartz grains show evidence of being extensively hydrolytically weakened. This weakening led to increased crystal plasticity, extensive recrystallization recovery, and strain softening. In this way, increased water infiltration was not merely a result of increased strain but progressively drove the system from low-strain to high-strain.

Although the quartz grains in the high-strain zone were extensively recrystallized, the recrystallized grains appear to have fewer impurities than the original quartz. This was evidenced by the low/dull cathodoluminescence seen in the recrystallized grains. If this is the case, it means water was likely driven out of the grain during this process which should lead to strain hardening; this prediction is opposite the typical effect recrystallization has on strain accumulation, where one expects strain softening due to due to removal of dislocation tangles

(Hirth & Tullis, 1992). So in this case, the effect of recrystallization on the rheology is likely more complex.

5.5 Regional Implications

The finding that fluid infiltration along a fault can drive a system from brittle deformation toward ductile deformation, allows for a deeper understanding of fault zones and the relationship between the hanging wall and footwall. In most thrust fault systems, the hanging wall is more greatly deformed than the footwall, and the deformation in the footwall may be absent entirely (Boyer & Elliott, 1982). However, this is not always true, as is the case with the Willard thrust fault. In this system, the footwall is significantly more deformed than the hanging wall, despite the footwall reaching a lower peak temperature (~300 to 350 °C) than the hanging wall (~350 to 400 °C) (Yonkee et al., 2013). While Yonkee et al. (2013) proposed that one of the reasons for this phenomenon within the Willard thrust fault could have been a difference in fluid composition between the hanging wall and footwall, this is a site specific solution. Hydrolytic weakening associated with fluid infiltration provides an explanation for how the footwall in a thrust fault system may become more deformed than the hanging wall that can be applied to many systems throughout the world.

Fluid infiltration and hydrolytic weakening are of major importance to the understanding of the brittle-ductile transition zone. This study showed that there is a positive feedback between deformation and fluid interactions with both leading to increased strain. This represents a competent model for how the brittle-ductile transition can be raised, allowing for

the deformation of rocks under temperatures and pressures where it would normally not be possible.

5.6 Project Design: Order of Operations

The thin section maps created with the petrographic microscope were invaluable to this study, but the ordering of sample analysis was problematic and should be refined in future studies. The methodological plan for this study included a more in-depth petrographic analysis of samples following FTIR analysis. The original plan was to capture close-up images of the same grains analyzed with FTIR to identify microstructures within and around them. That would have enabled an examination of evidence of water in the grain as well as brittle or crystal plastic deformation evidence. It would have then been possible to add these images to the final FTIR-CL overlays. This would have added another layer of insight to the final analysis of each grain. However, this was not possible due to the order in which the different analyses took place.

The plan was to take close up images using the petrographic microscope after the samples were run on FTIR; however, the samples were unusable after the FTIR process due to issues surrounding removing the rock slivers from each slide. This process often severely damaged the samples. Rather than having a cohesive sample at the end of FTIR analysis, many had broken into several smaller pieces.

An effort was made to reattach the pieces to the slide after conducting FTIR analysis. The slide was reheated to melt the epoxy, and then the sample was reattached. If the sample

had broken apart, it was difficult to try and place the pieces back on the slide where they were originally located or even to know which side to place up if the pieces had flipped when they broke. Even if the sample remained largely intact, and was reattached to the slide in one piece, it was still not usable on the petrographic microscope due to issues with the epoxy. Because the rock slivers were only 30 microns thick, it was extremely difficult to put enough pressure on the sample to properly reattach it to the slide without the sample shattering. Due to the lack of adequate pressure while the epoxy was setting, the thickness of the epoxy beneath the sample was uneven and filled with air bubbles. These issues prevented the samples from being used again for petrographic analysis.

It is recommended that future studies with similar goals change the order of sample analysis if they wish to perform a microstructural analysis on the same grains that are to be used on the SEM-CL and FTIR. The petrographic analysis should be performed after the samples are run on SEM-CL and before they are run on FTIR. At this stage, the samples are still properly attached to the slide and usable on the petrographic microscope. It should be noted that two additional steps will be needed. First, the carbon coating from the SEM will need to be removed. This can be done by polishing it away using lapping film, or by washing it away with acetone. Second, close up images will need to be taken for every grain selected in the SEM-CL, since the specific grains to be run on the FTIR will not be known at this point (cannot predict which grains will be destroyed in the epoxy removal process). This means that the microstructural analysis will need to be performed on many more grains than what will end up being run on FTIR (82 vs 8 for this study). However, this will also provide for a more robust analysis in general.

Chapter 6: Conclusions

The purpose of this study was to investigate whether fluids were able to infiltrate quartz grains found in quartzites collected from the Mineral Fork diamictite along the Willard thrust fault, the pathways that fluids may have used to infiltrate grains, and how this may have influenced deformation style and intensity. A new sample preparation technique was created to allow for the analysis of individual quartz grains on multiple instruments. These instruments included a petrographic microscope to identify microstructures and interpret deformation mechanisms; SEM-CL to identify healed microfractures that could not be seen otherwise; and synchrotron-source FTIR to create absorption maps to show if and where water was located within each sample. The results from the SEM-CL and FTIR were then combined to create maps showing a relationship between water location and healed microfractures within the grains. The results of this study have led to the following conclusions.

6.1 Deformation and Fluid Infiltration

- Petrographic analysis showed a transition from brittle deformation in the low-strain zone to ductile deformation in the high-strain zone. The low-strain zone contained microfractures and veins showing mostly brittle deformation. The high-strain zone contained undulose extinction, subgrains, and bulged boundaries showing mostly ductile deformation. The medium-strain zone contained a combination of brittle and ductile deformation features showing that it was a transition zone between the two types.

- SEM-CL analysis also showed a transition from brittle to ductile deformation. Quartz grains in the low-strain zone showed some evidence of healed microfractures, however, the microfractures were thin and many of the grains had not yet begun to fracture. Grains in the medium-strain zone were extensively fractured. The fractures were thicker than those found in the low-strain zone and often extended through multiple grains. In the high-strain zone, quartz grains were extensively recrystallized. They showed a mottled appearance due to the resetting of their crystal structure.
- Combined FTIR and SEM-CL analyses showed that water was able to infiltrate quartz grains through healed microfractures. The 3400 cm^{-1} wavelength peak, which is associated with molecular water, was strongly correlated with the healed microfractures showing that liquid water had entered the grain using these pathways. The 3600 cm^{-1} peak, which is likely associated with OH locked in micas, was largely absent within the grains and was constrained to the grain boundaries where micas are likely to be located.
- Hydrous fluids were able to enter quartz grains through microfractures. Once water was introduced into the grains, it likely diffused into other internal parts of the grains, allowing hydrolytic weakening which led to strain softening. Multiple generations of fractures suggest that there were periodic fracturing events, which allowed water to enter the grains and acted as a catalyst to ductile deformation accommodated by crystal plasticity. With each period of fracturing, more water was able to enter the grains causing further hydrolytic weakening, softening and deformation in progressive change from entirely brittle toward predominantly ductile deformation.

- Fluids along faults may play a significant role in local depth of the brittle-ductile transition. Fluid infiltration can cause hydrolytic weakening which greatly reduces the temperatures needed for ductile deformation. This effectively raises the depth of the brittle-ductile transition, allowing ductile deformation to occur at shallower depths where it normally would not. Quartz grains in the footwall of the Willard thrust showed evidence of dislocation creep. The footwall was buried 12-15 km deep which is equivalent to ~300-400 MPa of confining pressure. It reached temperatures of ~300-350 °C with differential stresses of ~30-40 MPa and strain rates of ~10^{-15} s^{-1} (Yonkee et al., 2013). It takes much higher values of temperature for quartz to deform dominantly by dislocation creep (~600 °C), and differential stresses of these values should not accumulate if dislocation creep efficiently progresses (Rutter, 1976).
- The footwall of the Willard thrust shows evidence of significant ductile deformation. This is generally not predicted in thrust faults (Boyer & Elliott, 1982). Yonkee et al. (2013) showed that there was extensive fluid infiltration into the footwall. The infiltration of fluids into the footwall led to hydrolytic weakening of the quartz grains as well as other softening processes which allowed for the footwall to become more deformed than the hanging wall.

6.2 Methodology

- The Mineral Fork diamictite is an excellent unit for studying heterogeneous strain due to the competency of the clasts compared to the matrix in which they are suspended. In

addition, the relatively large spacing between clasts allows for reduced interactions between clasts.

- A new sample preparation technique was created to allow for the same sample to be run on multiple instruments. The use of Crystalbond^{TM} 509, which is a heat removable epoxy, allowed for the petrographic microscope and SEM-CL to be used on the sample while it was still attached to the slide and then for the sample to be removed from the slide to analyze it using FTIR.
- Quartzite samples are competent enough to withstand the sample preparation techniques used in this study. This may not be the case for softer rocks. Future studies may need to find alternate techniques for removing the sample from the slide for FTIR.
- The creation of thin section maps is a vital step for being able to run the same individual grain on multiple instruments. SEM-CL and FTIR instruments use high magnifications, which make it difficult to locate exact locations within a slide. Thin section maps enable one to stay oriented within the slide while tracking a grain of interest.
- Synchrotron-source FTIR proved to be an excellent instrument for mapping and spatially constraining the location of water, with micron scale precision, within individual grains. This technique has not been widely used in the geologic community, however, it holds great promise for future studies, particularly those working with deformed rocks.
- A reorganization of the timeline used in this study is required if close up petrographic images are to be captured of the same grains analyzed on the FTIR. Future studies should take the close up images after the SEM-CL analysis, when the sample is still

attached to the slide. The samples are unusable after the FTIR analysis due to the slide removal process.

This study was one of the first of its kind to analyze water content in naturally deformed quartz grains. Water content has been studied on experimentally deformed grains for years, however, very little work has been done on naturally deformed grains due to the difficulties involved. This study showed that, through innovative sample preparation techniques and analyses, it is possible to perform an analysis of water content on naturally occurring quartz grains.

Chapter 7: References

Armstrong, R.L., 1968, Sevier orogenic belt in Nevada and Utah. Geological Society of America Bulletin 19, 429-458.

Axen, G.J., Selverstone, J., Wawrzyniec, T., 2001. High-temperature embrittlement of extensional Alpine mylonite zones in the midcrustal ductile-brittle transition. Journal of Geophysical Research 106(B3), 4337-4348.

Bakker, R.J., Jansen, B.H., 1990. Preferential water leakage from fluid inclusions by means of mobile dislocations. Nature 345, 58-60.

Bakker, R.J., Jansen, B.H., 1994. A mechanism for preferential H2O leakage from fluid inclusions in quartz, based on TEM observations. Contributions to Mineralogy and Petrology 116, 7-20.

Baline, L.M., 2007. Hydrothermal fluids and Cu-Au mineralization of the deep Grasber porphyry deposit, Papua, Indonesia. Thesis. University of Texas at Austin.

Barszewski, C.E., 2012. Microstructural and cathodoluminescence (SEM-CL) analyses of clasts in a tectonically deformed diamictite. Thesis-University of Wisconsin-Milwaukee, 1-107.

Barnes, J.J., Selverstone, J., Sharp, Z.D., 2004. Interactions between serpentinite devolatilization, metasomatism, and strike-slip strain localization during deep-crustal shearing in the eastern Alps. Journal of Metamorphic Geology 22, 283-300.

Barnett, D., Bowman, J.R., and Smith, H.A., 1993. Petrologic and geochronologic studies in the Farmington Canyon Complex, Wasatch Mountains and Antelope Island, Utah. Utah Geological Survey Contract Report 93. 5-34.

Beach, A., Fyfe, W.S., 1972. Fluid transport and shear zones at Scourie, Sutherland: Evidence for overthrusting?. Contributions to Mineralogy and Petrology 36, 175-180.

Bense, V.F., Gleeson, T., Loveless, S.E., Bour, O., Scibek, J., 2013. Fault zone hydrogeology. Earth-Science Review 127, 171-192.

Bense, V.F., Person, M.A., 2006. Faults as conduit-barrier systems to fluid flow in siliciclastic sedimentary aquifers. Water Resources Research 42 (5). https://doi.org/10.1029/2005WR004480

Boggs, S.J., Kwon, Y., I., Goles, G.G., rusk, B.G., Krinsley, D., seyedolali, A., 2002. Is quartz cathodoluminescence color a reliable provenance tool? A quantitative examination. Journal of Sedimentary Research 72, 408-415.

Boyer, S.E., Elliott, D., 1982. Thrust systems. The American Association of Petroleum Geologists Bulletin 66, 1196-1230.

Brace, W.F., Kohlstedt, D.L., 1980. Limits on lithospheric stress imposed by laboratory experiments. Journal of Geophysical Research 85 (B11), 6248-6252.

Bryant, B. 1988. Geology of the Farmington Canyon Complex, Wasatch Mountains, Utah. U.S. Geological Survey Professional Paper 1476.

Byerlee, J.D., 1968. The brittle-ductile transition in rocks. Journal of Geophysical Research 73, 4741-4750.

Caine, J.S., Evans, J.P., Foster, C.B., 1996. Fault zone architecture and permeability structure. Geology 24, 1025-1028.

Carter, N.L., Kronenberg, A.K., Ross, J.V., Wiltschko, D.V., 1990. Control of fluids on deformation of rocks. Geological Society, London, Special Publications 54, 1-13.

Chen, Y., Zou, C., Mastalerz, M., Hu, S., Gasaway, C., 2015. Applications of micro-fourier transform infrared spectroscopy (FTIR) in the geological sciences – A review. International Journal of Molecular Sciences 16, 30223-30250.

Chernak, L.J., Hirth, G., Selverstone, J., Tullis, J., 2009. Effect of aqueous and carbonic fluids on the dislocation creep strength of quartz. Journal of Geophysical Research 114 (B4).

Cordier, P., Doukhan, J.C., 1989. Water solubility in quartz and its influence on ductility. European Journal of Mineralogy 1, 221-237.

Crittenden Jr., M.D., 1972. Willard thrust and Cache Allochthon, Utah. Geological Society of America Bulletin 83, 2871-2880.

Crittenden Jr., M.D., Christie-Blick, N., Link, P.K., 1983. Evidence for two pulses of glaciation during the late Proterozoic in northern Utah and southeastern Idaho. Geological Society of America Bulletin 94, 437-450.

Crookes, W., 1879. Contributions to molecular physics in high vacua. Philosophical Transactions of the Royal Society of London, 641-662.

Czeck, D.M., Fissler, D.A., Horsman, E., Tikoff, B., 2003. Strain analysis and rheology contrasts in polymictic conglomerates: an example from the Seine meta-conglomerates, Superior Province, Canada. Journal of Structural Geology 31, 1365-1376.

DeCelles, G., Pile, H.T., Coogan, J.C., 1993. Kinematic history of the Meade thrust based on provenance of the Bechler conglomerate at Red Mountain, Idaho, Sevier thrust belt. Tectonics 12, 1436-1450.

Dieterich, J.H., Conrad, G., 1984. Effect of humidity on time- and velocity-dependent friction in rocks. Journal of Geophysical Research 89, 4196-4202.

Dunning, J.D., Petrovski, D., Schmyler, J., Owens, A., 1984. The effects of aqueous chemical environments on crack propagation in quartz. Journal of Geophysical Research 89, 4115-4123.

Etheridge, M.A., Wall, V.J., Cox, S.F., Vernon, R.H., 1984. High fluid pressures during regional metamorphism and deformation: Implications for mass transport and deformation mechanisms. Journal of Geophysical Research 89, 4344-4358.

Evans, J.P., Neves, D.S., 1992. Footwall deformation along the Willard thrust sevier orogenic belt: implications for mechanisms, timing, and kinematics. Geological Society of America Bulletin 104, 516-527.

Finch, M.A., Weinberg, R.F., Hunter, N.J.R., 2016. Water loss and the origin of thick ultramylonites. Geology 44, 599-602.

Fischer, G.J., Paterson, M.S., 1989. Dilatancy during rock deformation at high temperatures and pressures. Journal of geophysical Research 89, 4344-4358.

Frelinger, S.N., Ledvina, M.D, Kyle, J.R., Zhao, D., 2015. Scanning electron microscopy cathodoluminescence of quartz: Principles, techniques and applications in ore geology. Ore Geology reviews 65, 840-852.

Frost, C.D., Frost, B.R., Kirkwood, R., Chamberlain, K.R., 2006. The tonalite-trondhjemite-granodiorite (TTG) to granodiorite-granite (GG) transition in the late Archean plutonic rocks of the central Wyoming Province. Canadian Journal of Earth Sciences 43, 1419-1444.

Fyfe, W.S., Price, N.J., Thompson, A.B., 1978. Fluids in the Earth's crust. Amsterdam: Elsevier.

Gleason, G.C., DeSisto, S., 2008. A natural example of crystal-plastic deformation enhancing the incorporation of water into quartz. Tectonophysics 446, 16–30.

Griggs, D., 1967. Hydrolytic weakening of quartz and other silicates. Royal Astronomical Society Geophysical Journal 14, 19–31.

Griggs, D.T., 1974. A model of hydrolytic weakening in quartz. Journal of Geophysical Research 79, 1653-1661.

Heard, H.C., Carter, N.L., 1968. Experimentally induced “natural” intragranular flow in quartz and quartzite. American Journal of Science 266, 1-42.

Hetherington, G., Jack, K.H., 1962. Water in vitreous silica. Part I. influence of water content on the properties of vitreous silica. Physics and Chemistry of Glasses 3, 129-133.

Kekulawala, K.R.S.S., Paterson, M.S. Boland, J.N., 1978. Hydrolytic weakening in quartz. Tectonophysics 46, T1-T6.

Kerrich, R., 1986. Fluid transport in lineaments. Royal Society of London Philosophical Transactions 317, 219-251.

Kronenberg, A.K., Hasnan, H.F.B., Holyoke, C.W. III, Law, R.D., Liu, Z., Thomas, J.B., 2017. Synchrotron FTIR imaging of OH in quartz mylonites. Solid Earth 8, 1025-1045.

Kronenberg, A.K., Kirby S.H., Aines R.D., and Rossman G.R., 1986. Solubility and diffusional uptake of hydrogen in quartz at high water pressures: implications for hydrolytic weakening. Journal of Geophysical Research 91, 12723-12741.

Kronenberg, A.K., Segall, P., Wolf, G.H., 1990. Hydrolytic weakening and penetrative deformation within a natural shear zone, in: Duba, A.G., Durham, W.B., Handin, J.W., Wang, H.F. (Eds.), The Brittle-Ductile Transition in Rocks. American Geophysical Union, pp. 21-36.

Kronenberg, A.K., Wolf, G.H., 1990. FTIR determinations of intragranular water content in quartz-bearing rocks: implications for hydrolytic weakening in the laboratory and within the Earth. Tectonophysics 172, 255-271.

Lobato, L.M., Forman, J.M.A., Fazikawa, K., Fyfe, W.S., Kerrich, R., 1983. Uranium in over-thrust Archean basement, Bahia, Brazil. Canadian Mineralogist 21, 647-654.

Livaccari, R.F., 1991. Role of crustal thickening and extensional collapse in the tectonic evolution of the Sevier-Laramide orogeny, western United States. Geology 19 (11): 1104–1107.

Marshall, D.J., 1988. Cathodoluminescence of geological materials. Boston: Unwin Hyman.

McCaig, A.M., 1987. Deformation and fluid-rock interaction in metasomatic dilatant shear bands. Tectonophysics 135, 121-132.

McCaig, A.M., 1988. Deep fluid circulation in fault zones: Geology, v. 16, p. 867-870.

Nichols, A.R.L., Wysoczanski, R.J., 2007. Using micro-FTIR spectroscopy to mesure volatile contents in small and unexposed inclusions hosted in olivine crystals. Chemical Geology 242, 371-384.

Paterson, M.S., 1982. The determination of hydroxyl by infrared absorption in quartz, silicate glasses and similar materials. Bulletin de Mineralogie 105, 20-29.

Paterson, M.S., 2001. Relating experimental and geological rheology. International Journal of Earth Sciences 90, 157-167.

Reynolds, S.J., Lister, G.S., 1987. Structural aspects of fluid-rock interactions in detachment zones. Geology 15, 362-366.

Rusk, B.G., 2012. Cathodoluminescence and trace elements in hydrothermal quartz. *In*, Götze, J., Möckel, R., editors, Quartz: Deposits, mineralogy and analytics. Springer, Berlin, 307-329.

Rutter, E.H., 1976. The kinetics of rock deformation by pressure solution. Philosophical Transactions of the Royal Society of London Series A 283, 203–219.

Rutter, E.H., 1986. On the nomenclature of mode of failure transitions in rocks. Tectonophysics 122, 381-387.

Seamans, S.J., Williams, M.L., Jercinovic, M.J., Koteas, G.C., Brown, L.B., 2013. Water in nominally anhydrous minerals: implications for partial melting and strain localization in the lower crust. Geology, 41, 1051-1054.

Segall, P., Simpson, C., 1986. Nucleation of ductile shear zones on dilatant fractures. Geology 14, 56-59.

Sibson, R.H., 1981. Controls on low-stress hydro-fracture dilatancy in thrust, wrench and normal fault terrains. Nature 289, 655-667.

Sibson, R.H., 1983. Continental fault structure and the shallow earthquake source. Geological Society of London Journal 140, 747-767.

Sibson, R.H., 1984. Roughness at the base of seismogenic zone: Contributory factors. Journal of Geophysical Research 89, 5791-5799.

Smith, D.L., Evans, B., 1984. Diffusional crack healing in quartz. Journal of Geophysical Research 89, 4125-4135.

Tikoff, B., Chatzaras, V., Newman, J., Roberts, N.M., 2019. Big data in microstructure analysis: Building a universal orientation system for thin sections. Journal of Structural Geology 125, 226-234.

Treagus, S.H. and Treagus, J.E., 2002. Studies of strain and rheology of conglomerates. Journal of Structural Geology 24 (10), 1541-1567.

Tullis, J., Yund, R.A., 1989. Hydrolytic weakening of quartz aggregates: The effects of water and pressure on recovery. Geophysical Research Letters 16, 1343-1346.

Tullis, J., Yund, R., Farver, J., 1996. Deformation-enhanced fluid distribution in feldspar aggregates and implications for ductile shear zones. Geology 24, 63-66.

Watson, E.B., Brenan, J., 1987. Fluids in the lithosphere, 1. Experimentally determined wetting characteristics of CO_2-H_2O fluids and their implications for fluid transport, host-rock physical characteristics, and fluid inclusion formation. Earth and Planetary Science Letters 85, 497-515.

Wawrzyniec, T., Selverstone, J., Axen, G.J., 1999. Correlations between fluid composition and deepseated structural style in the footwall of the Simplon low-angle normal fault, Switzerland. Geology 27, 715-718.

Weil, A.B., Yonkee, A., 2010. The power of integration: combining paleomagneticdata with structural analysis to better understand thekinematics and mechanics of complex orogens. Trabajos De Geología 30, 322-330.

Willis, G.C., 1999. The Utah Thrust System – An Overview. Utah Geological Association Publication 27, p. 1-10.

Willis, G.C., Yonkee, W.A., Doelling, H.H., Jensen, M.E., 2000. Geology of Antelope Island State Park, Utah. *In*, Sprinkel, D.A., Chidsey, T.C. Jr., Anderson, P.B., editors, Geology of Utah's Parks and Monuments. Utah Geological Association Publication 28, 337-364.

Yonkee, W.A., 1992. Basement-cover relations. Sevier orogenic belt, norther Utah. Geological Society of America Bulletin 104 (3), 280-302.

Yonkee, W.A., 1997. Kinematics and mechanics of the Willard thrust sheet, central part of the Sevier orogenic wedge, north-central Utah. *In*, Link, P.K., Kowallis, B.J., editors, Proterozoic to Recent stratigraphy, tectonics, and volcanology, Utah, Nevada, southern Idaho and central Mexico. Brigham Young University Geology Studies 45, pt. 1, 341-354.

Yonkee, W.A., 2005. Strain patterns within part of the Willard thrust sheet, Idaho-Utah-Wyoming thrust belt. Journal of Structural Geology 27, 1315-1343.

Yonkee, W.A., Czeck, D.M., Nachbor, A.C., Barszewski, C., Pantone, S., Balgord, E.A., Johnson, K.R., 2013. Strain accumulation and fluid-rock interaction in a naturally deformed diamictite, Willard thrust system, Utah (USA): Implications for crustal rheology and strain softening. Journal of Structural Geology 50, 91-118.

Yonkee, W.A., Eleogram, B., Wells, M.L., Stockli, D.F., Kelley, S., Barber, D.E., 2019. Fault slip and exhumation history of the Willard thrust sheet, Sevier fold-thrust belt, Utah: Relations to wedge propagation, hinterland uplift and foreland basin sedimentation. Tectonics 38 (8), 2850-2893.

Yonkee, W.A., Parry, W.T., Bruhn, R.L., 2003. Relations between progressive deformation and fluid-rock interaction during shear-zone growth in a basement-cored thrust sheet, Sevier Orogenic Belt, Utah. American Journal of Science 303, 1-59.

Yonkee, W.A., Weil, A.B., 2015. Tectonic evolution of the Sevier and Laramide belts within the North American Cordillera orogenic system. Earth-Science Reviews 150, 531-593.

Yonkee, W.A., Willis, G.C., Doelling, H.H., 2000. Proterozoic and Cambrian sedimentary and low-grade metasedimentary rocks on Antelope Island, Utah. *In*, King, J.K., Willis, G.C., editors, The geology of Antelope Island, Davis County, Utah: Utah Geological Survey Miscellaneous Publication 00-1, 37-47.

Appendix A: Additional SEM-CL images

Low-strain sample AI-08-09-Q13

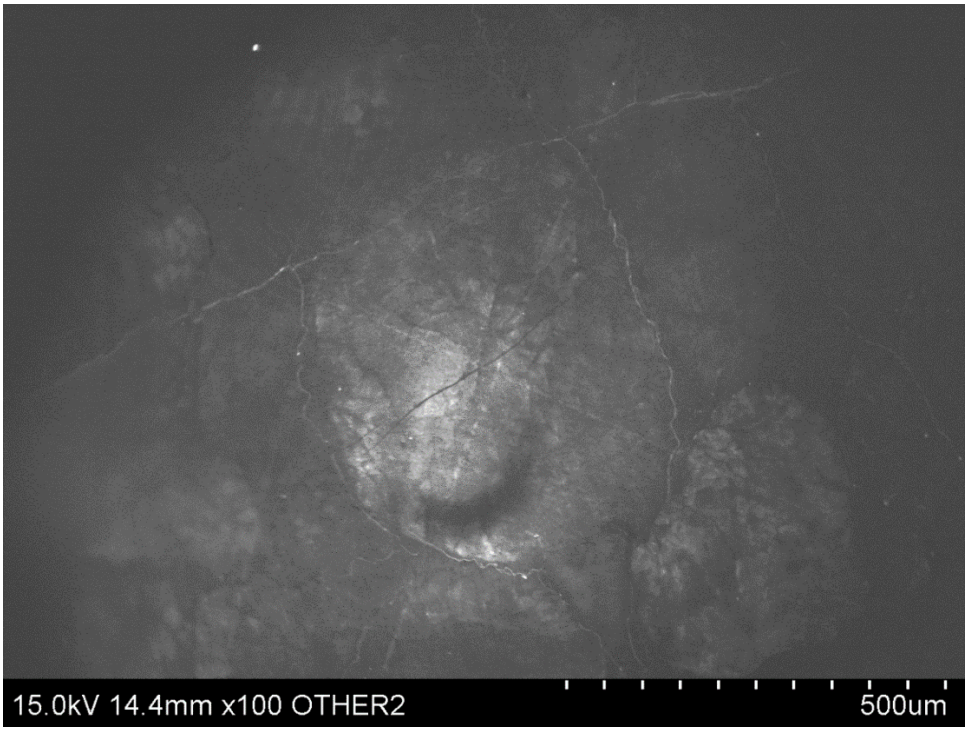

Low-strain sample AI-08-09-Q13-1

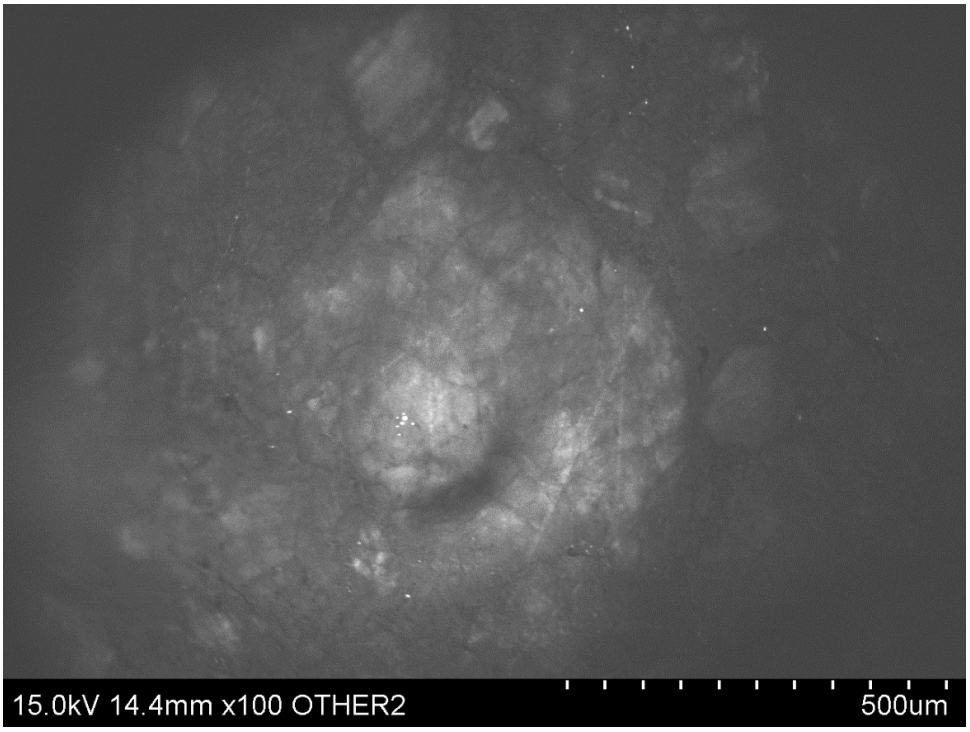

Low-strain sample AI-08-09-Q13-2

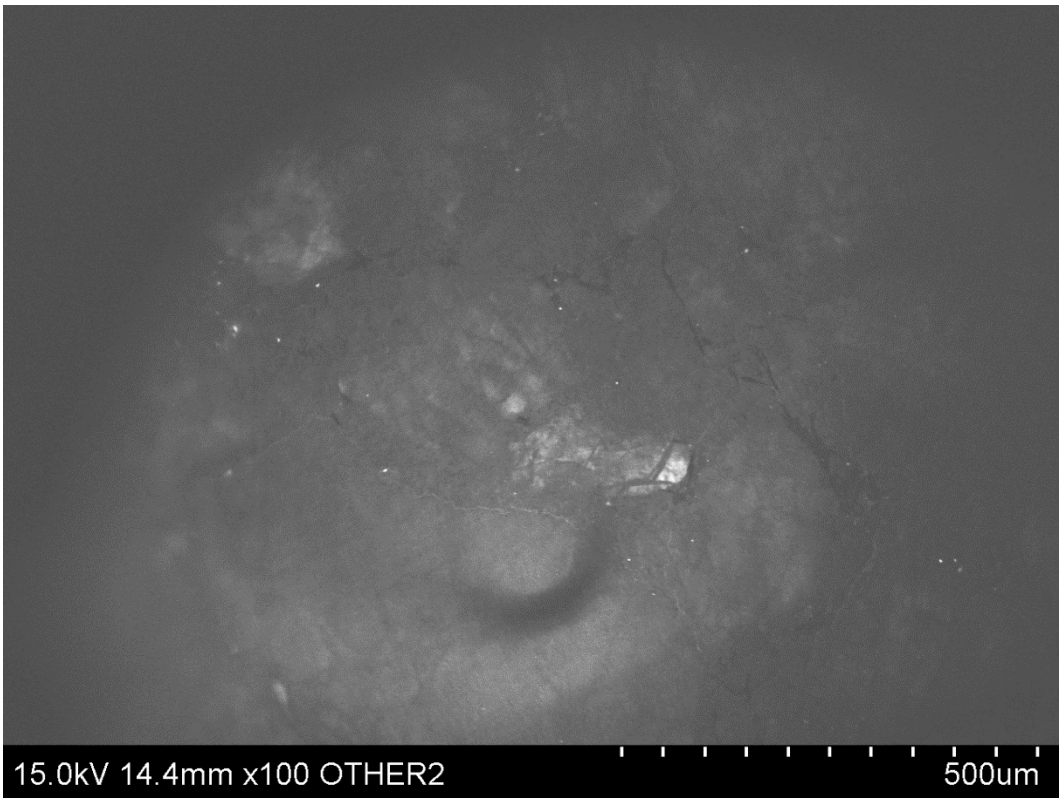

Low-strain sample AI-08-09-Q13-3

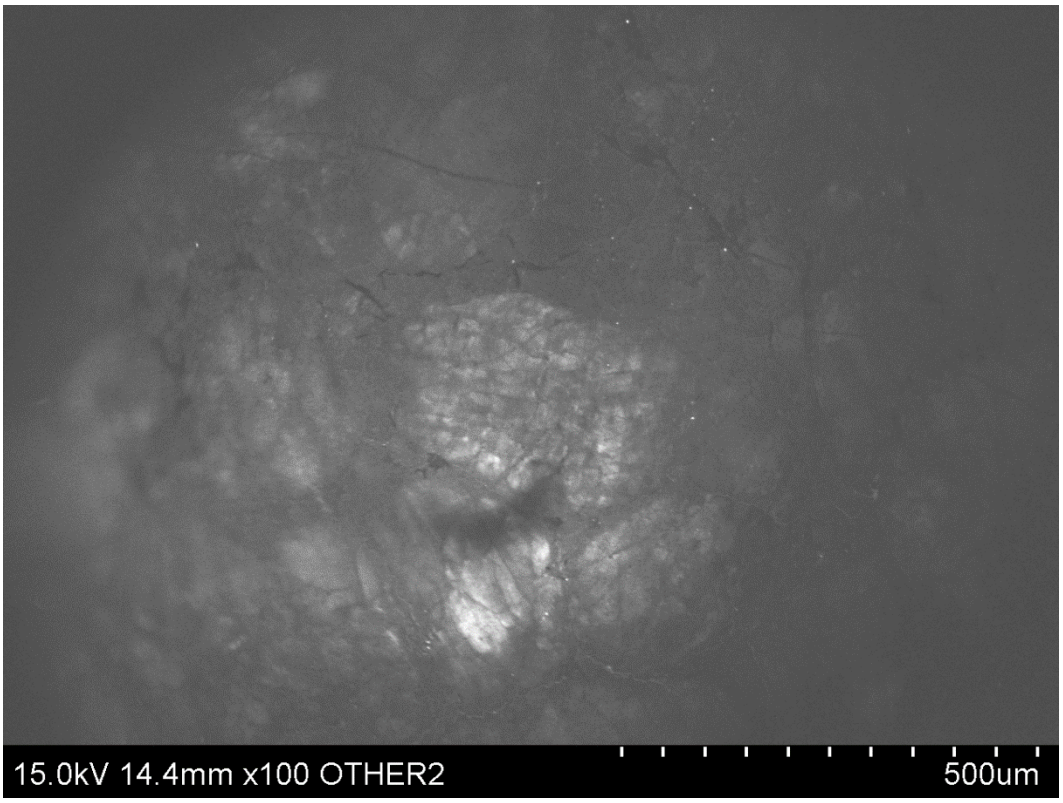

Low-strain sample AI-08-09-Q13-4

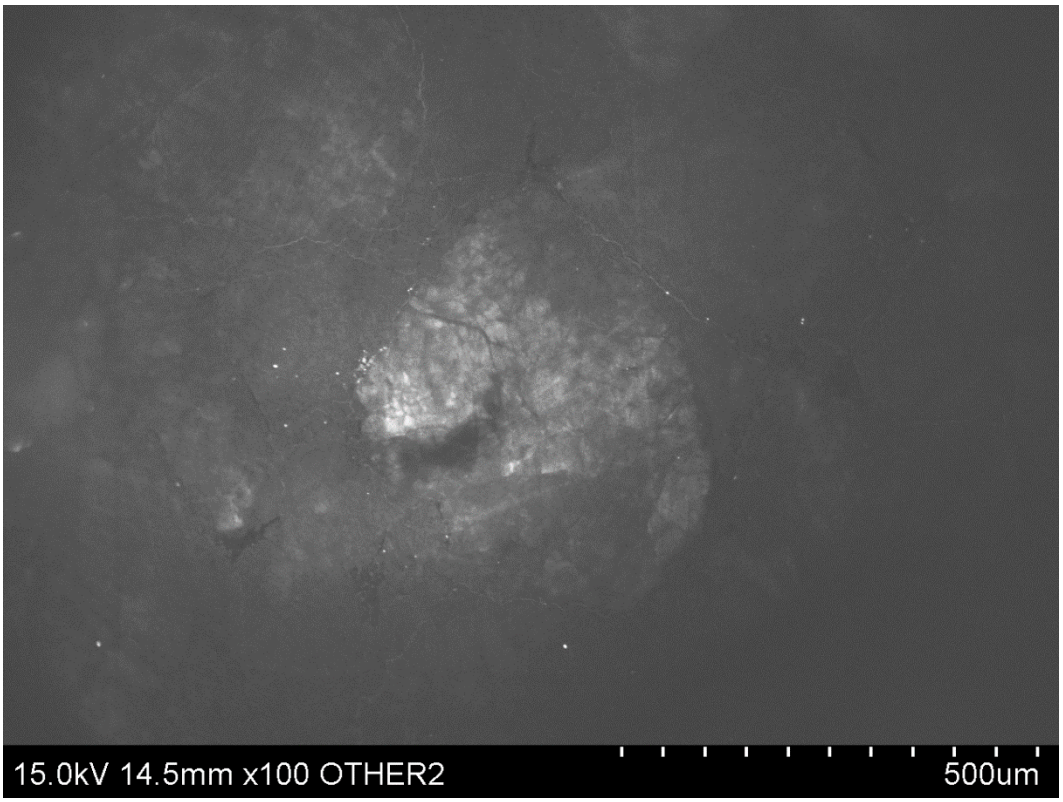

Low-strain sample AI-08-09-Q13-5

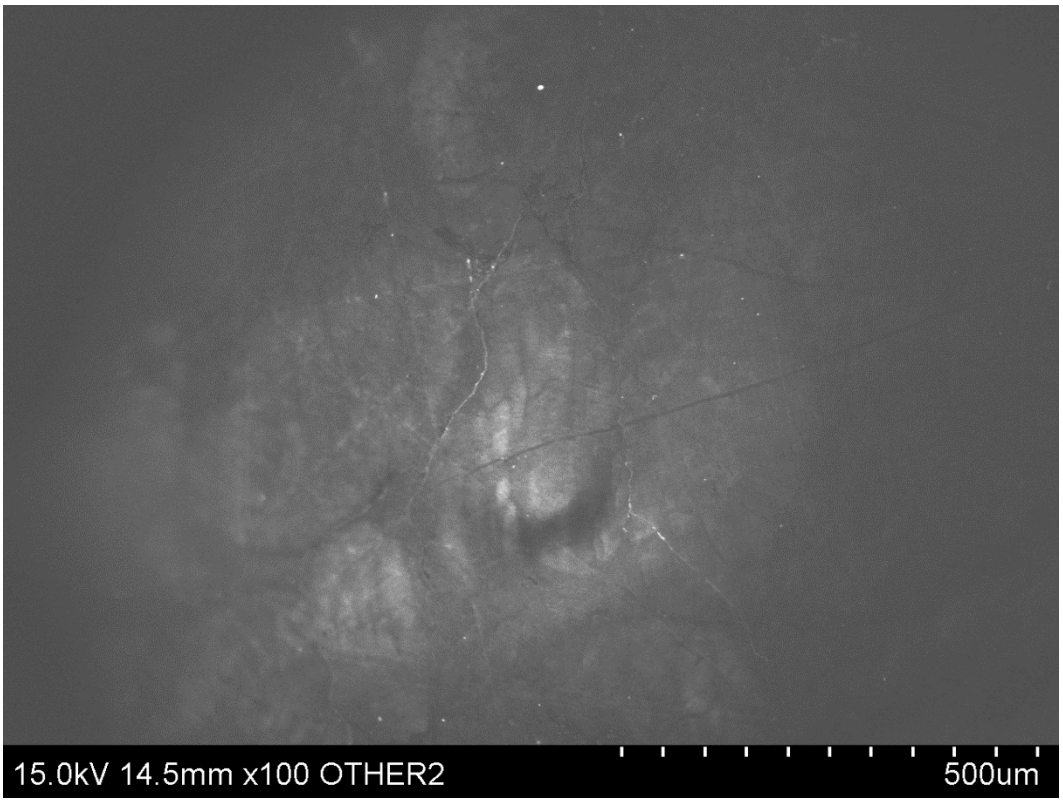

Low-strain sample AI-08-09-Q13-6

Low-strain sample AI-08-09-Q14

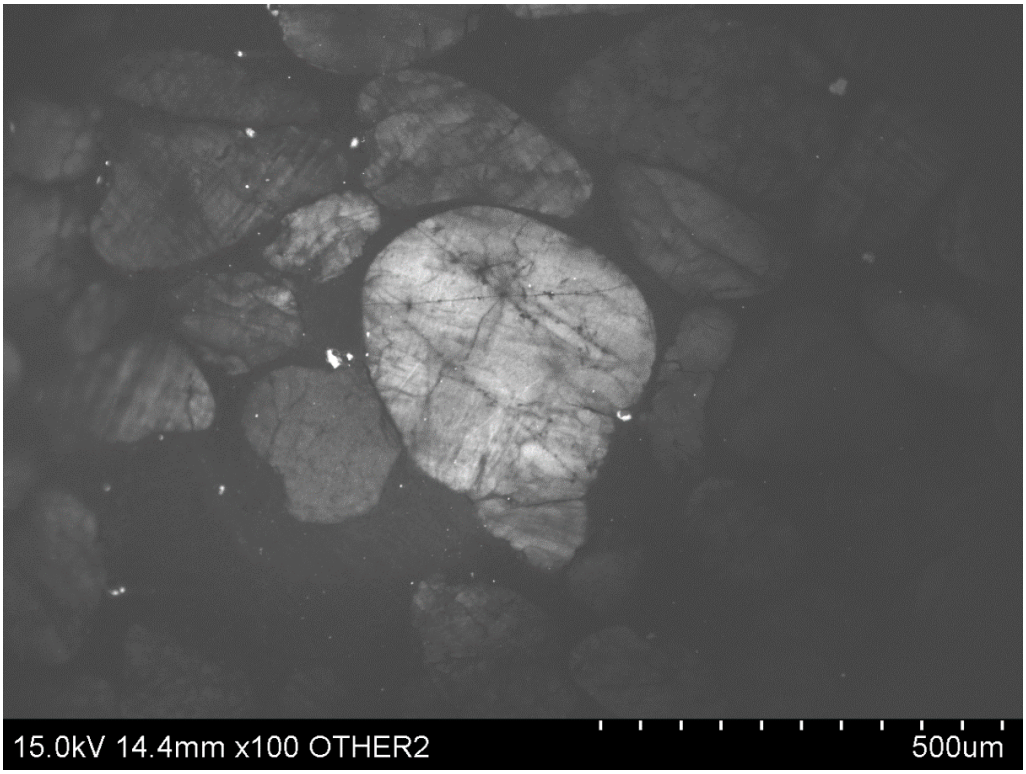

Low-strain sample AI-08-09-Q14-1

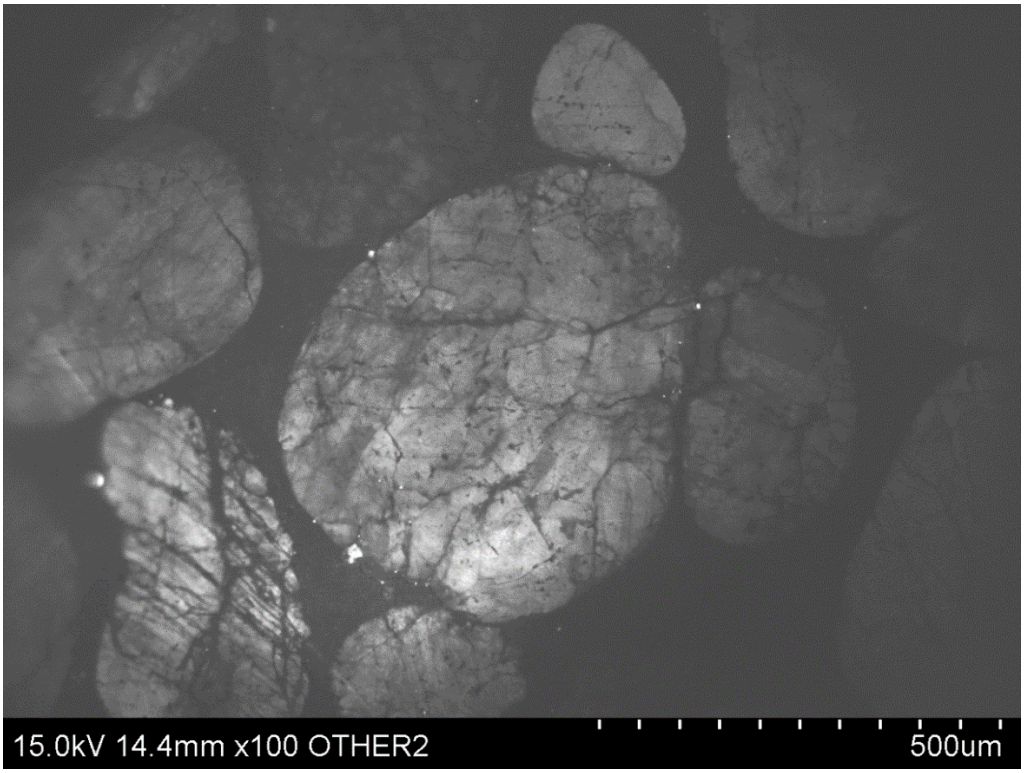

Low-strain sample AI-08-09-Q14-2

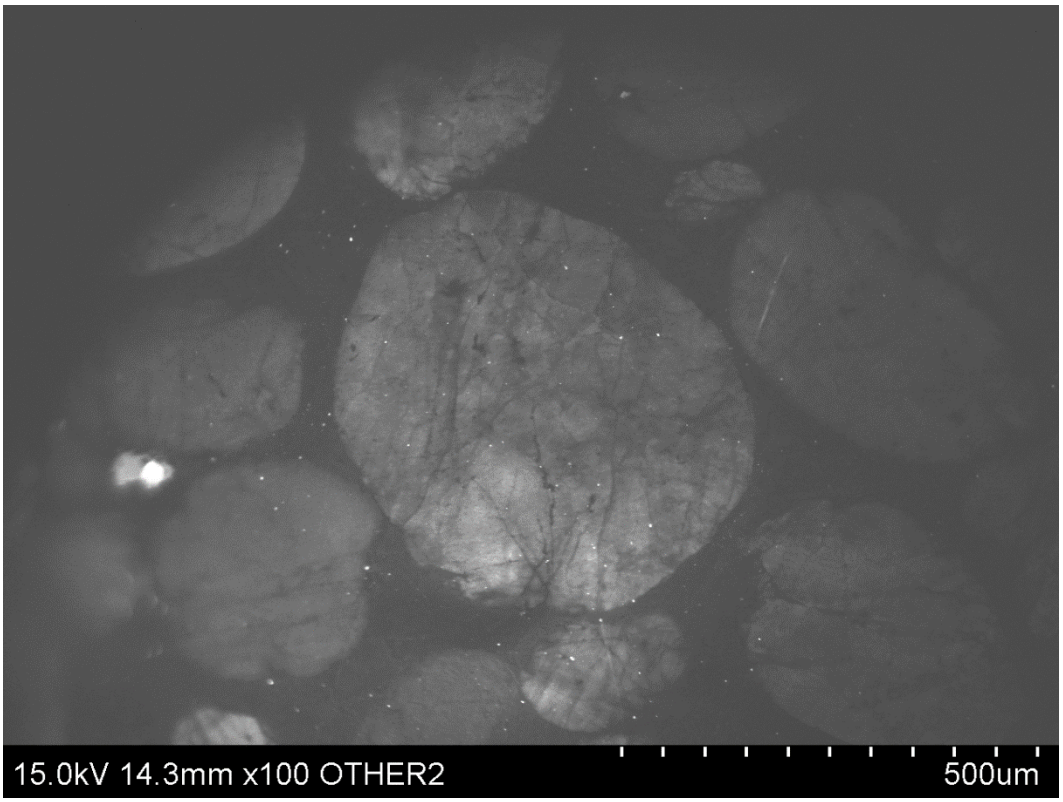

Low-strain sample AI-08-09-Q14-3

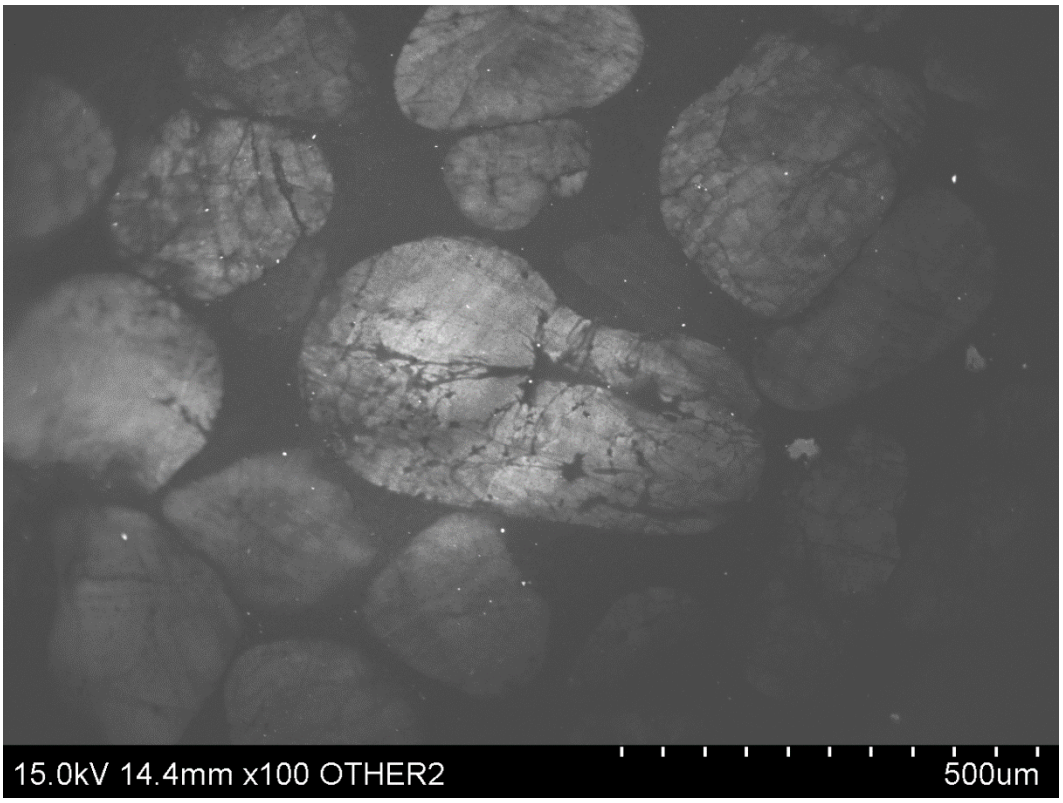

Low-strain sample AI-08-09-Q14-4

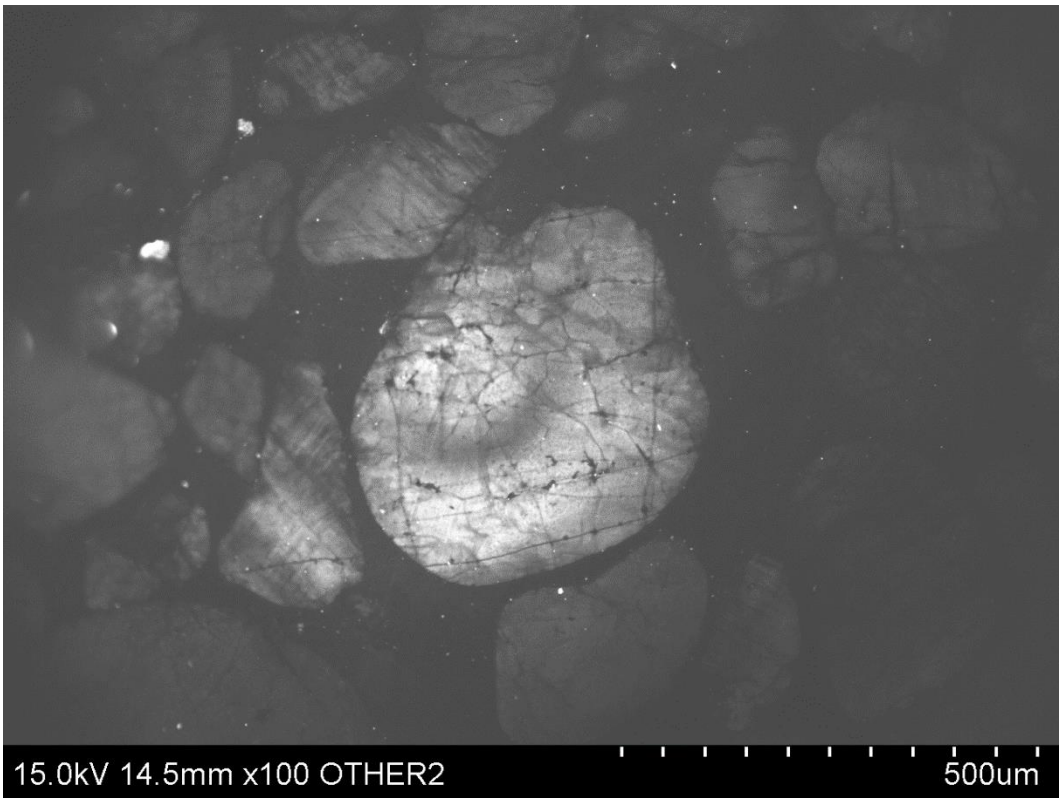

Low-strain sample AI-08-09-Q14-5

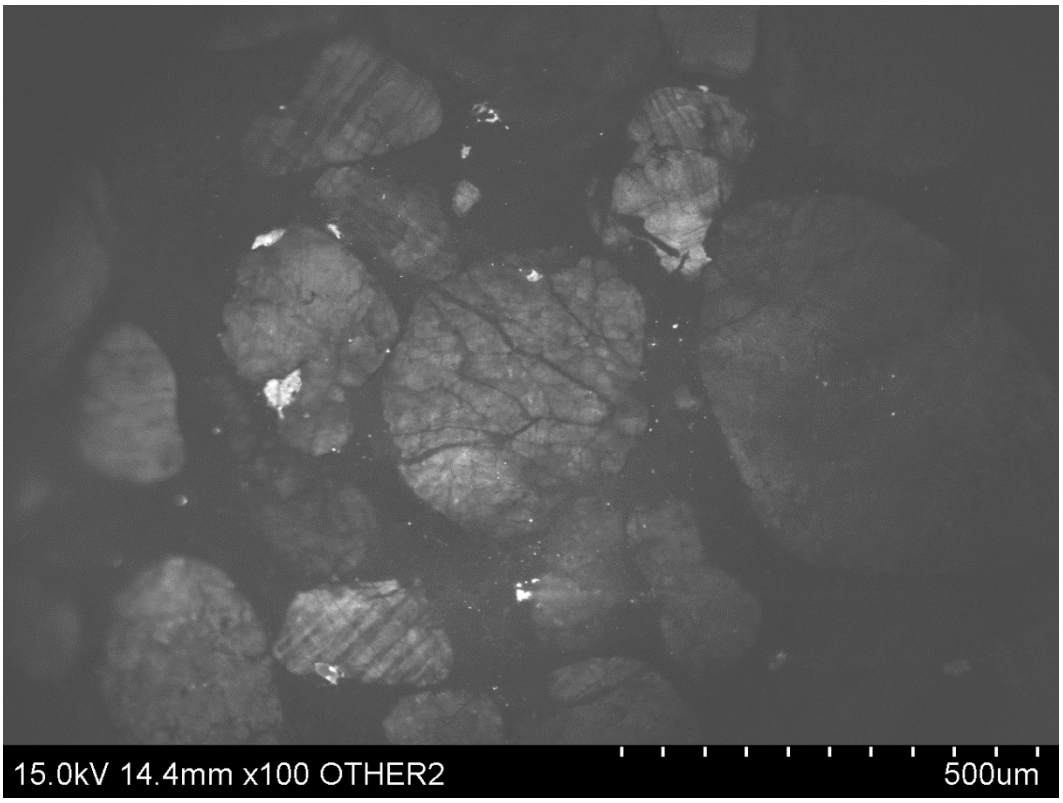

Low-strain sample AI-08-09-Q14-6

Medium-strain sample AI-08-03-Q12

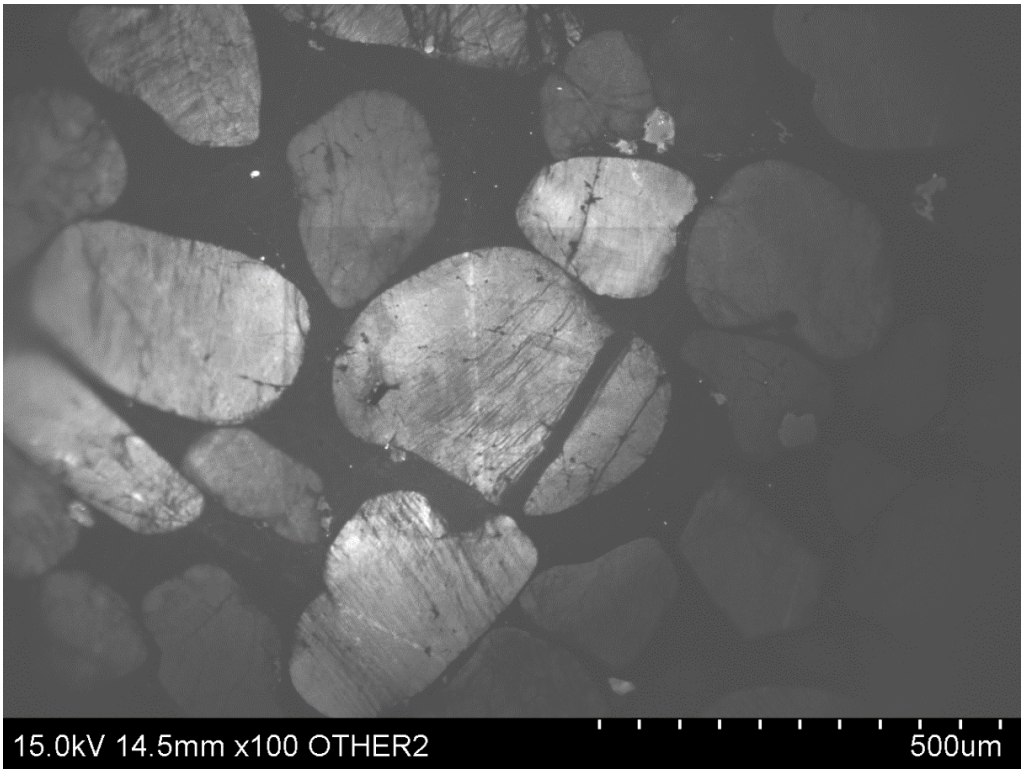

Medium-strain sample AI-08-03-Q12-1

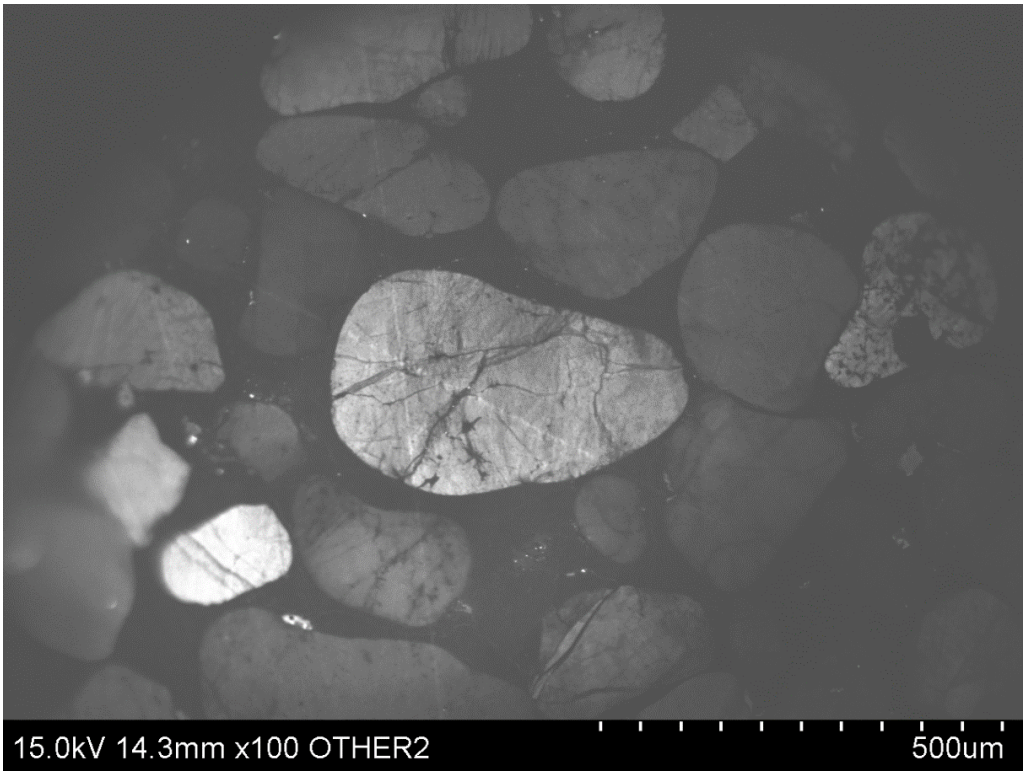

Medium-strain sample AI-08-03-Q12-2

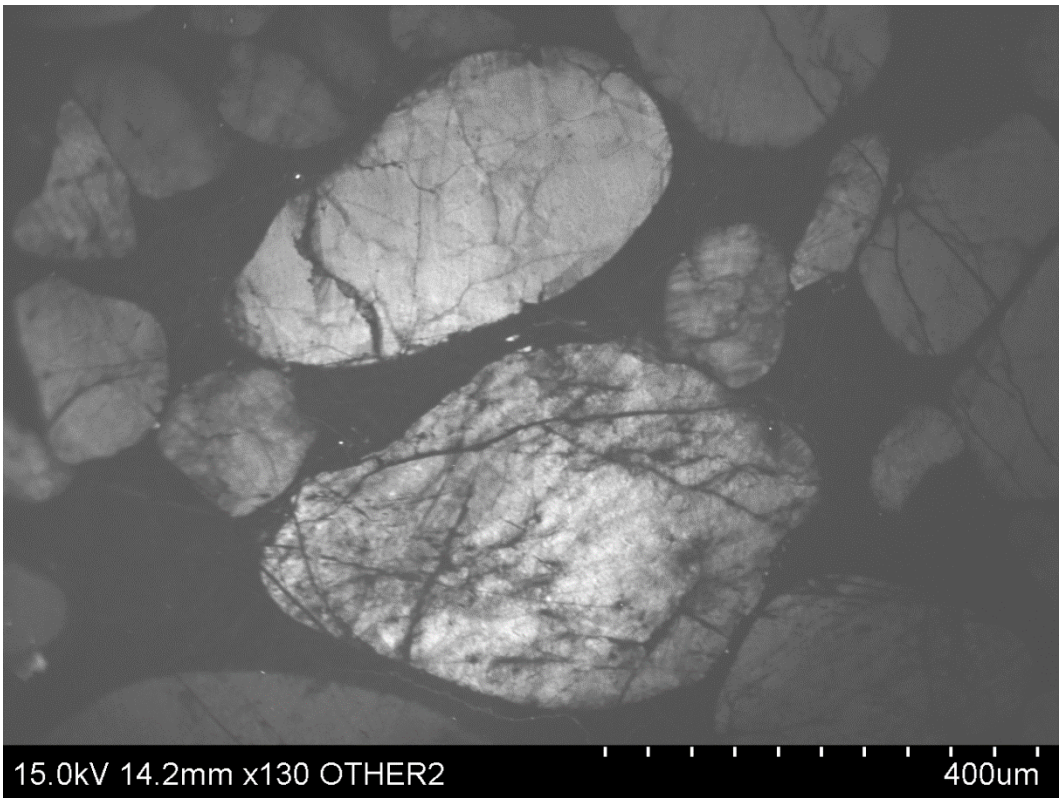

Medium-strain sample AI-08-03-Q12-3

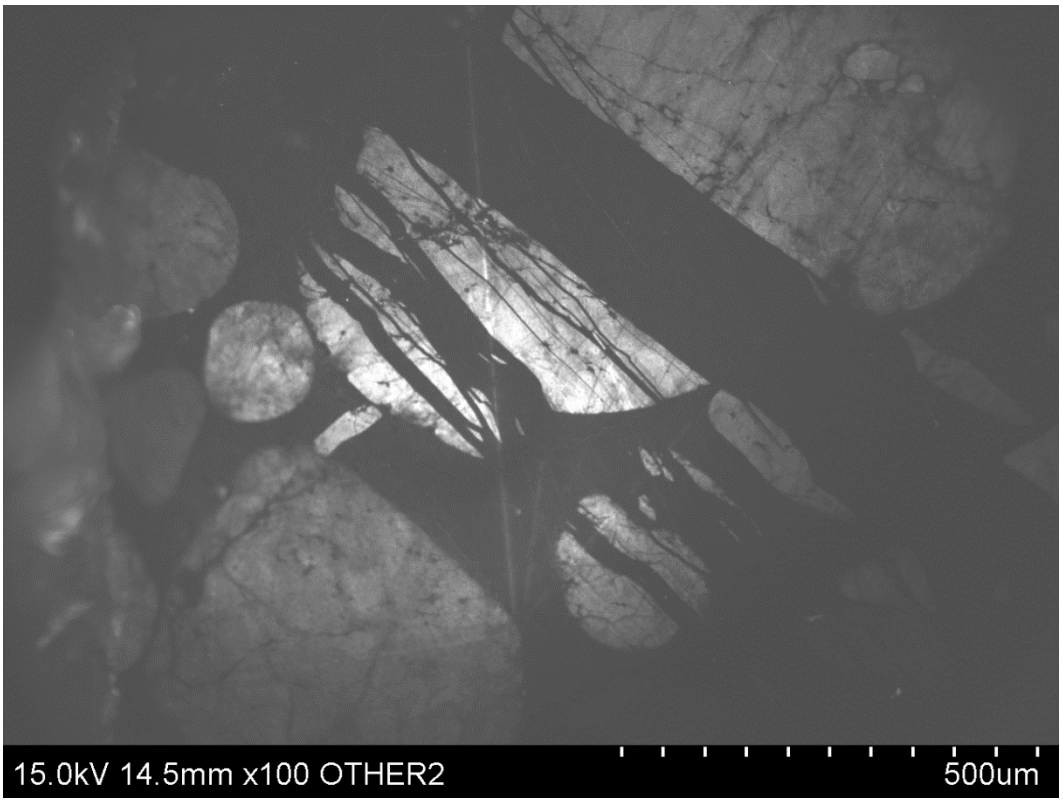

Medium-strain sample AI-08-03-Q12-4

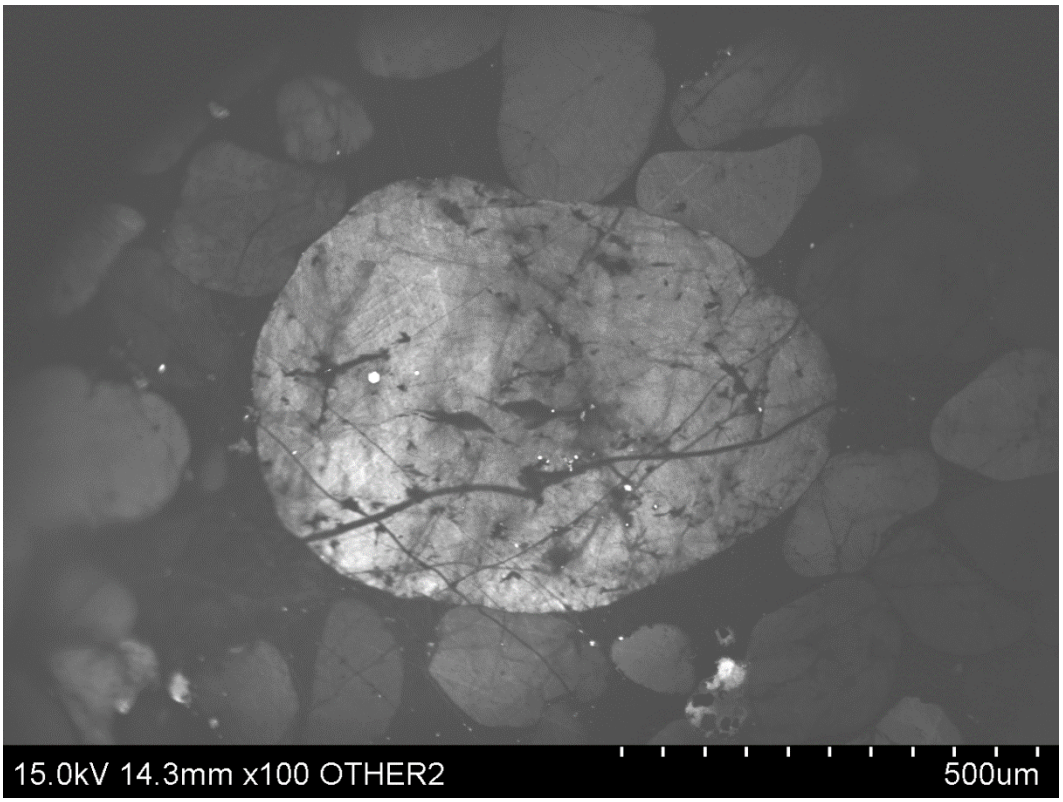

Medium-strain sample AI-08-03-Q12-5

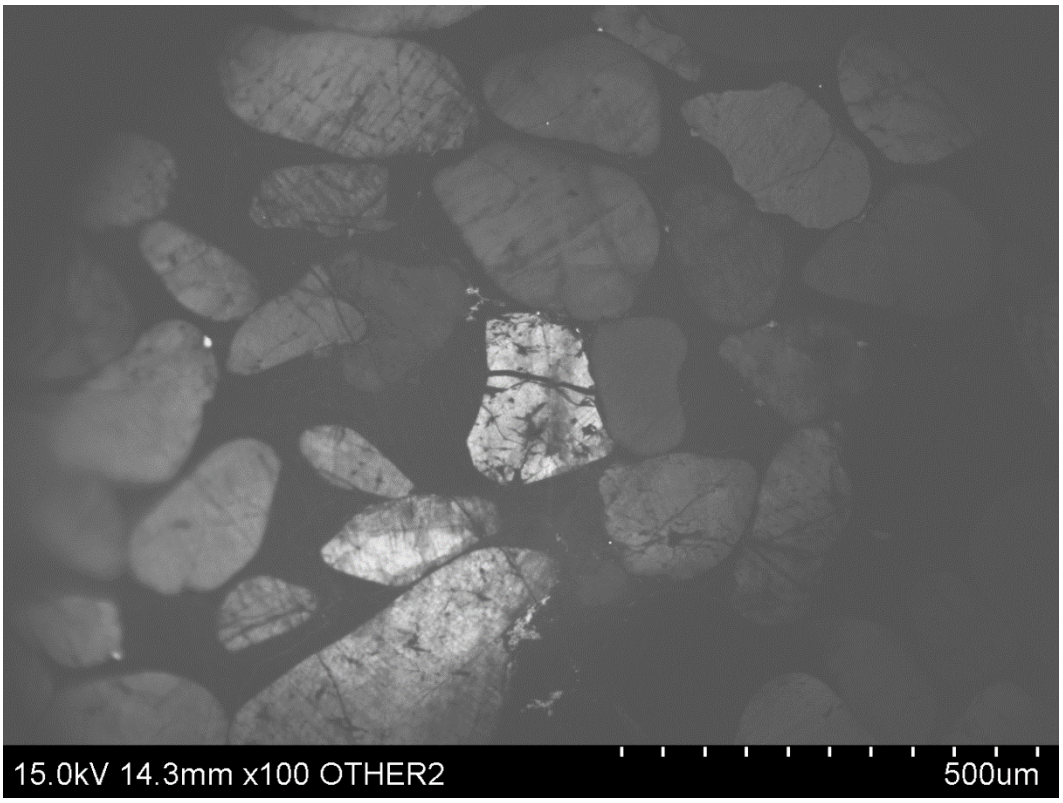

Medium-strain sample AI-08-03-Q12-6

Medium-strain sample AI-08-02-Q12

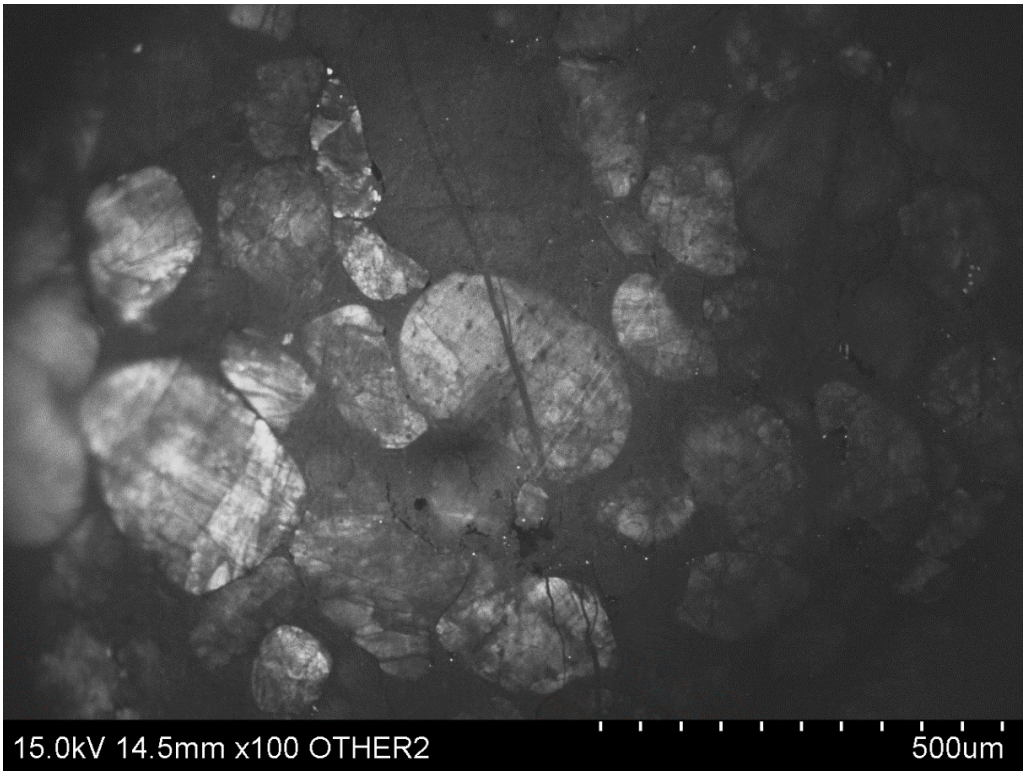

Medium-strain sample AI-08-02-Q12-1

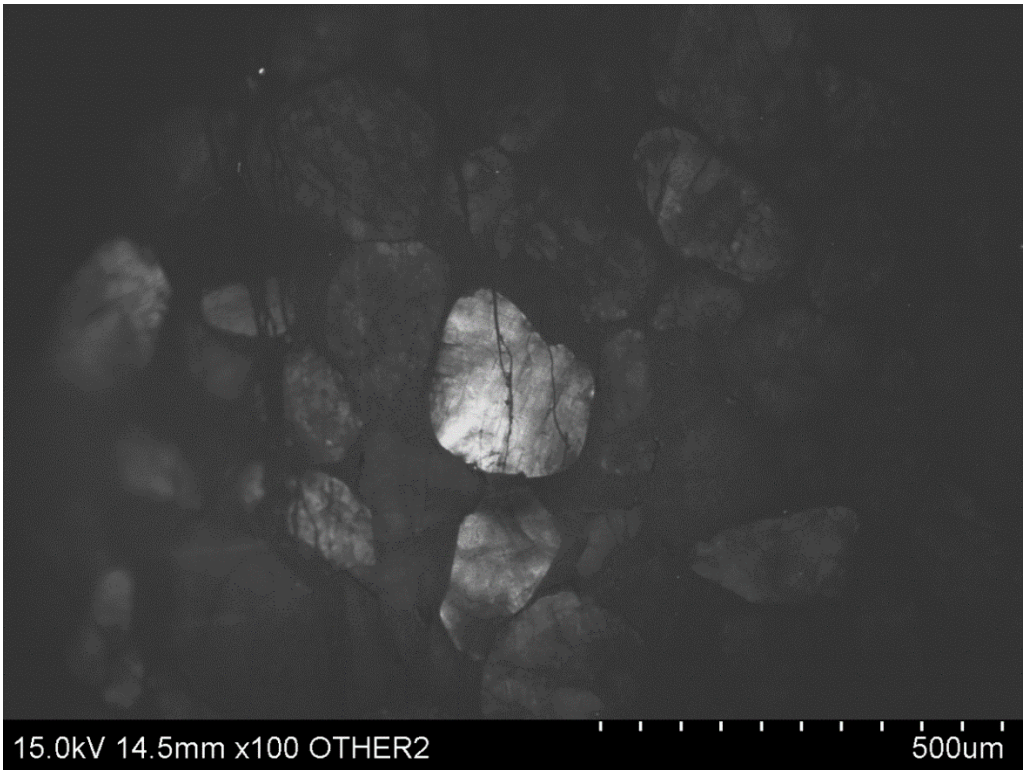

Medium-strain sample AI-08-02-Q12-2

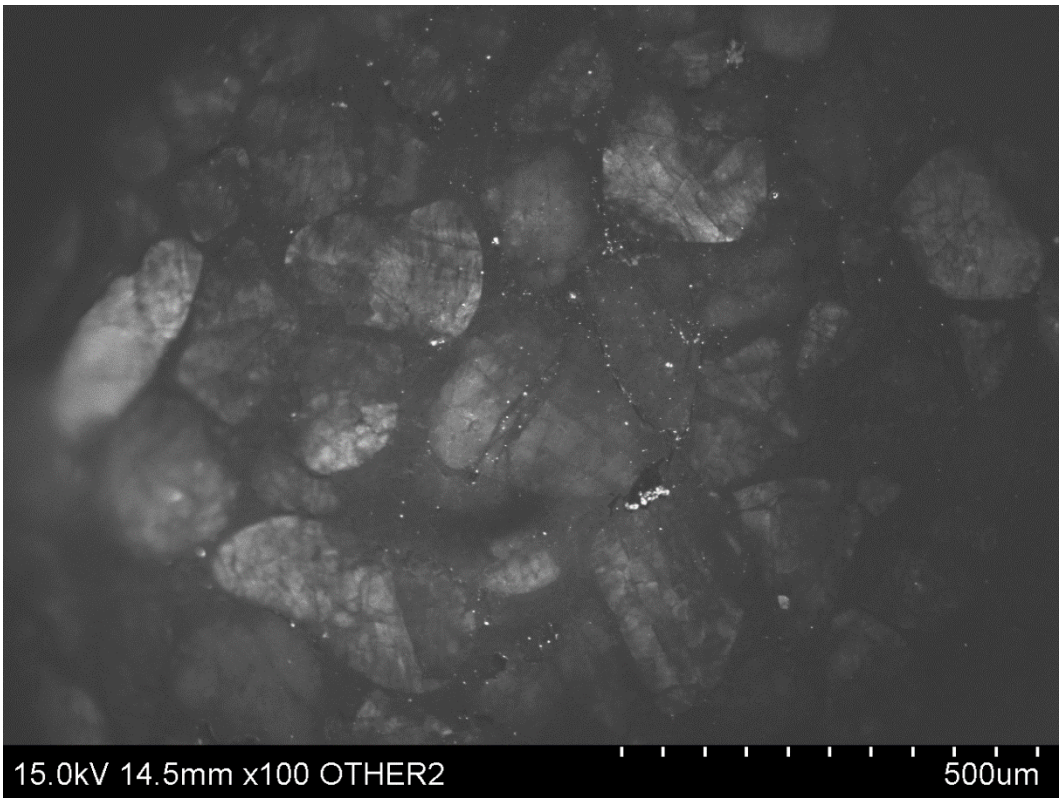

Medium-strain sample AI-08-02-Q12-3

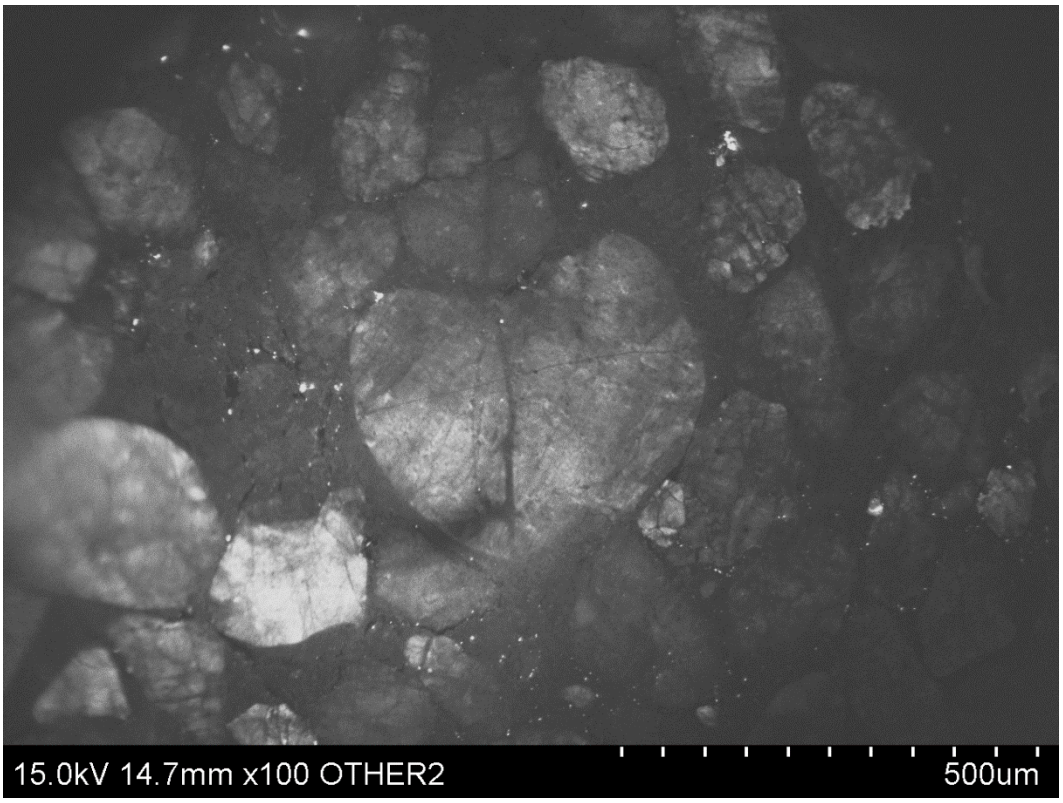

Medium-strain sample AI-08-02-Q12-4

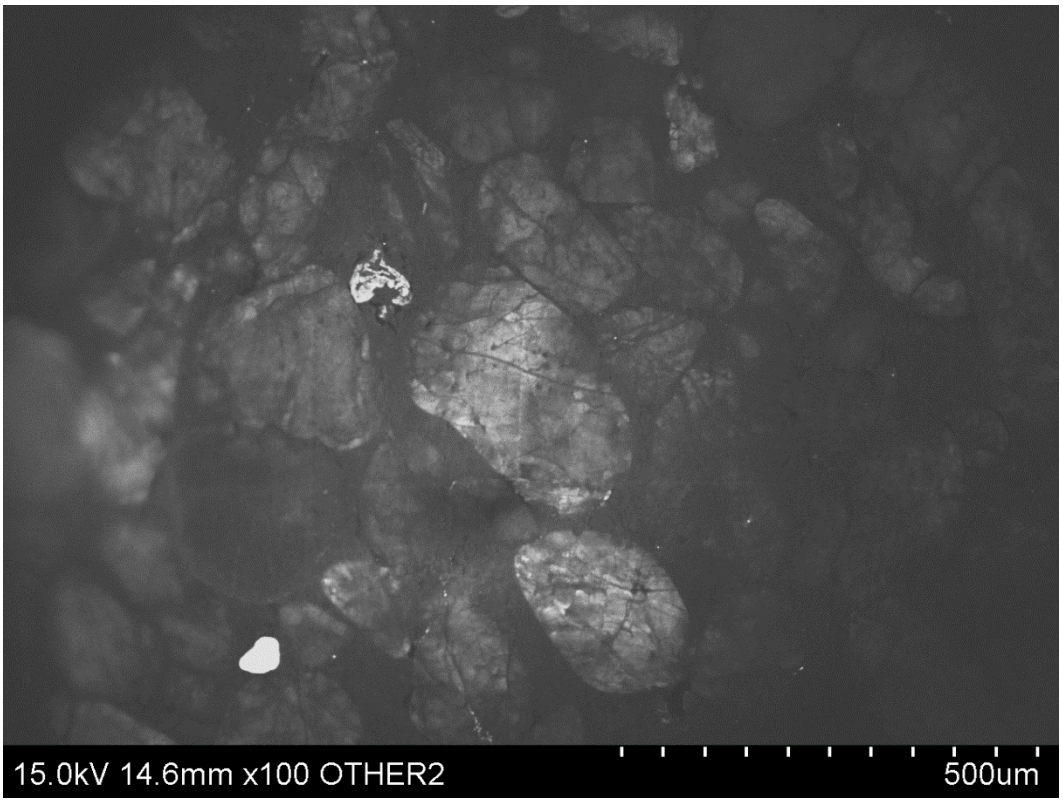

Medium-strain sample AI-08-02-Q12-5

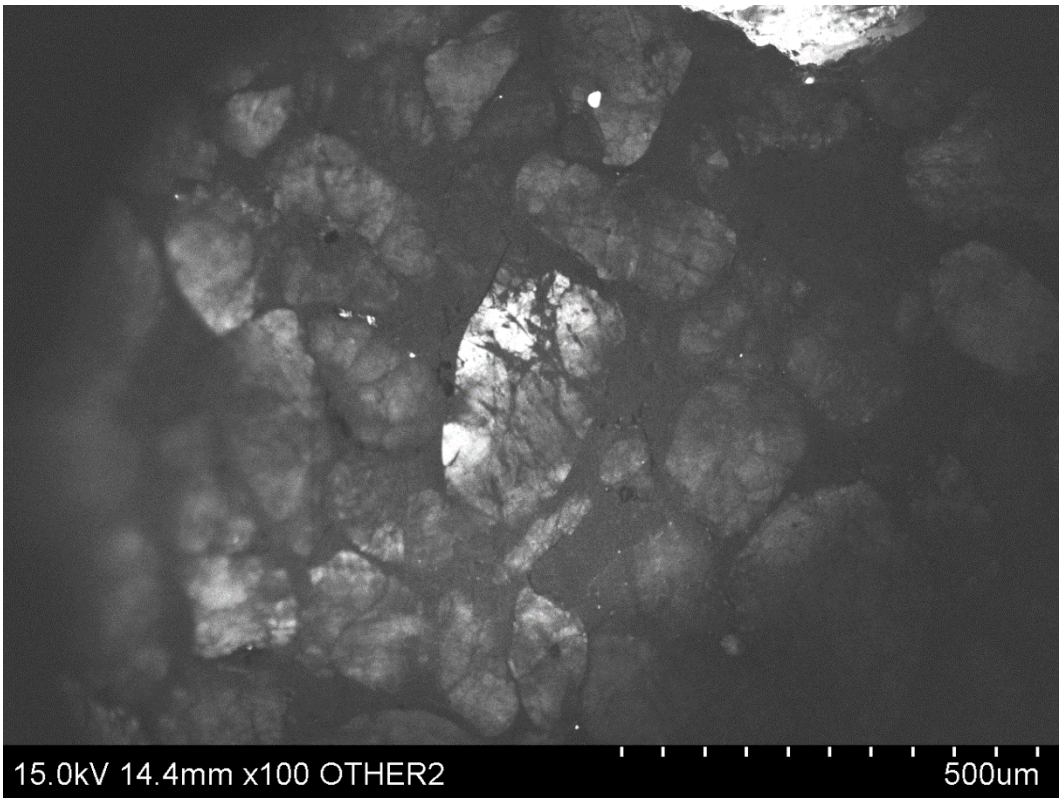

Medium-strain sample AI-08-02-Q12-6

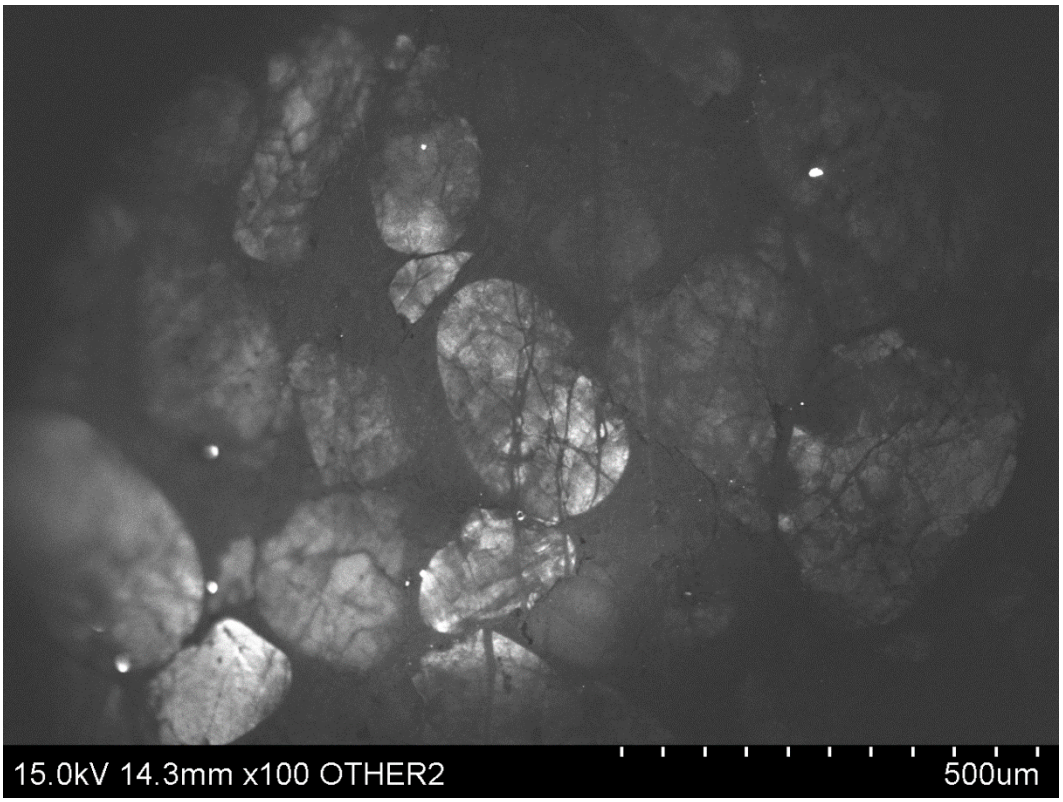

Medium-strain sample AI-08-02-Q12-7

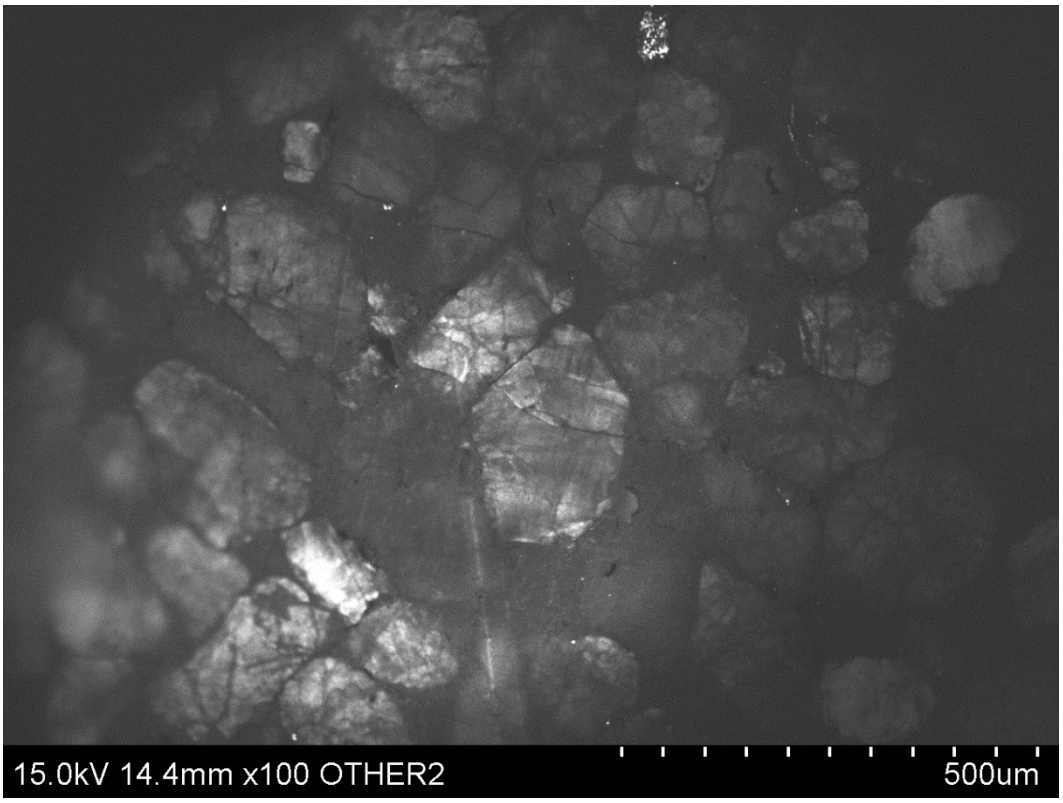

Medium-strain sample AI-08-02-Q12-8

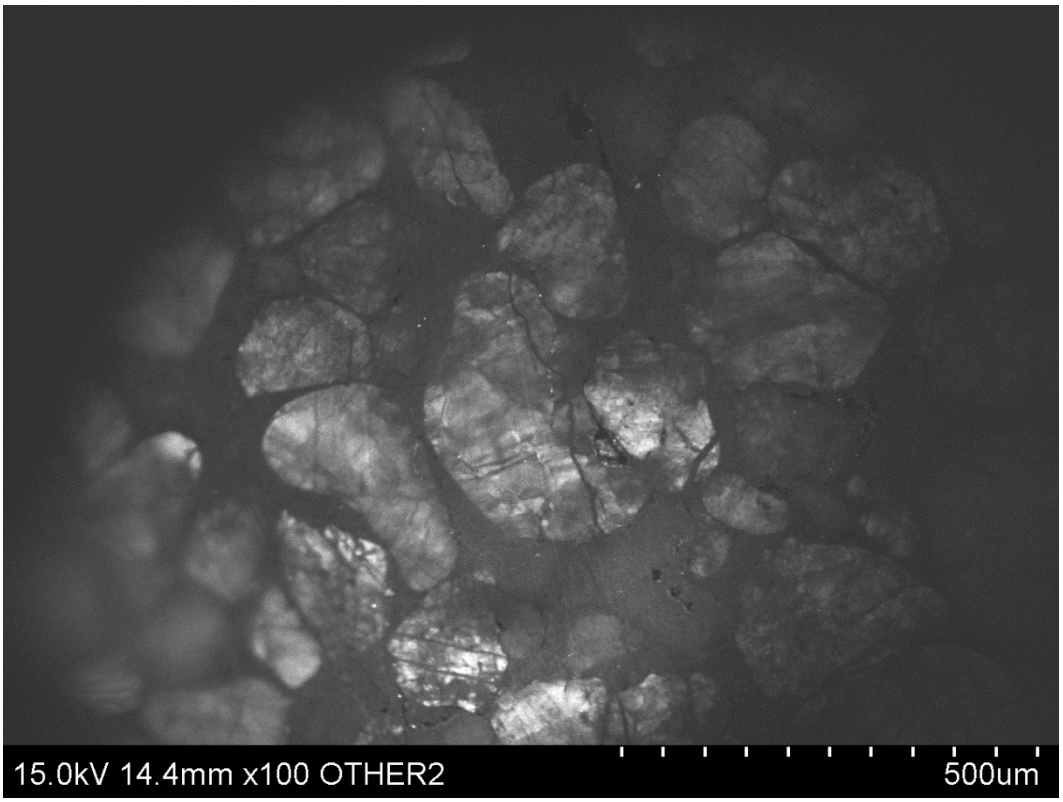

Medium-strain sample AI-08-02-Q12-9

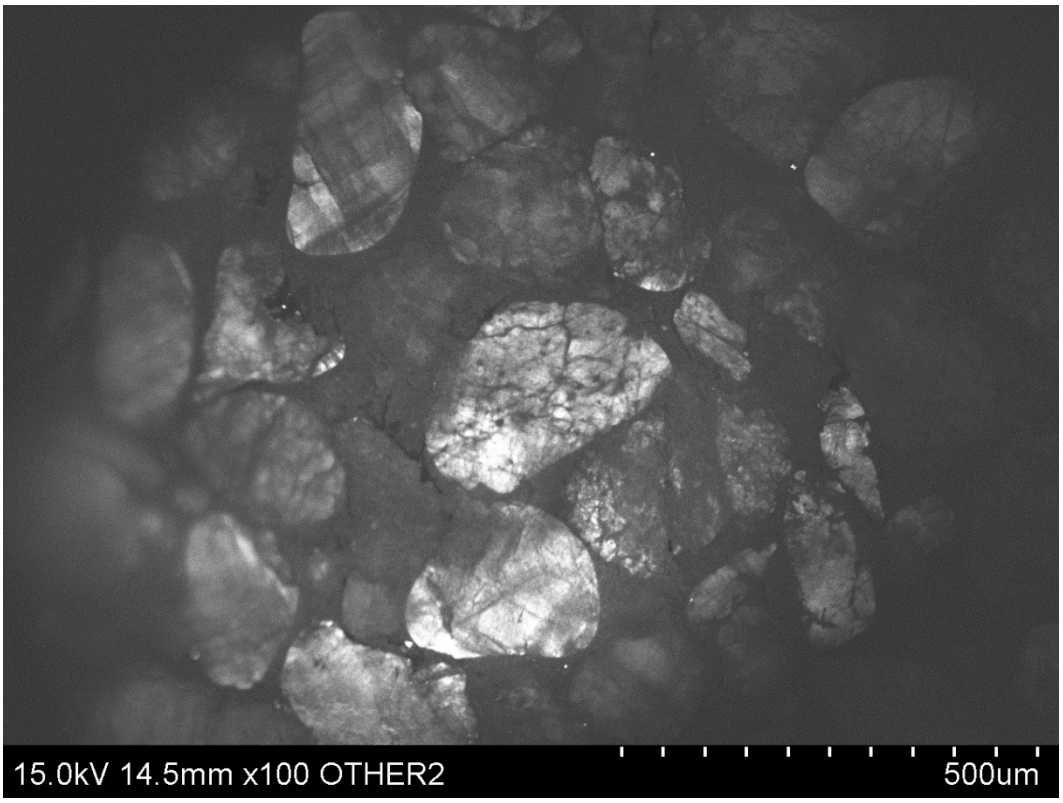

Medium-strain sample AI-08-02-Q12-10

Medium-strain sample AI-08-02-Q14

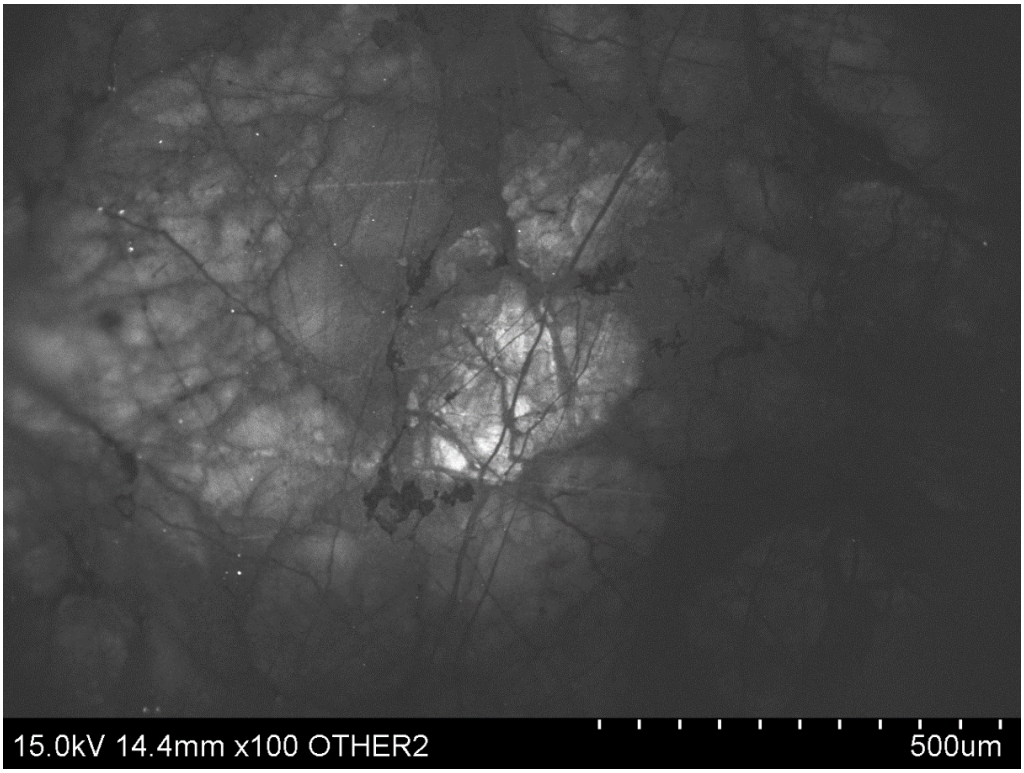

Medium-strain sample AI-08-02-Q14-1

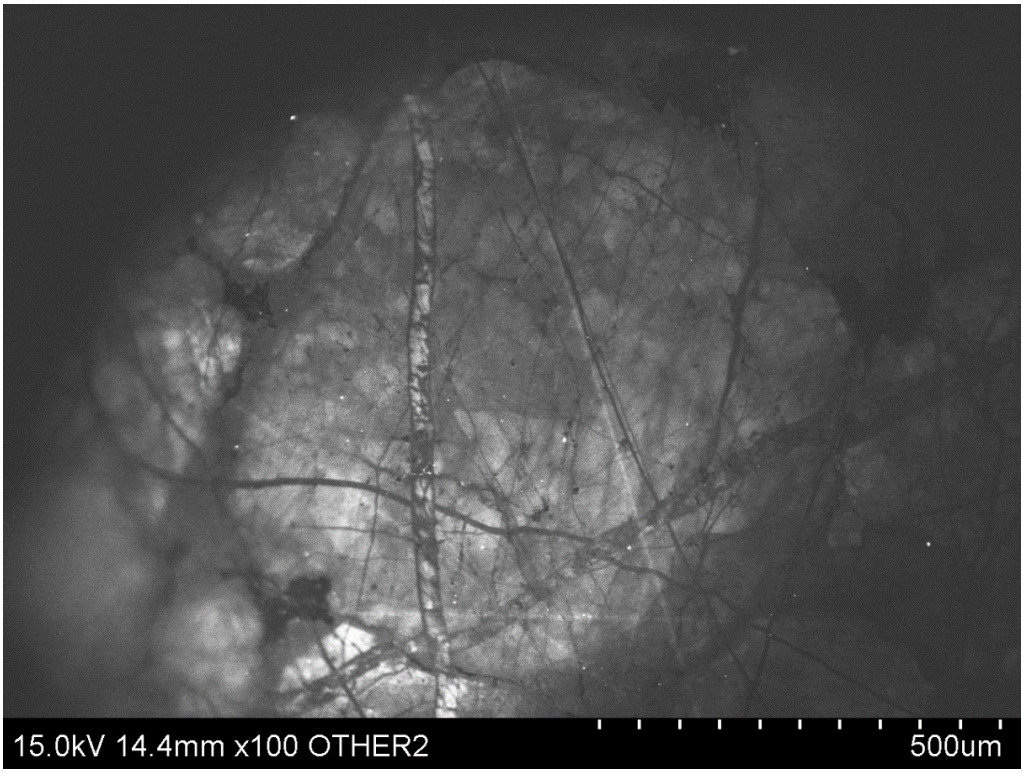

Medium-strain sample AI-08-02-Q14-2

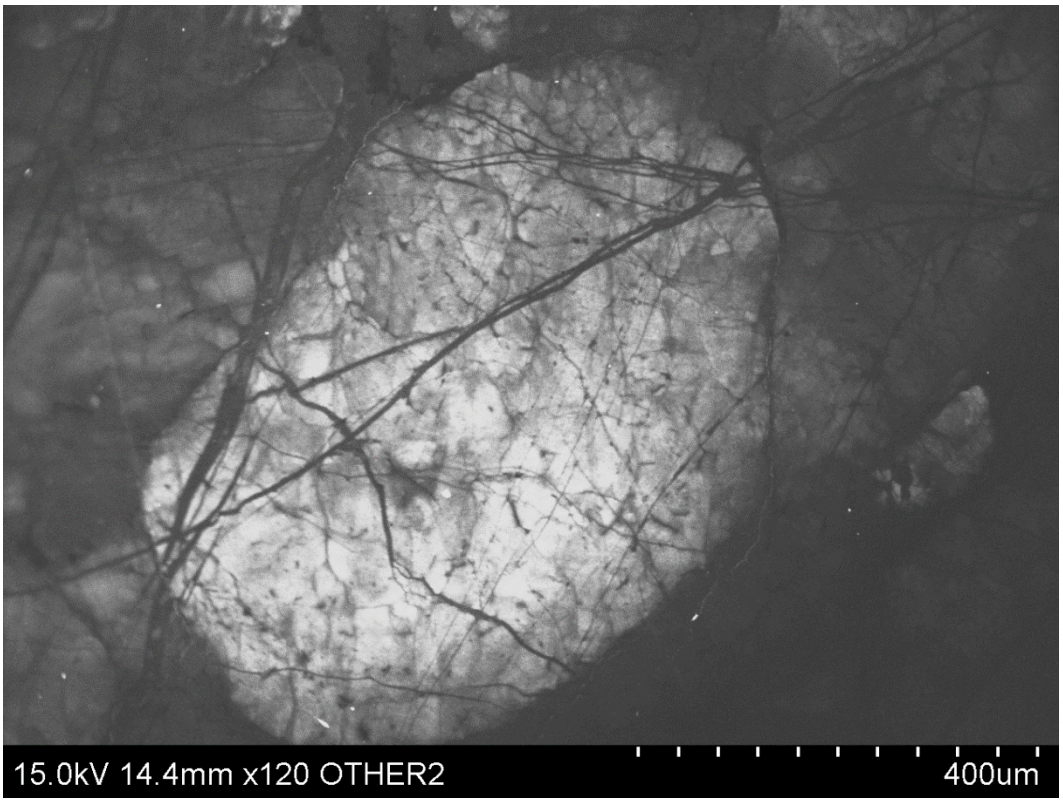

Medium-strain sample AI-08-02-Q14-3

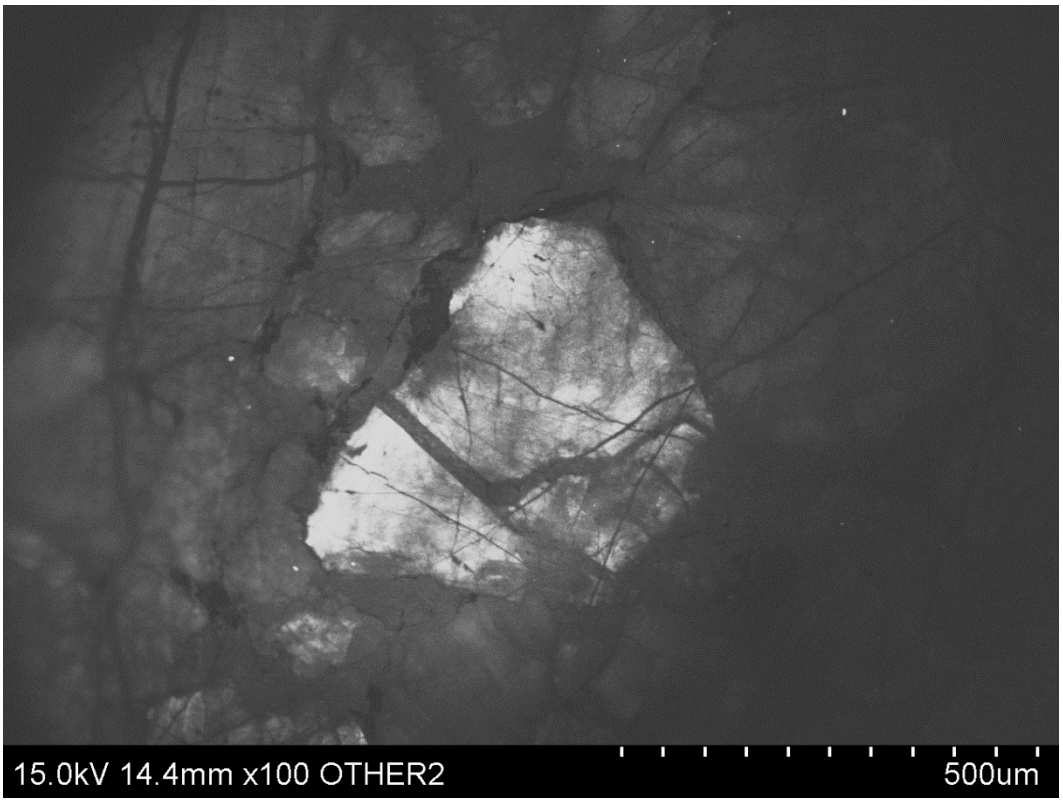

Medium-strain sample AI-08-02-Q14-4

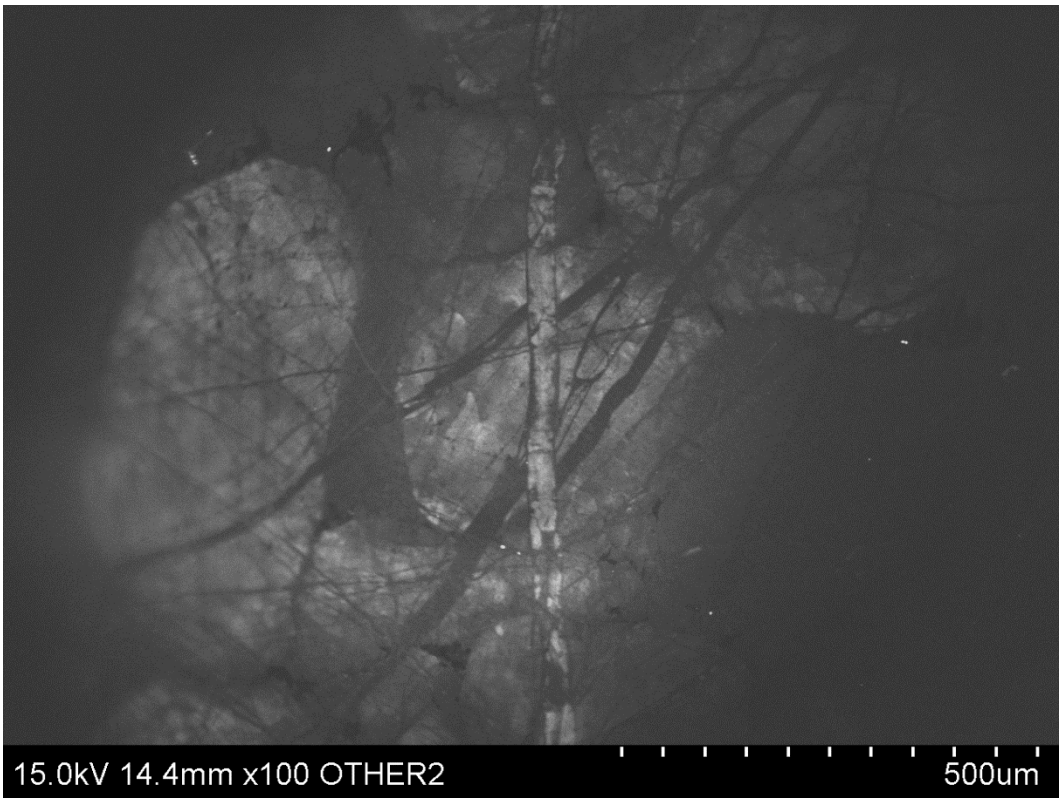

Medium-strain sample AI-08-02-Q14-5

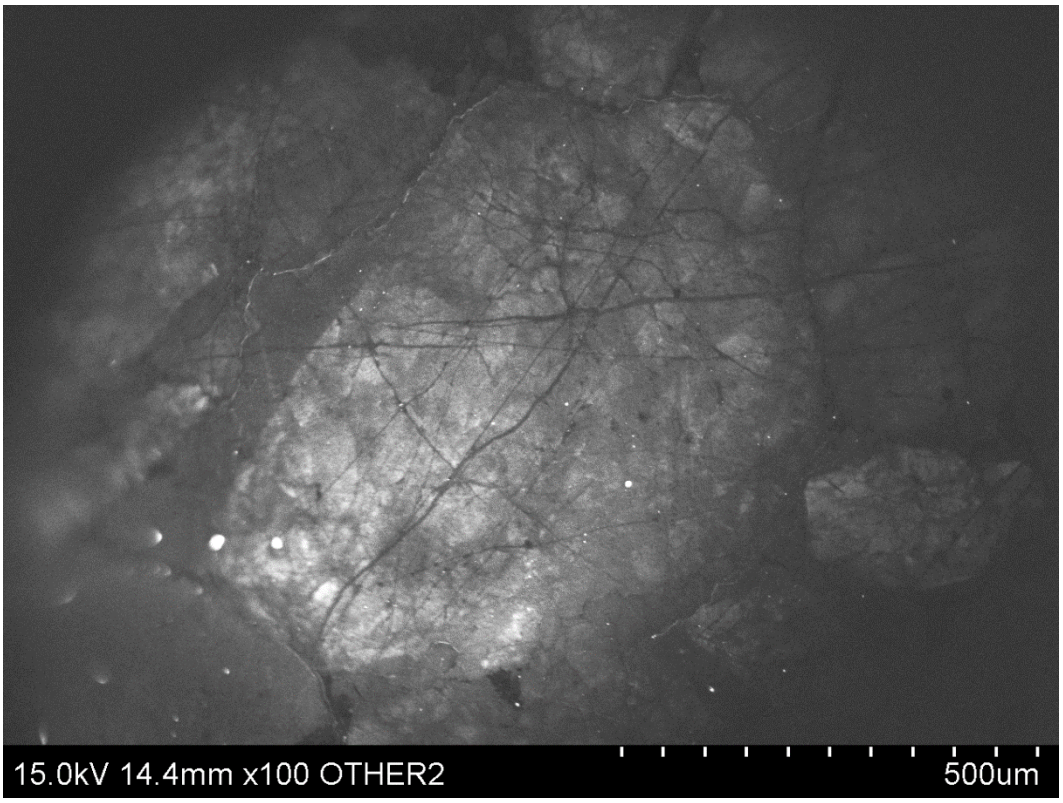

Medium-strain sample AI-08-02-Q14-6

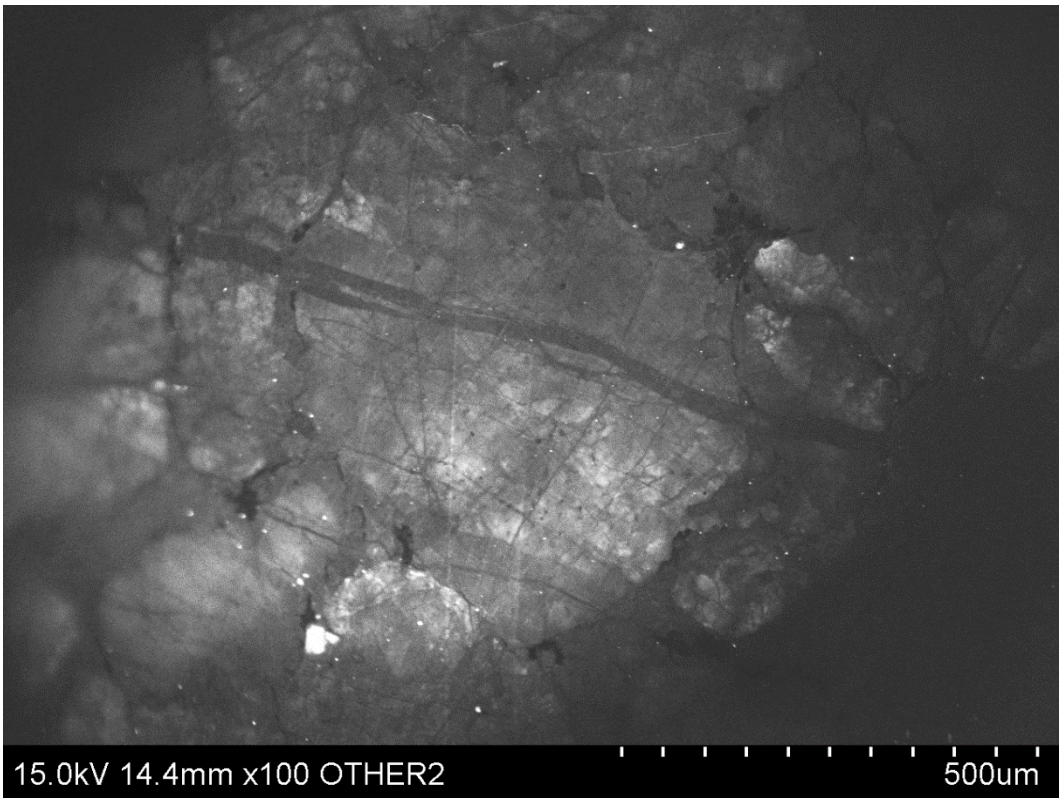

Medium-strain sample AI-08-02-Q14-7

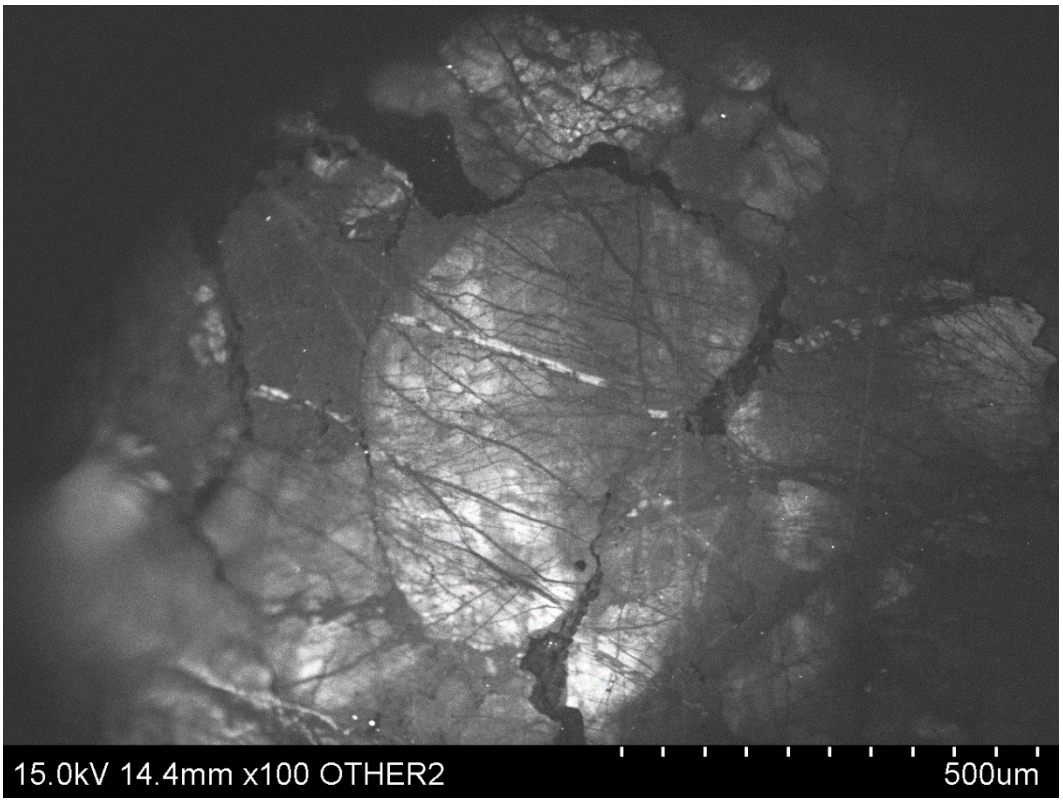

Medium-strain sample AI-08-02-Q14-8

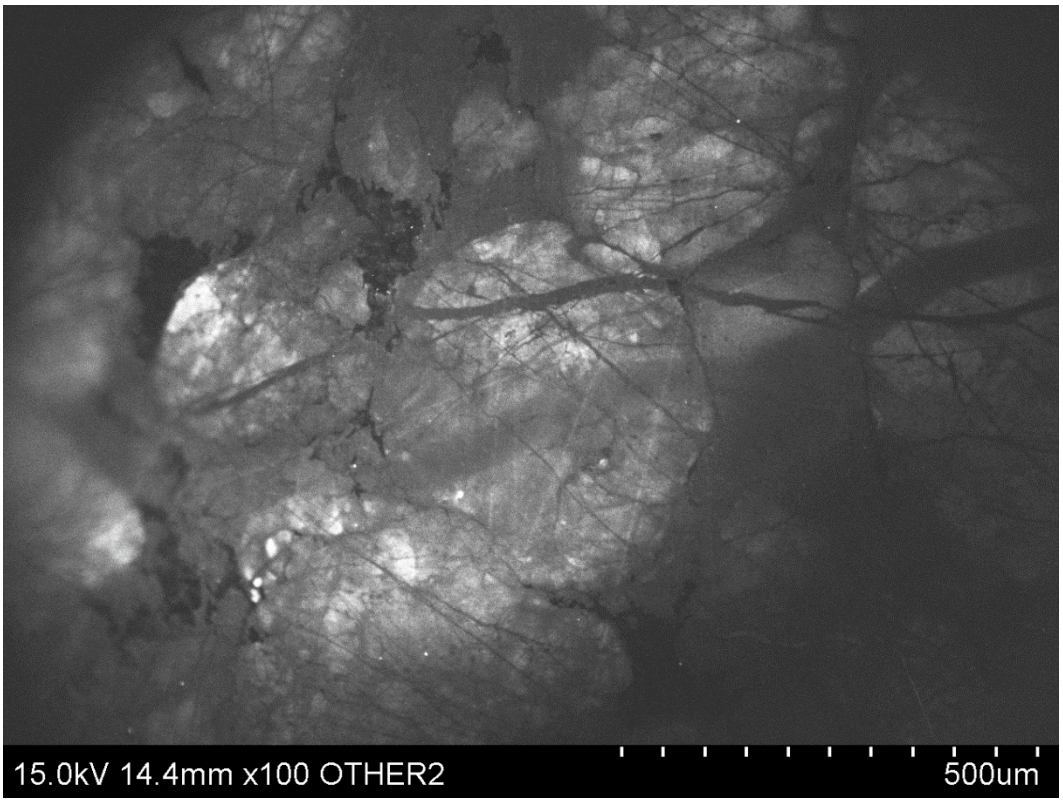

Medium-strain sample AI-08-02-Q14-9

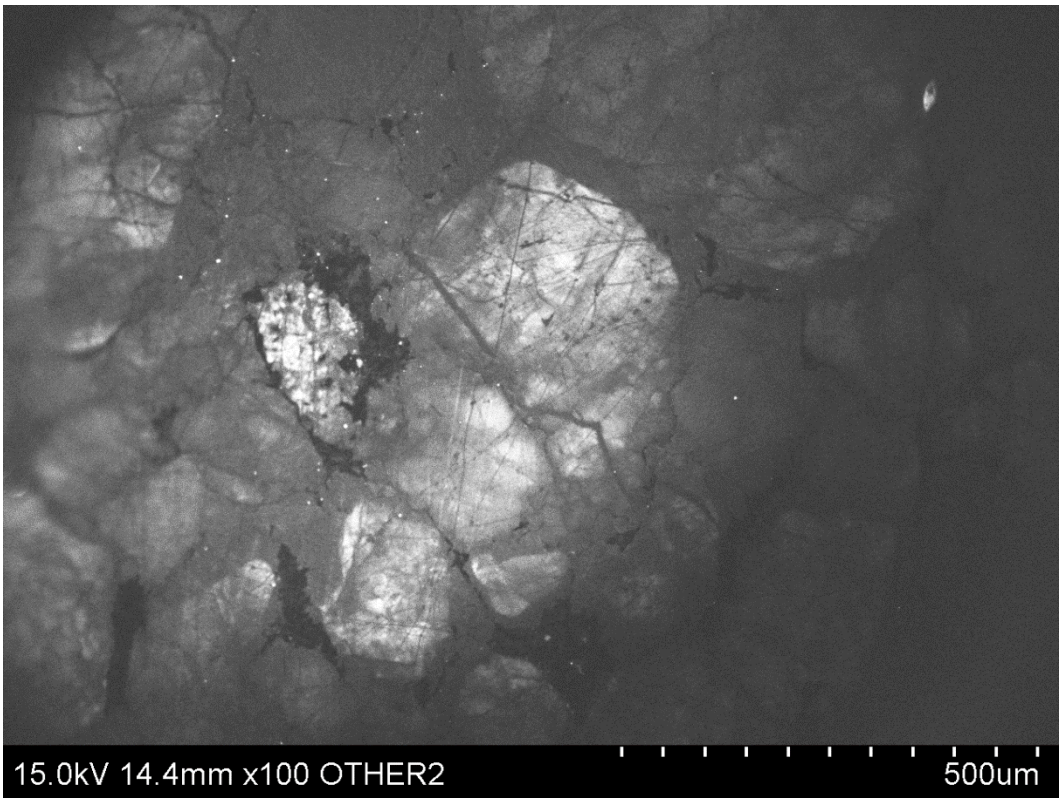

Medium-strain sample AI-08-02-Q14-10

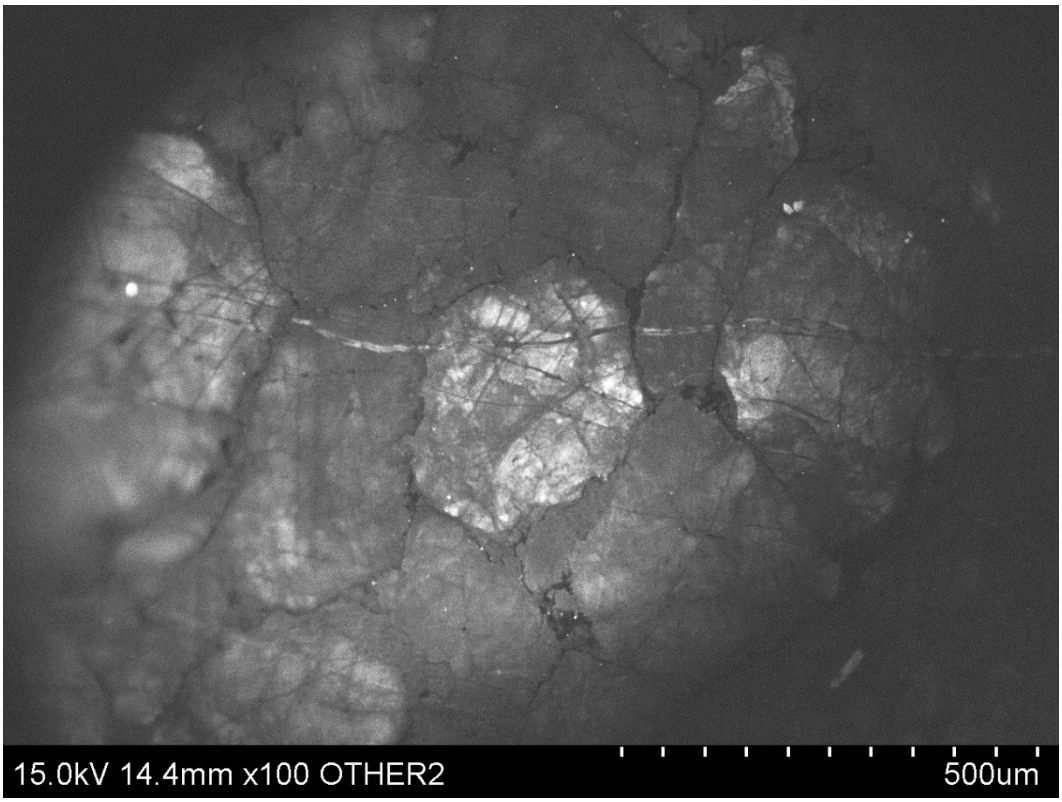

Medium-strain sample AI-08-02-Q14-11

High-strain sample AI-08-06-Q11

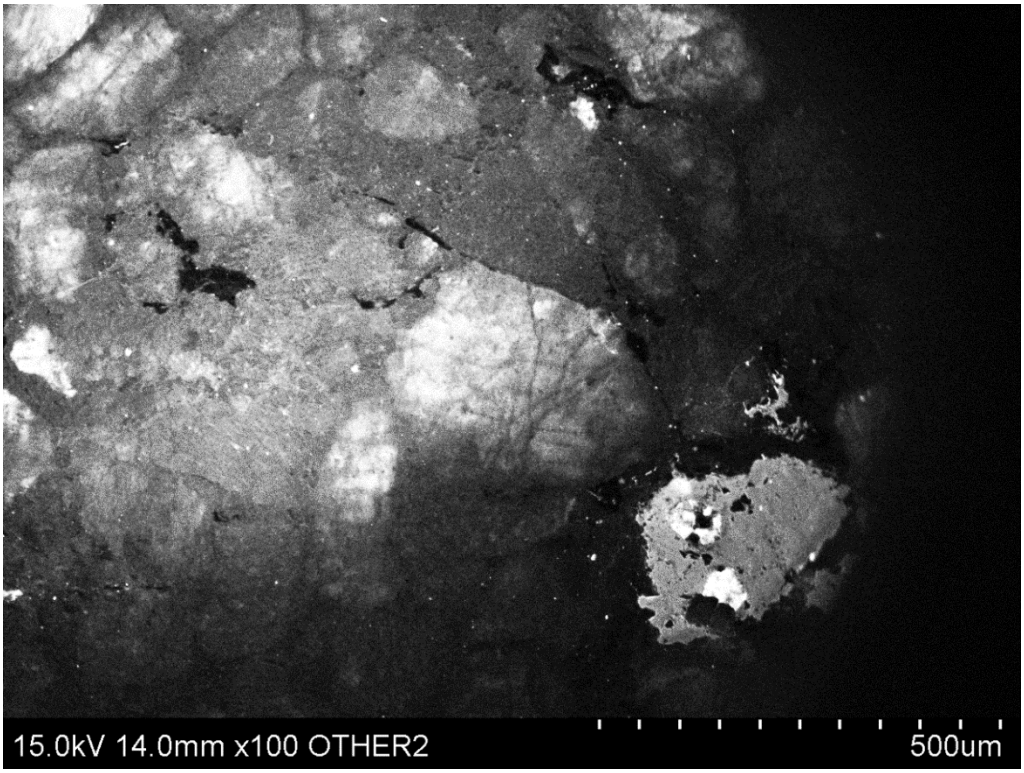

High-strain sample AI-08-06-Q11-1

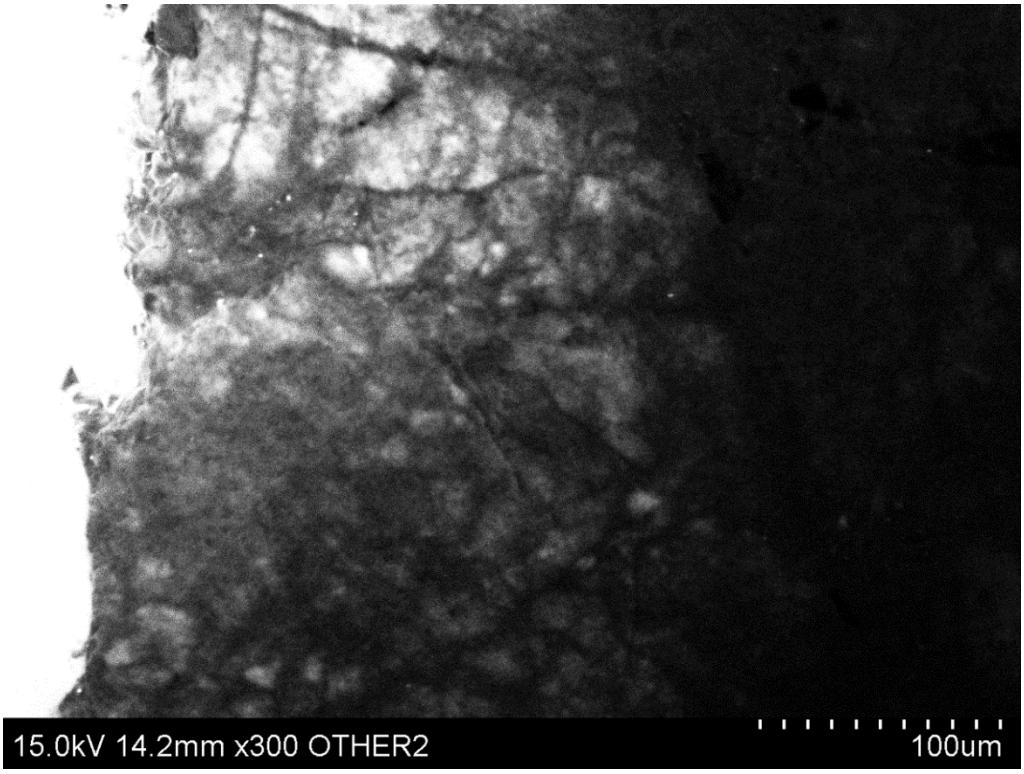

High-strain sample AI-08-06-Q11-2

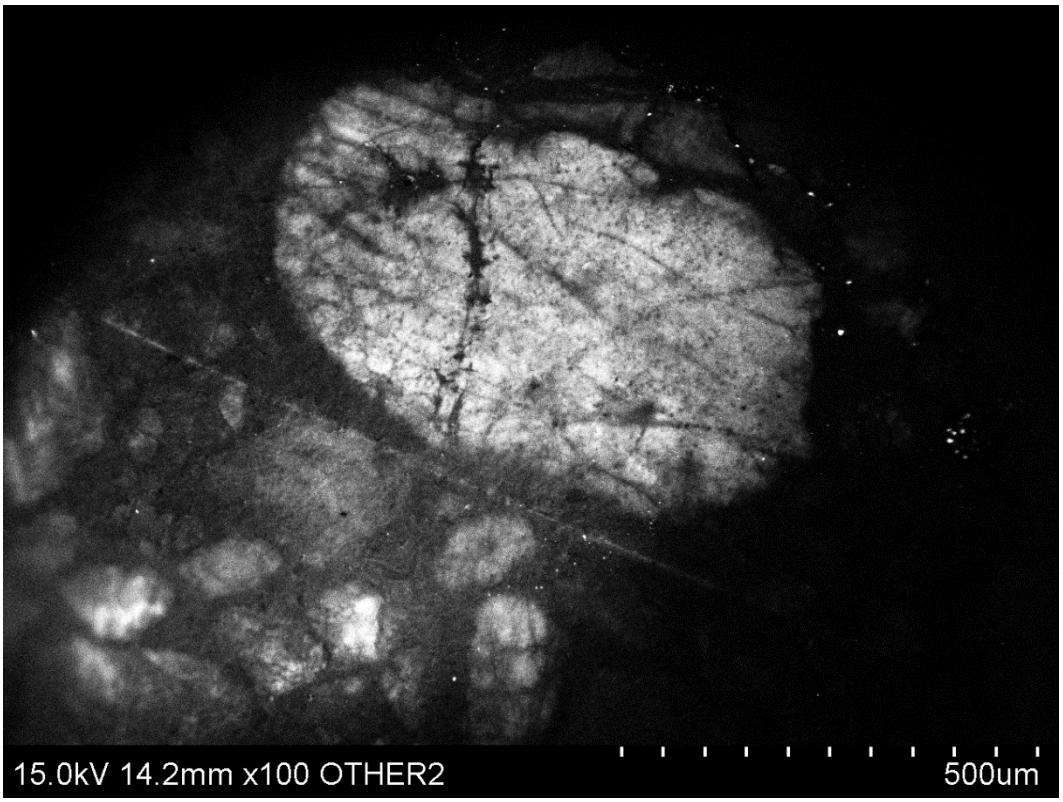

High-strain sample AI-08-06-Q11-3

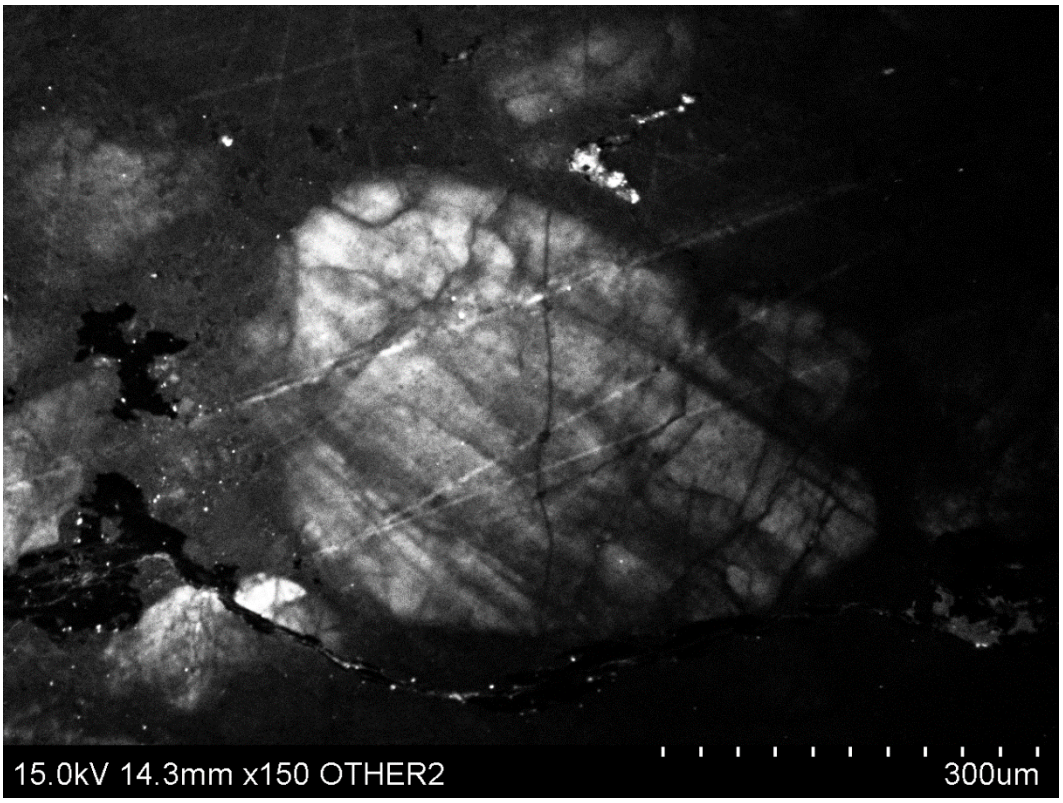

High-strain sample AI-08-06-Q11-4

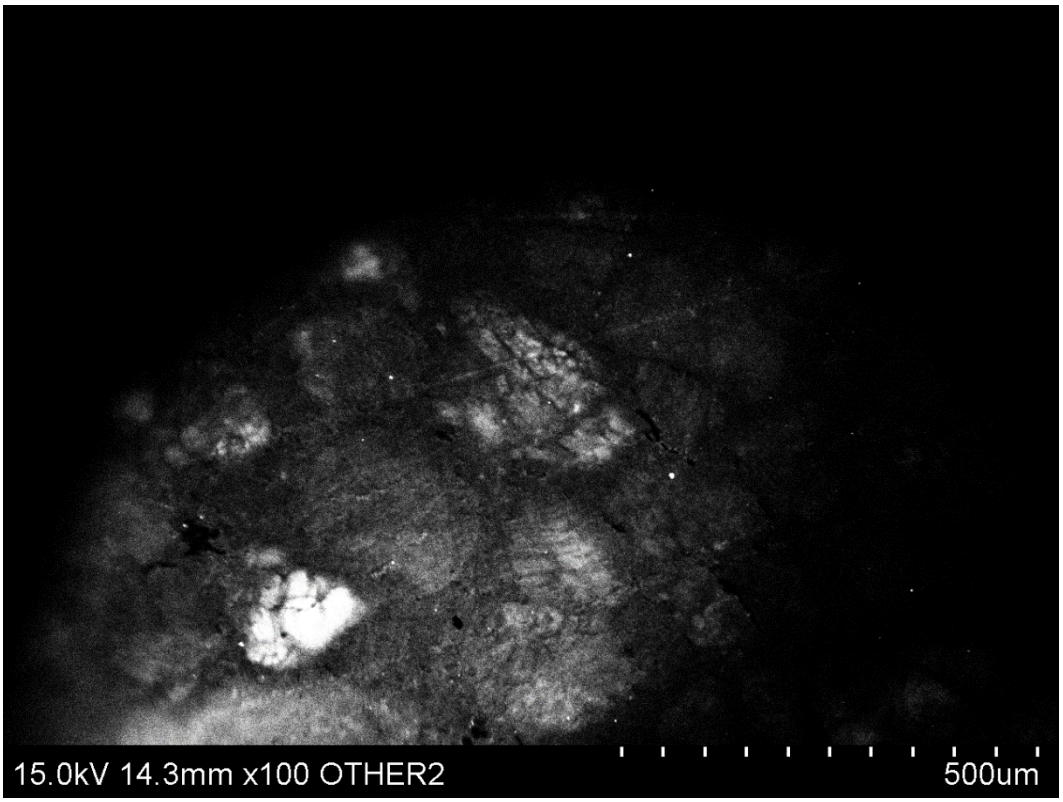

High-strain sample AI-08-06-Q11-5

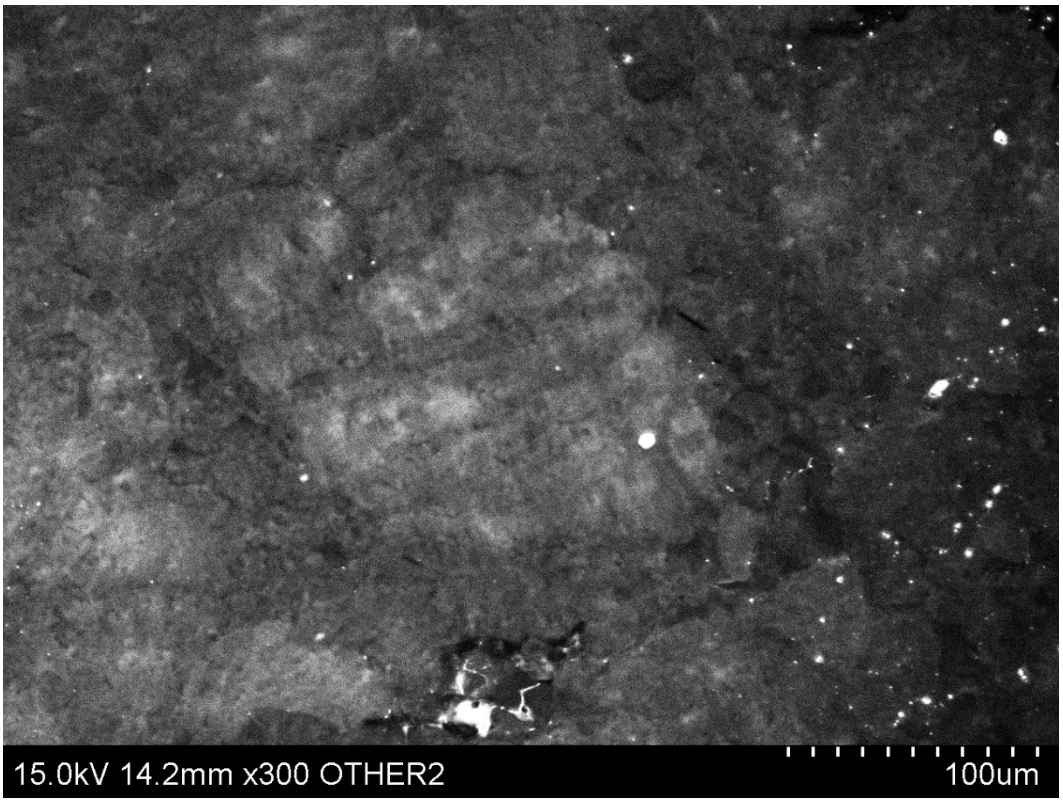

High-strain sample AI-08-06-Q11-6

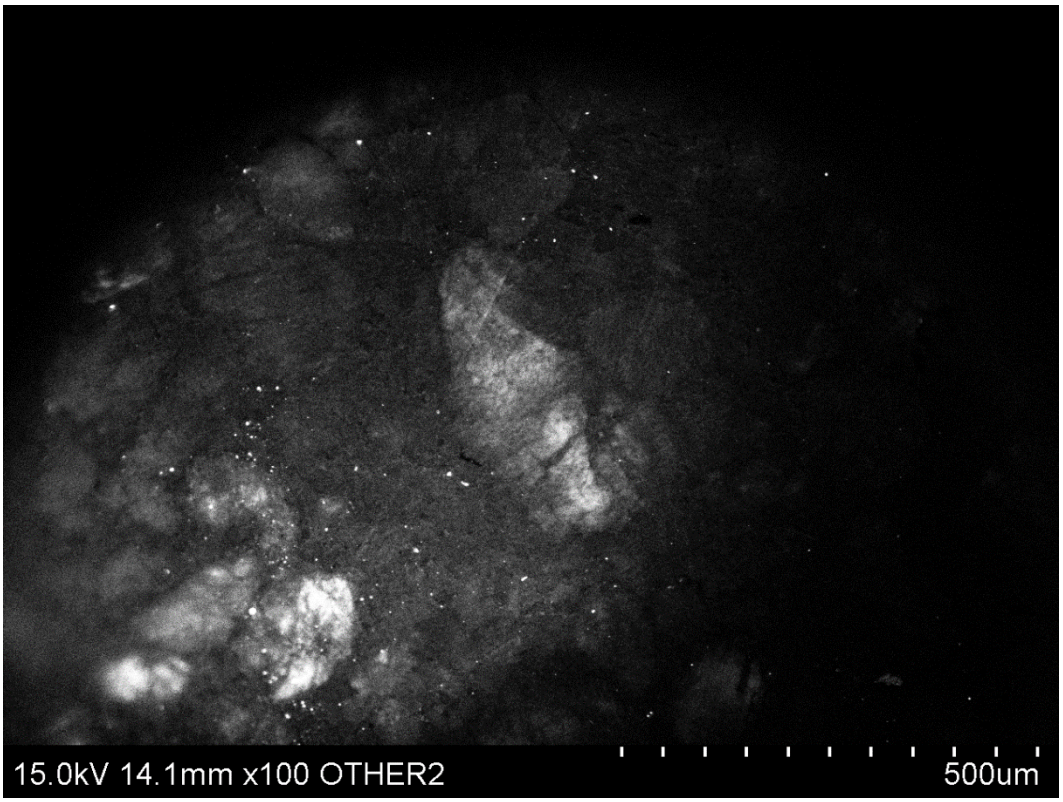

High-strain sample AI-08-06-Q11-7

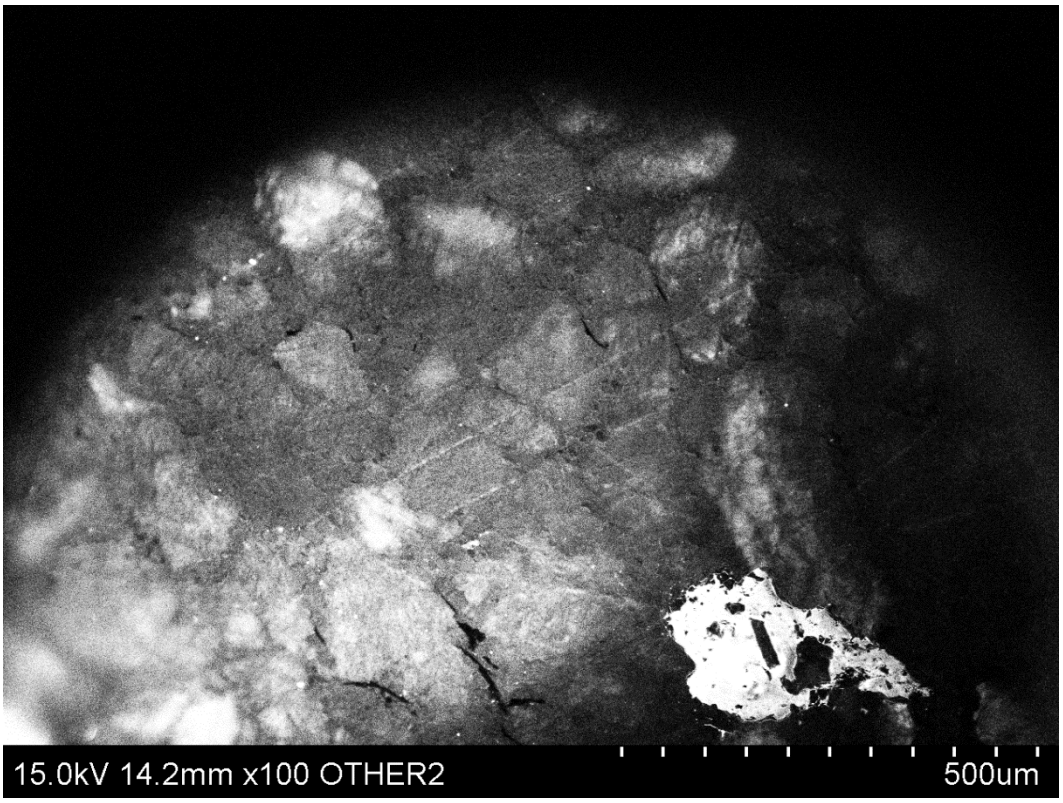

High-strain sample AI-08-06-Q11-8

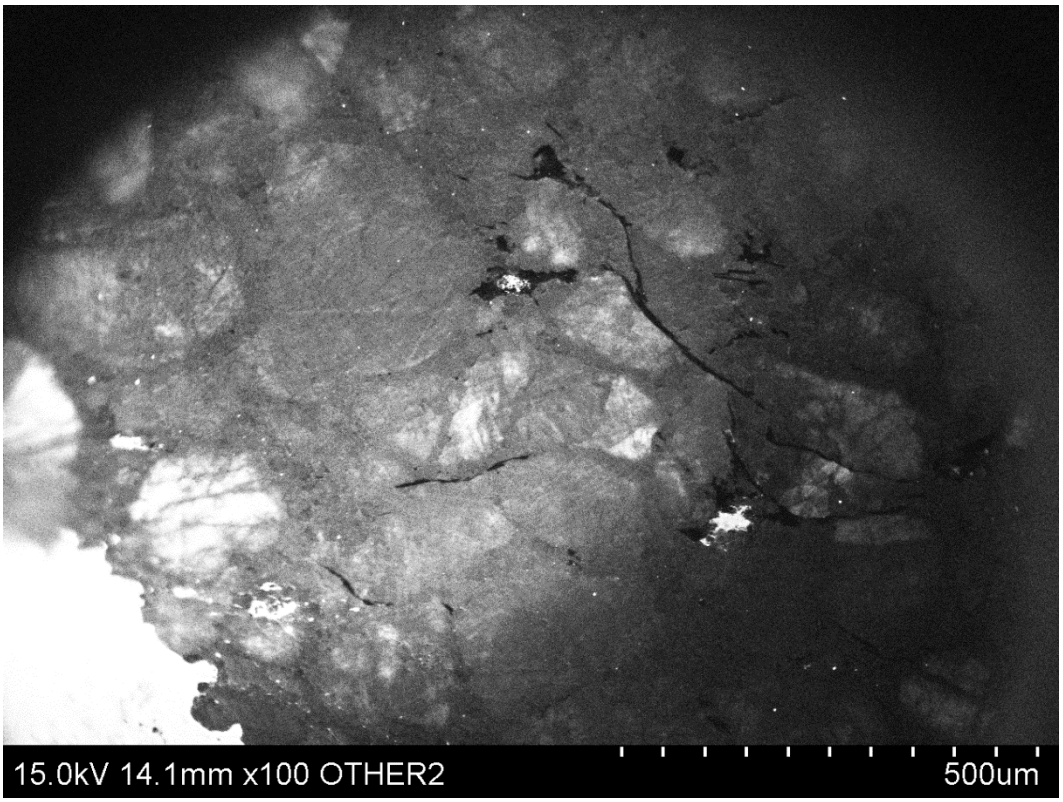

High-strain sample AI-08-06-Q11-9

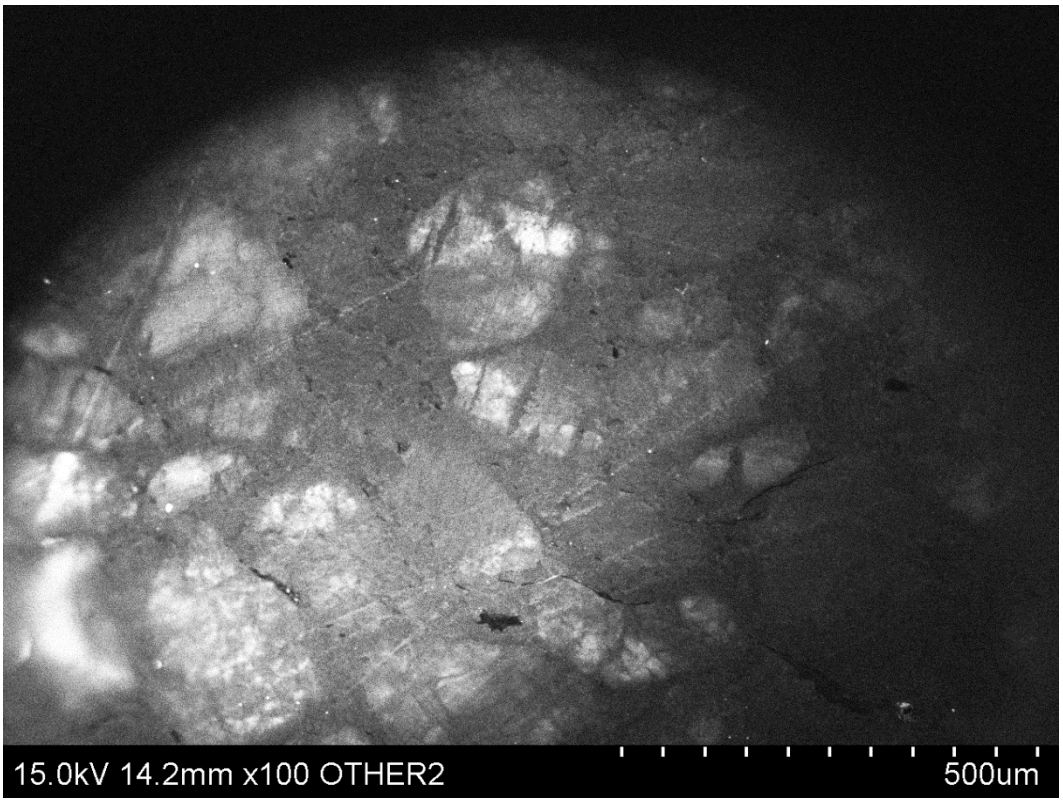

High-strain sample AI-08-06-Q11-10

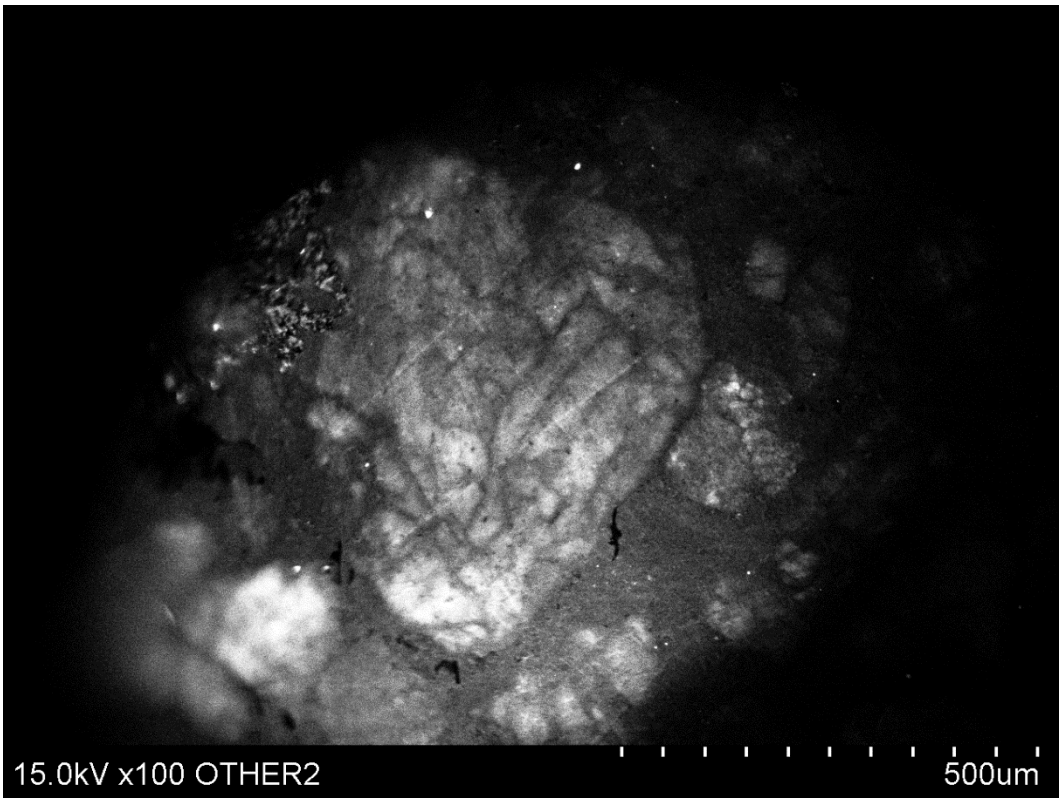

High-strain sample AI-08-06-Q11-11

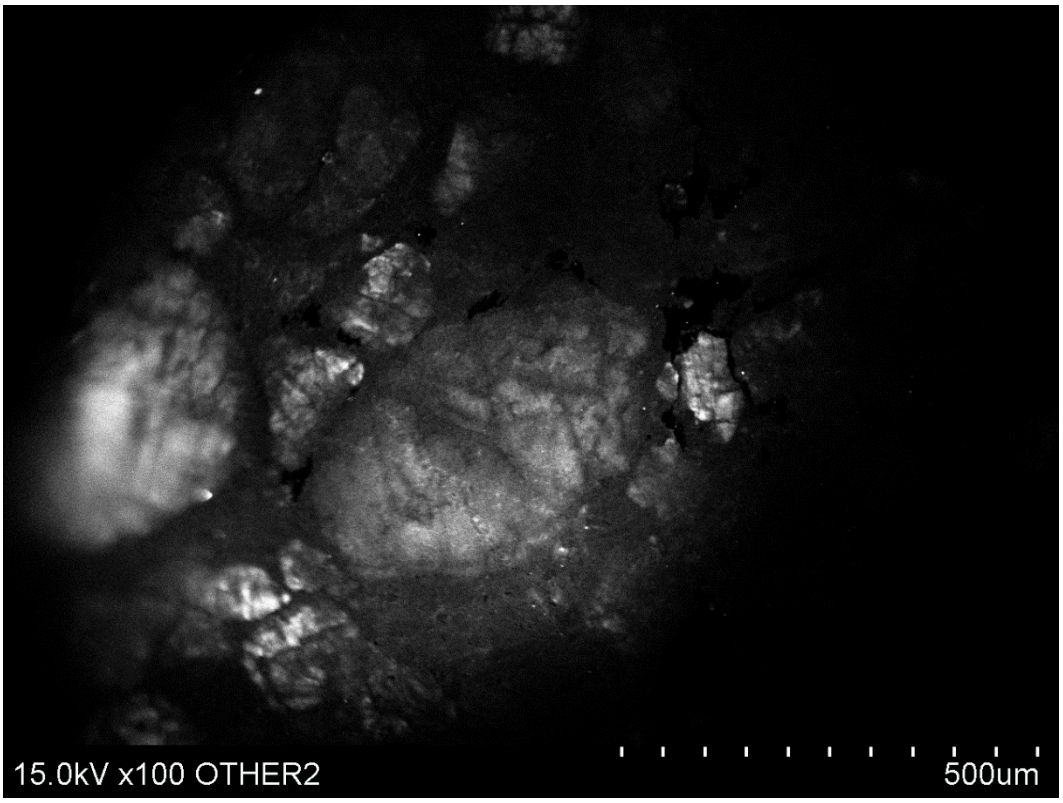

High-strain sample AI-08-06-Q11-12

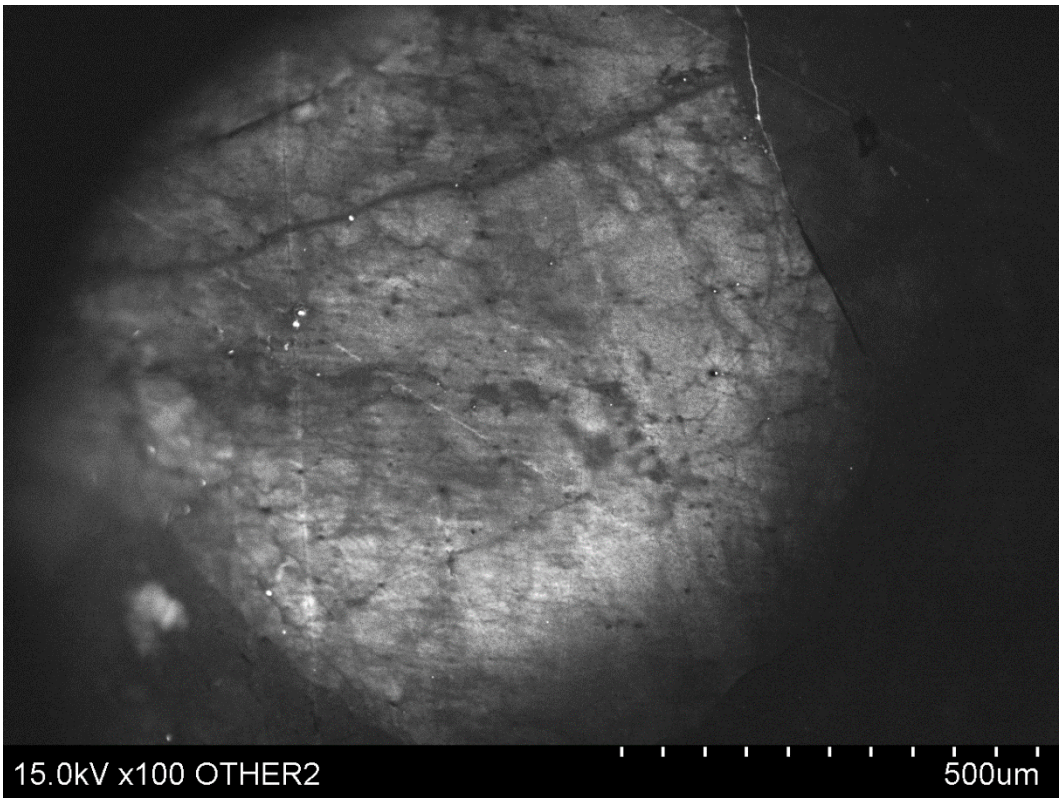

High-strain sample AI-08-06-Q11-13

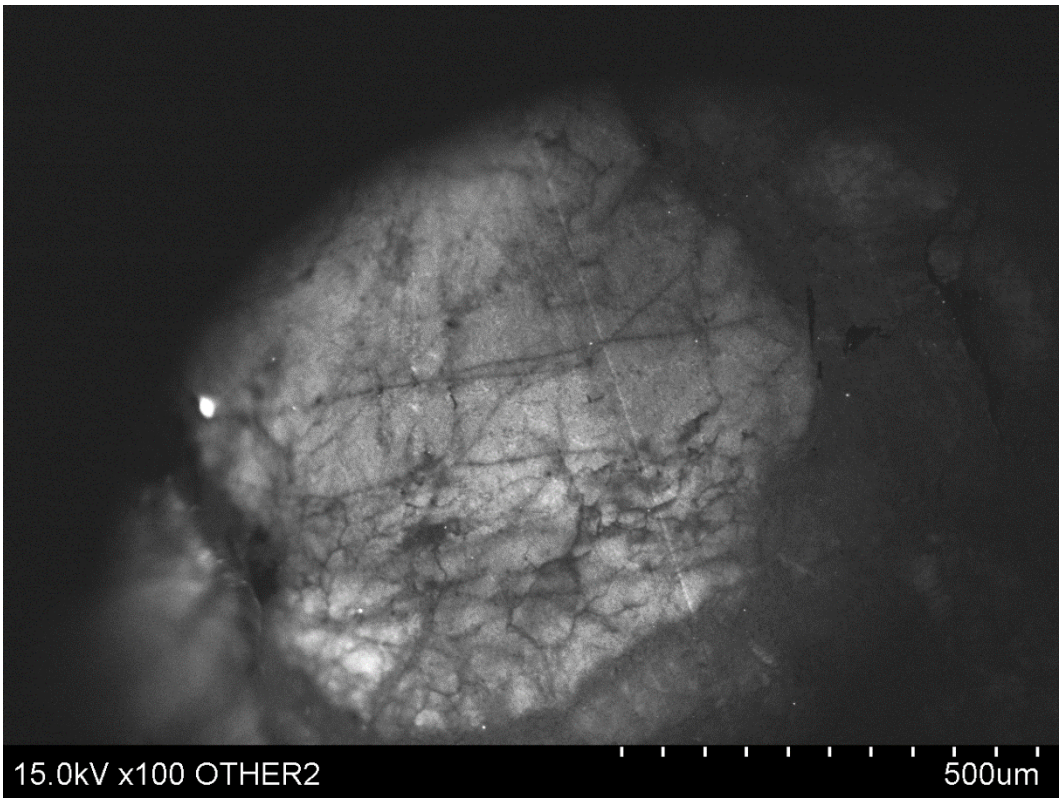

High-strain sample AI-08-06-Q11-14

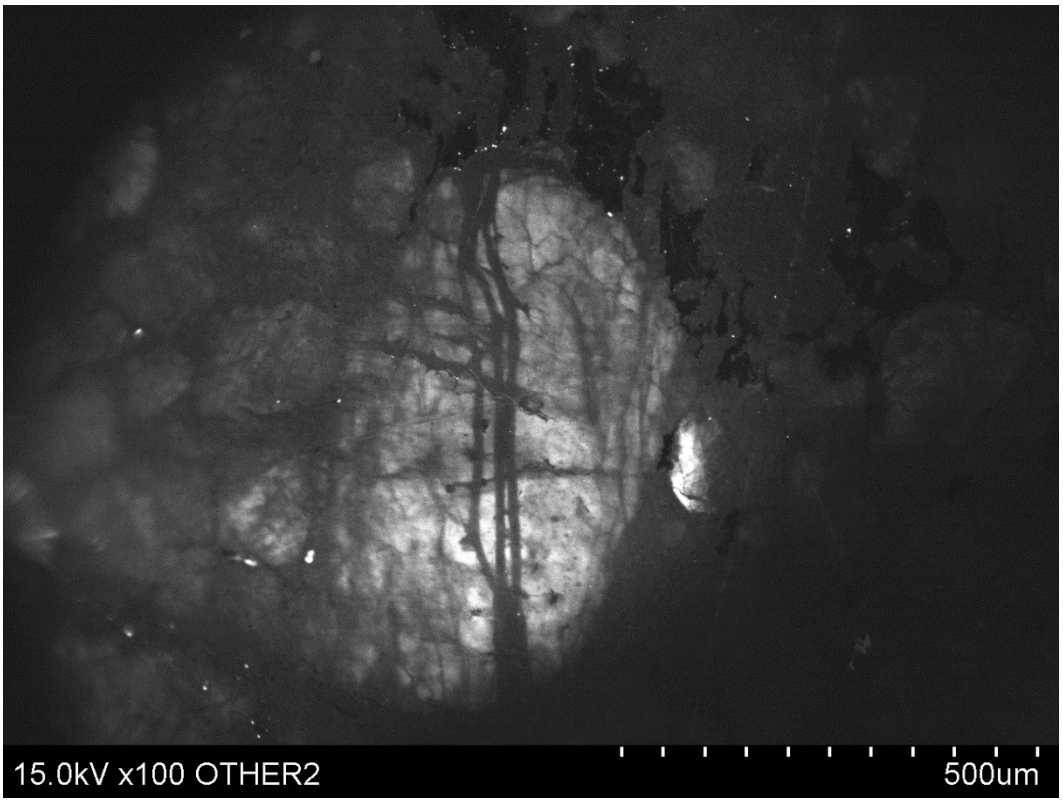

High-strain sample AI-08-06-Q11-15

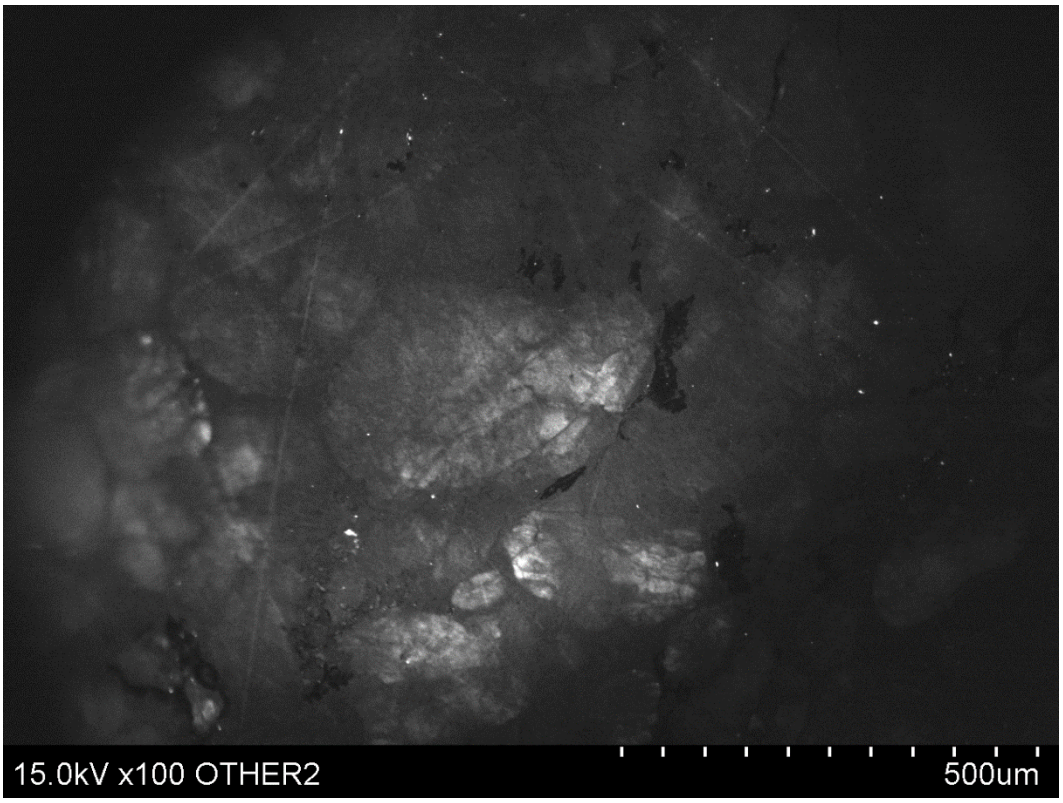

High-strain sample AI-08-06-Q11-16

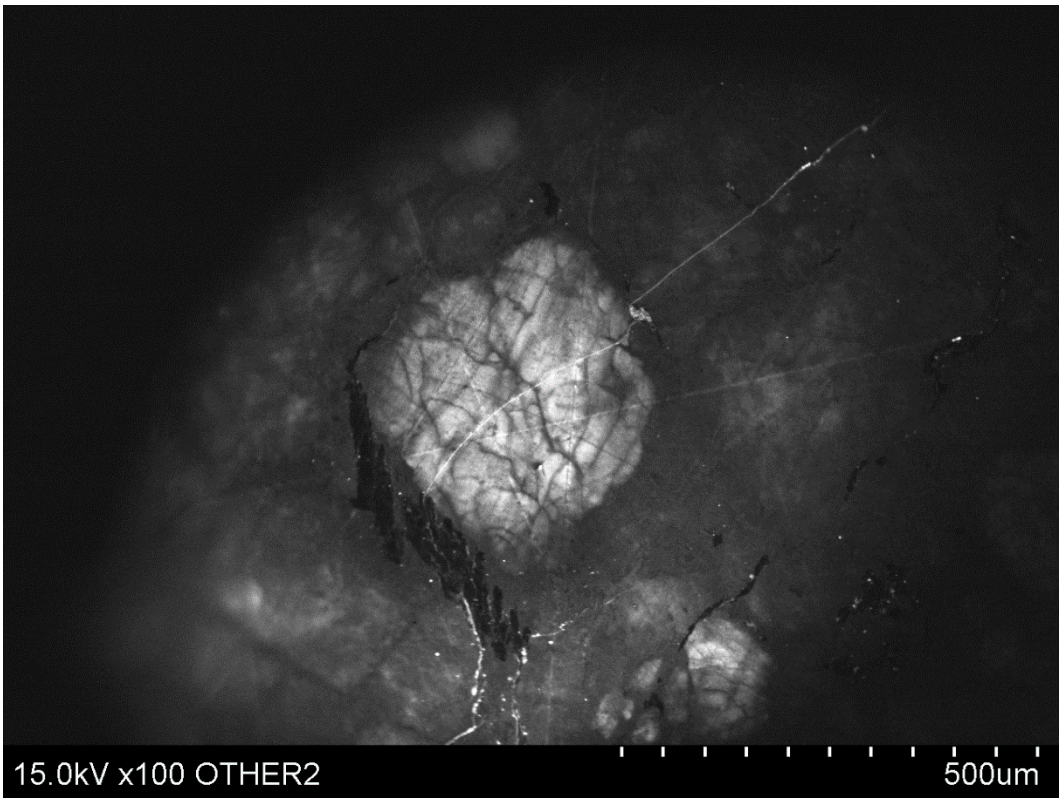

High-strain sample AI-08-06-Q11-17

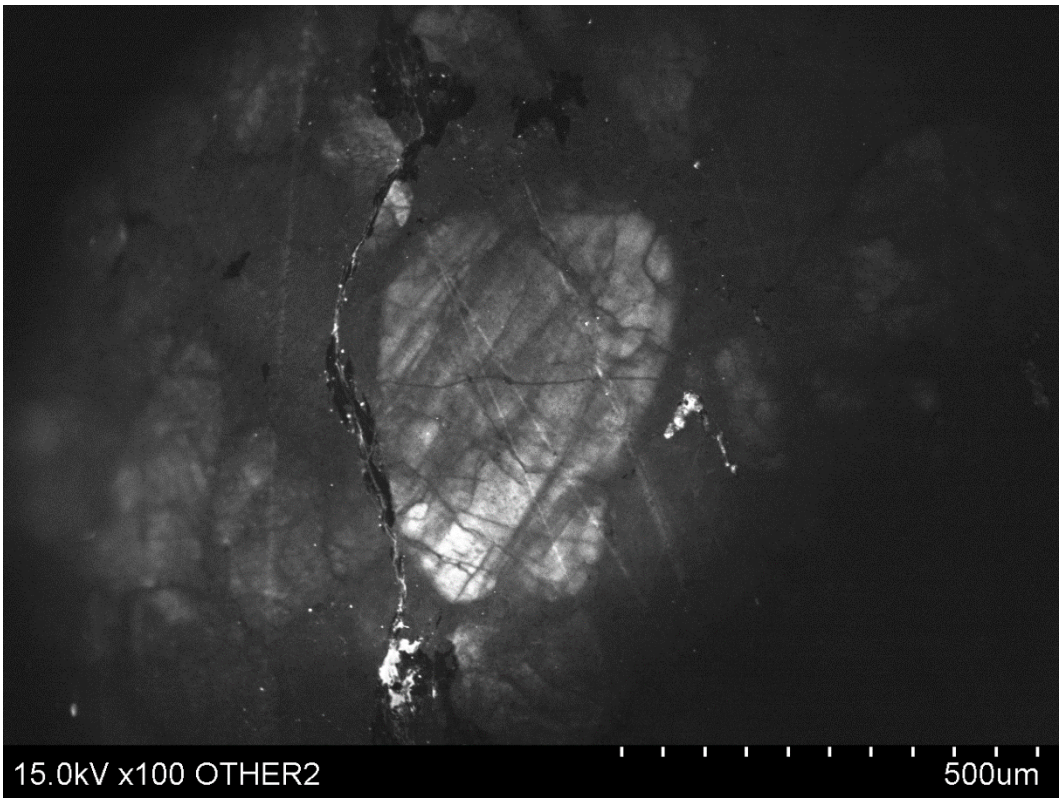

High-strain sample AI-08-06-Q11-18

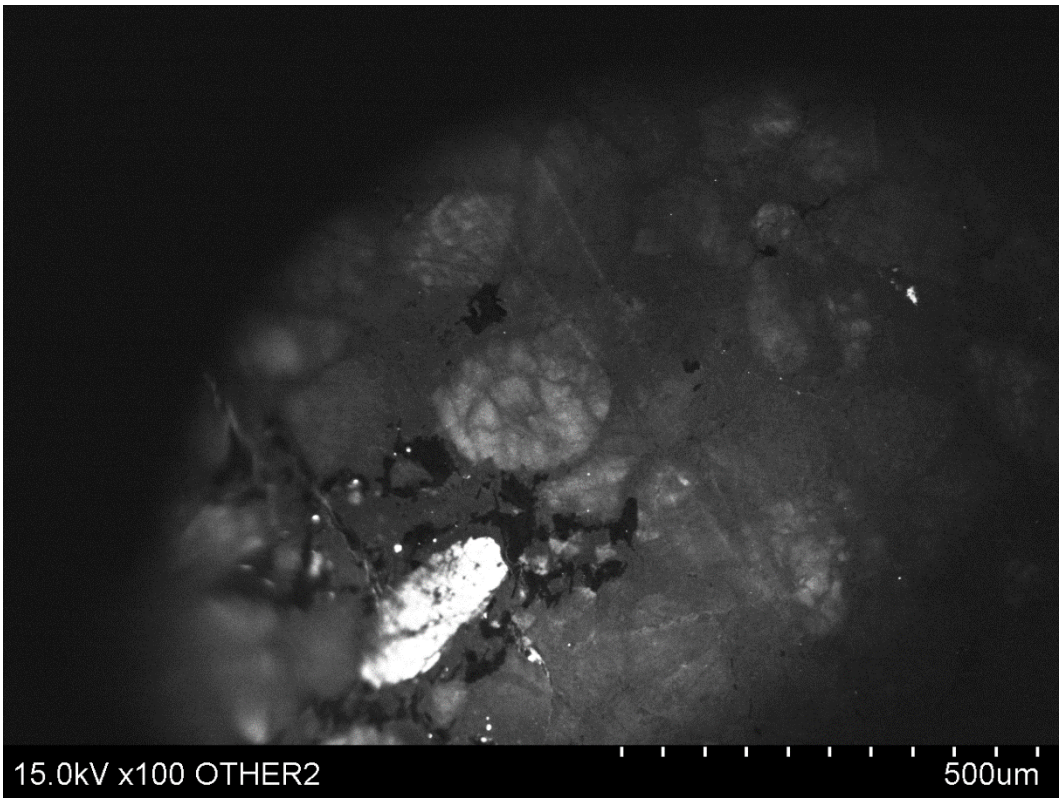

High-strain sample AI-08-06-Q11-19

High-strain sample AI-08-06-Q12

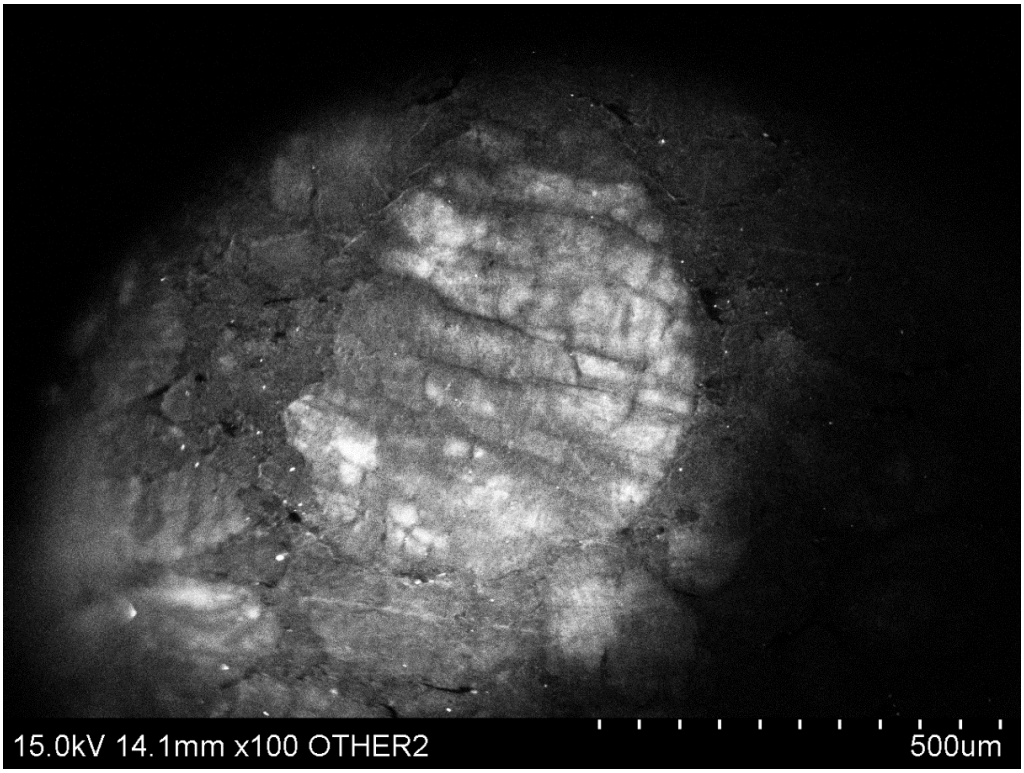

High-strain sample AI-08-06-Q12-1

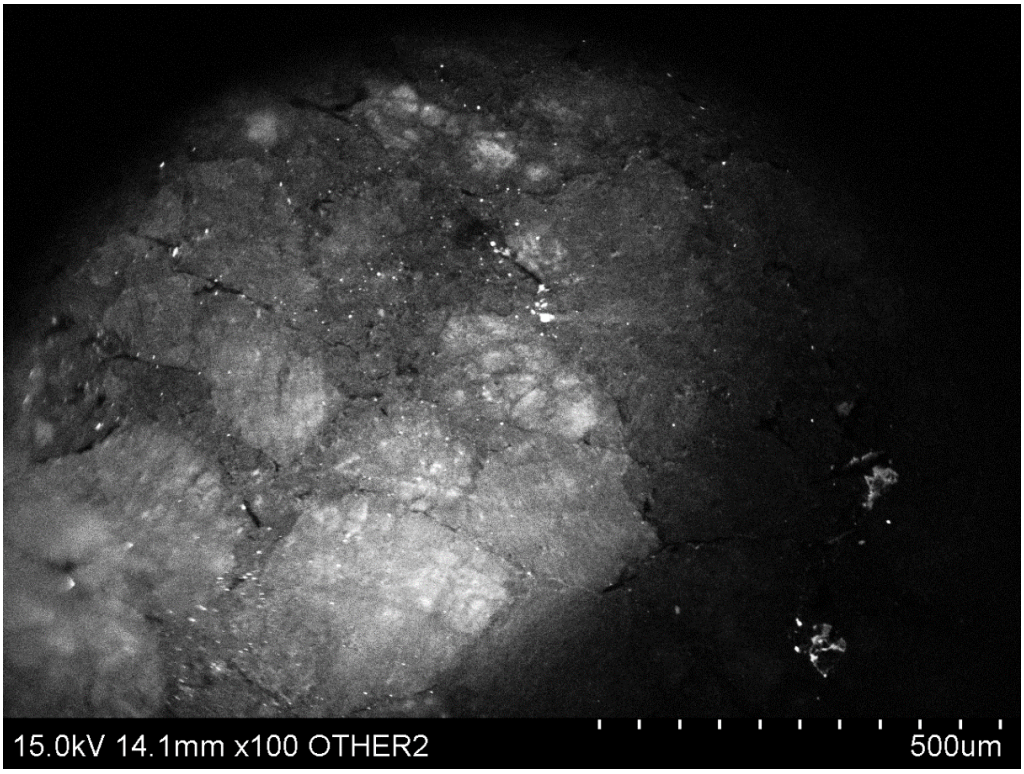

High-strain sample AI-08-06-Q12-2

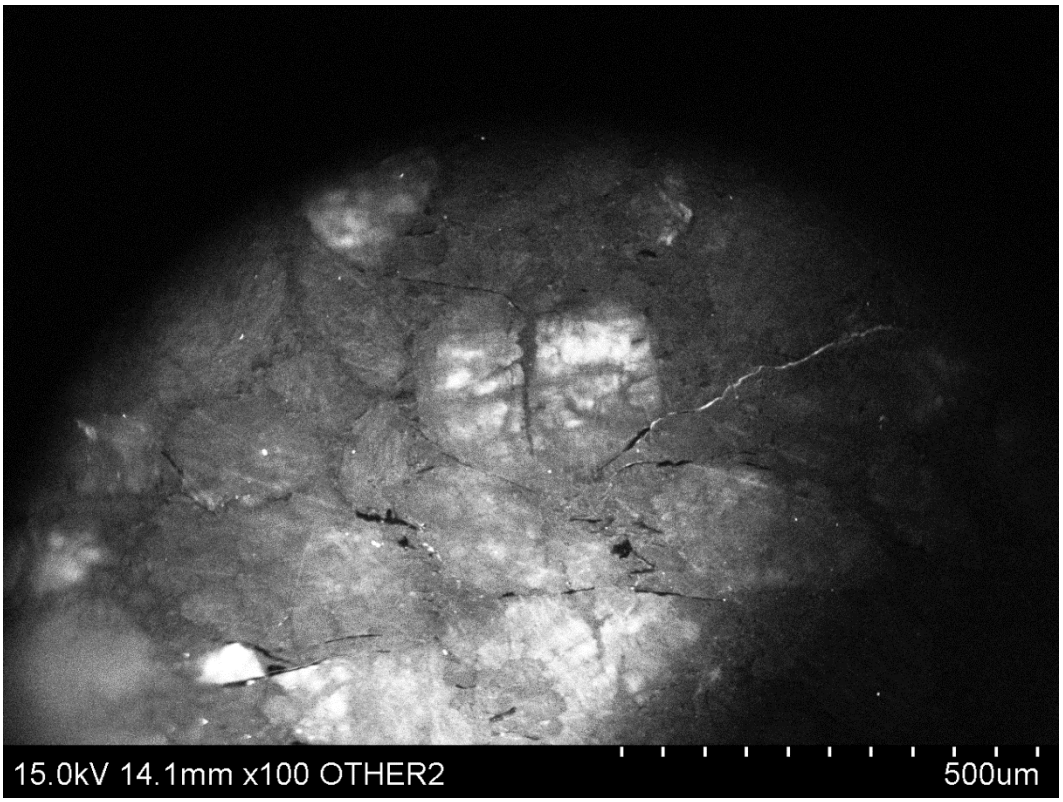

High-strain sample AI-08-06-Q12-3

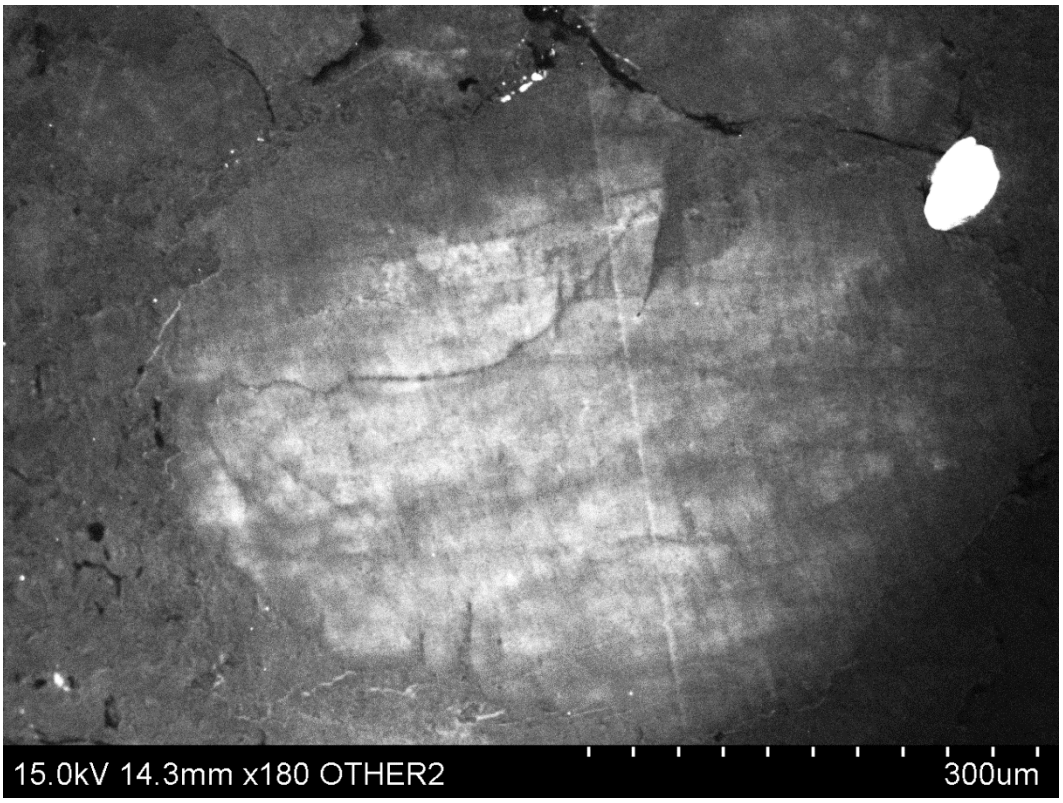

High-strain sample AI-08-06-Q12-4

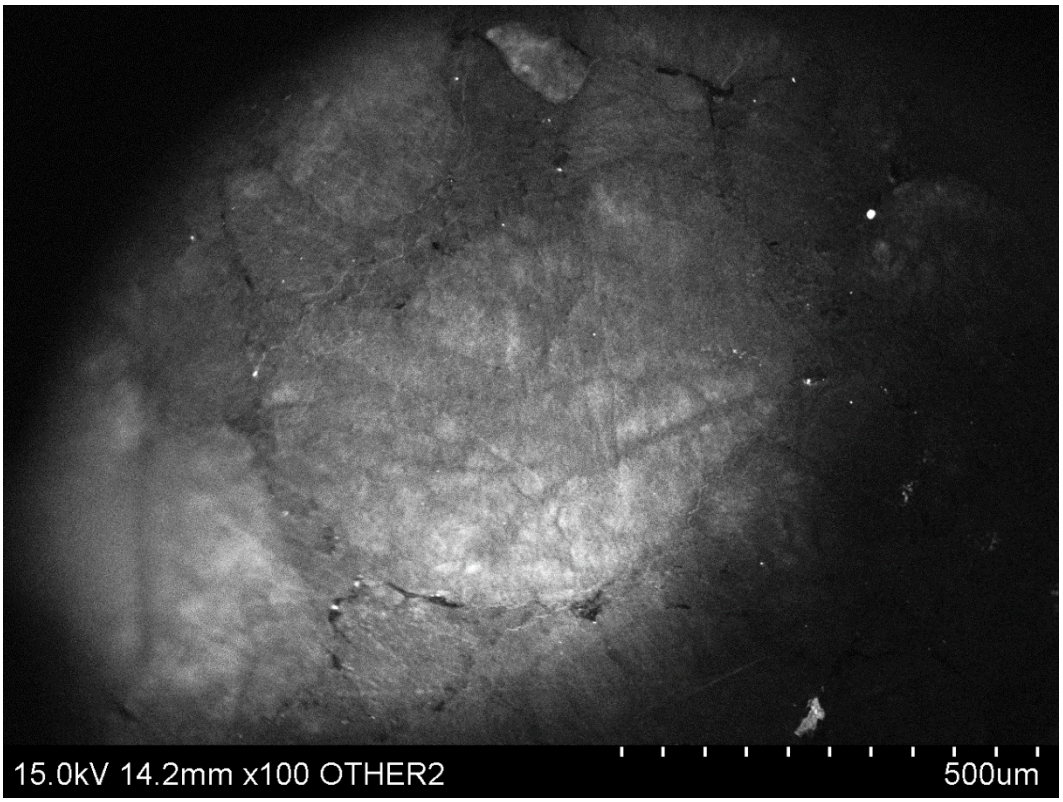

High-strain sample AI-08-06-Q12-5

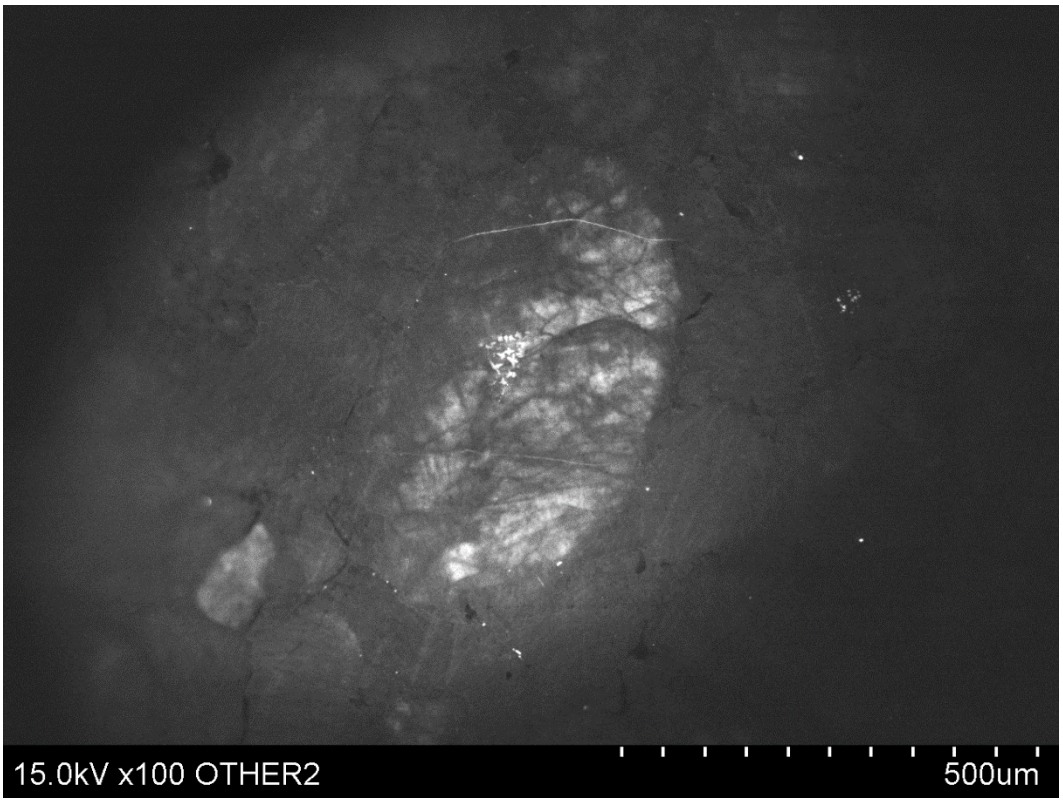

High-strain sample AI-08-06-Q12-6

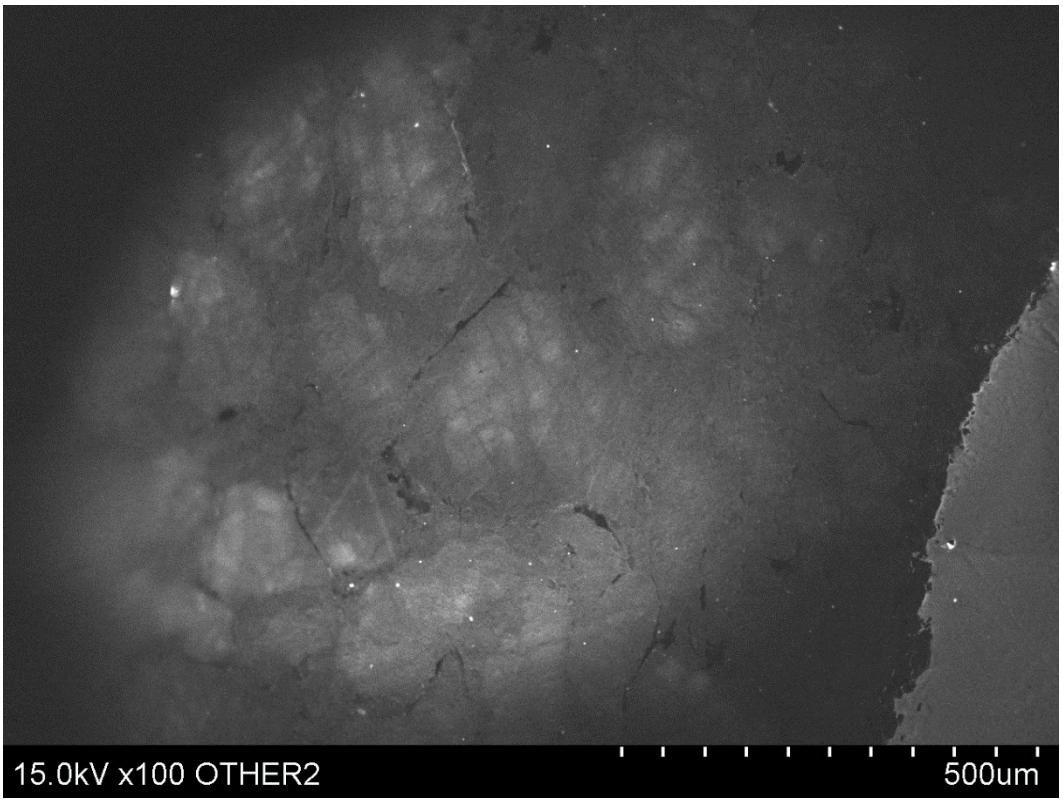

High-strain sample AI-08-06-Q12-7

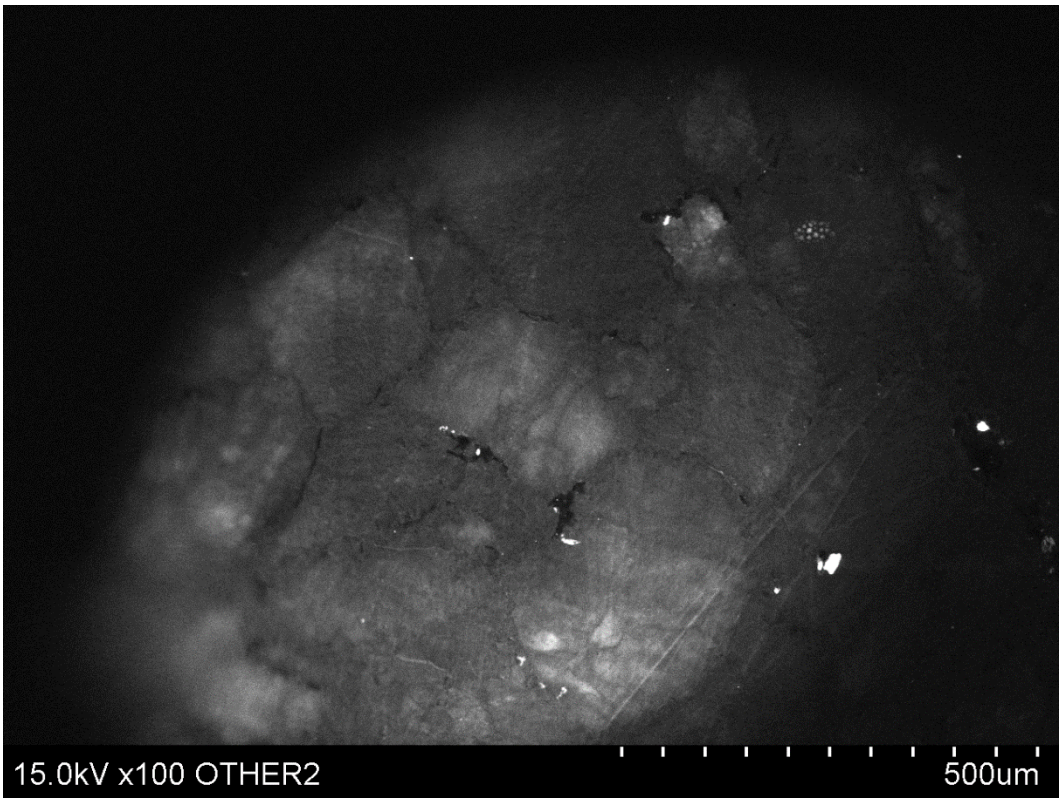

High-strain sample AI-08-06-Q12-8

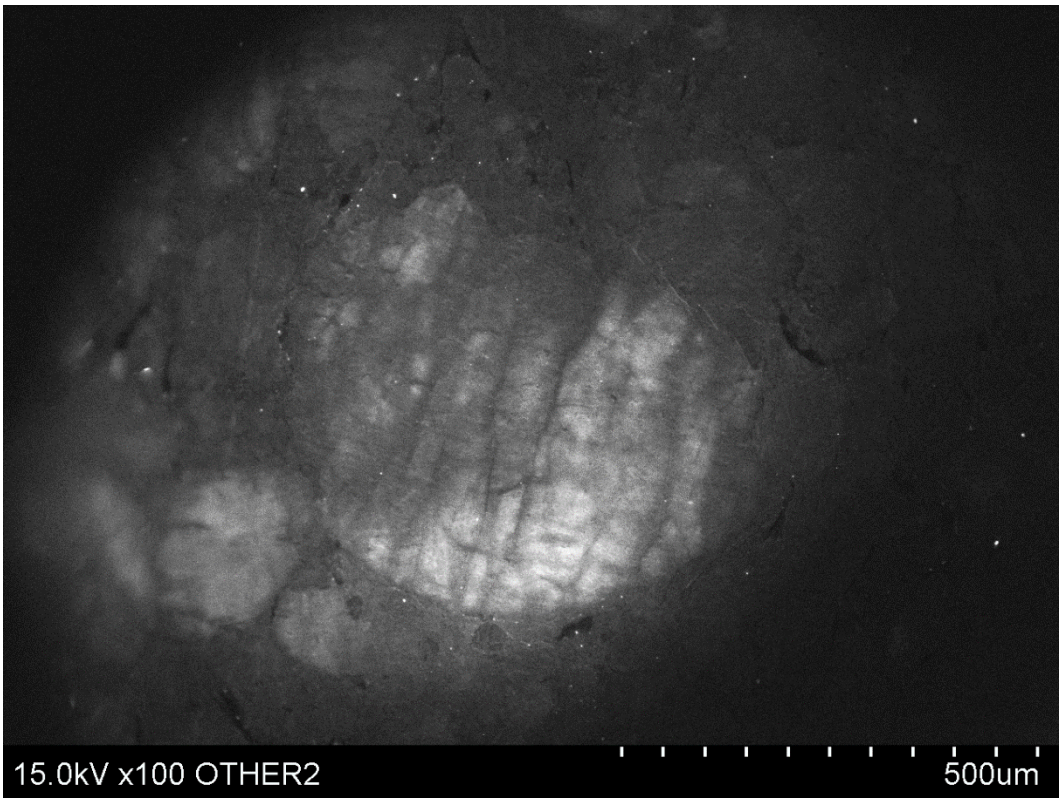

High-strain sample AI-08-06-Q12-9

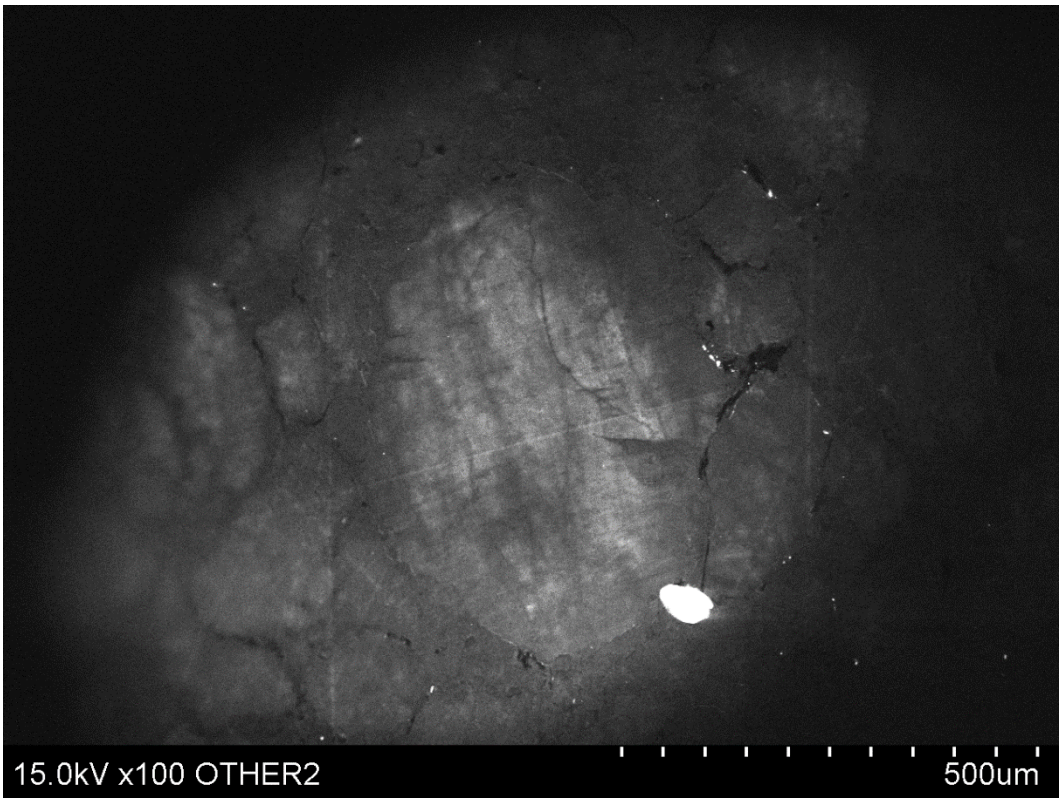

High-strain sample AI-08-06-Q12-10

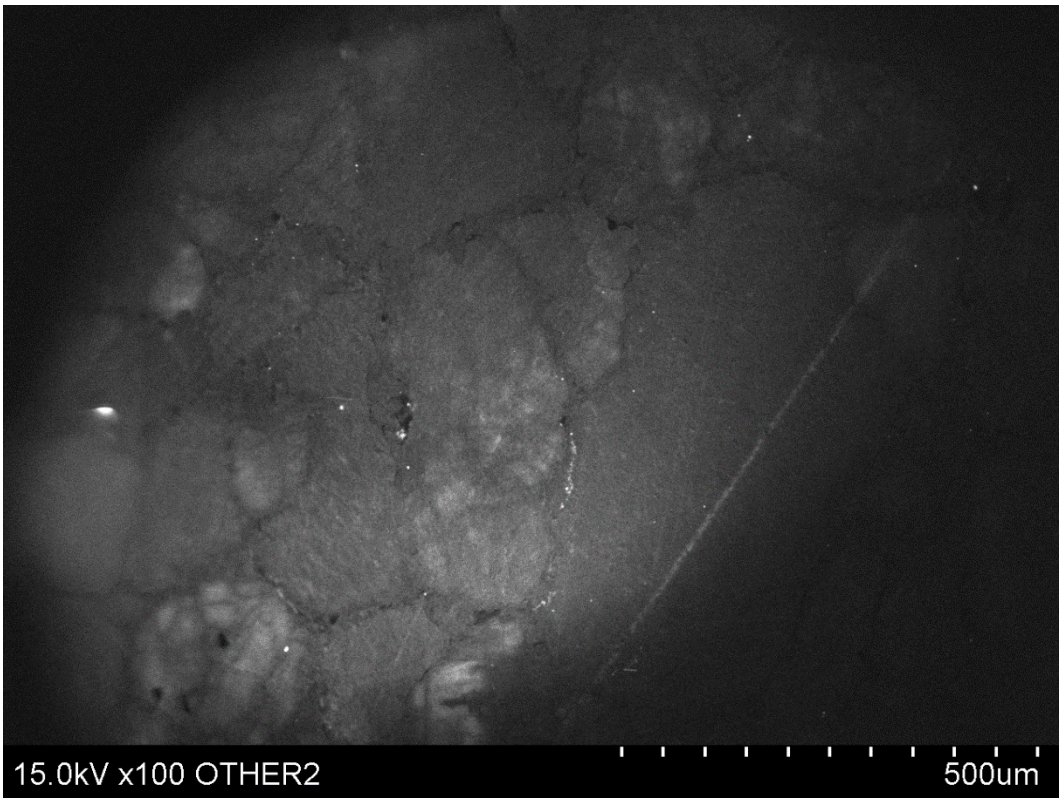

High-strain sample AI-08-06-Q12-11

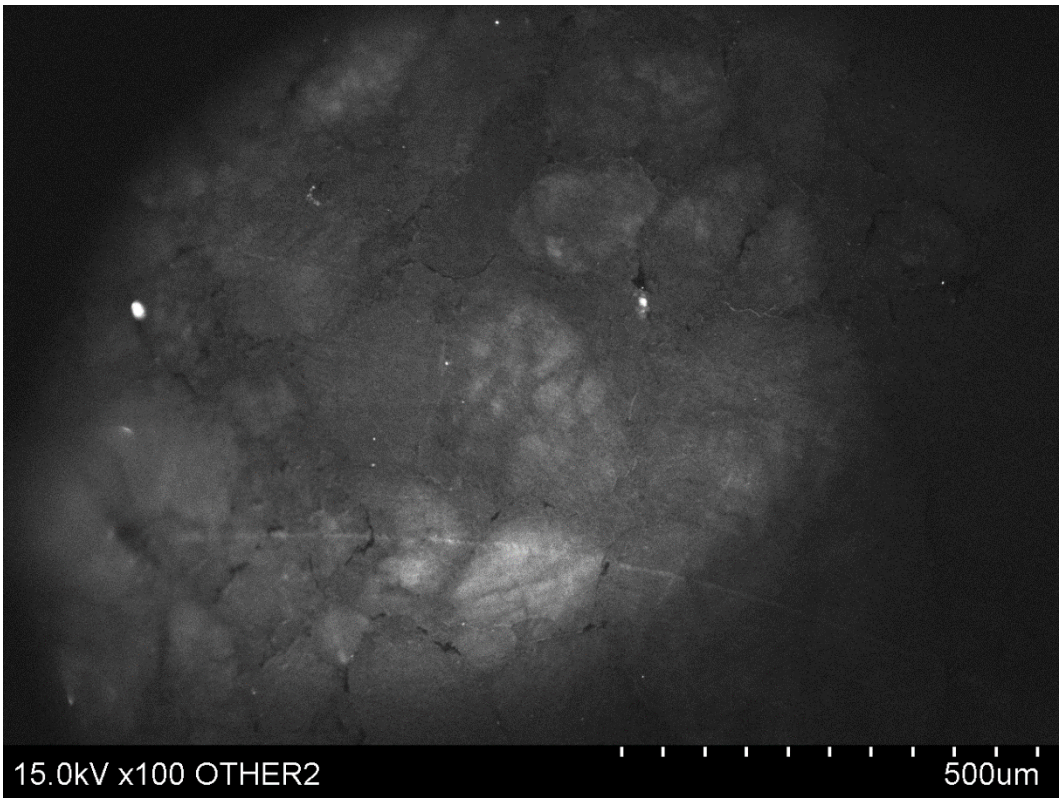

High-strain sample AI-08-06-Q12-12

High-strain sample AI-08-06-Q13

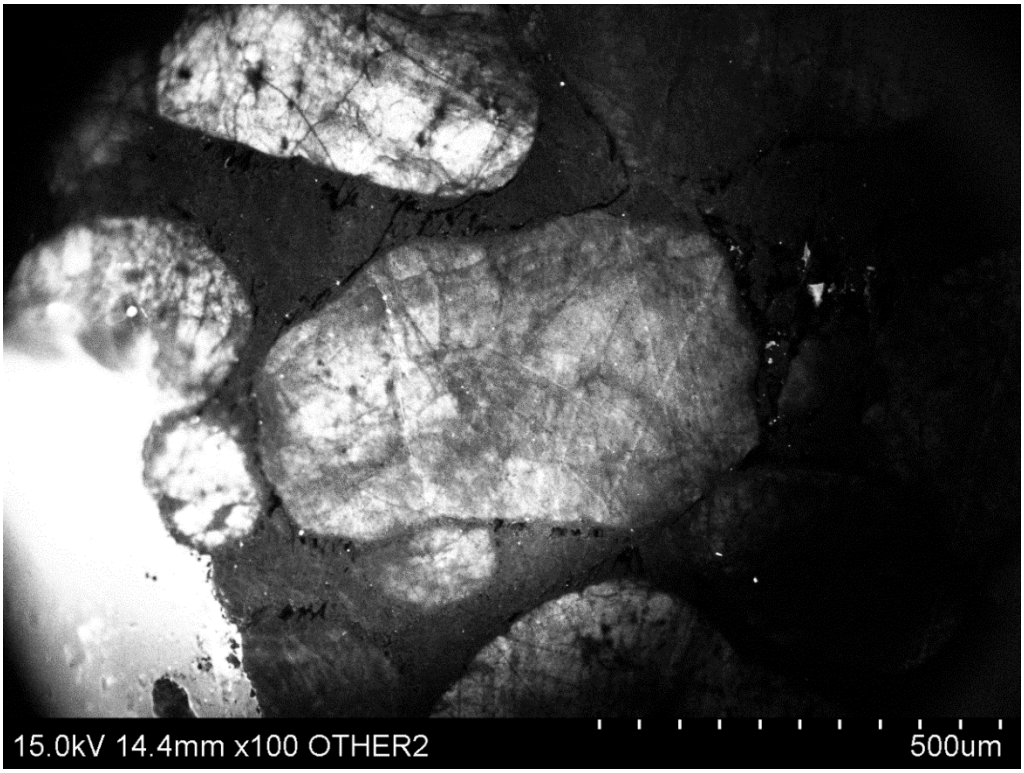

High-strain sample AI-08-06-Q13-1

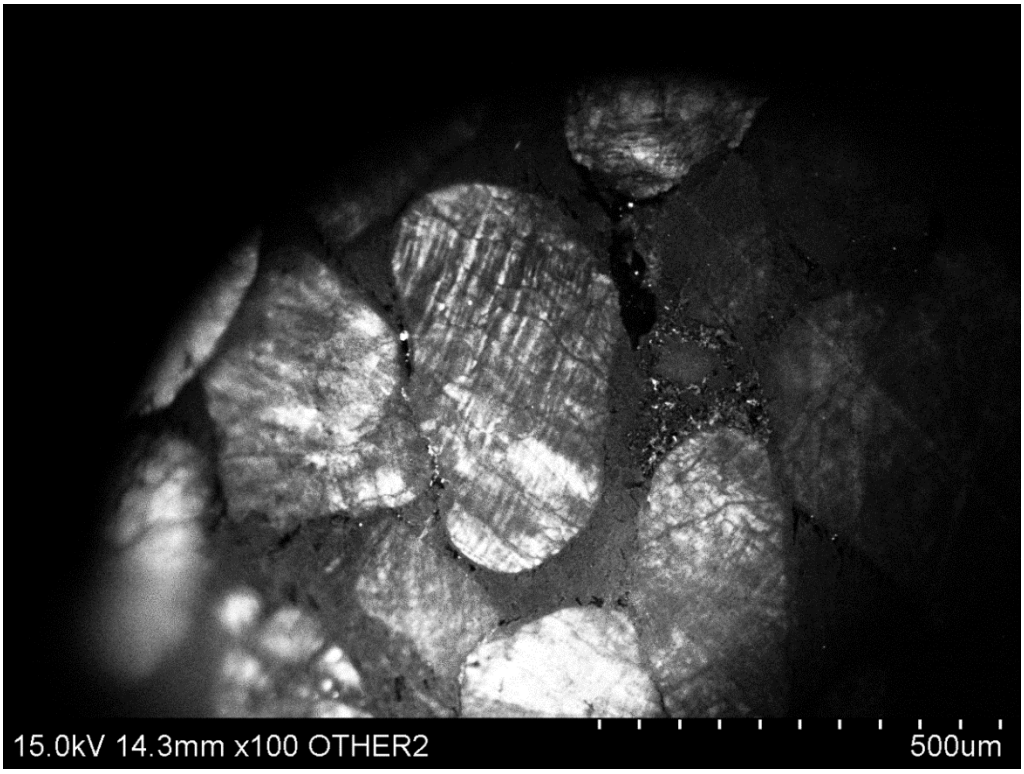

High-strain sample AI-08-06-Q13-2

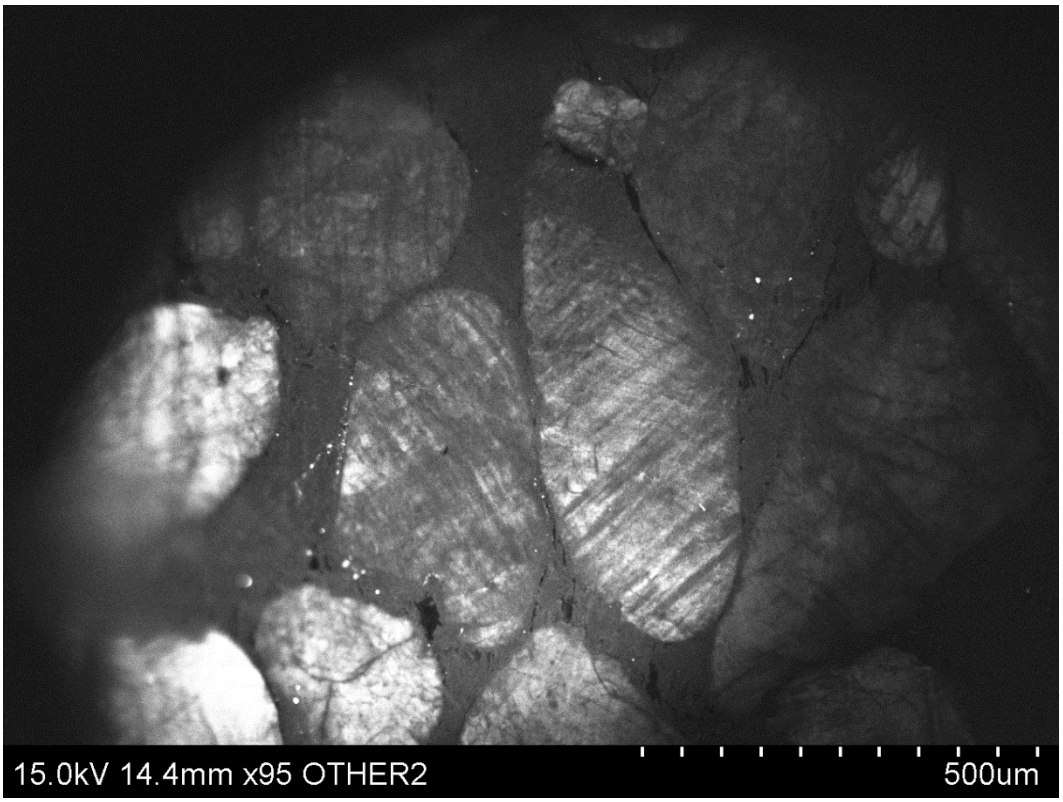

High-strain sample AI-08-06-Q13-3

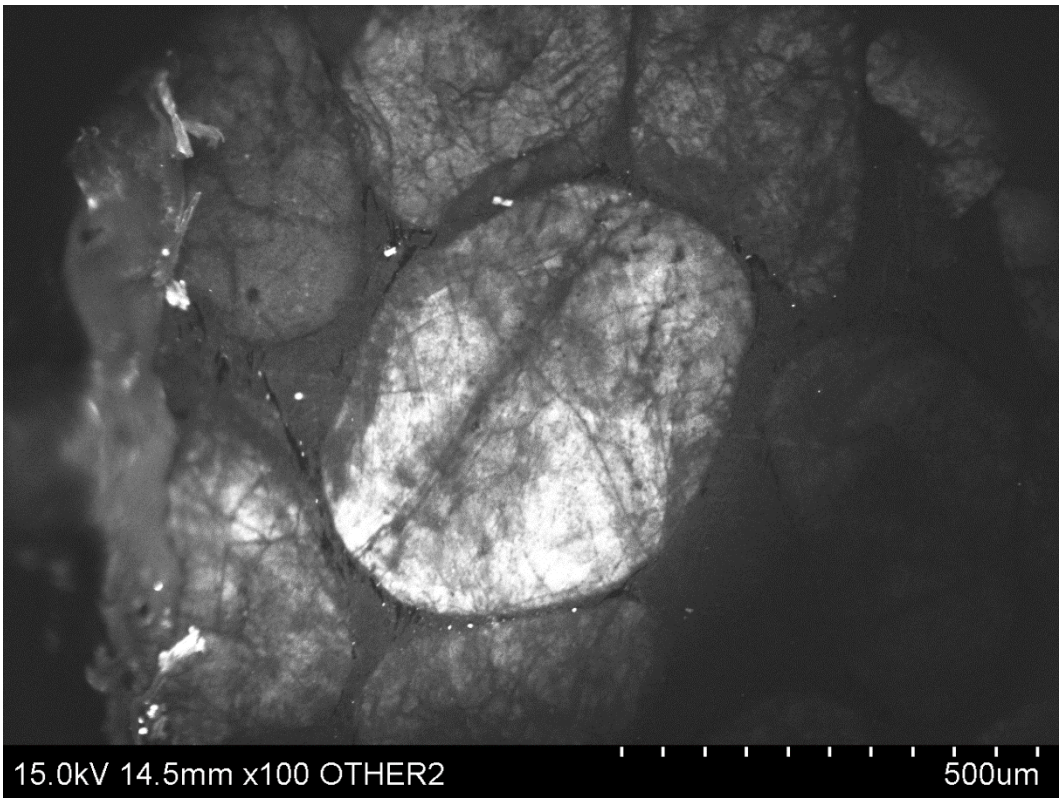

High-strain sample AI-08-06-Q13-4

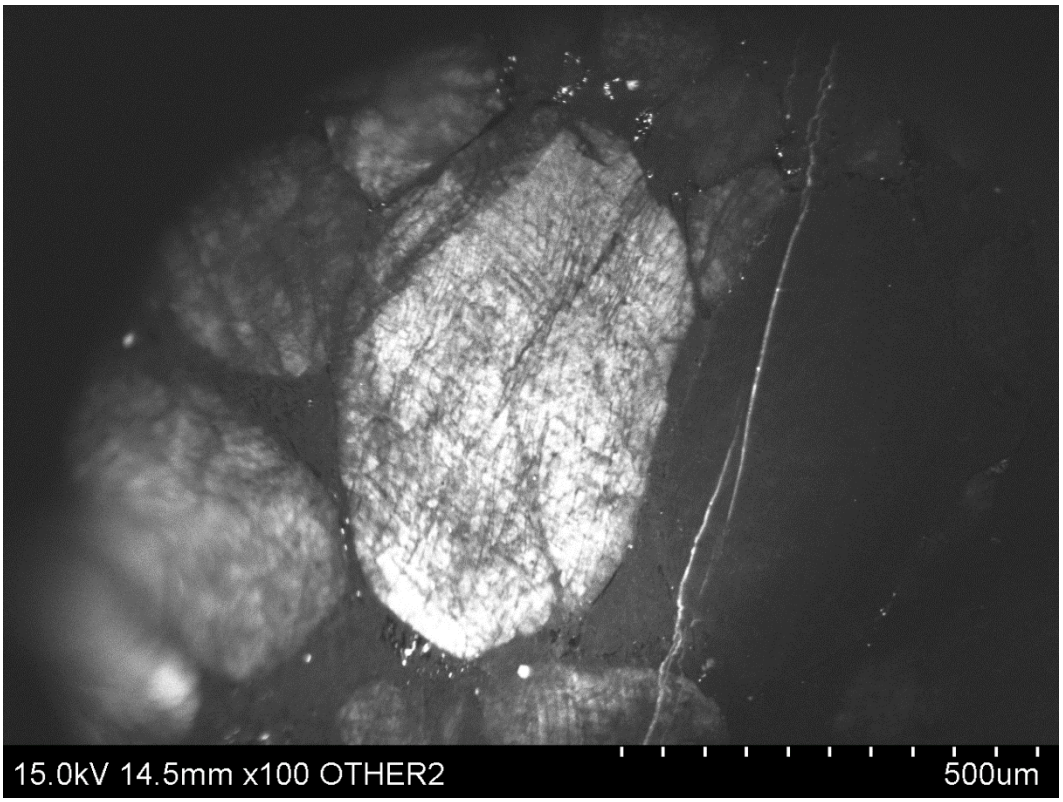

High-strain sample AI-08-06-Q13-5

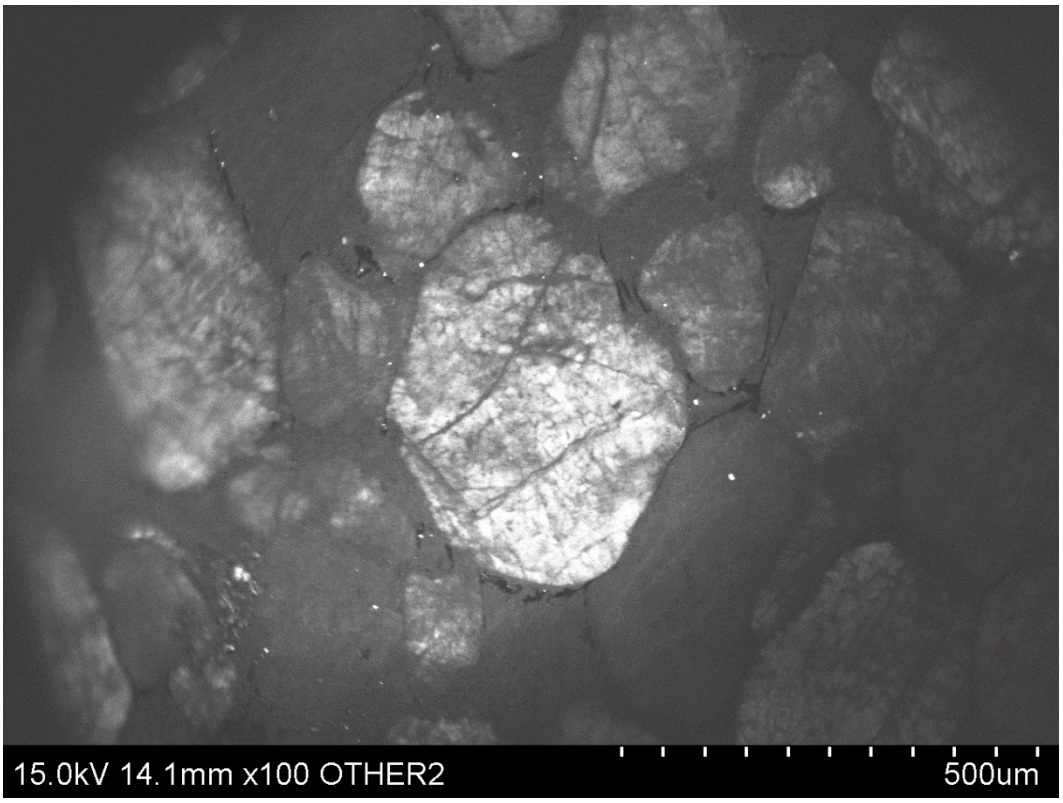

High-strain sample AI-08-06-Q13-6

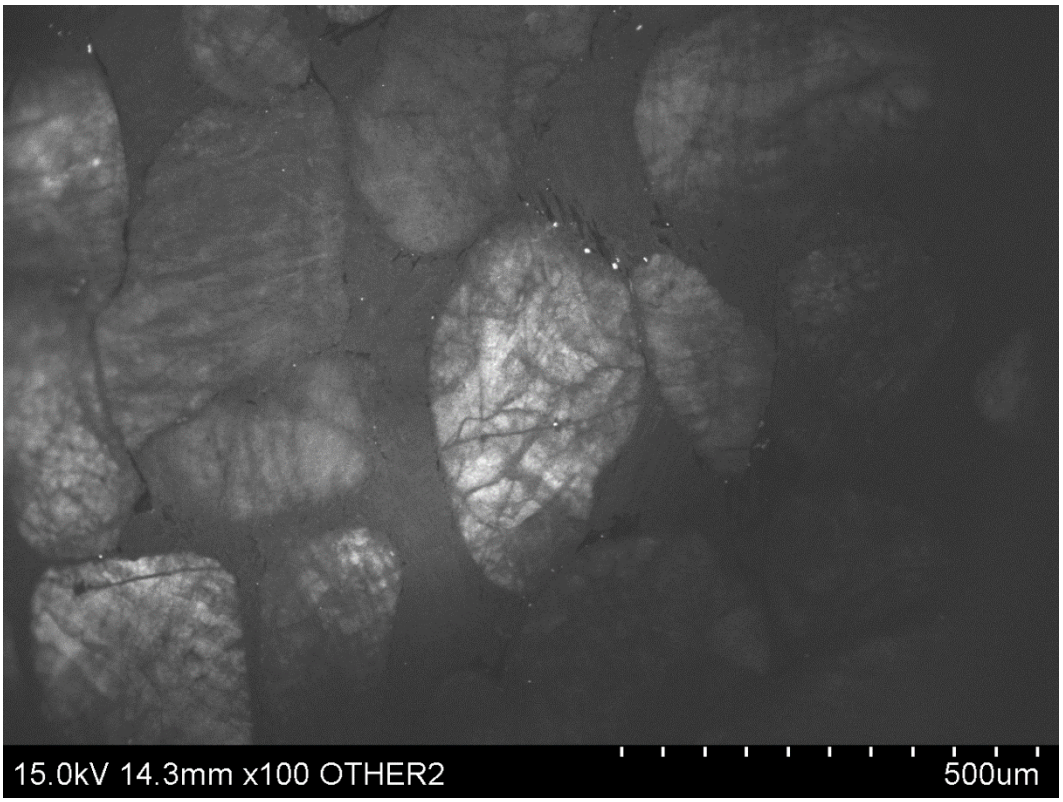

High-strain sample AI-08-06-Q13-7

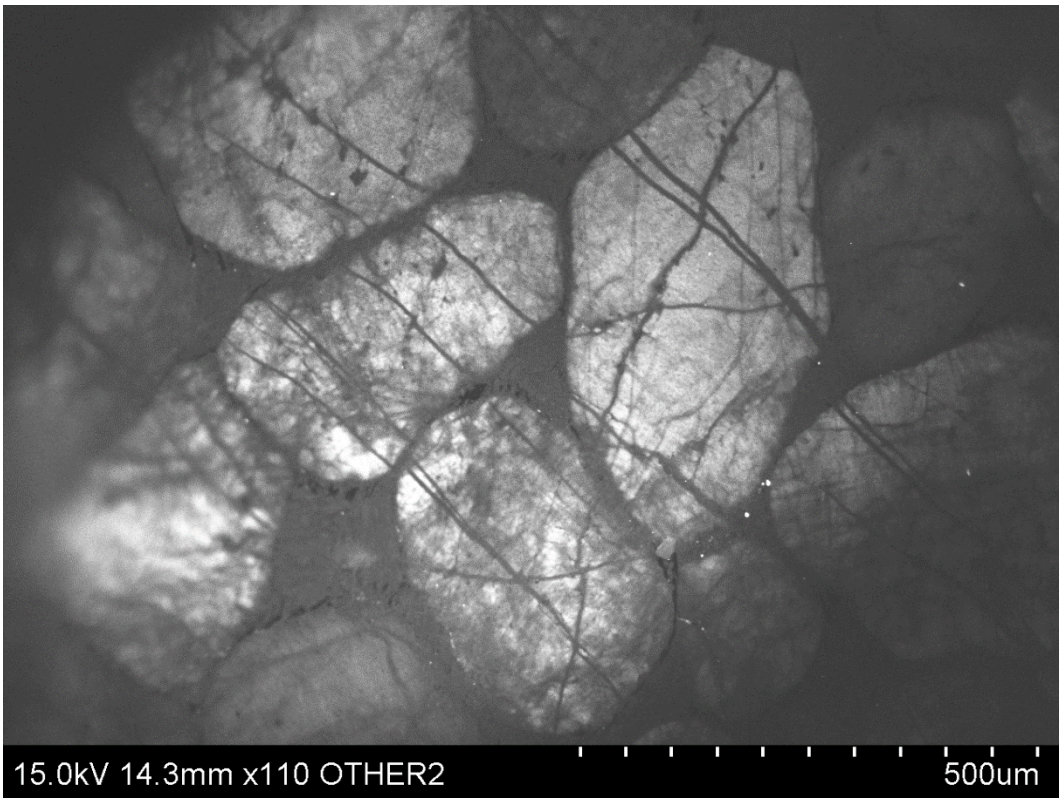

High-strain sample AI-08-06-Q13-8

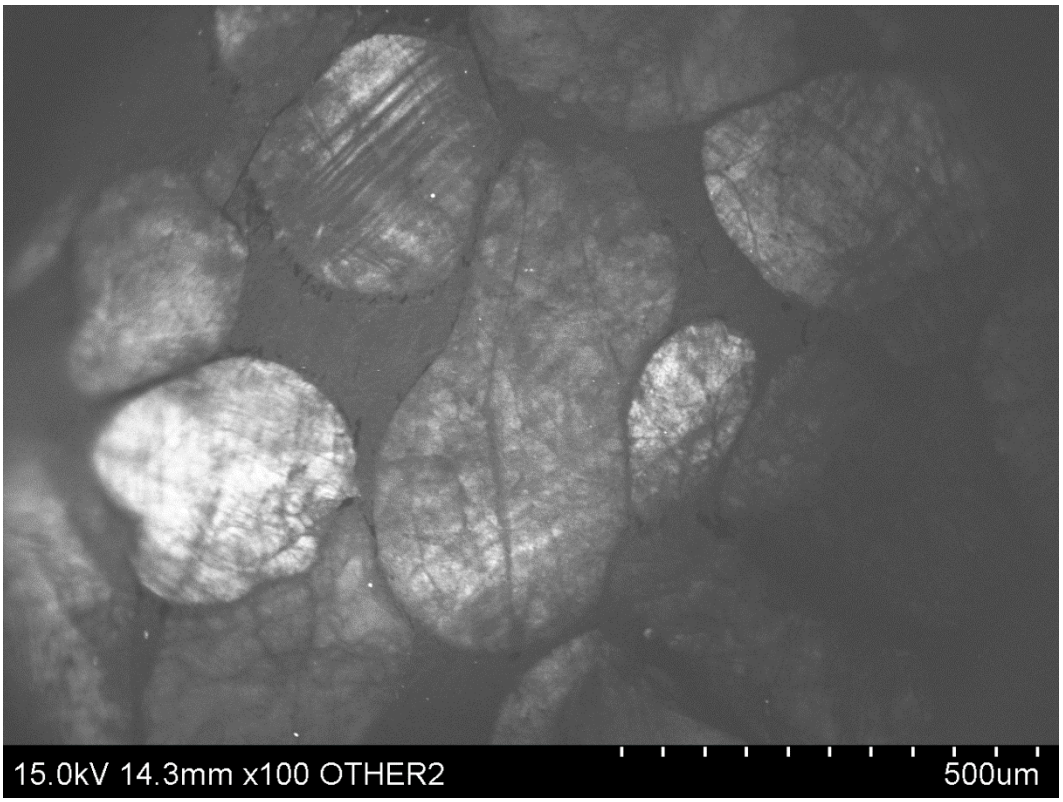

High-strain sample AI-08-06-Q13-9

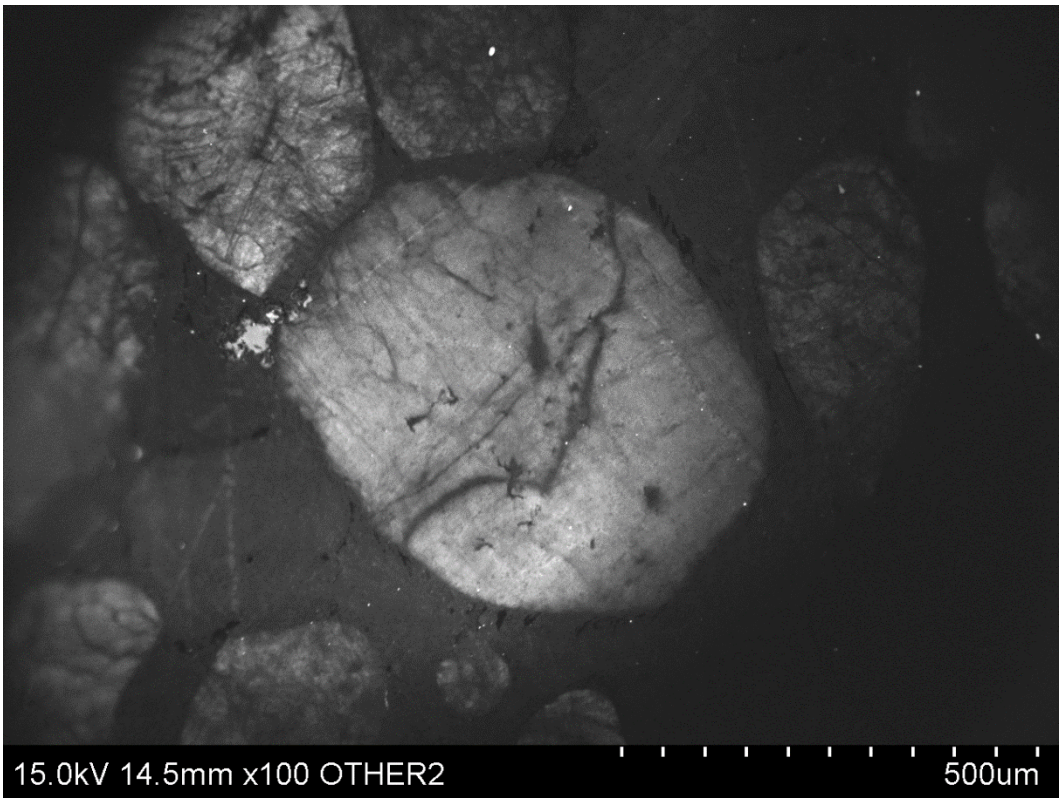

High-strain sample AI-08-06-Q13-10

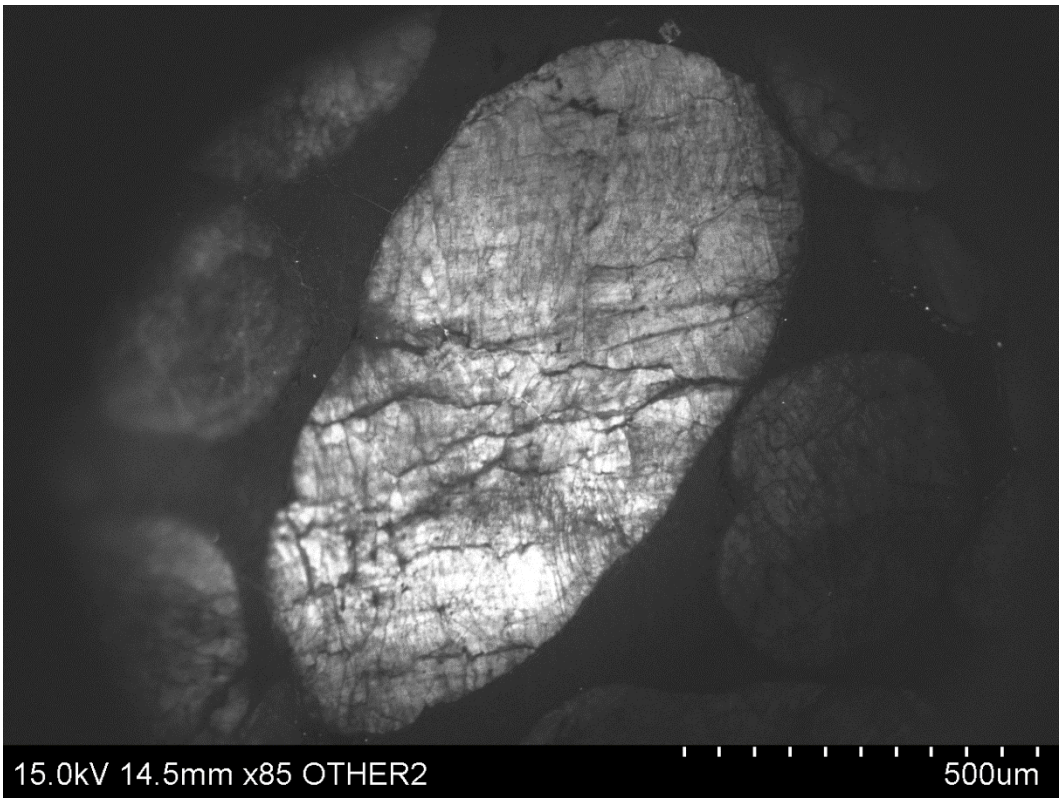

High-strain sample AI-08-06-Q13-11

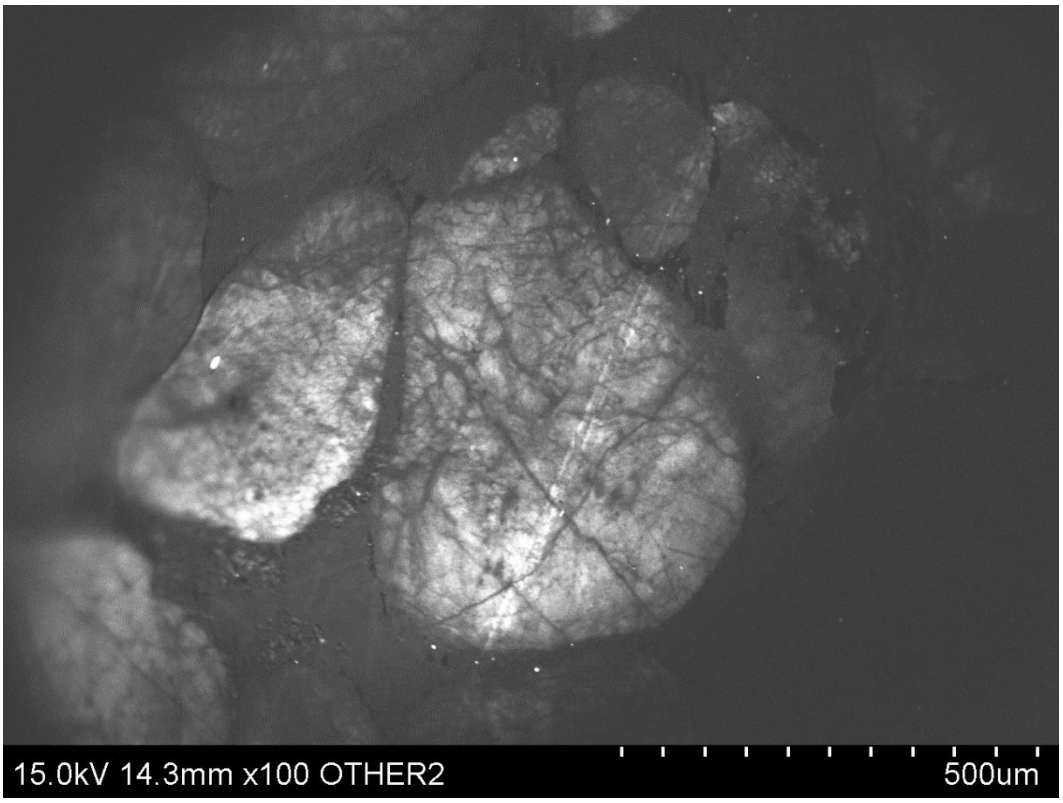

High-strain sample AI-08-06-Q13-12

Appendix B: Additional FTIR Data

Medium-strain sample AI-08-03-Q12-5

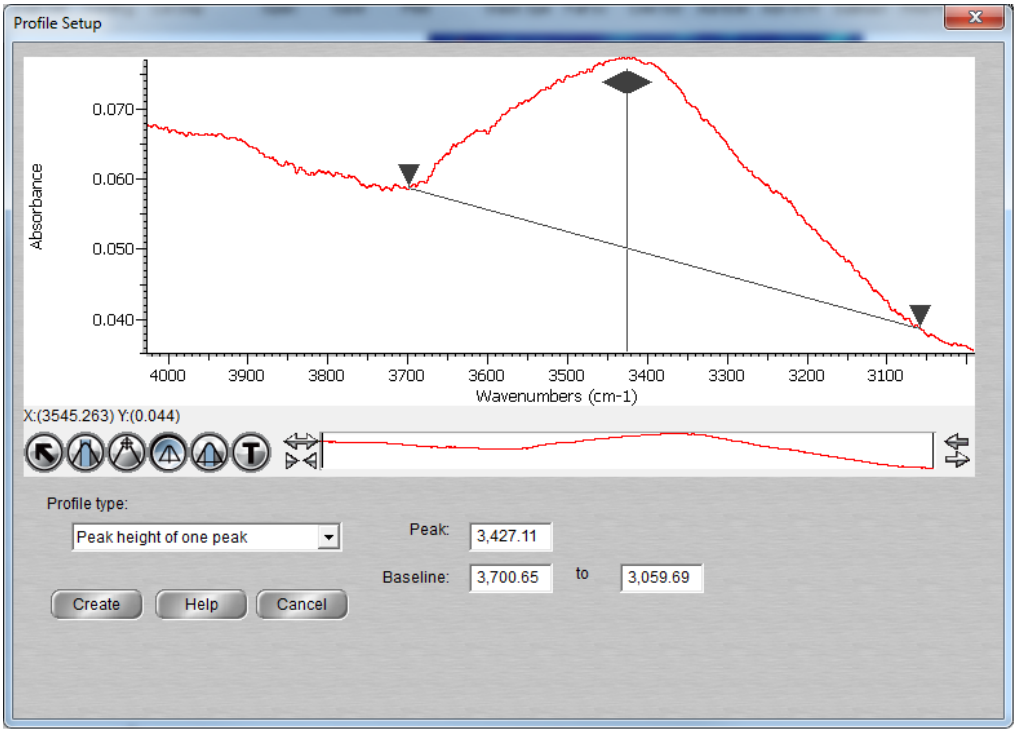

Peak height function used on 3427 cm^{-1} wavelength.

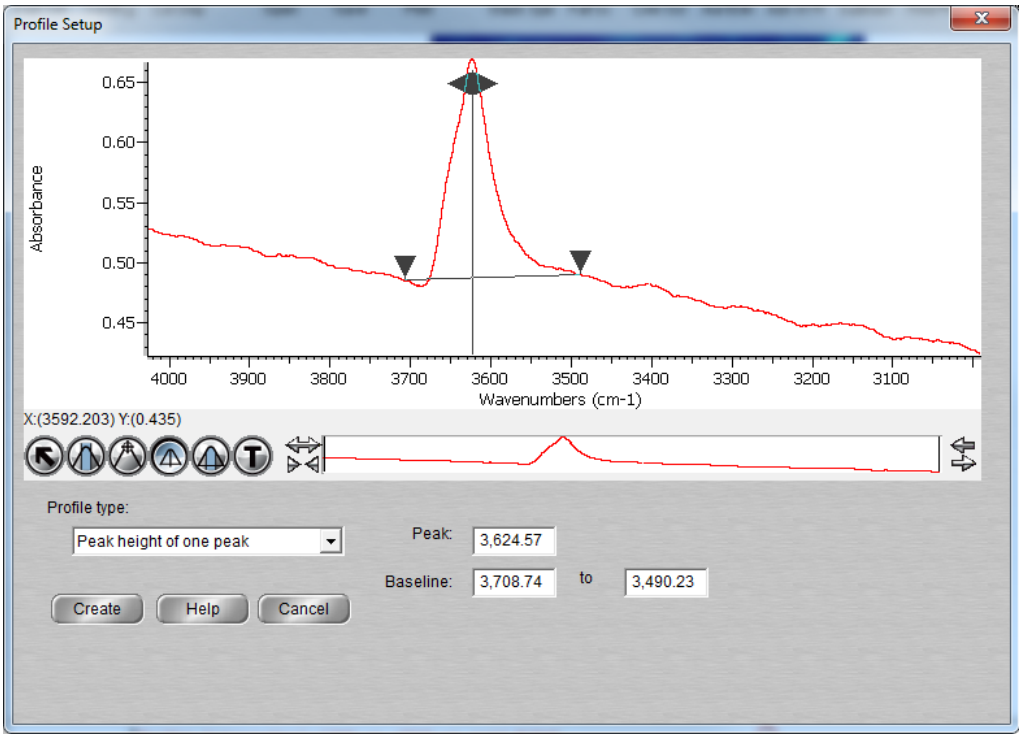

Peak height function used on 3624 cm^{-1} wavelength.

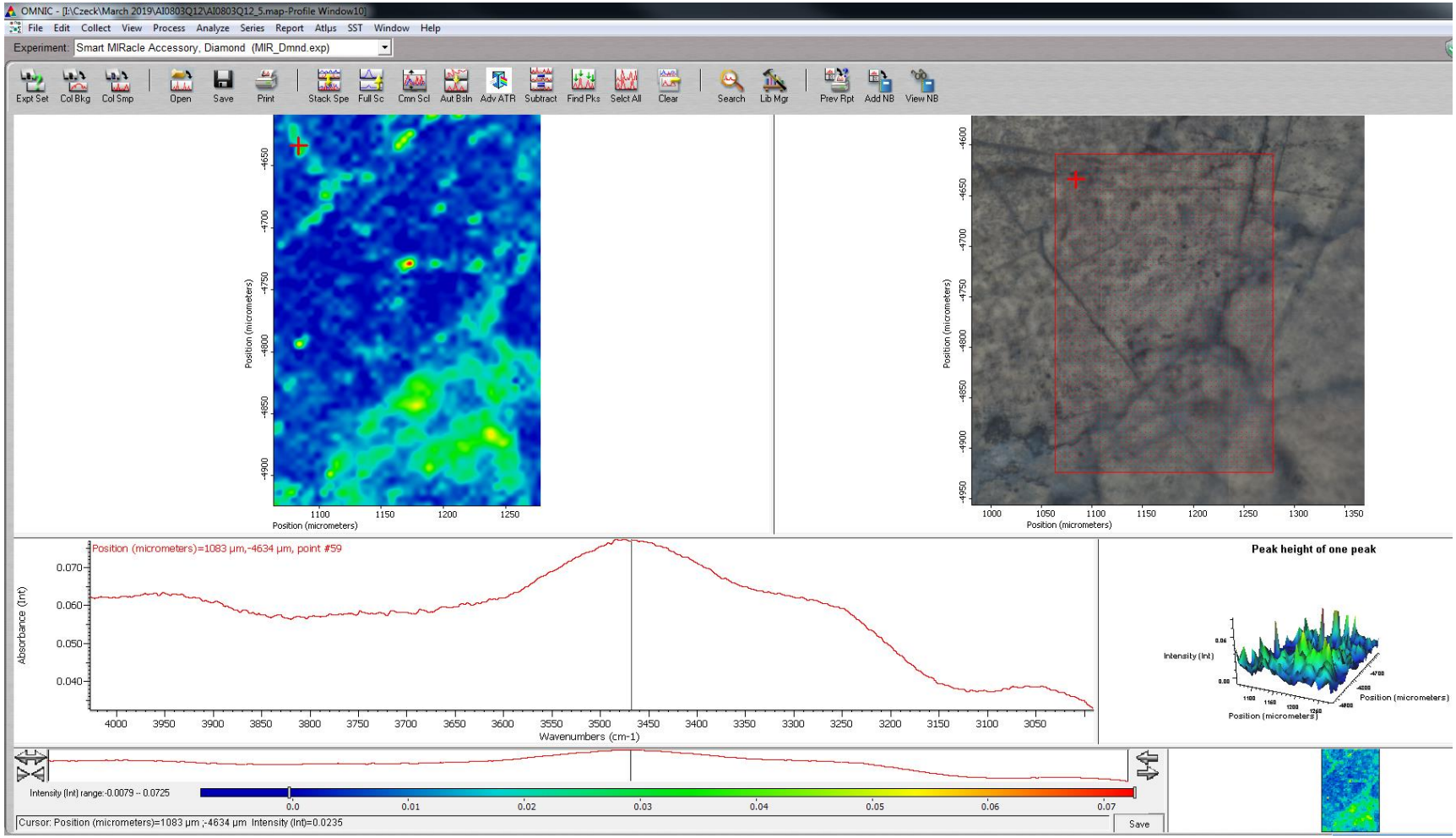

Sample AI-08-03-Q12-5 absorption map with peak height function run for 3427 cm^{-1} wavelength. 2816 total spectra collected. Intensity range adjustments shown at bottom.

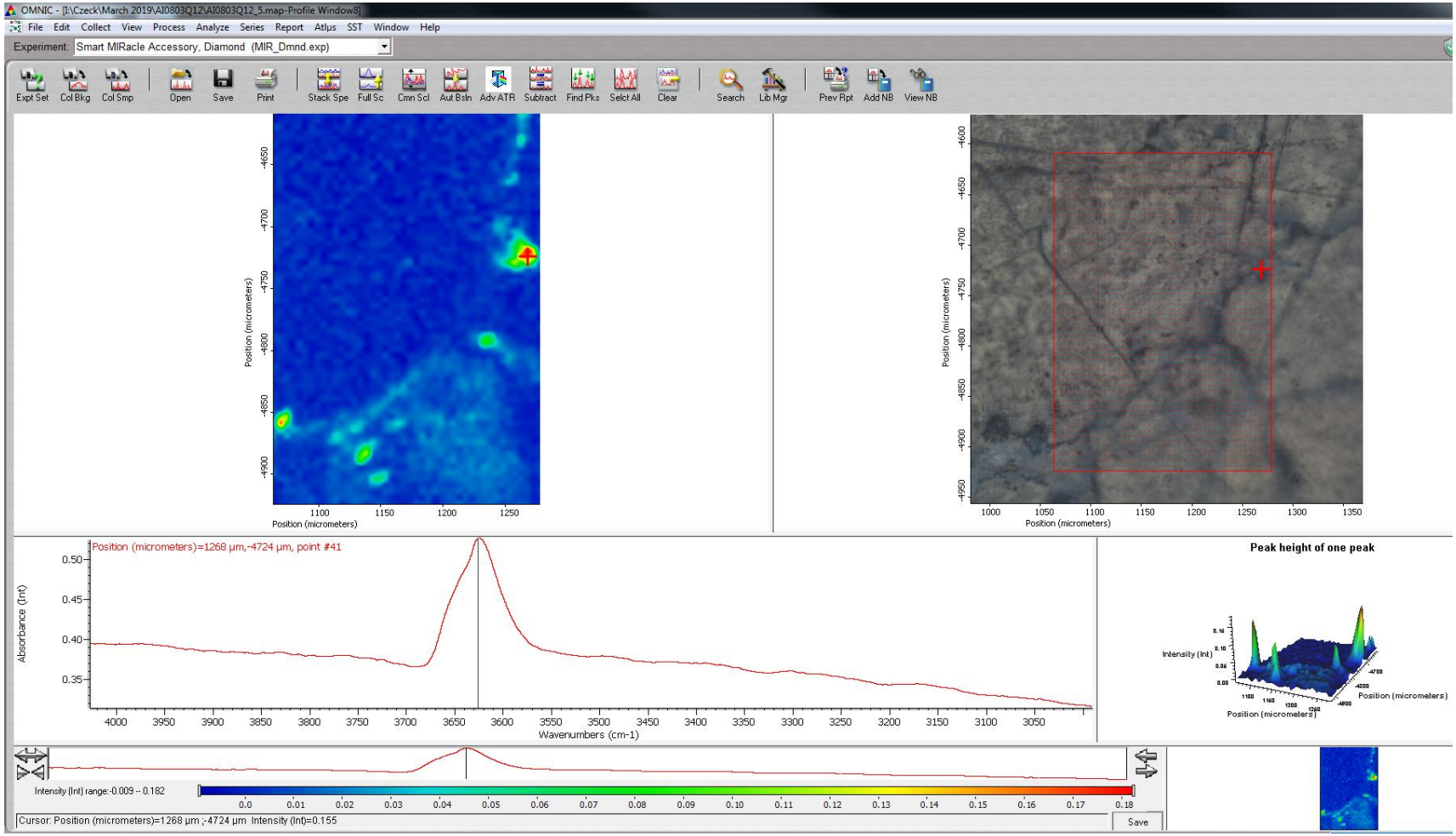

Sample AI-08-03-Q12-5 absorption map with peak height function run for 3624 cm^{-1} wavelength. 2816 total spectra collected. Intensity range adjustments shown at bottom.

Medium-strain sample AI-08-02-Q12-1

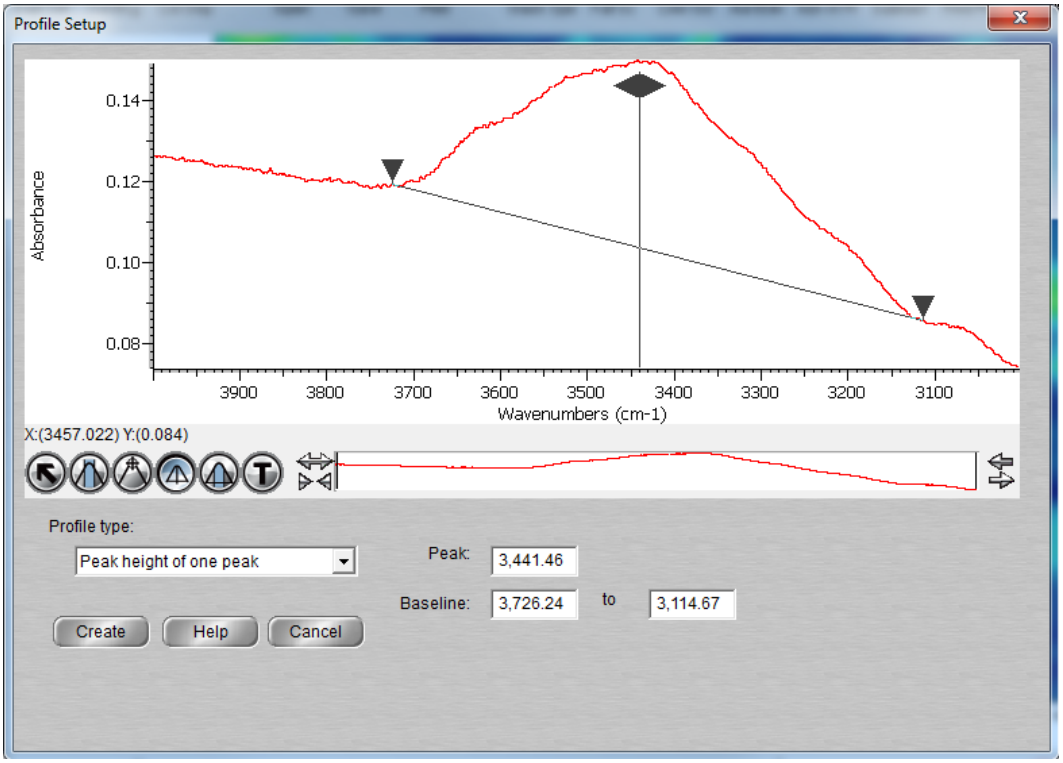

Peak height function used on 3441 cm^{-1} wavelength.

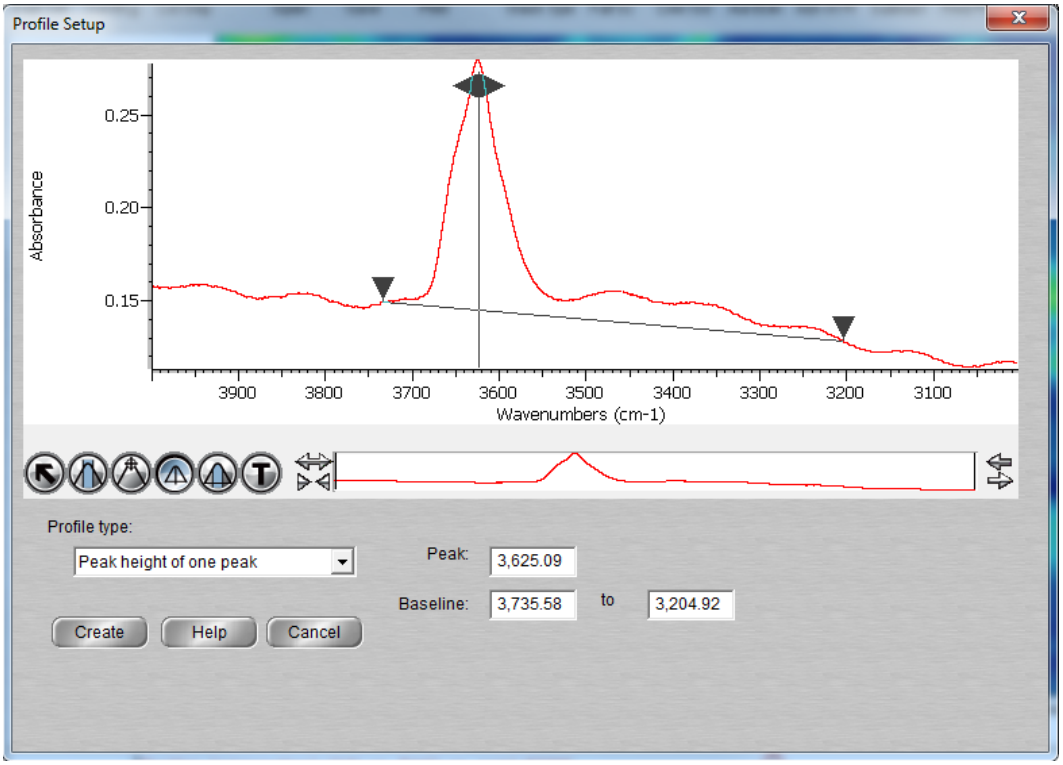

Peak height function used on 3625 cm^{-1} wavelength.

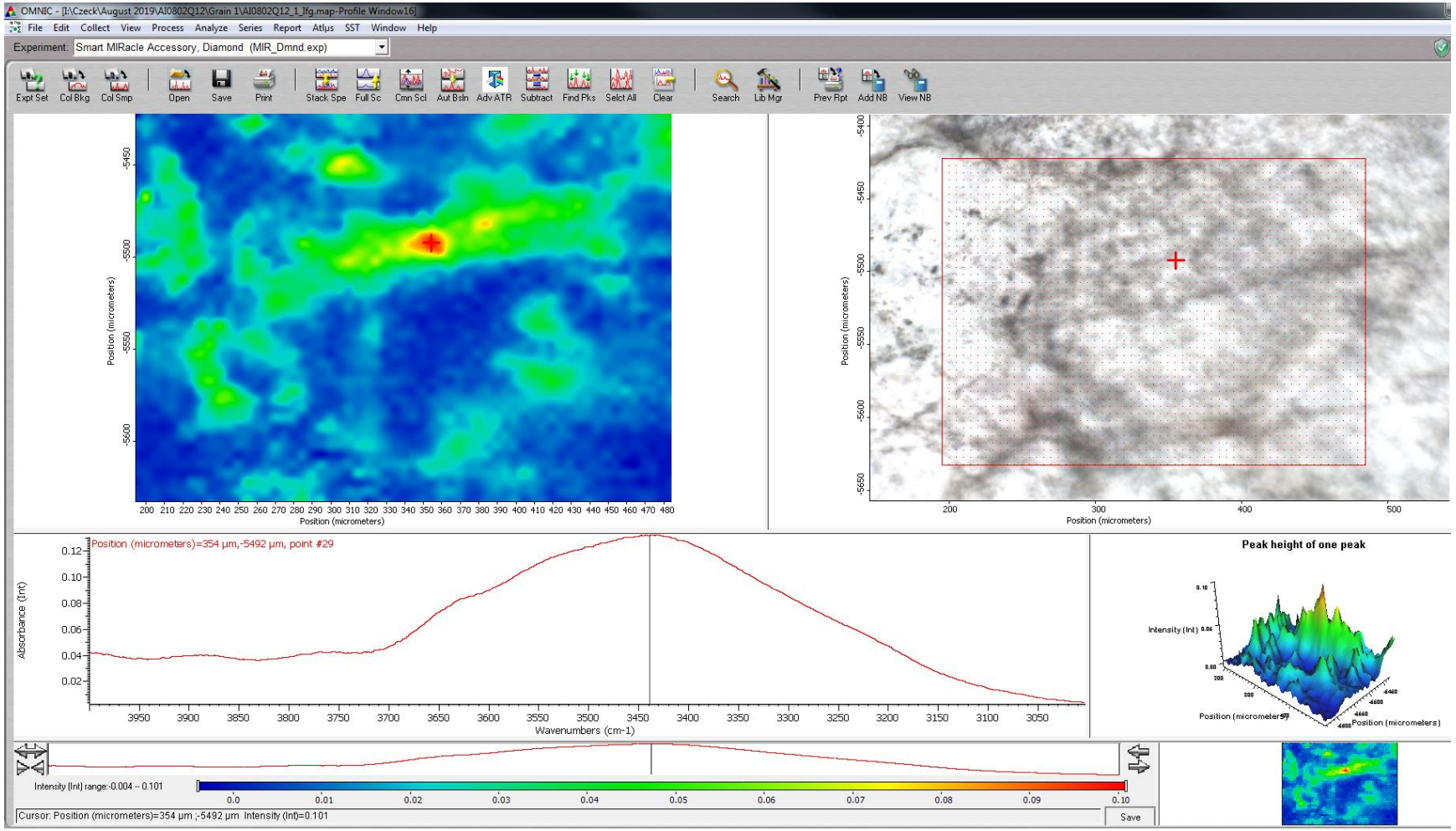

Sample AI-08-02-Q12-1 absorption map with peak height function run for 3427 cm^{-1} wavelength. 2537 total spectra collected. Intensity range adjustments shown at bottom.

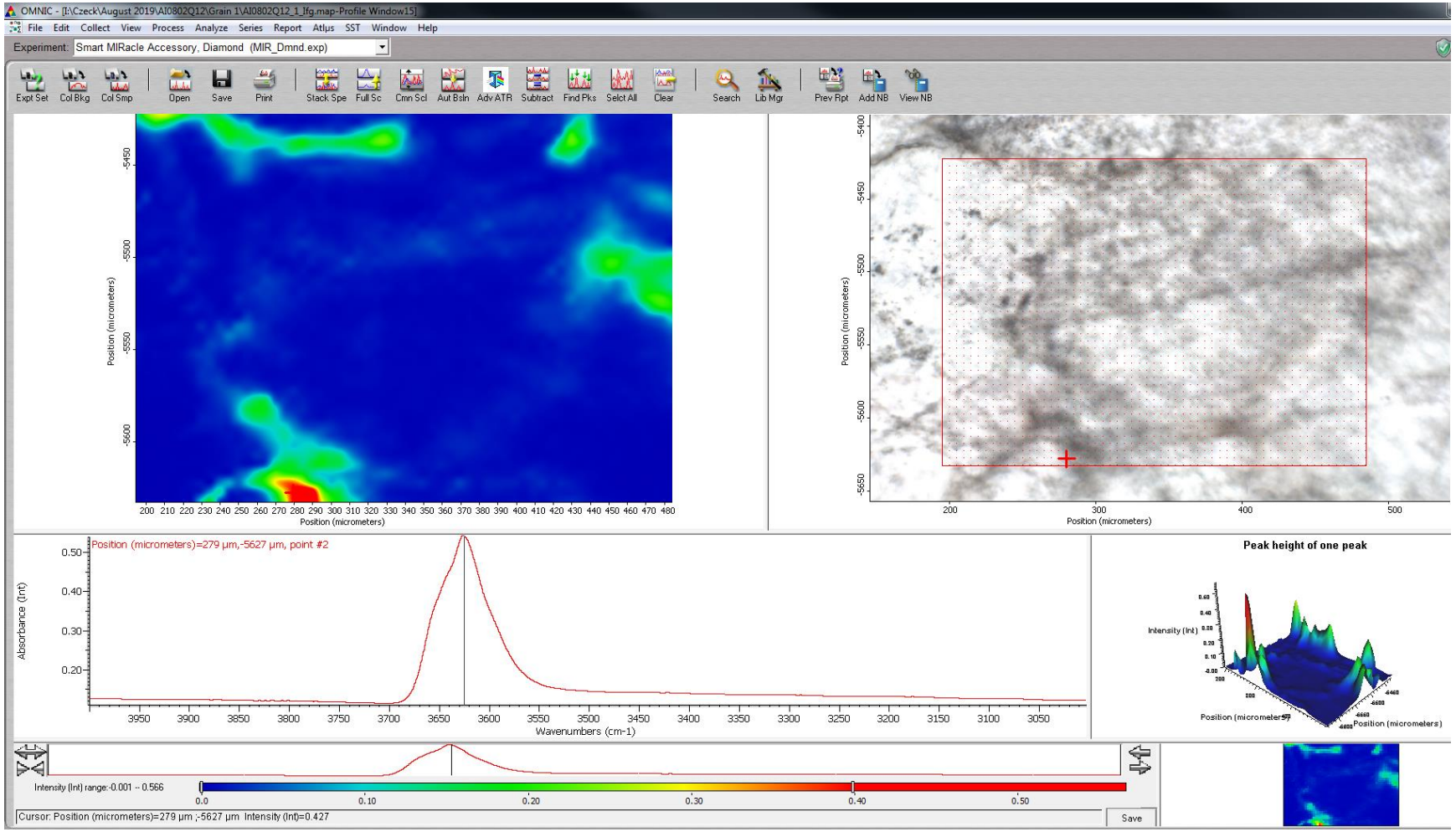

Sample AI-08-02-Q12-1 absorption map with peak height function run for 3625 cm^{-1} wavelength. 2537 total spectra collected. Intensity range adjustments shown at bottom.

Medium-strain sample AI-08-02-Q12-2, 1st run

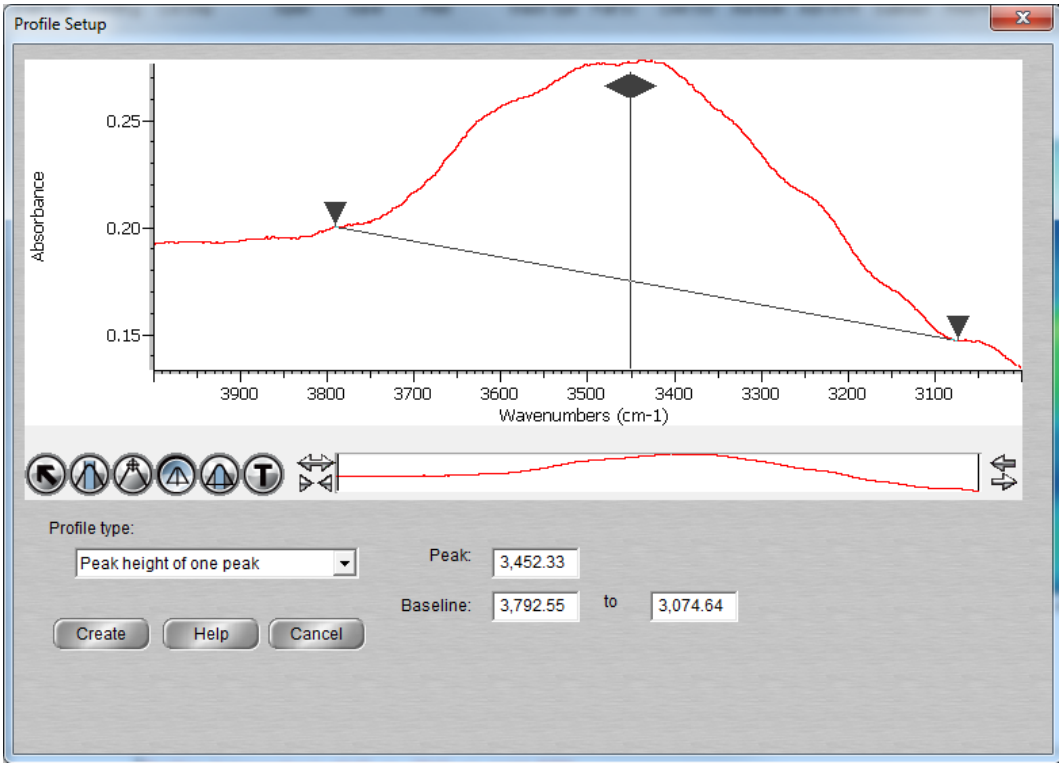

Peak height function used on 3452 cm^{-1} wavelength.

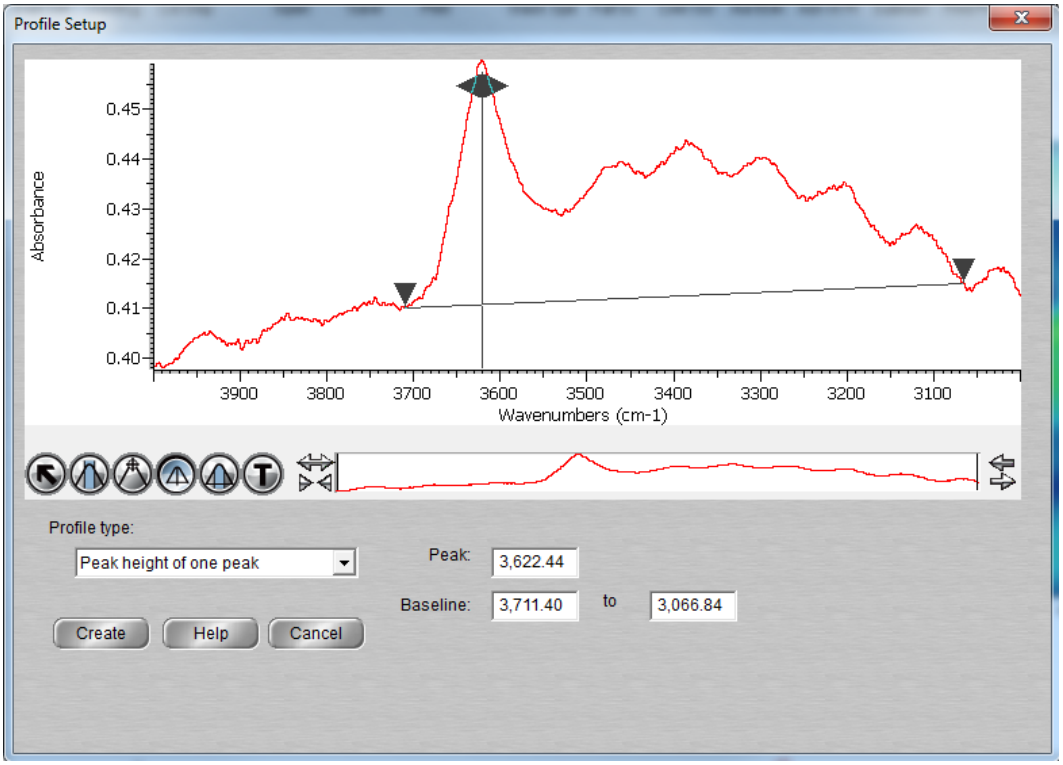

Peak height function used on 3622 cm^{-1} wavelength.

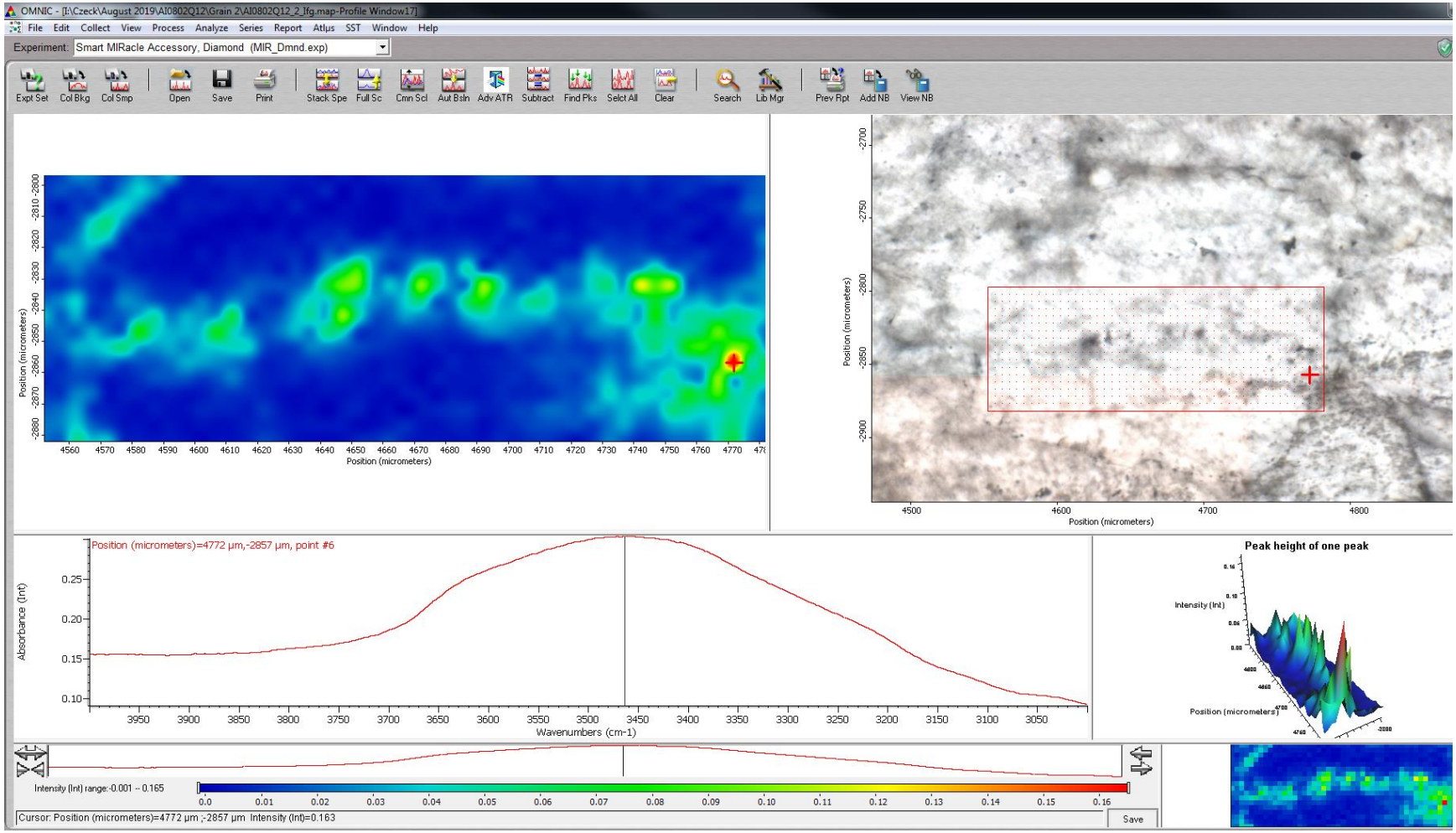

Sample AI-08-02-Q12-2 1st run absorption map with peak height function run for 3452 cm^{-1} wavelength. 720 total spectra collected. Intensity range adjustments shown at bottom.

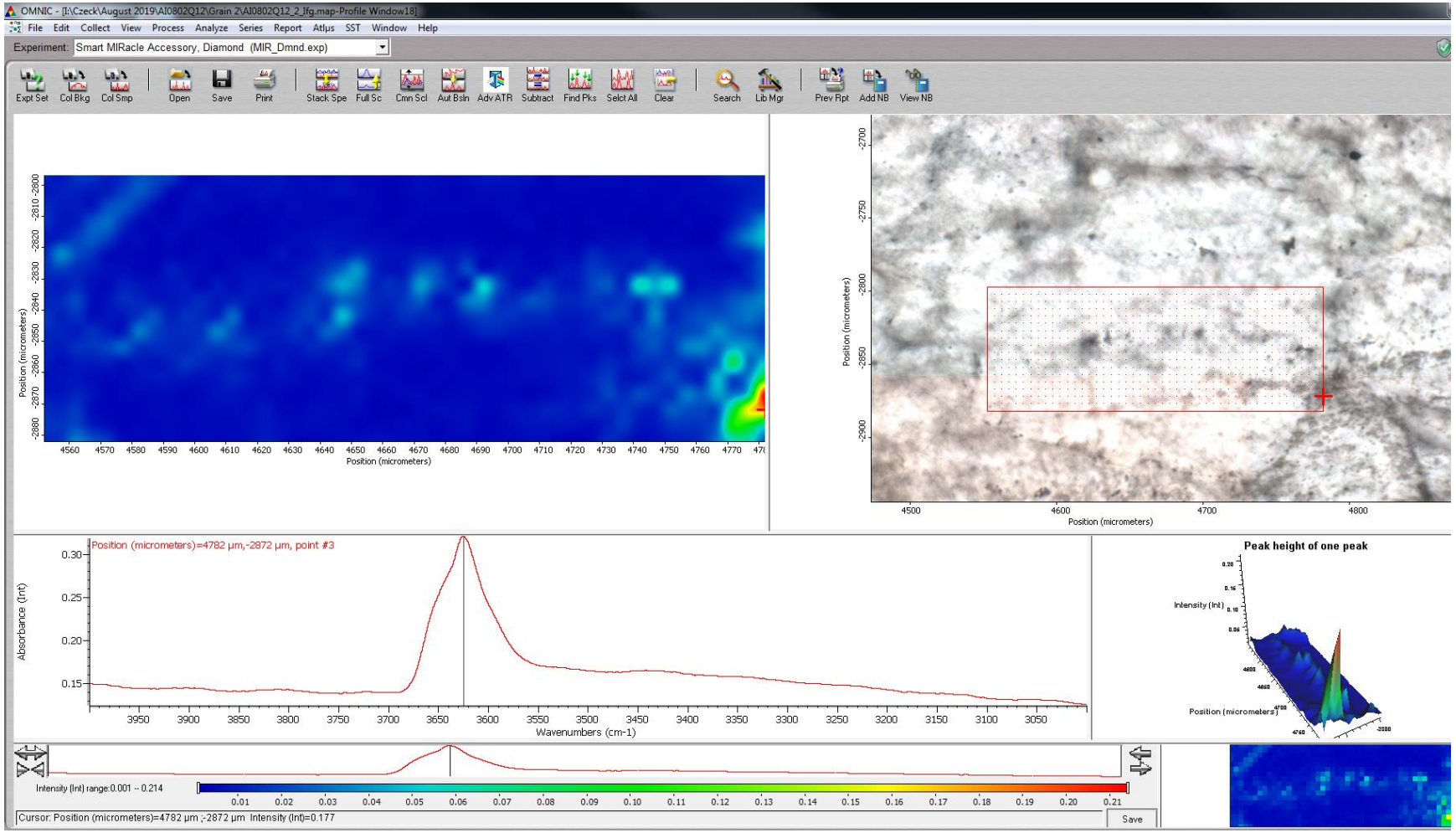

Sample AI-08-02-Q12-2 1st run absorption map with peak height function run for 3622 cm^{-1} wavelength. 720 total spectra collected. Intensity range adjustments shown at bottom.

Medium-strain sample AI-08-02-Q12-2, 2nd run

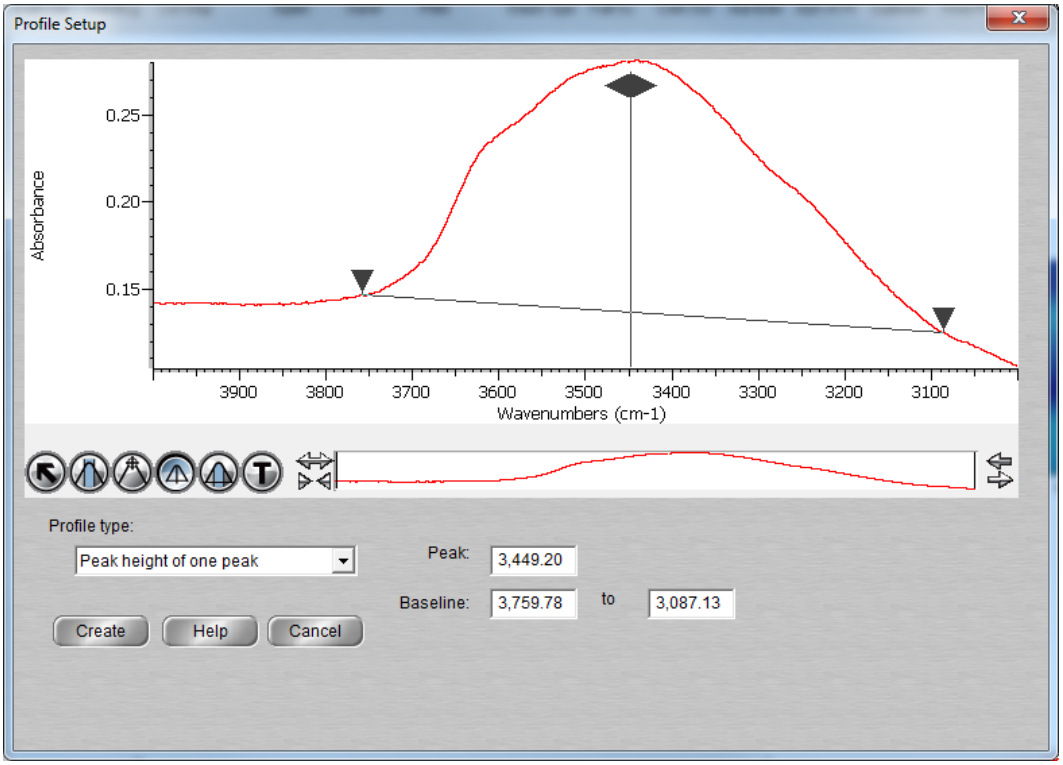

Peak height function used on 3449 cm^{-1} wavelength.

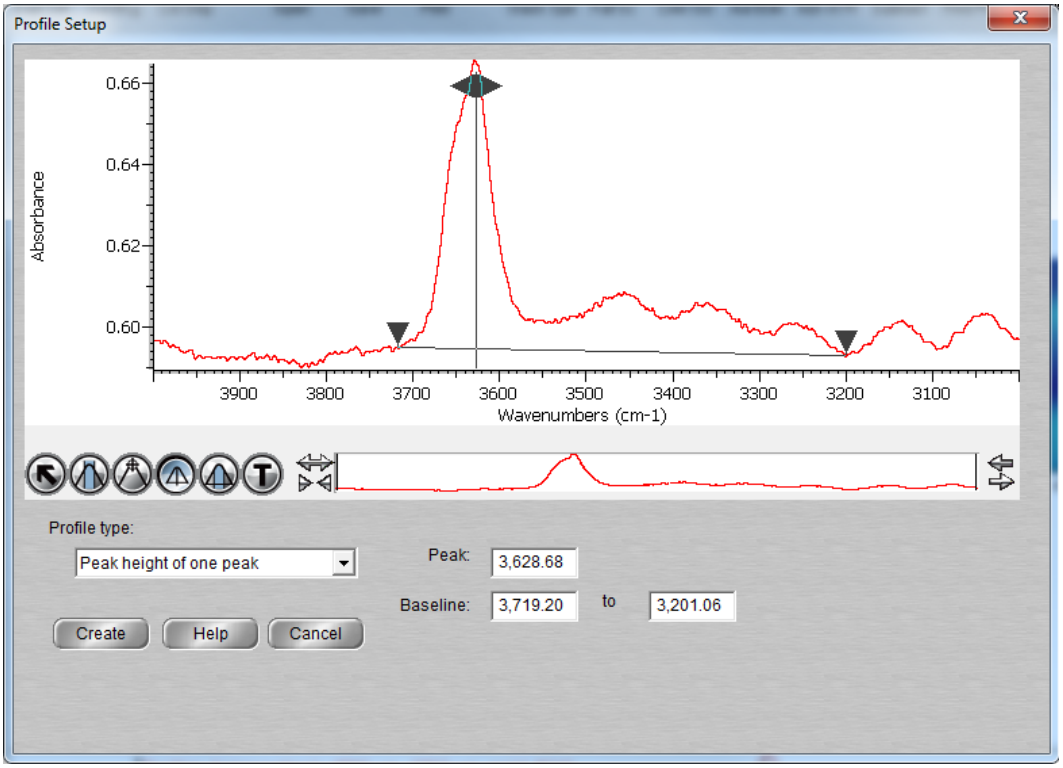

Peak height function used on 3628 cm^{-1} wavelength.

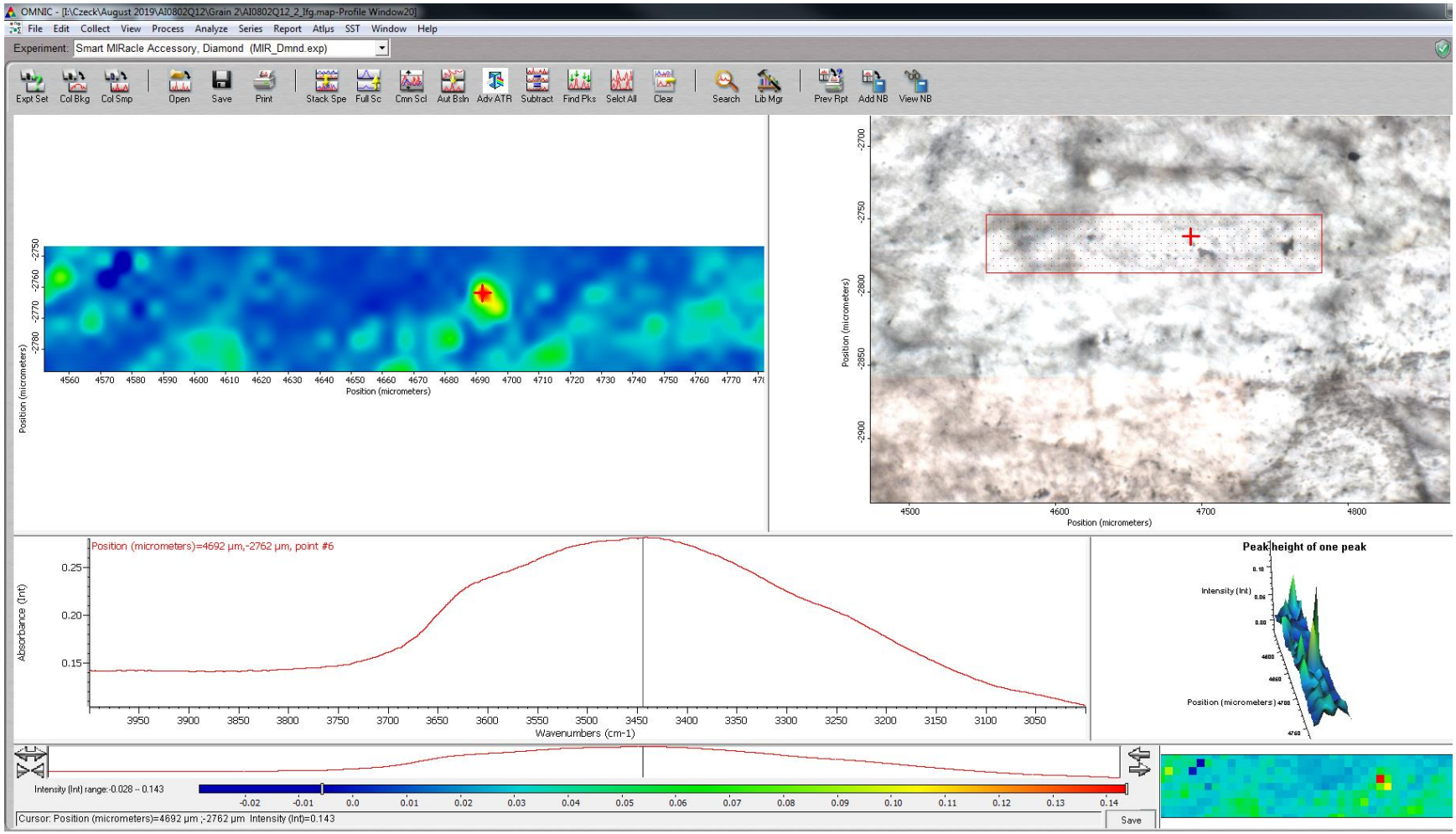

Sample AI-08-02-Q12-2 2nd run absorption map with peak height function run for 3449 cm^{-1} wavelength. 315 total spectra collected. Intensity range adjustments shown at bottom.

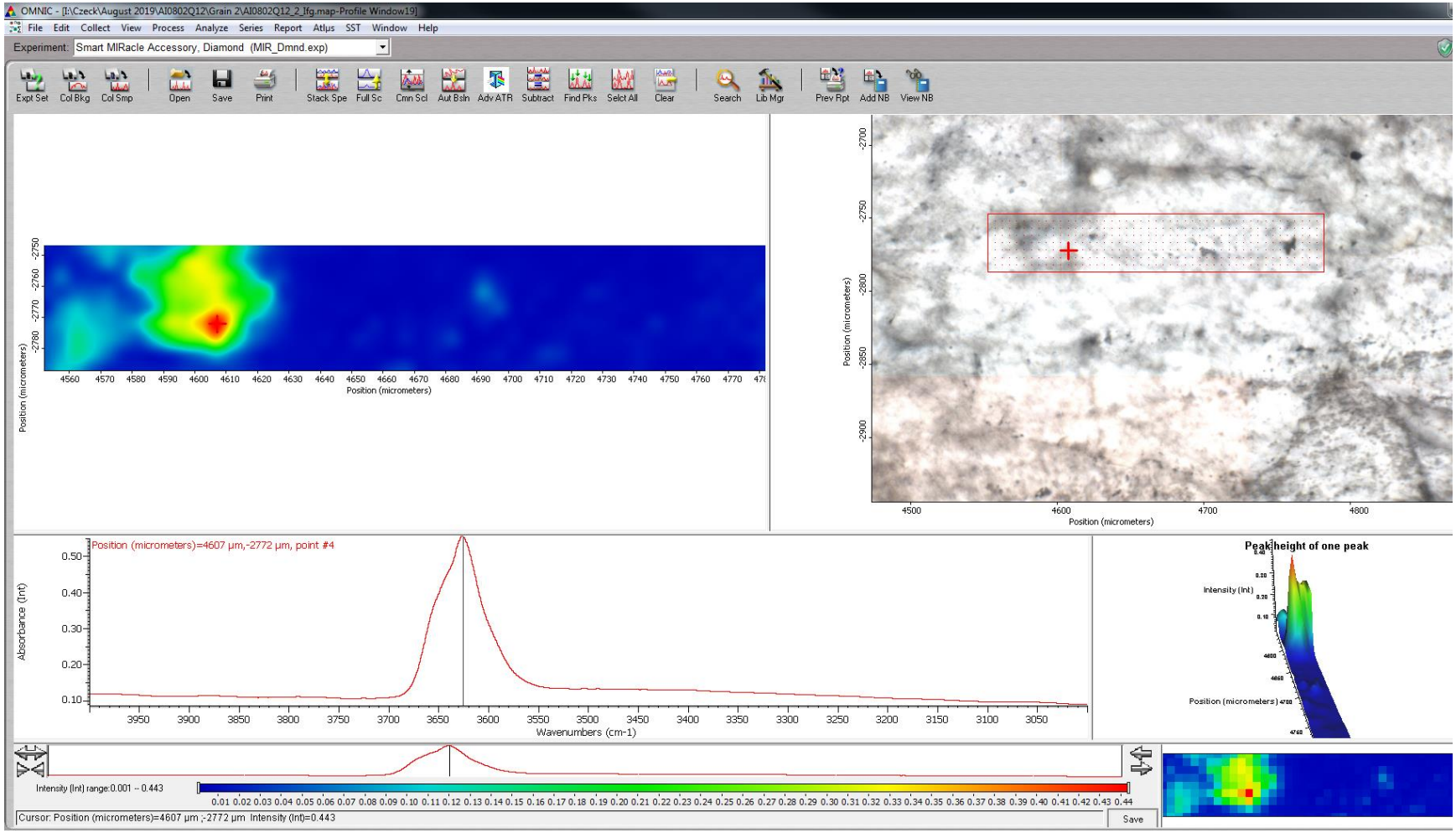

Sample AI-08-02-Q12-2 2nd run absorption map with peak height function run for 3628 cm^{-1} wavelength. 315 total spectra collected. Intensity range adjustments shown at bottom.

Medium-strain sample AI-08-02-Q14-4

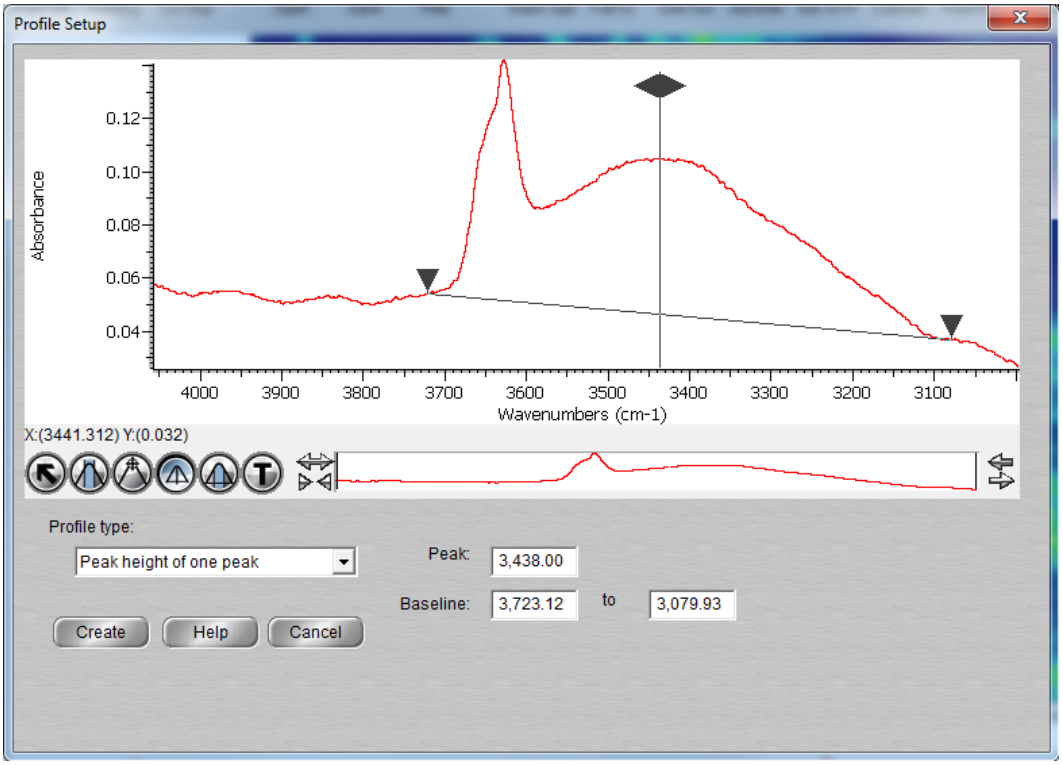

Peak height function used on 3438 cm^{-1} wavelength.

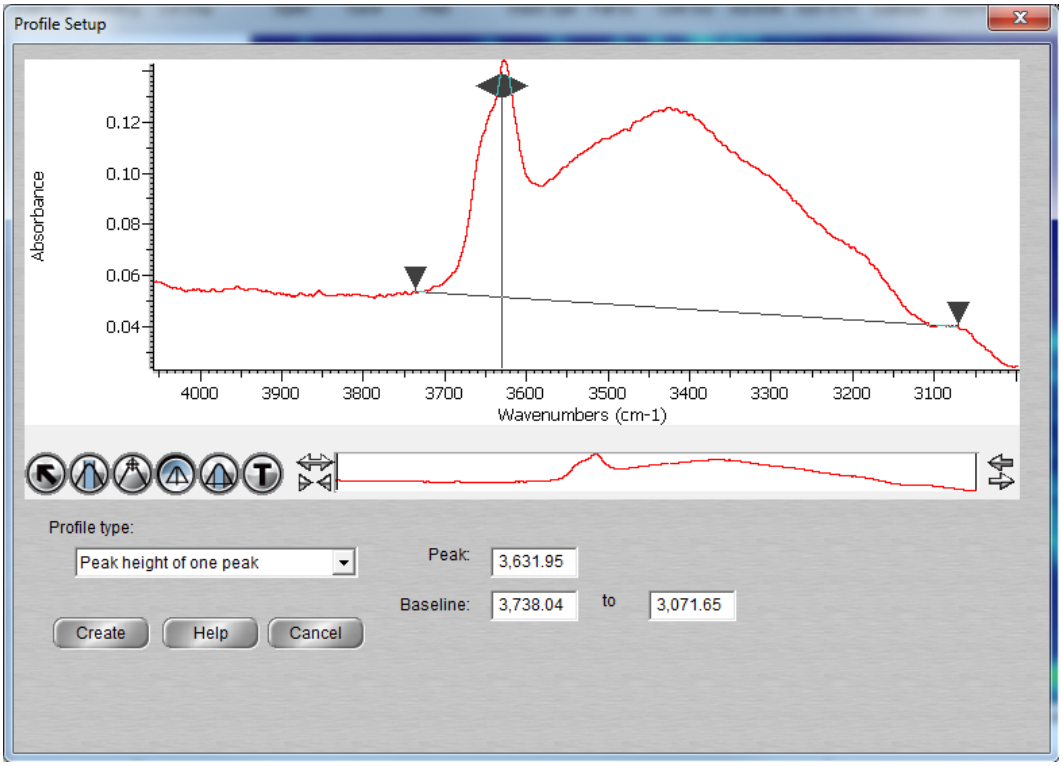

Peak height function used on 3632 cm^{-1} wavelength.

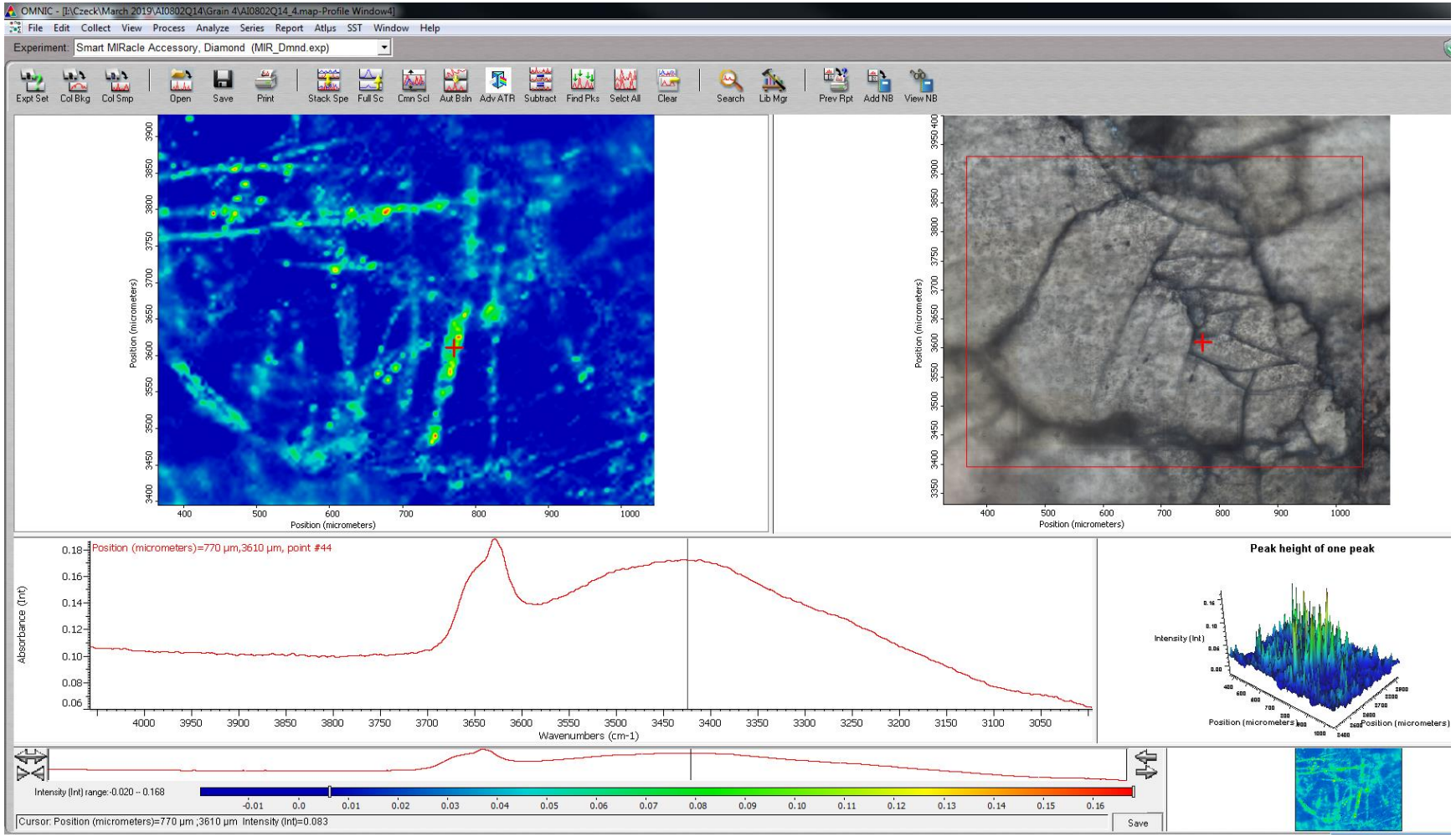

Sample AI-08-02-Q14-4 absorption map with peak height function run for 3438 cm^{-1} wavelength. 14796 total spectra collected. Intensity range adjustments shown at bottom.

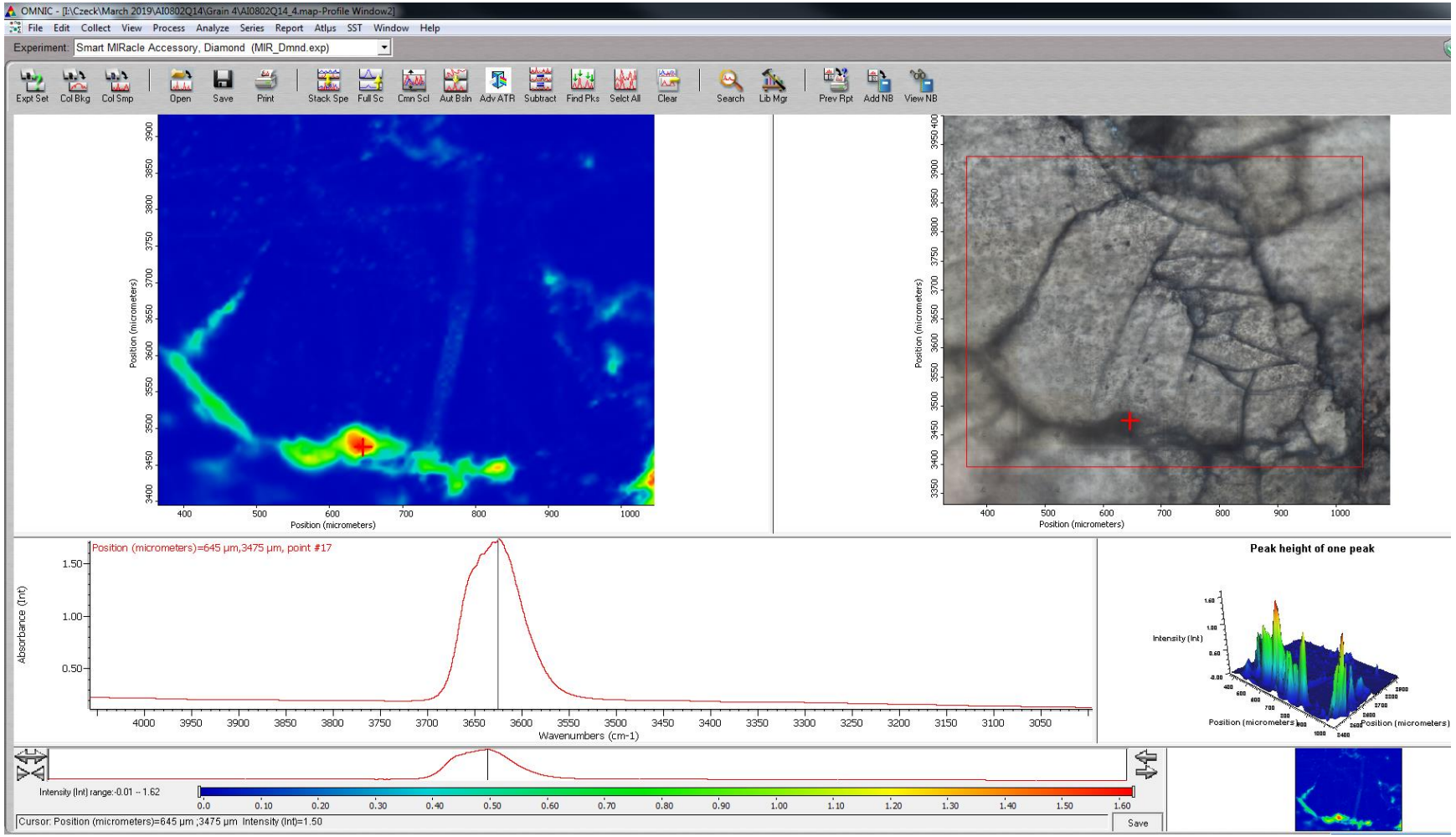

Sample AI-08-02-Q14-4 absorption map with peak height function run for 3632 cm^{-1} wavelength. 14796 total spectra collected. Intensity range adjustments shown at bottom.

High-strain sample AI-08-06-Q11-15

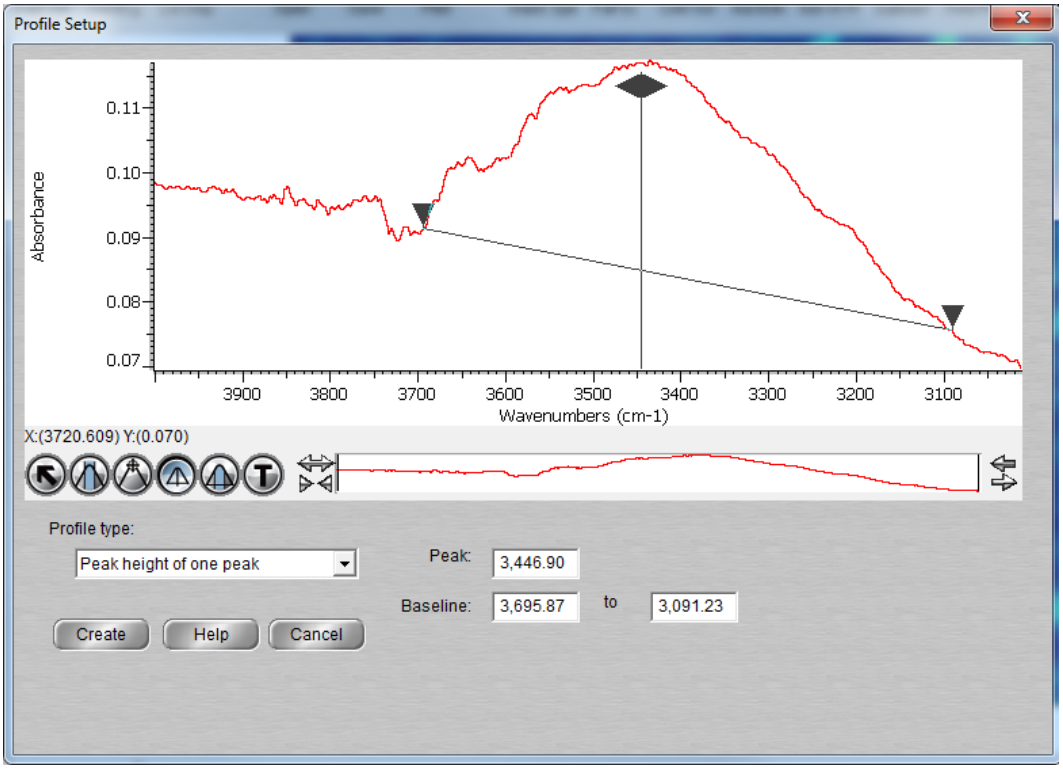

Peak height function used on 3447 cm^{-1} wavelength.

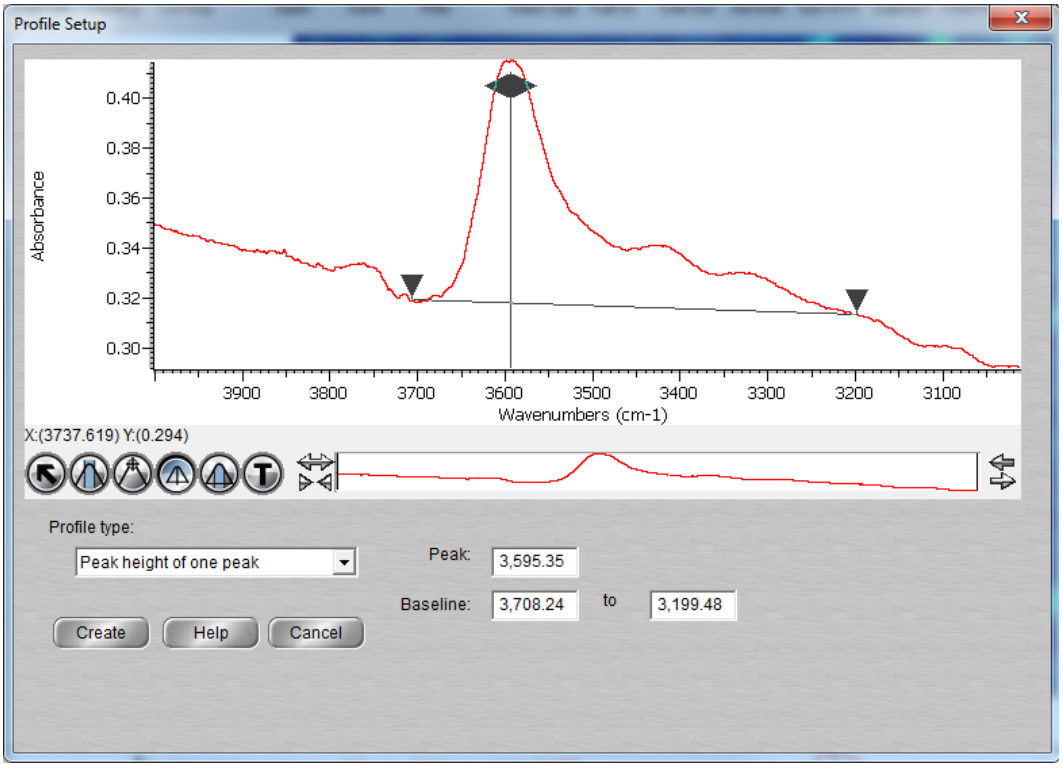

Peak height function used on 3595 cm^{-1} wavelength.

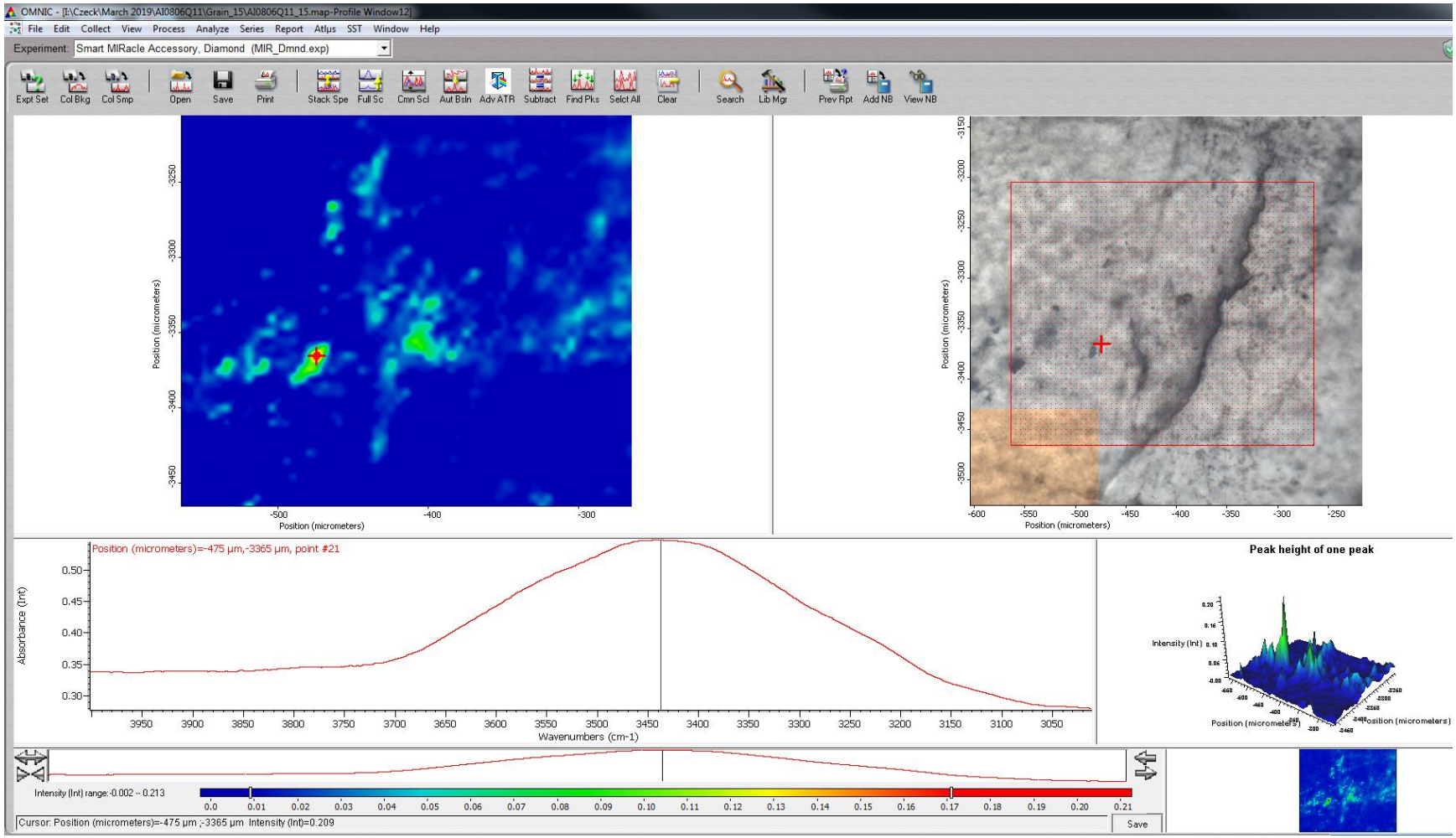

Sample AI-08-06-Q11-15 absorption map with peak height function run for 3447 cm^{-1} wavelength. 3233 total spectra collected. Intensity range adjustments shown at bottom.

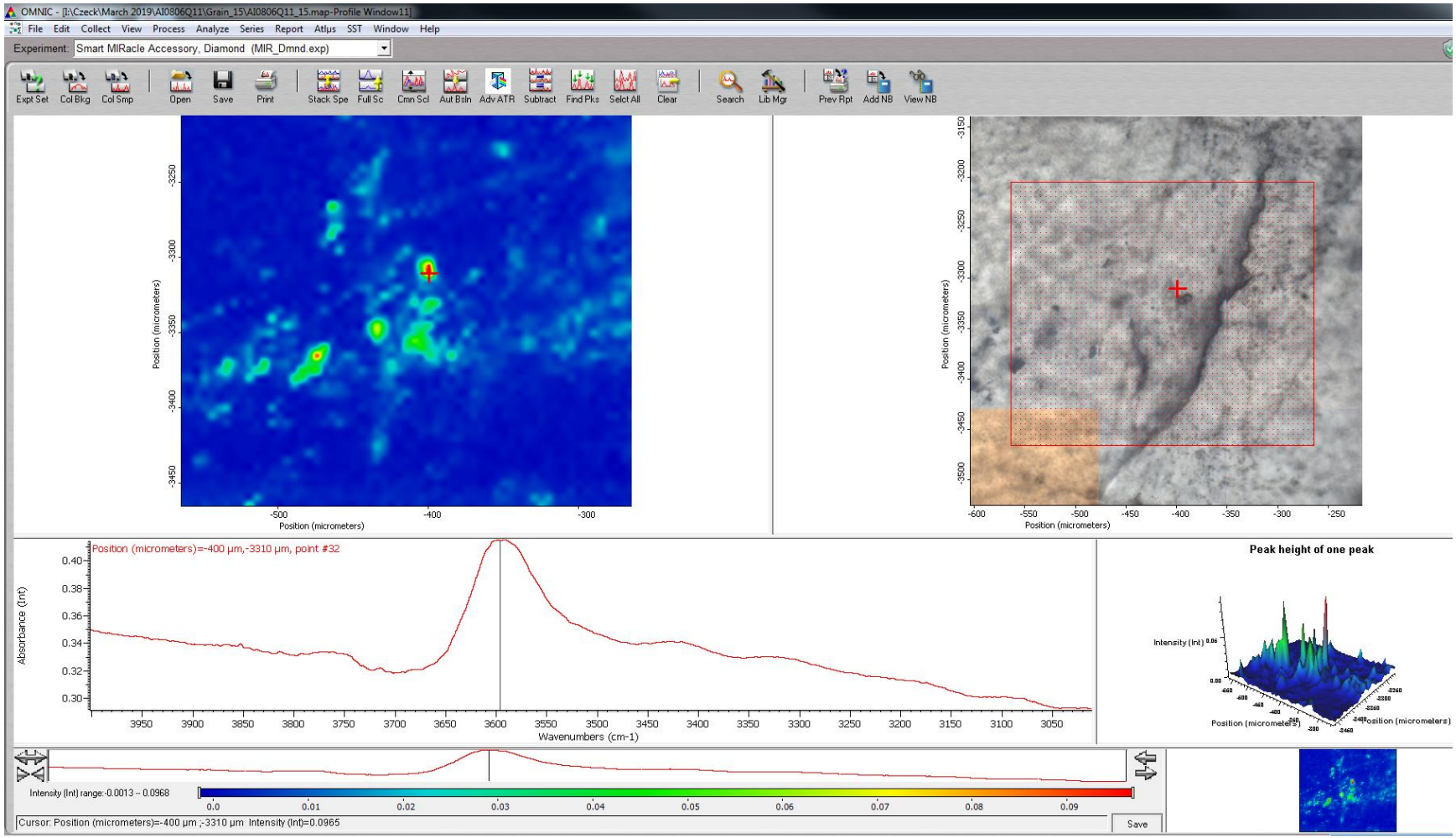

Sample AI-08-06-Q11-15 absorption map with peak height function run for 3595 cm^{-1} wavelength. 3233 total spectra collected. Intensity range adjustments shown at bottom.

High-strain sample AI-08-06-Q11-16

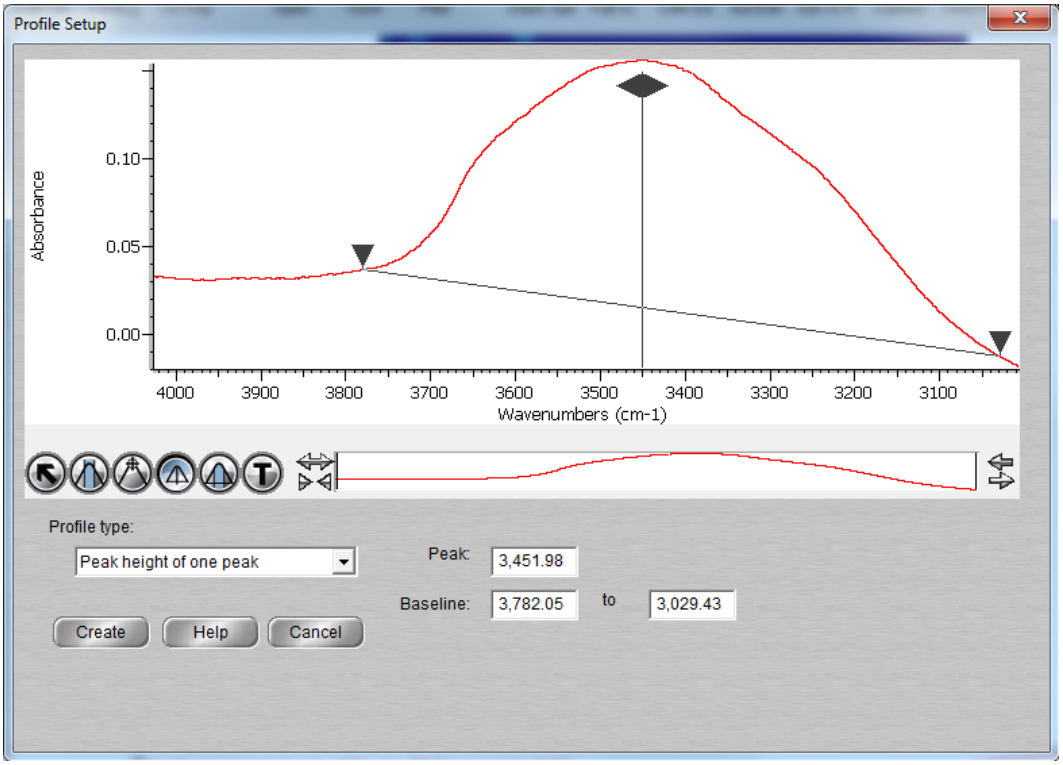

Peak height function used on 3452 cm^{-1} wavelength.

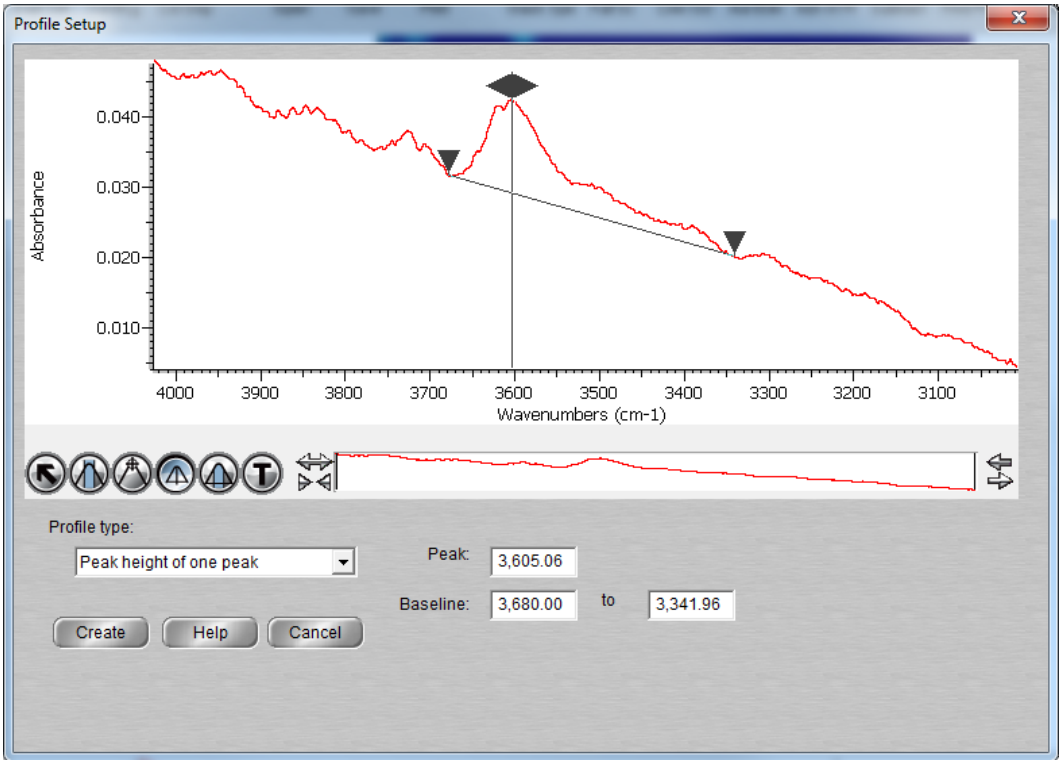

Peak height function used on 3605 cm^{-1} wavelength.

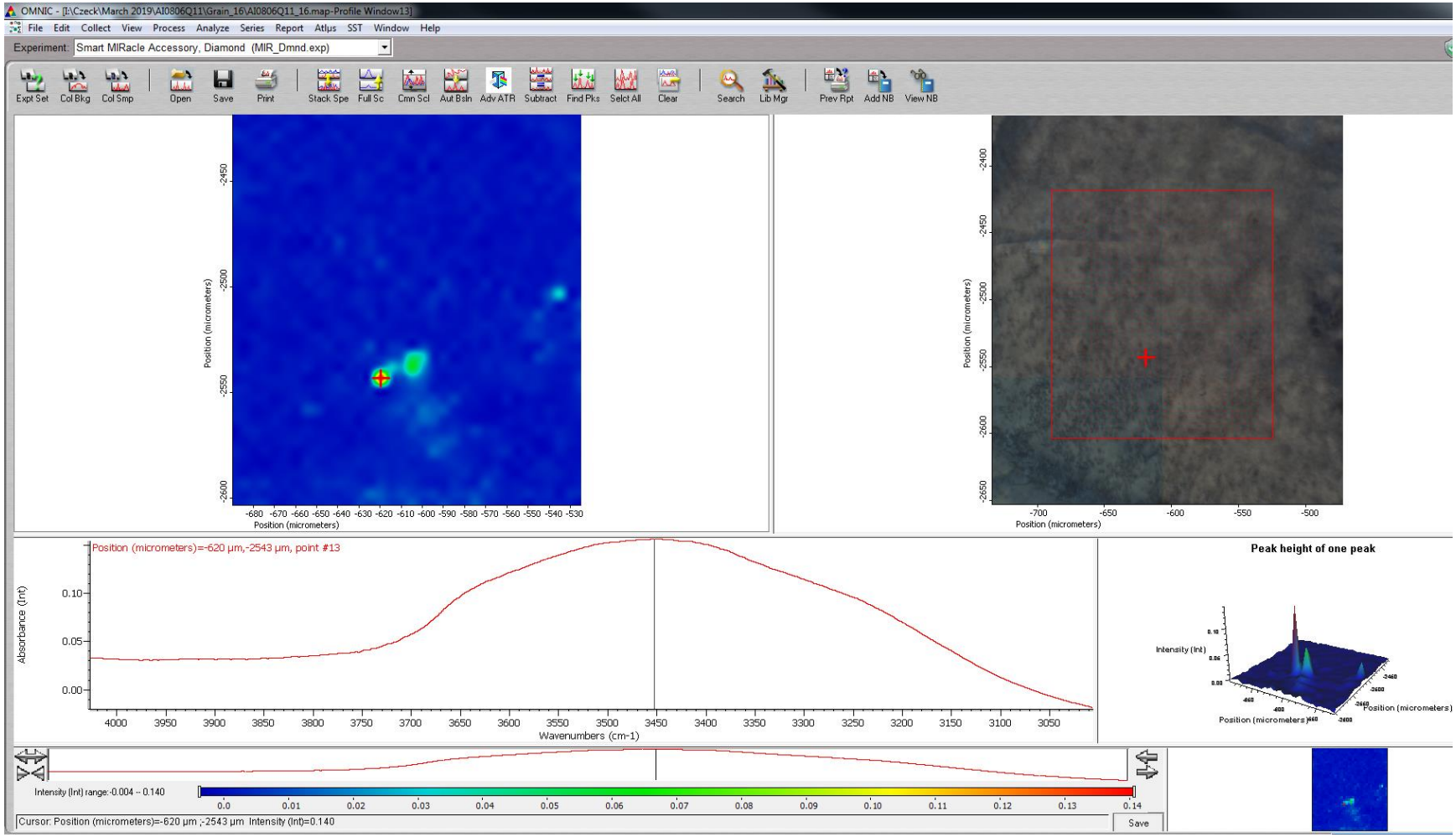

Sample AI-08-06-Q11-16 absorption map with peak height function run for 3452 cm^{-1} wavelength. 1292 total spectra collected. Intensity range adjustments shown at bottom.

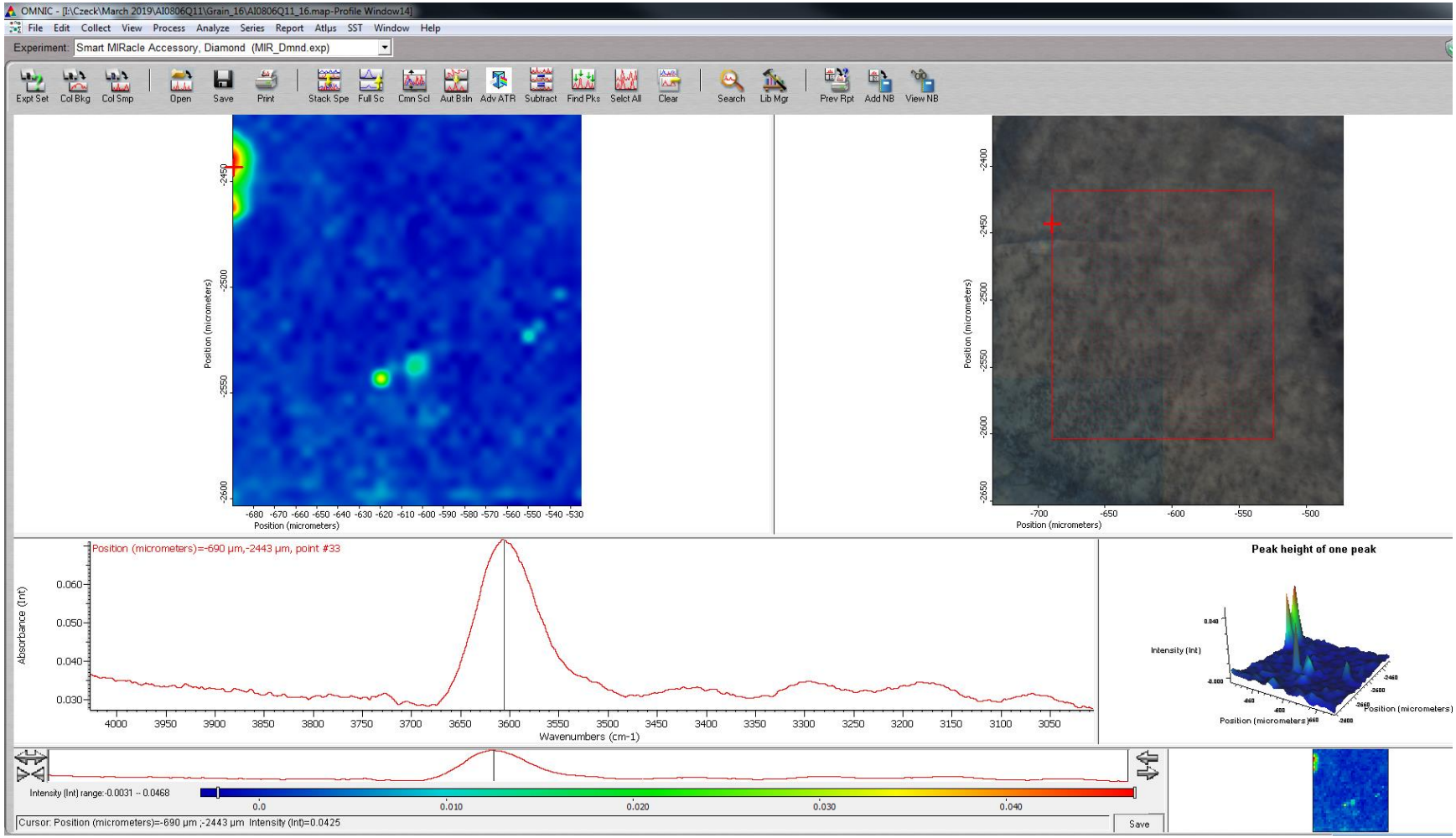

Sample AI-08-06-Q11-16 absorption map with peak height function run for 3605 cm^{-1} wavelength. 1292 total spectra collected. Intensity range adjustments shown at bottom.

High-strain sample AI-08-06-Q13-6

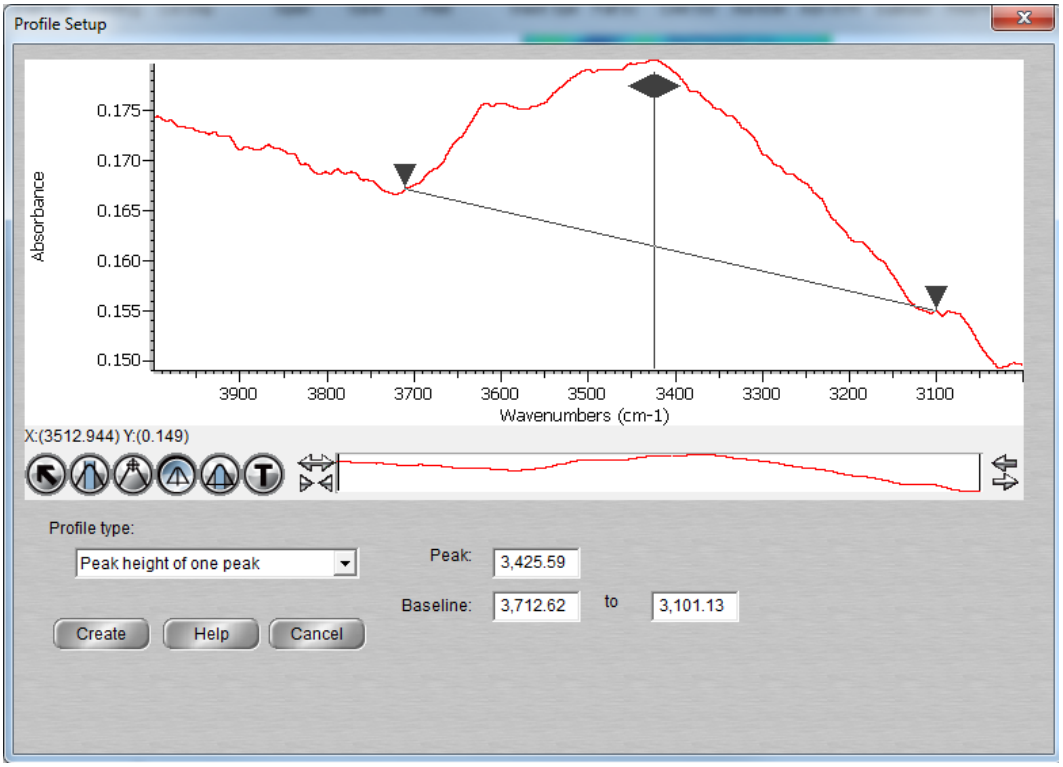

Peak height function used on 3462 cm^{-1} wavelength.

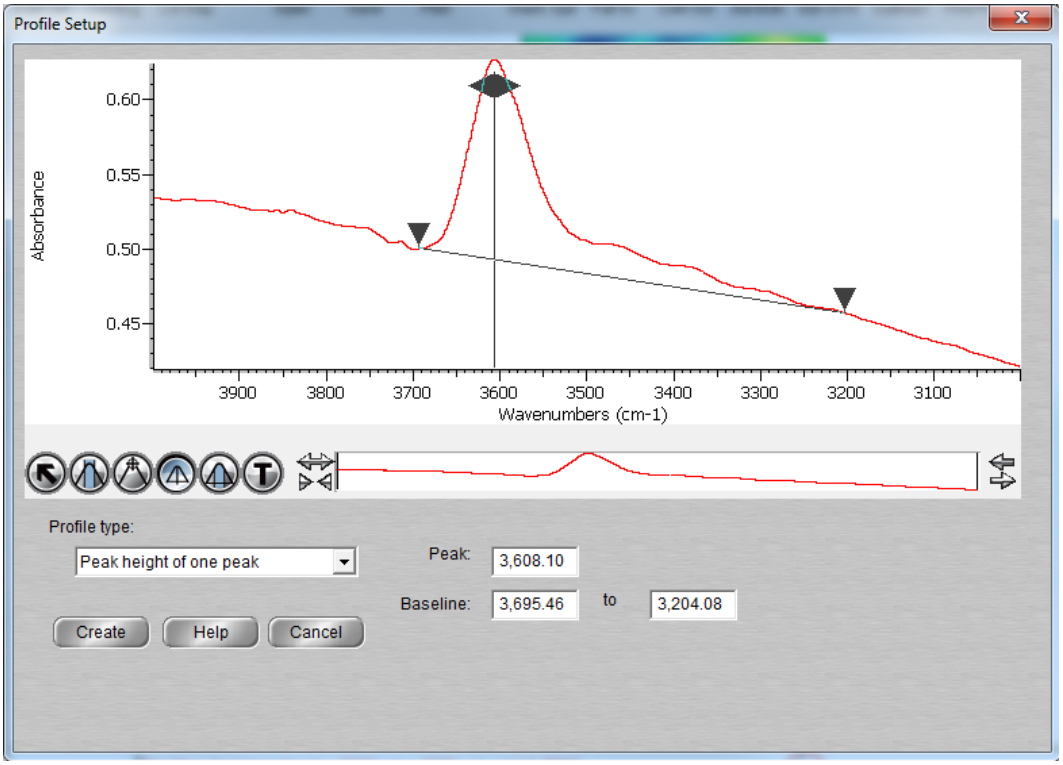

Peak height function used on 3608 cm^{-1} wavelength.

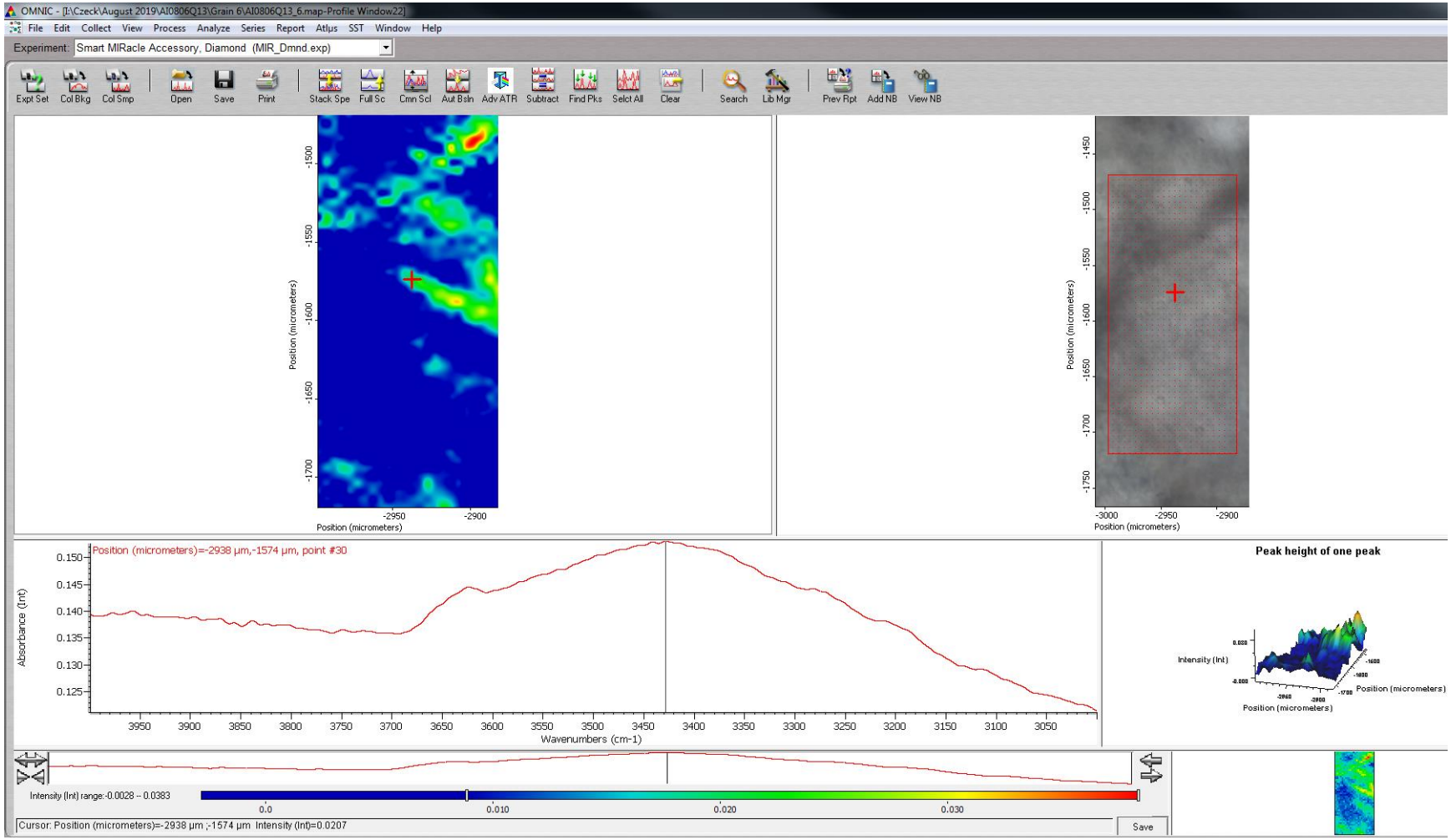

Sample AI-08-06-Q13-6 absorption map with peak height function run for 3462 cm^{-1} wavelength. 1224 total spectra collected. Intensity range adjustments shown at bottom.

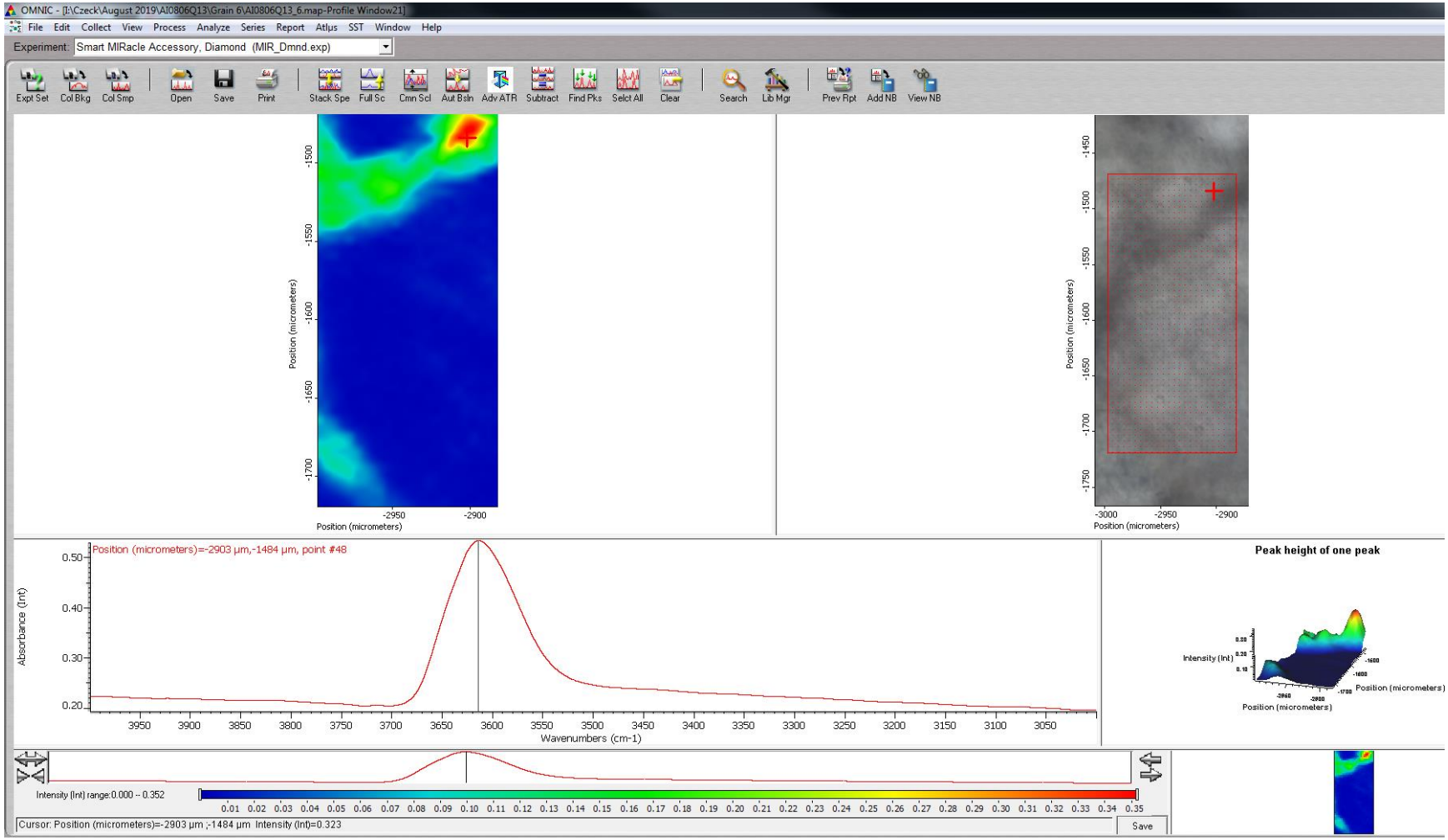

Sample AI-08-06-Q13-6 absorption map with peak height function run for 3608 cm^{-1} wavelength. 1224 total spectra collected. Intensity range adjustments shown at bottom.

High-strain sample AI-08-06-Q13-8, 1st run

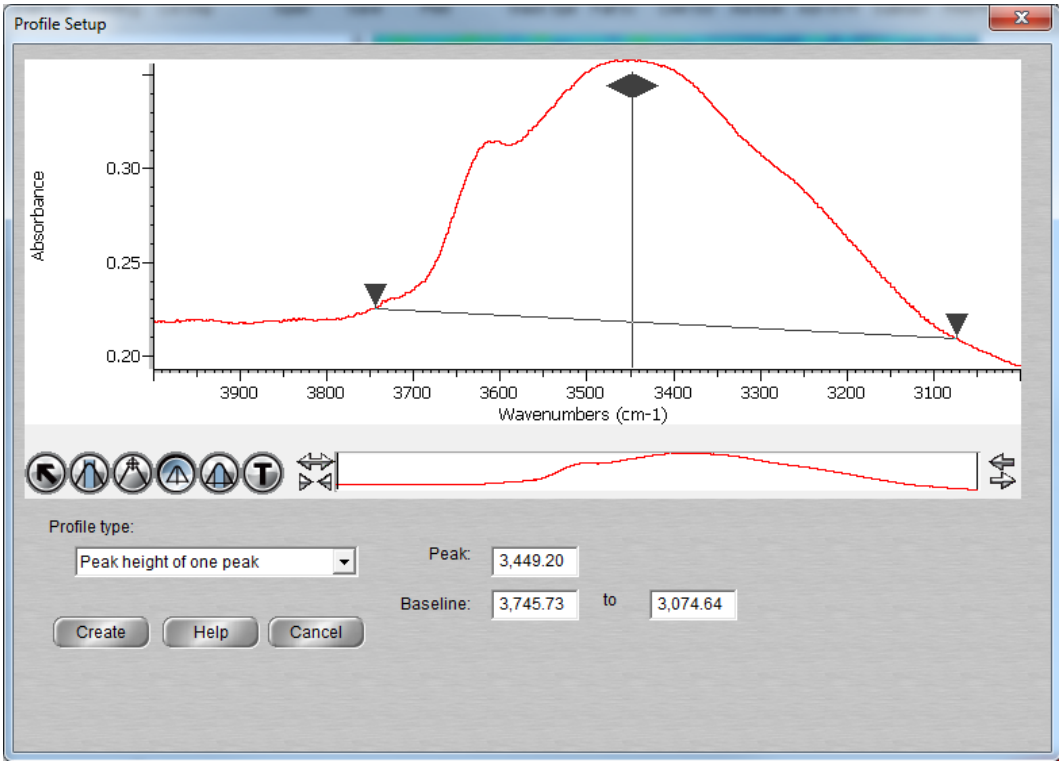

Peak height function used on 3449 cm^{-1} wavelength.

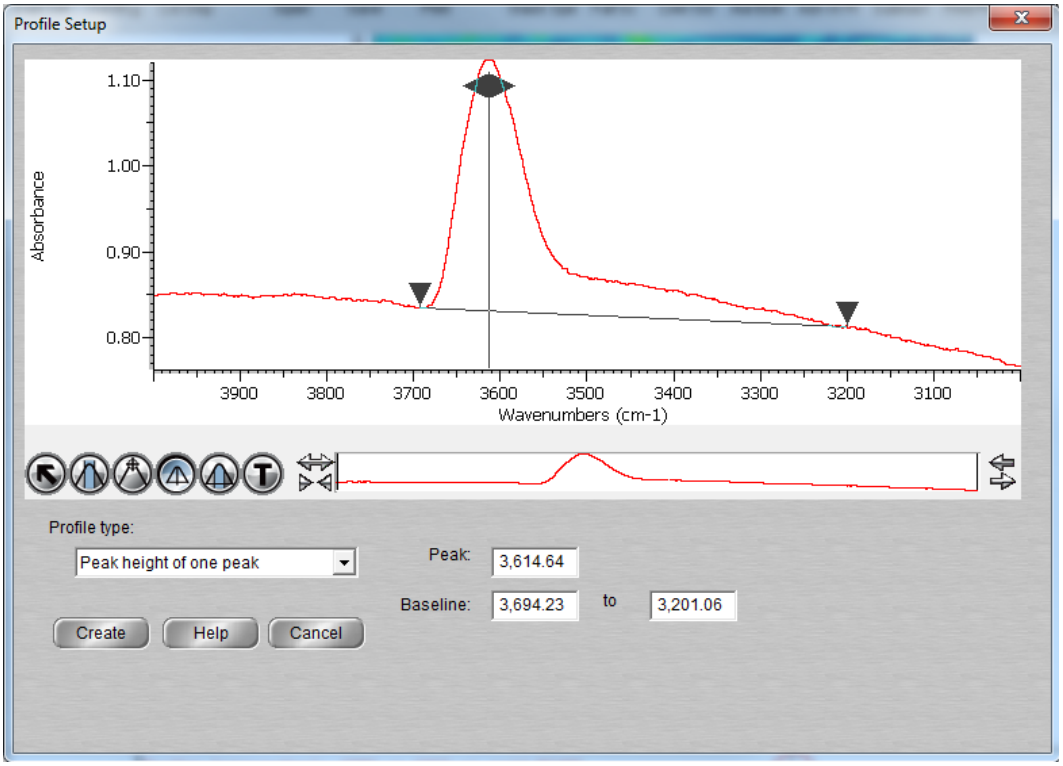

Peak height function used on 3615 cm^{-1} wavelength.

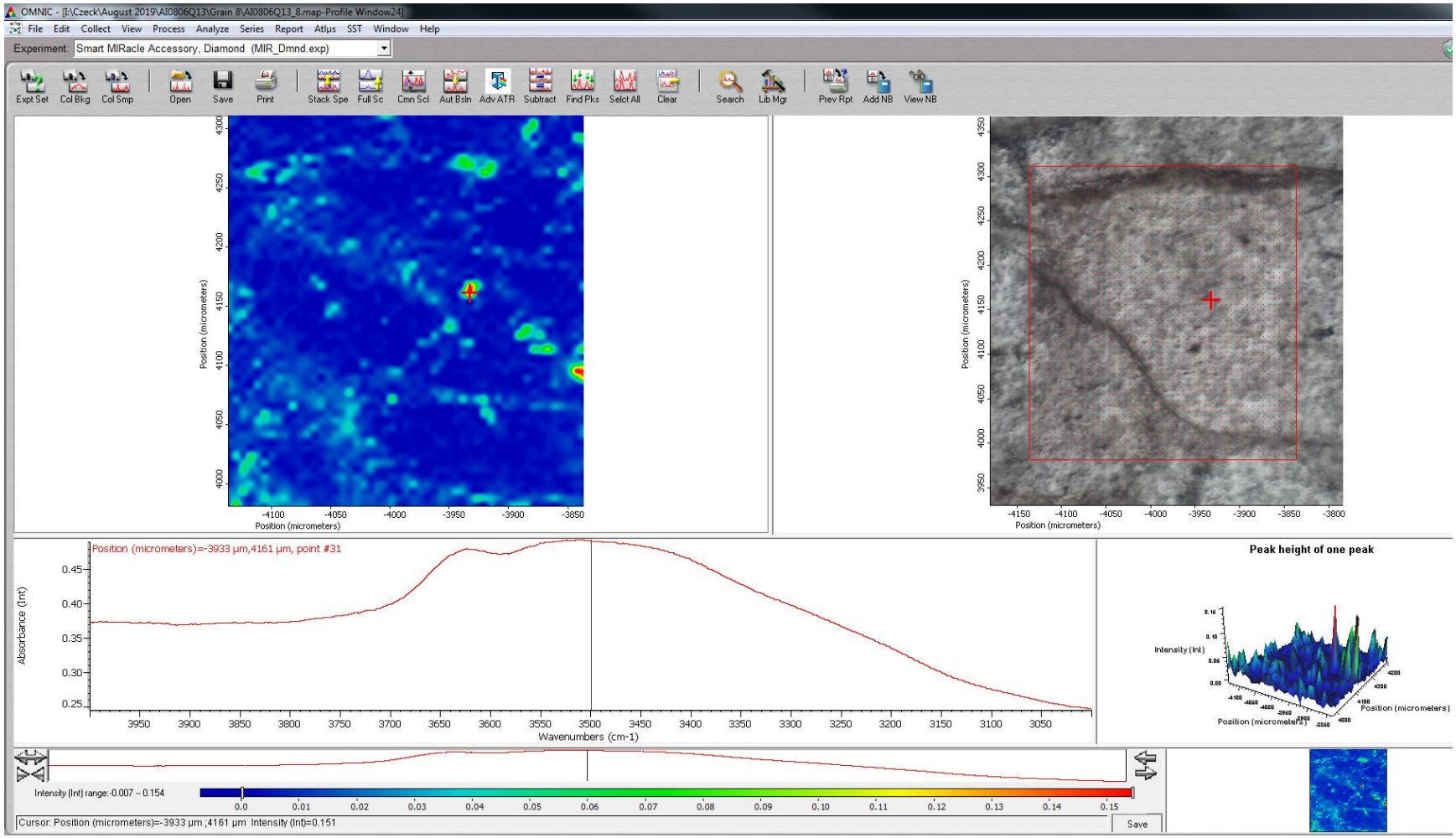

Sample AI-08-06-Q13-8 1st run absorption map with peak height function run for 3449 cm^{-1} wavelength. 2856 total spectra collected. Intensity range adjustments shown at bottom.

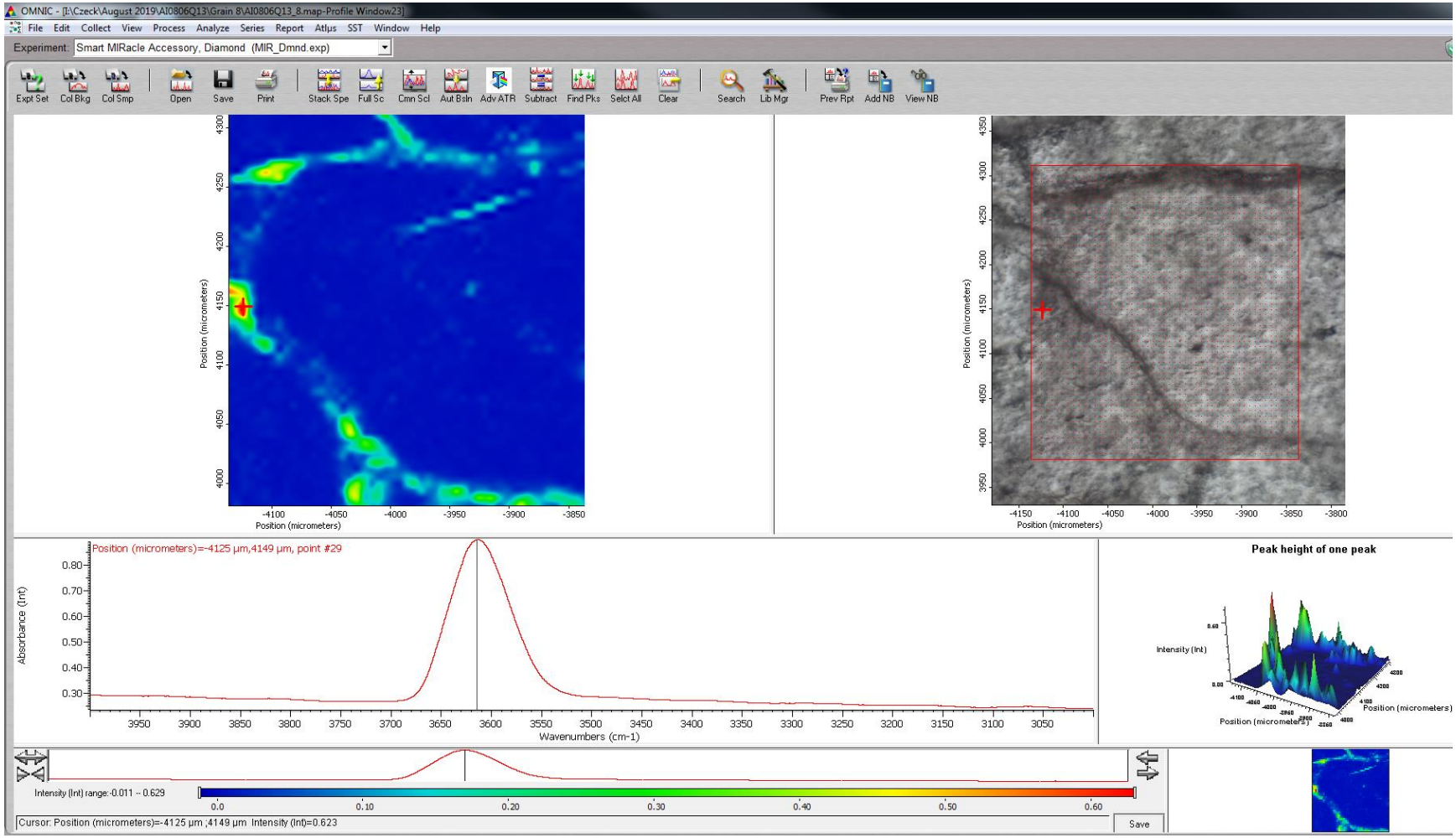

Sample AI-08-06-Q13-8 1st run absorption map with peak height function run for 3615 cm^{-1} wavelength. 2856 total spectra collected. Intensity range adjustments shown at bottom.

High-strain sample AI-08-06-Q13-8, 2nd run

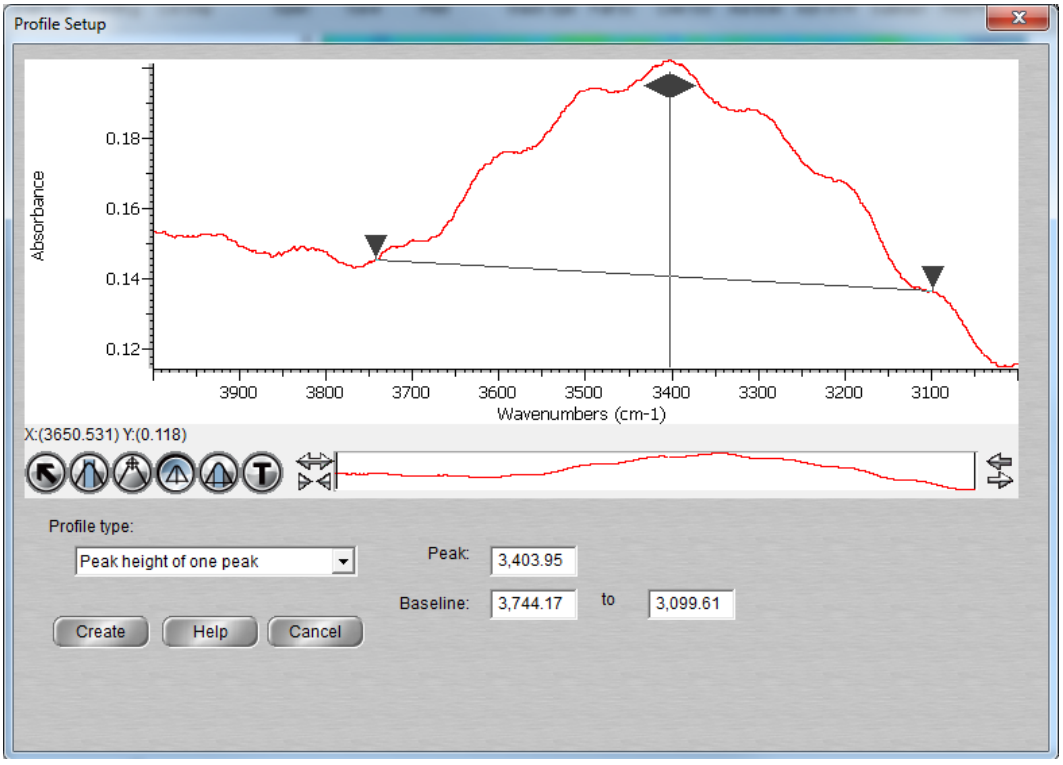

Peak height function used on 3404 cm^{-1} wavelength.

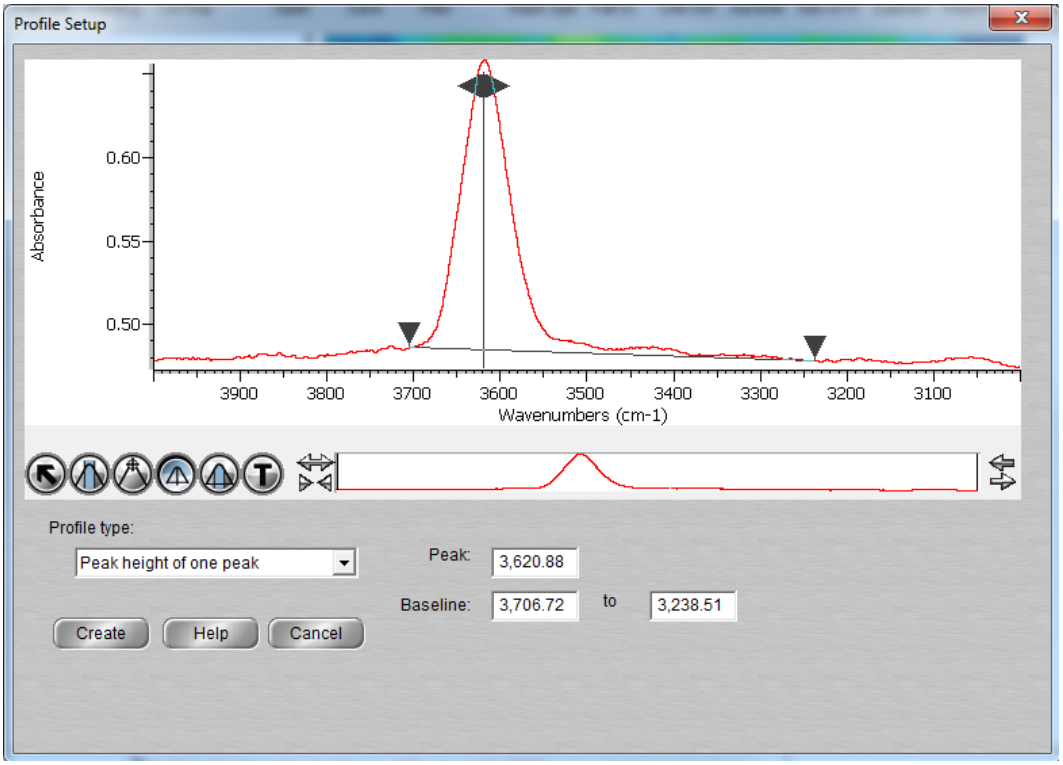

Peak height function used on 3621 cm^{-1} wavelength.

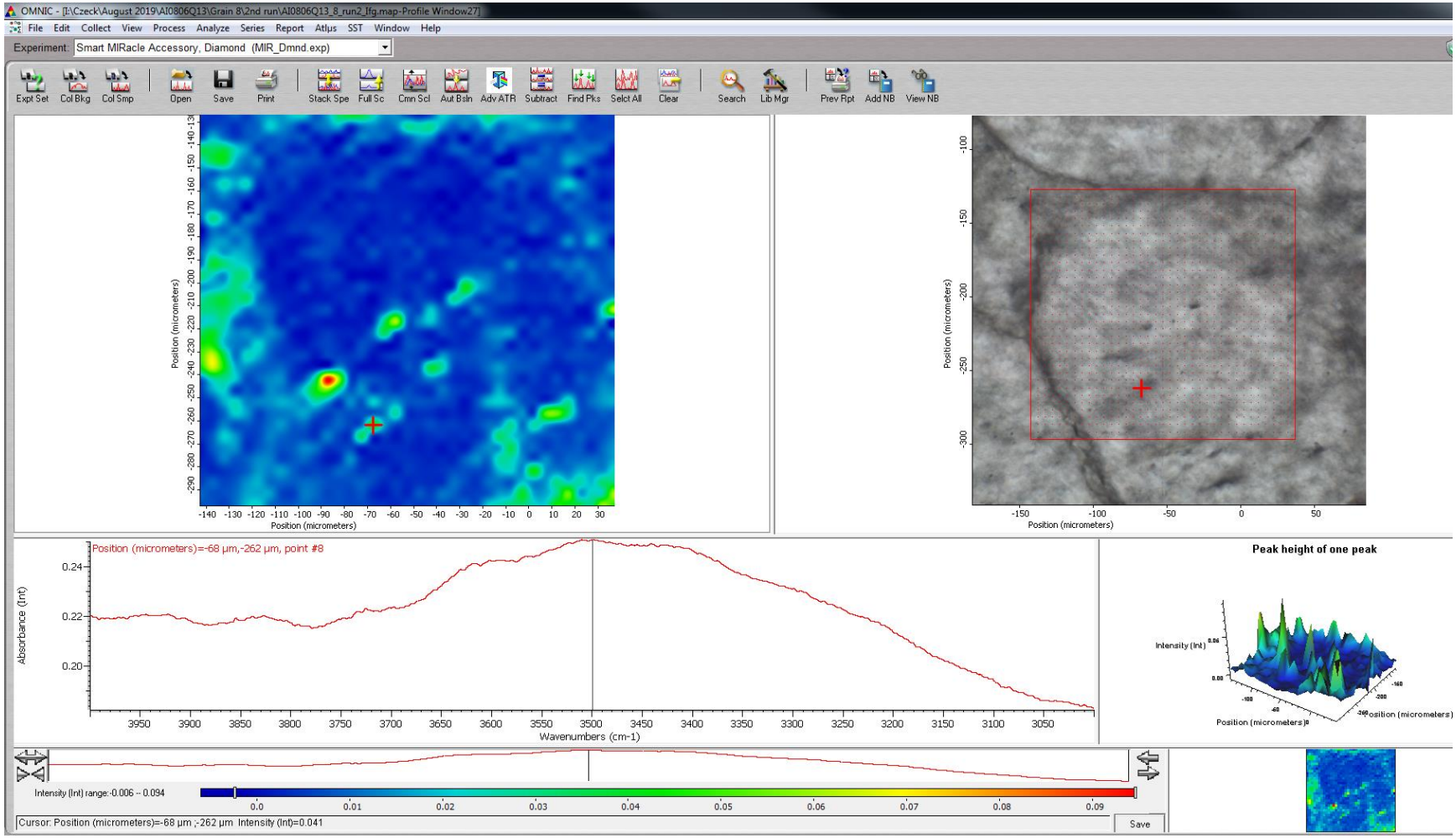

Sample AI-08-06-Q13-8 2nd run absorption map with peak height function run for 3404 cm^{-1} wavelength. 1295 total spectra collected. Intensity range adjustments shown at bottom.

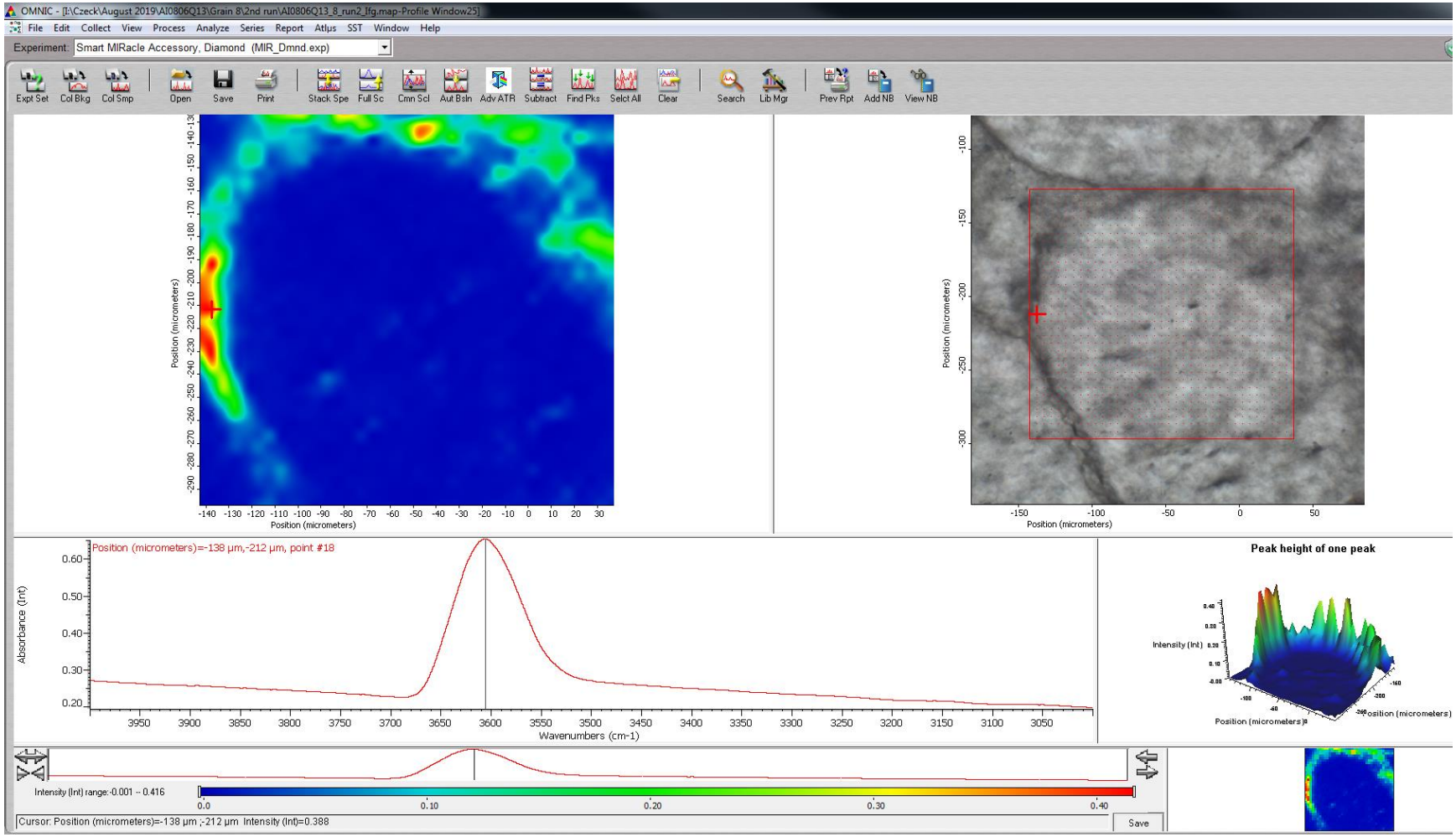

Sample AI-08-06-Q13-8 2nd run absorption map with peak height function run for 3621 cm^{-1} wavelength. 1295 total spectra collected. Intensity range adjustments shown at bottom.

High-strain sample AI-08-06-Q13-8, 3rd run

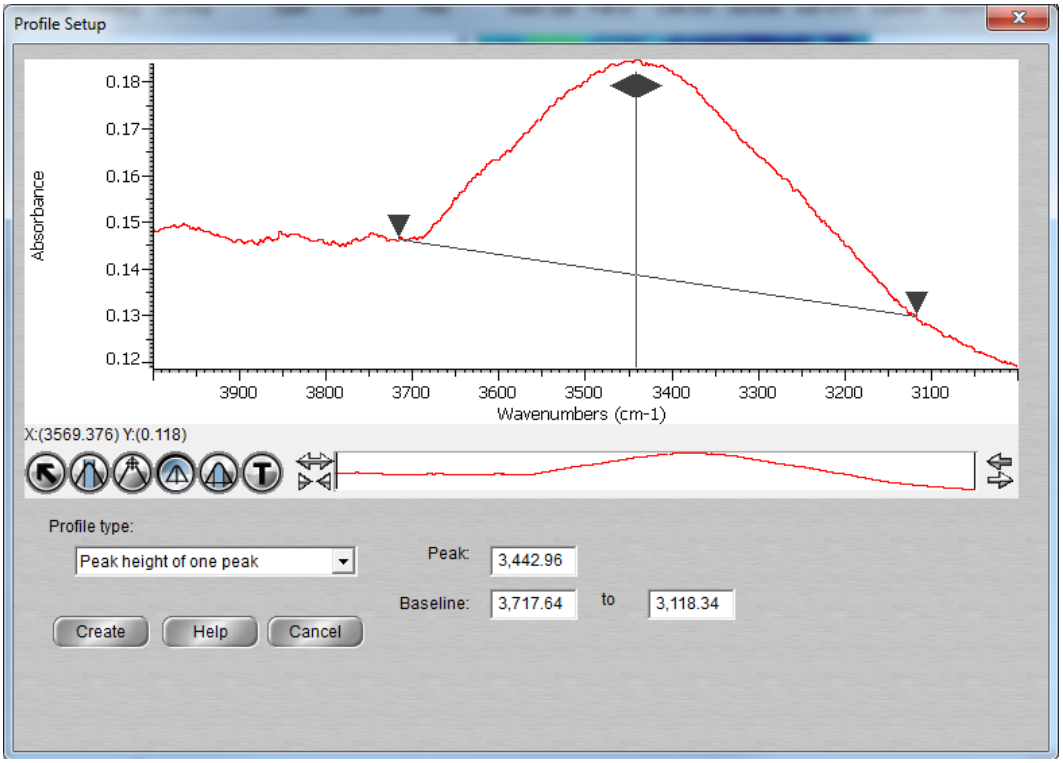

Peak height function used on 3443 cm^{-1} wavelength.

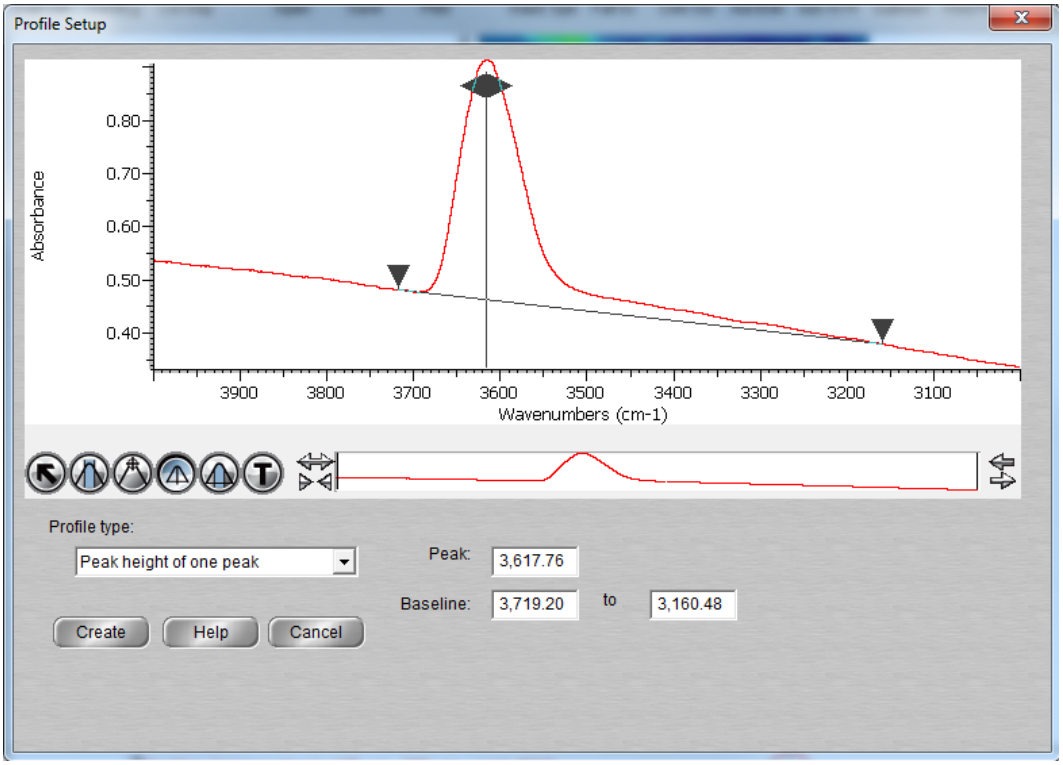

Peak height function used on 3618 cm^{-1} wavelength.

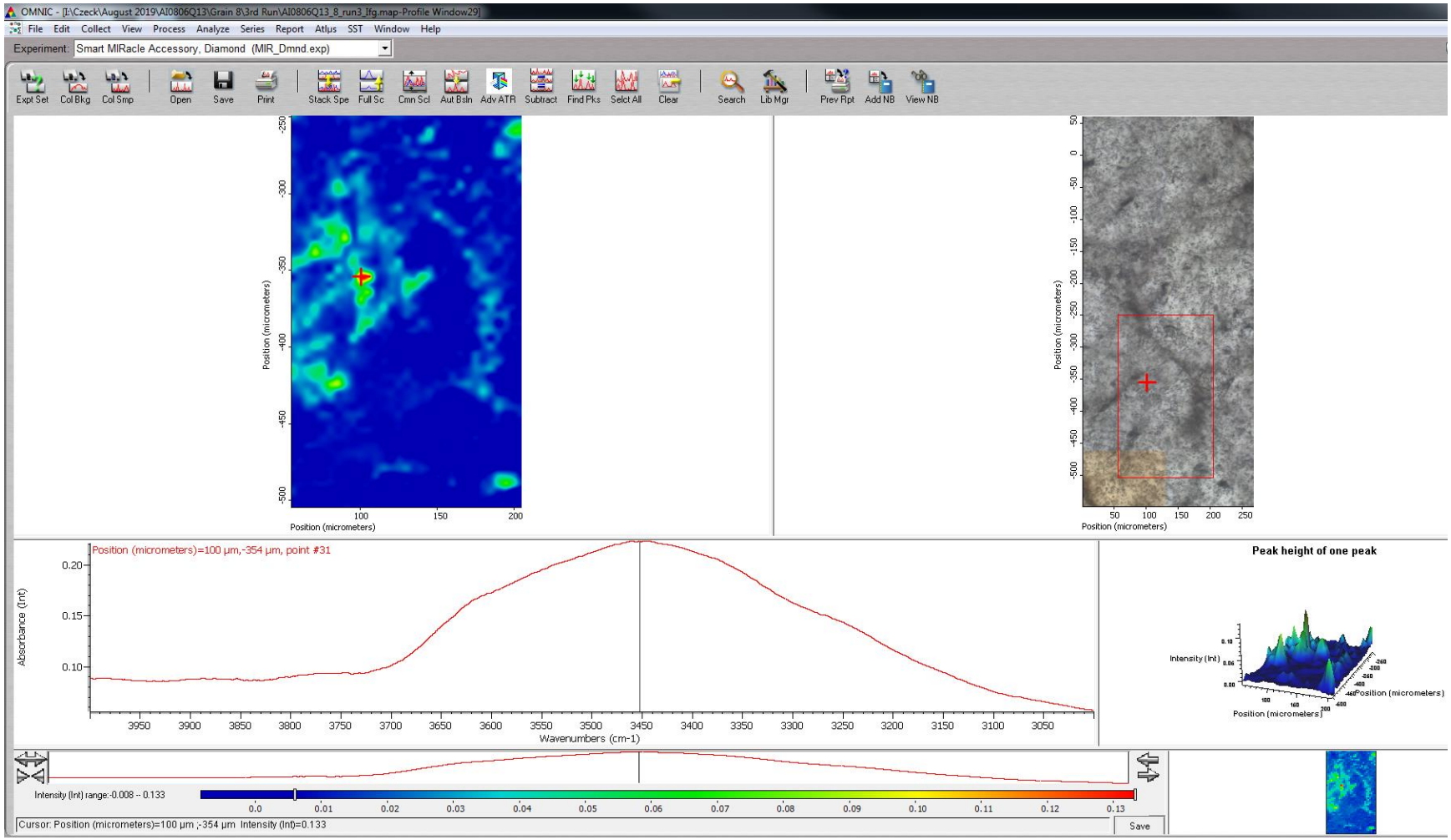

Sample AI-08-06-Q13-8 3rd run absorption map with peak height function run for 3443 cm^{-1} wavelength. 1610 total spectra collected. Intensity range adjustments shown at bottom.

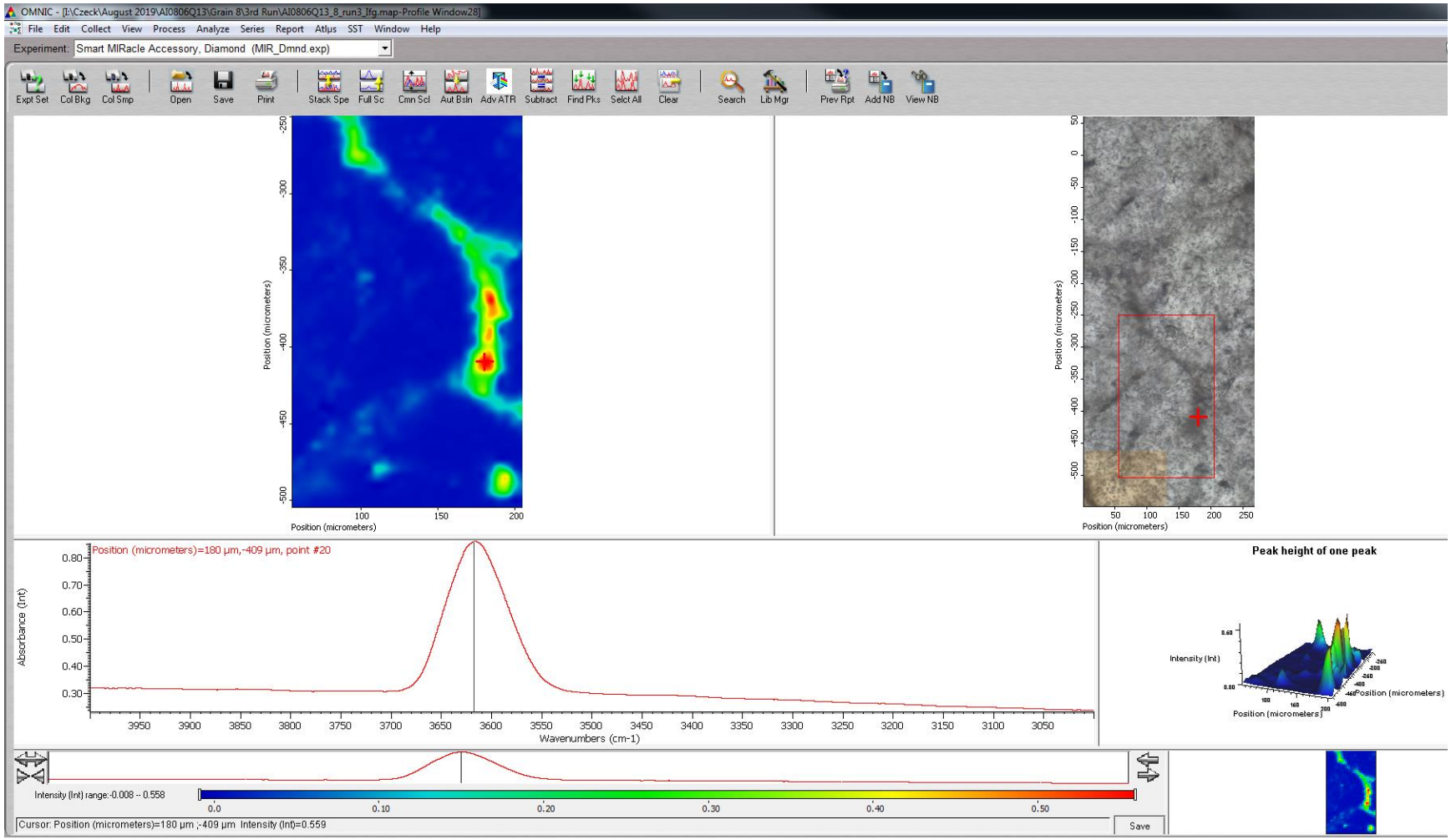

Sample AI-08-06-Q13-8 3rd run absorption map with peak height function run for 3618 cm^{-1} wavelength. 1610 total spectra collected. Intensity range adjustments shown at bottom.

High-strain sample AI-08-06-Q13-8, 4th run

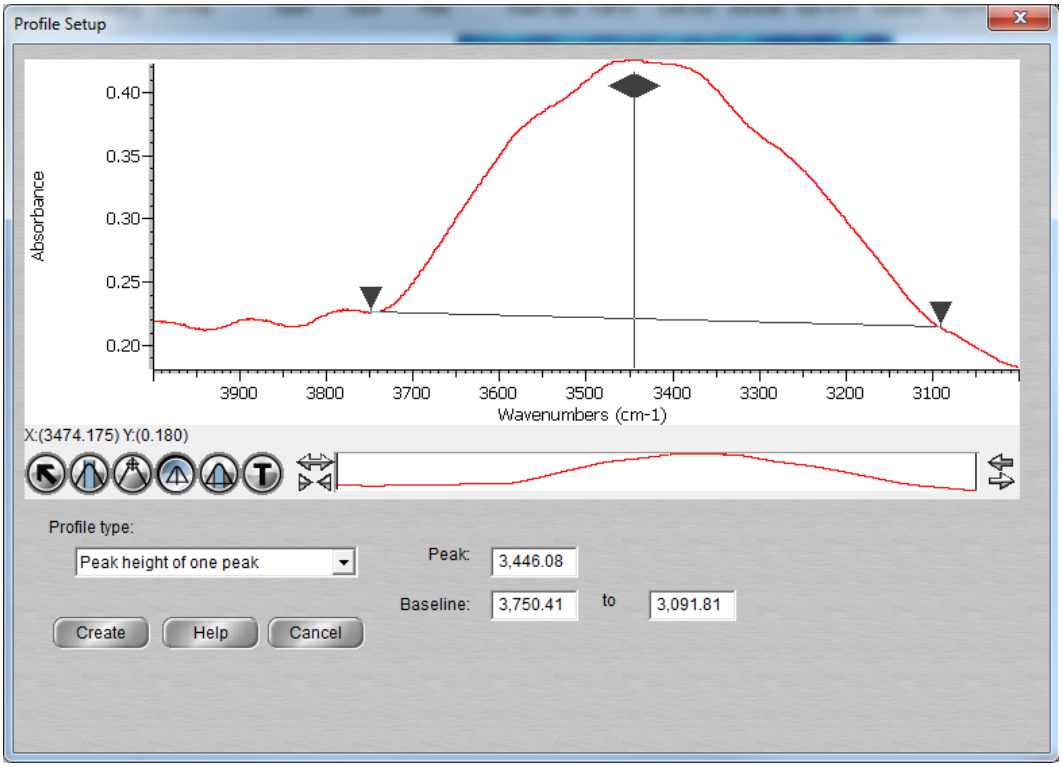

Peak height function used on 3446 cm^{-1} wavelength.

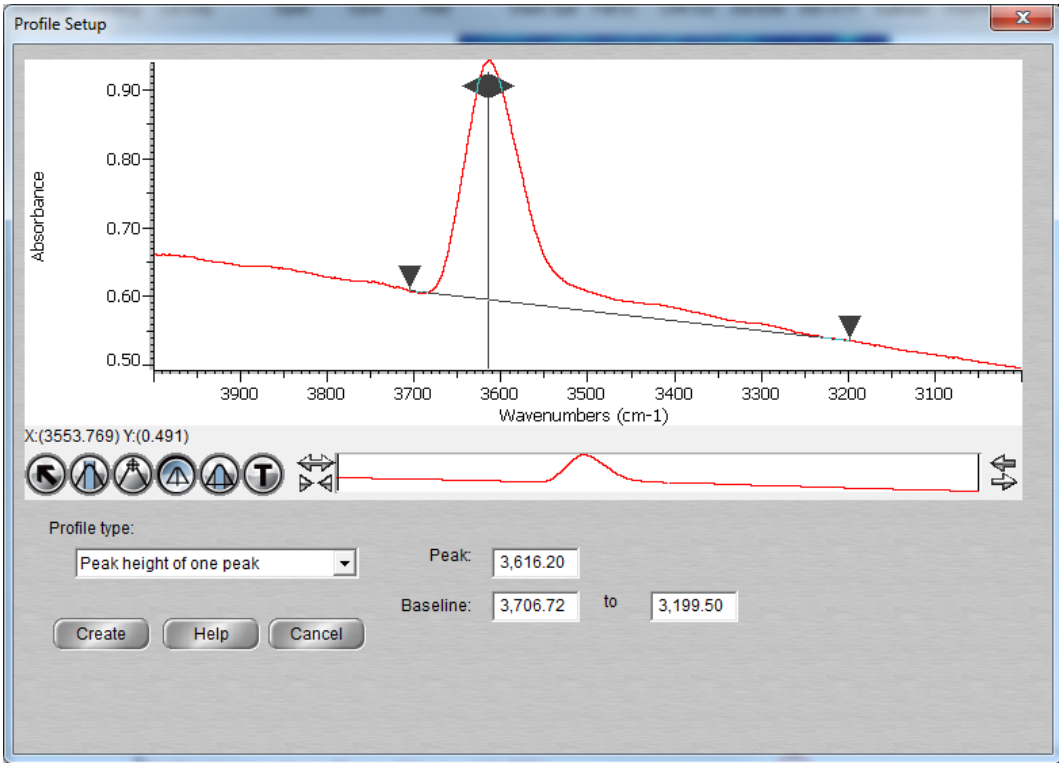

Peak height function used on 3616 cm^{-1} wavelength.

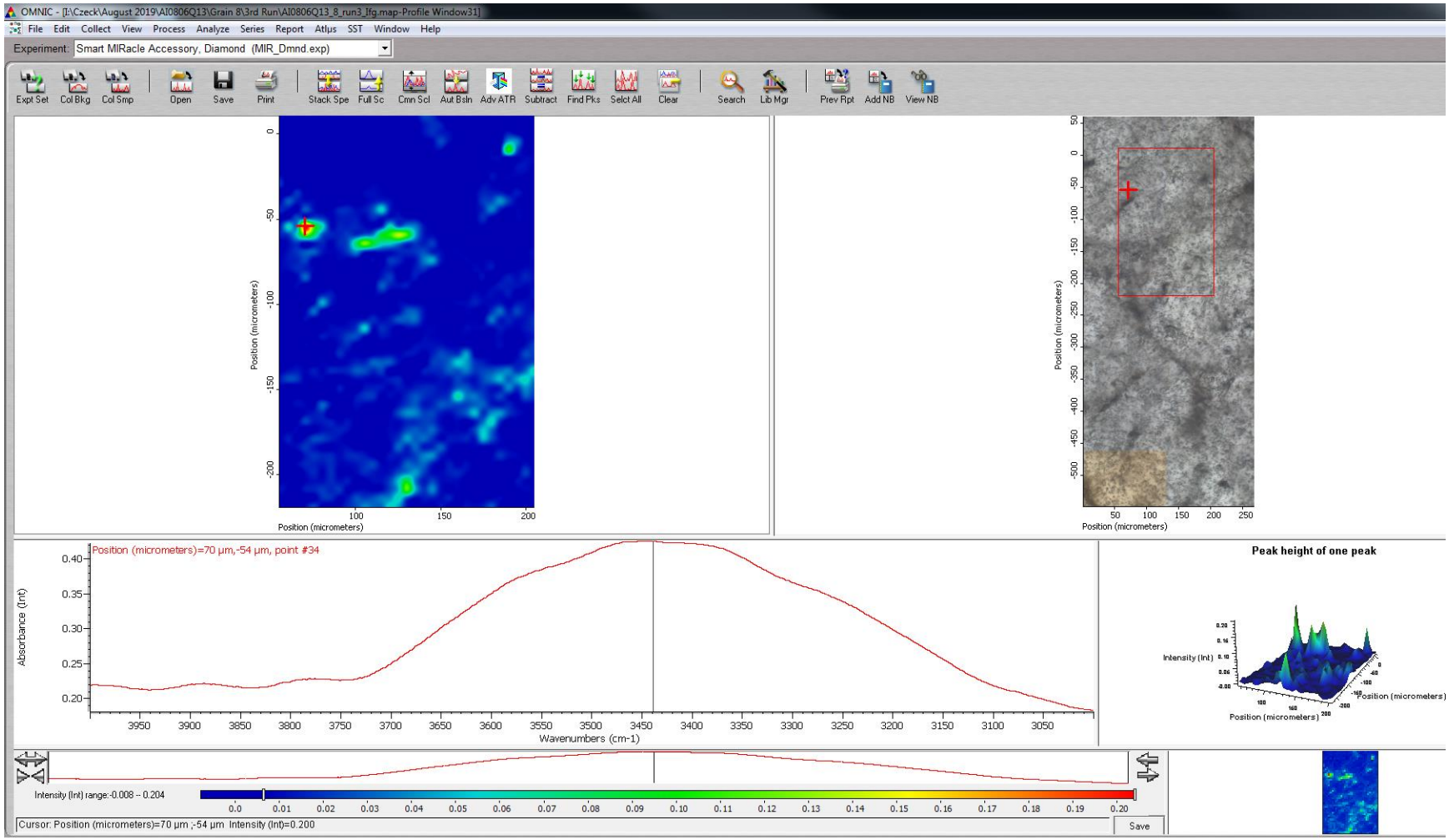

Sample AI-08-06-Q13-8 4th run absorption map with peak height function run for 3446 cm^{-1} wavelength. 1590 total spectra collected. Intensity range adjustments shown at bottom.

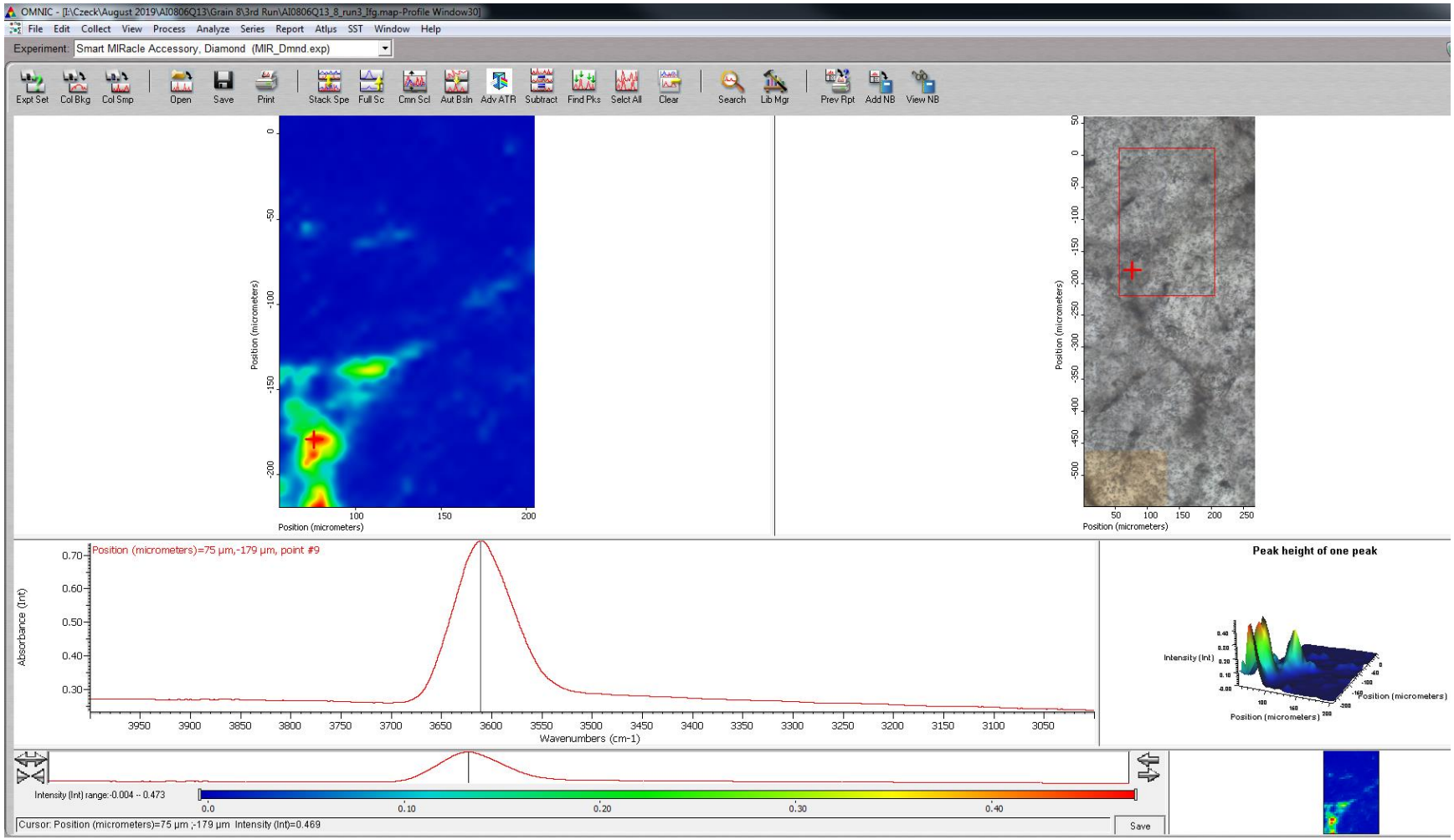

Sample AI-08-06-Q13-8 4th run absorption map with peak height function run for 3616 cm^{-1} wavelength. 1590 total spectra collected. Intensity range adjustments shown at bottom.